University of Alberta

Metal–Metal Bonding in Ternary and Quaternary Early–Late Transition Metal Pnictides

by

Meitian Wang ©

A thesis submitted to the Faculty of Graduate Studies and Research in partial fulfillment of the requirements for the degree of Doctor of Philosophy

Department of Chemistry

Edmonton, Alberta

Fall 2001

University of Alberta

Library Release Form

Name of Author: Meitian Wang

Title of Thesis: Metal–Metal Bonding in Ternary and Quaternary Early–Late Transition Metal Pnictides

Degree: Doctor of Philosophy

Year this Degree Granted: 2001

Meitian Wang
Apt. 5, 10811-86 Avenue
Edmonton, Alberta T6E 2N1

August 22, 2001

University of Alberta

Faculty of Graduate Studies and Research

The undersigned certify that they have read, and recommend to the Faculty of Graduate Studies and Research for acceptance, a thesis entitled *Metal–Metal Bonding in Ternary and Quaternary Early–Late Transition Metal Pnictides* submitted by Meitian Wang in partial fulfillment of the requirements for the degree of Doctor of Philosophy.

Prof. A. Mar

Prof. R. B. Jordan

Prof. J. Takats

Prof. R. R. Tykwinski

Prof. R. L. Eadie

Prof. G. J. Miller

August 21, 2001

To my family

Abstract

Several series of ternary compounds in the (Zr, Hf, Nb)–(Ni, Pd, Pt)–(P, As, Sb) systems, and one family of quaternary antimonides containing three transition metals have been synthesized through reactions of the elements or binary pnictides. Their structures were determined by X-ray diffraction methods and their electronic structures were calculated using the extended Hückel method. This work extends the relatively well studied early transition metal–Ni–pnicogen systems to the much more sparsely investigated Pd and Pt systems. Some of them are the first examples in their ternary or quaternary systems, or adopt new structure types. All compounds are metal-rich phases with extended early–late transition metal bonding interactions and no pnicogen-pnicogen bonding contacts.

The structures of $Zr_3Pd_4P_3$, $Hf_3Pd_4P_3$, $Nb_5Pd_4P_4$, $Nb_5Pd_4As_4$, Nb_9PdAs_7, and HfPdSb share the common structural motif of pnicogen–centred trigonal prisms with transition metals as ligands, $^{tp}[PnTM_6]$. These trigonal prisms are further condensed by sharing edges, triangular faces, or quadrilateral faces. The diversity of structures adopted arises from the differing connectivity of pnicogen–filled trigonal prisms. $Zr_3Ni_3Sb_4$, $Hf_3Ni_3Sb_4$, and $Zr_3Pt_3Sb_4$ extend the $Y_3Au_3Sb_4$-type structure to compounds containing a non-rare earth component. $Nb_{28}Ni_{33.5}Sb_{12.5}$ adopts the *X*-phase structure type, which belongs to the set of tetrahedrally close-packed (TCP) structures adopted by many intermetallic compounds. Typical of such TCP structures, the atoms reside in sites of high coordination number, with Ni and Sb in CN12 and Nb in CN14, 15 and 16 sites. The compounds $Nb_4Pd_{0.5}ZSb_2$ (Z = Cr, Fe, Co, Ni, Si) represent the first examples of

quaternary antimonides containing three transition metals in an ordered arrangement. They are distinguished by the filling of interstitial *Z* atoms into the centres of Nb_8 square antiprismatic clusters that are linked by $PdSb_4$ tetrahedra.

All compounds are metallic on the basis of resistivity measurements or predictions from band structure calculations except for $Zr_3Ni_3Sb_4$ (or $Hf_3Ni_3Sb_4$, $Zr_3Pt_3Sb_4$), which is predicted to be a small band-gap semiconductor. The Zintl concept and other electron counting rules are not applicable to any of these metal-rich pnictides except for $Zr_3Ni_3Sb_4$-type compounds. The chemical bonding, especially the various metal–metal bonding interactions, are discussed on the basis of extended Hückel band structure calculations.

Acknowledgements

I wish to extend my gratitude to my supervisor, Professor Arthur Mar, for his guidance and patience during my four years of study in Edmonton, as well as for his encouragement and support to attend several conferences and workshops. I am also grateful for the help and friendship of the past and present members of the Mar group, especially Mike Ferguson, Rob Lam, Allison Mills, Laura Deakin, and Devon Moore.

I must acknowledge the following individuals for their valuable contributions to this research: Grace Chan and Chris Sheets for their outstanding work on the quaternary transition metal antimonides; Bob McDonald (Faculty Service Officer, X-ray Crystallography Laboratory) for the X-ray data collection, and for teaching me small molecule crystallography and the use of the Platform/CCD and CAD4 diffractometers during my stay in his lab as an assistant; Tina Barker (Department of Chemical and Materials Engineering) for assistance with the EDX analyses. This work was supported financially by the Natural Sciences and Engineering Research Council (NSERC) of Canada and the University of Alberta.

Finally, I would like to thank my family for their support throughout the course of my degree.

Table of Contents

List of Tables

List of Figures

List of Crystallographic Abbreviations and Symbols

a, b, c	lengths of basis vectors, lengths of cell edges
α, β, γ	interaxial angles between b and c, a and c, and a and b axes, respectively
d_{hkl}	interplanar distance, or spacing, of neighbouring net planes (hkl)
F_c	calculated structure factor
F_o	observed structure factor
hkl	indices of the Bragg reflection (Laue indices) from the set of parallel equidistant net planes (hkl)
(hkl)	indices of a crystal face, or of a single net plane (Miller indices)
[hkl]	indices of a lattice direction
λ	wavelength
μ	linear absorption coefficient
P	experimental instability factor in weighting scheme (used in the calculation of $\sigma(I)$ to downweight intense reflections)
R	residual index
R_w	weighted residual index
R_{int}	residual index for averaged symmetry equivalent reflections
ρ	density
σ	standard deviation
U_{eq}	equivalent isotropic atomic displacement parameter
U_{ij}	elements of anisotropic atomic displacement parameter tensor
V	cell volume of the direct lattice
w	weighting factor applied to structure factor
x, y, z	coordinates of a point (location of an atom) expressed in units of a, b, and c
Z	number of formula units per unit cell

Chapter 1

Introduction

Intermetallic Compounds

Intermetallic compounds or phases are compounds of metals whose crystal structures are different from those of the constituent metals. Since the beginnings of metallurgy more than 2000 years ago, intermetallics have been exploited for various applications because of their outstanding hardness and wear resistance.[1] The alloy CuZn was used as a coinage metal by ancient civilizations.[2] Early Chinese, Etruscans, and Romans made mirrors using high tin bronze $Cu_{41}Sn_{11}$. However, owing to their inherent brittleness, the use of intermetallics as structural materials has been restricted to specialized applications. For example, the mercury compounds Ag_2Hg_3 and Sn_8Hg are used in dental fillings;[3,4] since the 1970s, the titanium aluminides Ti_3Al and TiAl have drawn considerable attention as structural materials for high-temperature applications.[5]

The varied electronic and magnetic properties of intermetallic compounds, combined with their mechanical properties, have justified their use as functional materials in numerous contexts. Many A15-type intermetallic compounds are superconductors (*e.g.*, V_3Si (T_c = 16.9 K), Nb_3Sn (T_c = 18.0 K), Nb_3Ge (T_c = 22.5 K)).[1] In particular, Nb_3Sn is used commercially as a high-field magnet.[1b] More recently, the well-known AlB_2-type intermetallic MgB_2 was discovered to undergo a superconducting transition at

39 K,[6] a breakthrough that signals the potential for uncovering even better superconductors in intermetallic systems. The magnetic properties and wear resistance of $Fe_3(Si,Al)$ have led to its wide use in the magnetic heads of tape recorders.[7] Co_5Sm and $Nd_2Fe_{14}B$ are used as permanent magnetic materials.[1,8] Bi_2Te_3 is a traditional thermoelectric material.[1] Recent studies of the $RE Fe_{4-x}Co_xSb_{12}$ (RE = La, Ce; $0 < x < 4$)[9] and $RE_3Ni_3Sb_4$ classes of compounds[10] have shed light on the design of new thermoelectric materials with improved properties.

Although intermetallic compounds have inherently superior practical advantages over organic compounds as functional materials in some applications, such as high density and wear resistance. Ironically, our ability to design intermetallic compounds is much poorer than for organic molecules. Considering that most of the elements in the Periodic Table are metals, the possible numbers of binary, ternary, quaternary, or even quintenary intermetallic compounds are almost unlimited mathematically. Of course, the real numbers will be restricted by the thermodynamics of each individual system and by the preparative conditions that we can realize. Large numbers of intermetallic compounds have already been isolated and characterized:[11,12] there are 27686 entries in the 1997 Desk Edition of Pearson's Handbook (Crystallographic Data for Intermetallic Phases).[13] These compounds can be classified into more than 2000 structure types. Still more intermetallic phases with known structure types, or even new structure types, continue to be found today. However, our understanding of the structural principles of intermetallics is fairly limited because of the complexity of the chemical bonding involved.[14] This is perhaps part of the reason that historically chemists have not entered

this field enthusiastically. Generally, it is very difficult to design new intermetallic compounds with desired properties.

If one or more constituent elements are more electronegative than the others, the compound is called a polar intermetallic because some degree of electron density redistribution will take place. Furthermore, if the number of metalloid (*e.g.*, Sb, Te) or nonmetal (*e.g.*, Si, P, As) atoms in the compound is small, metal-rich compounds result. In our definition, the term metal-rich is not necessarily related to the proportion of metal atoms in a compound. A transfer of valence electrons occurs, in principle, from the metal atoms to the more electronegative metalloids or nonmetal atoms to form metal–metalloid or –nonmetal bonds in a polar intermetallic compound. If the metal atoms have enough extra valence electrons to form metal–metal bonds, such a compound can also be regarded as a metal-rich compound. According to this definition, NbO and $MoCl_2$ are metal-rich compounds and NaCl and Li_3N are not. Metal-rich halides (F, Cl, Br, I),[15-19] chalcogenides (O, S, Se, Te),[15-17,20,21] and pnictides (N, P, As, Sb, Bi)[15,17,25-63] have been studied by chemists since the 1960s. These metal-rich compounds bridge intermetallics and normal valence compounds from the points of view of both chemical bonding and structural chemistry. Further studies of the structural chemistry and bonding patterns in metal-rich compounds will hopefully improve our understanding of intermetallic compounds. The focus of this thesis is the synthesis and structural characterization of new ternary and quaternary transition metal-rich pnictides.

Ternary Transition Metal Pnictides

The group 15 elements (*Pn* = N, P, As, Sb, Bi) are known as the pnicogens. Compounds containing the pnicogens as anions are called pnictides. The nitrides are unique;[22] their preparations, stabilities, structures, and properties are quite different from the other pnictides, and will not be discussed further here. The transition metals (group 3 to group 12) can be roughly separated into two regions, early transition metals (E-*TM*) and late transition metals (L-*TM*), with group 7 (Mn, Tc, Re) as the boundary. Early transition metals have few valence electrons in relatively expanded d orbitals. These d orbitals can overlap considerably with the orbitals of neighbouring atoms to form chemical bonds. The d orbitals of late transition metals, on the other hand, are rather contracted. Mixed early transition metal ternary pnictides, such as $Zr_{6.45}Nb_{4.55}P_4$,[23] have been investigated systematically since the early 1960s. In this class of compounds, some ternaries can adopt structures that are not formed in either of the corresponding binary systems. An important principle resulting from studies of the mixed early-transition-metal pnictides is the concept of differential fractional site occupancy (DFSO),[24] which serves as a useful tool for interpreting structure and bonding in this class of compounds. The preparation of mixed late transition metal pnictides is still an unexplored area.

In this work, investigations of the ternary (E-*TM*)–(L-*TM*) pnictides, particularly the (group 4 (Zr, Hf) or 5 (Nb, Ta))–(group 10 (Ni, Pd, Pt))–pnicogen systems, are described. All known ternary phosphides, arsenides, and antimonides in the above systems are listed in Tables 1-1 and 1-2.[25-63] Only two bismuthides, Zr_6NiBi_2 (Fe_2P-type)[47] and Hf_6NiBi_2 (Fe_2P-type)[47], have been reported to date. This group of compounds usually contains (E-*TM*)–(L-*TM*) interactions that can be understood in terms of a Lewis

acid-base stabilization.[64] The strengths of early–late transition metal interactions (sometimes called polar intermetallic bonds by chemists) can also be rationalized by the study of the heats of formation of binary early–late transition metal alloys.[64,65] Specifically, binary alloys involving group 4 and group 8, 9, or 10 metals were predicted to have the largest heats of formation. These ideas can be transferred to the study of other metal-rich compounds. All compounds in Tables 1-1 and 1-2 are metal-rich phases, but different degrees of metal–metal bonding exist in each compound. This reflects the importance of metal-metal bonding in stabilizing ternary transition metal pnictides. These compounds can be further divided into two classes based on the presence or absence of *Pn–Pn* bonds. It seems strange that it is possible to have both metal–metal bonds and *Pn–Pn* bonds coexisting in one compound. One would think that, under the high temperature conditions often employed in the preparation of solid state compounds, the pnicogens would be reduced by the extra metal atoms, destroying any *Pn–Pn* bonds. However, if the metal–metal and *Pn–Pn* bonds are strong, there is no reason that they have to be replaced by metal–*Pn* bonds, at least from a chemical bonding point of view. Compounds containing both *Pn–Pn* bonds and metal–metal bonds in different parts of their structures can be formed at the right stoichiometries and reaction conditions.

Most of the compounds have been prepared by high temperature (800–1100°C) direct reactions. Their structures have been determined by single crystal or powder X-ray diffraction methods. The unit cells of transition metal-rich phosphides and arsenides usually have one short axis of about 3–4 Å, and two layers of atoms along this axis. Therefore, most of the structures are most clearly presented in projection view along the short axis, rather than in 3D view, in figures. In order to better understand the structures,

it would help to first introduce the 2D projections of different polyhedra. In Schemes **1**, **2**, **3**, and **4**, the lower part shows a 3D representation of the polyhedron and the upper part shows a projection view approximately along the vertical axis of the corresponding 3D view. In the projection view, light and heavy lines indicate different heights along the projection axis, and dashed lines connect atoms at different heights. In **1**, trigonal prisms in two common modes of connectivity, face-sharing of the trigonal faces or of the quadrilateral faces, are portrayed.

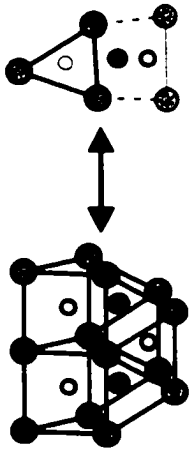

Trigonal prisms
1

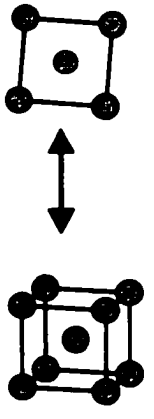

Body centred cube
2

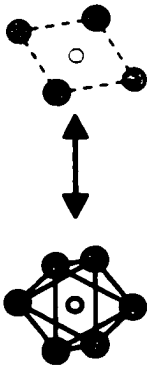

Octahedron
3

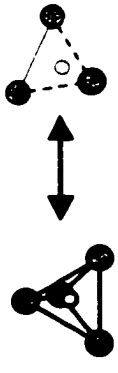

Tetrahedron
4

Structures with *Pn–Pn* Bonds. $ZrNi_{0.75}P_2$, $ZrNi_{0.75}As_2$, and $HfNi_{0.75}As_2$ are isostructural and adopt a defect $ZrCuSi_2$-type structure. The $ZrNi_{0.75}P_2$ structure is depicted in Figure 1-1(a). The structure contains 2D phosphorus square sheets with P–P distances of 2.558(2) Å that indicate weak bonding (*cf.*, sum of Pauling single bond radii $2r_P = 2(1.10) = 2.20$ Å).[66] Similar 2D nickel square sheets with phosphorus atoms above and below coordinating each nickel atom tetrahedrally form a second layer substructure, $^{2}_{\infty}[Ni_2P_2]$. The two 2D substructures are separated by Zr atoms. The Ni–Ni distances of 2.558(2) Å in the 2D nickel square sheets are definitely bonding contacts (*cf.*, sum of Pauling single bond radii $2r_{Ni} = 2(1.149) = 2.298$ Å).[66] The Zr and Ni atoms are also bonded, with Zr–Ni distances of less than 3.0 Å. The $ZrNi_2P_2$ structure is closely related to the $ZrNi_{0.75}P_2$ structure, as is clearly shown in Figure 1-1(b). Here, two $^{2}_{\infty}[Ni_2P_2]$ sheets are separated by Zr atoms. The $^{2}_{\infty}[Ni_2P_2]$ sheets are stacked in such a way that each P atom has one other P atom above or below it along the *c* axis, as indicated by dashed lines in Figure 1-1(b). Even though a single crystal structure refinement is not available, the P–P bonds can be assumed solely on the basis of cell parameters determined by powder diffraction. Finally, the $NbNiP_2$ structure contains parallel corrugated 2D sheets in the *ab* plane that are built up from $^{tp}[Zr_4Ni_2]$ trigonal prisms (Figure 1-2). The centres of the prisms are alternately occupied by P atoms. These 2D sheets resemble a fragment of the simple binary WC structure. P–P pairs are stuffed between the 2D sheets. The P–P distance of 2.8 Å is long, but still indicates weak bonding.

Structures without *Pn–Pn* bonds. Most transition metal-rich phosphide and arsenide structures can be described in terms of P- or As-centred polyhedra (trigonal

prisms in most cases) with metal atoms as ligands. However, it is more convenient to describe the $Zr_2Ni_3P_3$ structure as being composed of metal-centred polyhedra with P atoms as ligands (Figure 1-3). The Zr(1) and Zr(2) atoms are each coordinated by 6 P atoms in trigonal prismatic $^{tp}[Zr(1)P_6]$ and octahedral fashions $^{oct}[Zr(2)P_6]$, respectively. All Ni atoms are bonded to 4 P atoms, forming $^{tet}[NiP_4]$ tetrahedra. The whole structure is constructed from $^{tp}[Zr(1)P_6]$, $^{oct}[Zr(2)P_6]$, and $^{tet}[NiP_4]$, which share faces and edges in such a manner that metal–metal bonds are formed through shared faces. Therefore, the metal coordination numbers (CN) increase to 17, 13, 12, 10, and 12 for Zr(1), Zr(2), Ni(1), Ni(2), and Ni(3), respectively, if a distance of 3.6 Å is considered as a Zr–Zr bond. These high coordination numbers are commonly observed in metal-rich phases.

ZrNiP and HfNiP crystallize in the Ni_2In- and Co_2Si-type structures, respectively. As can be seen in Figure 1-4, both structures contain P–centred trigonal prisms with metal atoms as ligands, $^{tp}[PM_6]$. These trigonal prisms are linked to adjacent prisms through two edges to form a one-dimensional chain. Each trigonal prism also shares its two trigonal faces with adjacent prisms above and below resulting in a two-dimensional corrugated sheet. In the Ni_2In structure, one quadrilateral face of each trigonal prism is aligned with adjacent prisms along the *c* direction, as indicated by an arrow in Figure 1-4(a). In contrast, the trigonal prisms are connected in a more flexible manner in the Co_2Si structure; therefore, the Co_2Si type should be adopted by a larger number of compounds. In fact, only ZrNiP crystallizes in the Ni_2In-type structure, while *M*NiP (*M* = Hf, Nb, Ta), *M*NiAs (*M* = Zr, Hf, Nb, Ta), and even the antimonides ZrNiSb and HfNiSb all adopt the Co_2Si-type structure. Another common structure adopted by metal-rich compounds with a metal-to-nonmetal ratio of 2 is the Fe_2P-type structure, shown in

Figure 1-5(a). Six P-centred trigonal prisms form a six-membered ring that surrounds another P-centred trigonal prism in the centre. $(Nb_{17}Ni_{50})P_{33}$ adopts this structure, with 25% Nb and 75% Ni atoms randomly occupying the Fe sites. M_6NiPn_2 (M = Zr, Hf, Pn = Sb, Bi) are ternary substitutional variants of the Fe_2P-type structure. The Fe sites are occupied by Zr or Hf atoms, and the P sites (0, 0, 1/2) and (1/3, 2/3, 0) are occupied by Ni and Sb, or Bi atoms, respectively. The recently discovered $M_5Pd_9P_7$ (M = Zr, Hf) compounds, again with a metal-to-nonmetal ratio of 2, adopt a new structure type (Figure 1-5(b)). It is very clear that the $Zr_5Pd_9P_7$-type structure is a hybrid version of the Co_2Si- and Fe_2P-type structures when Figure 1-5(b) is compared with Figures 1-4(b) and 1-5(a). $Zr_2Ni_{12}P_7$ and $Zr_6Ni_{20}P_{13}$ have hexagonal structures composed of different numbers of P-centred and Ni-centred trigonal prisms (Figures 1-6(a) and (b)). The $Zr_2Ni_{12}P_7$ structure has only P-centred trigonal prisms, ${}^{tp}[PZr_2Ni_4]$ and ${}^{tp}[PNi_6]$. In addition to ${}^{tp}[PZr_4Ni_2]$, ${}^{tp}[PZr_2Ni_4]$, and ${}^{tp}[PNi_6]$ prisms, the $Zr_6Ni_{20}P_{13}$ structure also contains Ni-centred trigonal prisms with Zr ligands, ${}^{tp}[NiZr_6]$. Such late transition metal-centred trigonal prisms with early transition metal atoms as ligands, ${}^{tp}[(L\text{-}TM)(E\text{-}TM)_6]$, are another commonly observed structural feature in transition metal-rich compounds. $Nb_2Ni_2P_3$ is also isostructural to $Zr_2Ni_{12}P_7$ but with different atomic arrangements. The phosphorus atoms occupy the zirconium sites and the niobium atoms occupy half the nickel sites ($Zr_2Ni_{12}P_7 \rightarrow P_2(Ni_6Nb_6)P_7 = Nb_2Ni_2P_3$).

The $ZrNi_4P_2$ structure also contains P-centred trigonal prisms, ${}^{tp}[PZr_2Ni_4]$, which are connected by Ni_4 tetrahedral clusters at the centres of the a and b axes (Figure 1-7). The Ni_4 tetrahedra share opposite edges to form one-dimensional chains, which are not unusual for late transition metal-rich compounds. For example, $RECo_4B_4$ (RE = La, Pr,

Nd, Sm) contain Co_4 tetrahedral chains.[67] In the $Zr_9Ni_2P_4$ structure, P- and Ni-centred trigonal prisms, $^{tp}[PZr_6]$ and $^{tp}[NiZr_6]$, are connected in such a way that body centred cubic niobium fragments form (Figure 1-8(a)). These cubes are condensed via opposite faces to form linear chains along the *c* axis at the corners and centre of the unit cell. Two such chains fused together by sharing faces are located at the centres of the *a* and *b* axes. Body centred cubic (bcc) fragments, which resemble the elemental structures of the early transition metals, are common structural motifs in early-transition metal-rich phases. Similar structural features exist in the Nb_3Ni_2P structure (Figure 1-8(b)). Phosphorus and nickel atoms centre Nb trigonal prisms. Bcc fragments also exist, but the centres of the cubes are randomly occupied by 50% Nb and 50% Ni.

The structures presented in Figures 1-4, 1-5, 1-6, 1-7, and 1-8 contain trigonal prism building blocks aligned along the same direction. In other words, the pseudo threefold axes of the trigonal prisms are all parallel. These prisms can also be arranged with their threefold axes perpendicular to each other (Scheme **1**). This possibility reveals the rich structural chemistry of metal-rich compounds. $Zr_2Ni_{1-x}P$ and $Hf_5Ni_{1+x}P_3$ are two examples, and projections along the *b* axis of these two structures are shown in Figure 1-9(a) and (b). They have similar structural features: ribbons made up of P- and Ni-centred trigonal prisms with their pseudo threefold axes in the projection plane (*ac* plane) are connected by P-centred trigonal prisms whose pseudo threefold axes are along the projection axis (*b* axis). The difference is that the width of the ribbons is three trigonal prism units for $Zr_2Ni_{1-x}P$ and four units for $Hf_5Ni_{1+x}P_3$. Some degree of non-stoichiometry (partial occupancy of the centres of the trigonal prisms) exists for both compounds, as is revealed by the formulae.

The Zr_2NiP_2 structure is different from other structures discussed so far. Phosphorus atoms occupy not only the centres of Zr trigonal prisms, ${}^{tp}[PZr_6]$, but also the centres of Zr octahedra, ${}^{oct}[PZr_6]$ (Figure 1-10). If all of the Ni atoms are removed from the structure, the binary TiP-type structure results. Square antiprismatic coordination of the P and Ni atoms, $[PNb_8]$ and $[NiNb_8]$, is also observed in the Zr_4NiP structure, as shown in Figure 1-11.

The antimonides *M*NiSb (*M* = Zr, Hf) and M_6NiSb_2 (*M* = Zr, Hf) have been discussed with the phosphides and arsenides. The rest of the ternary antimonides adopt structures more commonly observed for intermetallic compounds, consistent with Sb being more electropositive than P and As. The $M_3Ni_3Sb_4$ (*M* = Zr, Hf) structure will be discussed in Chapter 4. $Hf_{10}Ni_xSb_{6-x}$ adopts the W_5Si_3-type structure, which is discussed in Chapter 6. $Nb_{28}Ni_{33.5}Sb_{10.5}$ is the topic of Chapter 5. The remaining antimonide structure Zr_5NiSb_3 is discussed here. Two different kinds of one-dimensional chains made up of trigonal antiprisms sharing opposite triangular faces exist in this structure (Figure 1-12). One is a Ni-centred Zr_6 trigonal antiprism chain, ${}^{2}_{\infty}[NiZr_{6/3}]$, and the other is a Zr-centred Sb_6 trigonal antiprism chain, ${}^{2}_{\infty}[ZrSb_{6/3}]$, which is connected further to adjacent ${}^{2}_{\infty}[ZrSb_{6/3}]$ chains by sharing all corners.

In general, all of the ternary compounds listed in Tables 1-1 and 1-2 have metal–metal bonds, and only a few contain *Pn*–*Pn* bonds as well. The phosphides and arsenides show similar structural chemistry, featuring *Pn*–centred trigonal prisms in particular. The structures of the antimonides resemble more classical intermetallic structures. Ternaries containing Ni have been studied the most extensively. The corresponding chemistry of Pd and Pt has only recently begun to be explored.

Chemical Bonding in Metal-Rich Compounds

An instructive band structure diagram for binary Zintl phases[68] can be adapted to formulate a general bonding scheme for binary and ternary transition metal-rich compounds (TM_pX_q, (E-TM)$_p$(L-TM)$_q$$X_r$). The band structures can be constructed conceptually in several steps. First, the metal atoms transfer their valence electrons to the valence shell of the nonmetal component to form metal–nonmetal bonds (TM–X)^b as shown in **5(a)**. Closed shell electronic configurations are then achieved for the nonmetal atoms. Therefore, there is usually no impetus to form X–X bonds. By our earlier definition of metal-rich compounds, the metal atoms should still have available valence electrons, which may be used to form metal–metal bonds as in elemental metals (TM–TM)^b, **5(b)**. For most metal-rich phases, these interactions are insufficient to open up a band gap, shown in **5(b)**, between metal–metal bonding and antibonding bands, and metallic behaviour results. In ternary compounds involving early (E-TM) and late (L-TM) transition metals, heteroatomic (E-TM)–(L-TM) bonding interactions may be found by donating essentially non-bonding d electrons of the late transition metal L-TM to empty acceptor d orbitals of the early transition metal E-TM, **5(c)**. Although the extent of overlap between the different bands in metal-rich compounds will depend on the details of an actual band structure calculation, the qualitative pictures are generally preserved.

As an example, the band structure (density of states, DOS) of a ternary metal-rich phosphide, $Nb_5Pd_4P_4$,[69] which was calculated using the semi-empirical extended Hückel tight binding (EHTB) method, is shown in **6** to verify the qualitative picture in **5**. Most of the phosphorus 3p states are located from –13.5 to –16.0 eV mixed with some Nb and

Pd d states, where Nb–P and Pd–P bonding interactions take place. The narrow peak centred around –12.5 eV consists of Pd 4d states, which are mixed with some Nb 4d states in the same region. Nb–Pd bonding interactions occur in this region. The DOS is dominated by Nb 4d states above –11 eV. The Nb–Nb interactions change from bonding $(Nb–Nb)^{b}$ to antibonding $(Nb–Nb)^{ab}$ gradually as the energy increases. The horizontal line at –9.6 eV indicates the Fermi level. Electrons fill all states up to the Fermi level. Overall, most of Nb–P, Pd–P, Nb–Pd, and Nb–Nb bonding levels are filled in $Nb_5Pd_4P_4$ structure.

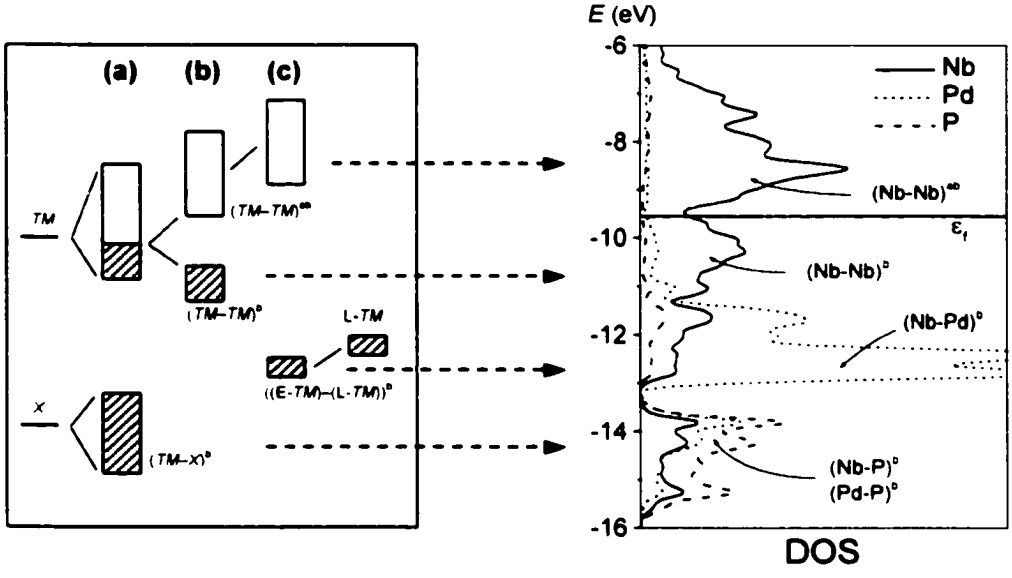

5 6

Objective

In view of the breathtaking structural richness of ternary transition metal pnictides revealed in yet far from complete investigations, the goal of this research was to expand on their structural chemistry and extend studies to quaternary systems. Investigations were focused on (Zr, Hf, Nb, Ta)–(Ni, Pd, Pt)–(P, As, Sb) systems with the expectation

that early–late transition metal interactions would stabilize some new structure types. The importance of homo- and heteroatomic metal–metal bonding in stabilizing different structures was examined via electronic band structure calculations. The recurring structural motifs described earlier such as pnicogen-centred trigonal prisms and square antiprisms are used as building blocks, where applicable, to construct new structure types throughout this thesis. Several new ternary pnictides are presented in Chapters 2, 3, 4, and 5. Quaternary systems are discussed in Chapter 6. Generalizations on crystal growth and structural relationships for most compounds presented are given in the conclusions in Chapter 7. Studies of $ZrPd_3Si_3$ and $RECu_{1+x}As_2$ (RE = La, Ce, Pr) are contained in Appendix A and B, respectively. More crystallographic data of compounds discussed are presented in Appendix C.

Experimental Methods

Synthesis. Conventional methods for the synthesis of solid-state compounds typically involve high-temperature (~ 1000 °C or higher) treatments over long time periods (weeks or even months) in order to overcome huge kinetic barriers.[70-72] Under such extreme reaction conditions, only thermodynamically stable compounds result in most cases. There have been some developments in the use of low-temperature synthetic routes. For example, alkali-metal polychalcogenide fluxes have been applied extensively in the preparation of ternary and quaternary chalcogenides.[73] Low-temperature fluxes (200–600 °C) serve as a solvent to facilitate particle mixing, and also allow access to compounds that are thermodynamically unstable at high temperatures. A low-temperature solvothermal route for the synthesis of metal-rich phosphides has been

discovered.[74] However, most of this work has been restricted to binary systems. No general low-temperature routes are yet available for pnictide systems. Therefore, high-temperature direct reactions were employed during our investigations. Reactions were routinely carried out by loading stoichiometric mixtures of the elements, usually in the form of powders, into fused silica tubes (typically ~70 mm long and 10 mm in diameter). The tubes were then sealed under dynamic vacuum. Since it is difficult to monitor the progress of high-temperature reactions and the reaction mechanisms of such complex systems are generally unknown, the reaction conditions have to be optimized by trial and error. Most reactions were carried out between 800 and 1000 °C for several days. At such high temperatures, the silica tube can sometimes participate in the reaction, giving "undesired" silicides or even oxides. If this is a serious problem, alumina or metal (Nb, Ta) tubes can be used instead.

Single crystals are crucial for the determination of new structures. Crystal growth in sealed silica tube reactions can be promoted by slowly cooling the reaction mixtures, by adding a low melting solid (*e.g.*, Sn, mp = 232 °C) as a flux to enhance diffusion of the reactants and to facilitate nucleation, or by adding a small amount of a volatile solid (usually I_2 or a binary halide) to enhance gas phase chemical transport. It is worth mentioning that the surface of the silica tube itself can promote crystal growth in some cases; it is not unusual to observe that reactions carried out in silica tubes give impure products but better crystals, and that reactions that took place in alumina or metal tubes produce pure products but poor quality crystals. Nature plays cruel tricks on the hapless solid state chemist.

The highest temperature that normal furnaces can reach is about 1200–1500°C. If even higher temperatures are desired, arc-melting is the method of choice.[72] Basically, an arc is produced by passing a high current from a tungsten cathode to a crucible anode, which is also the container for the pressed pellet of reactants, under an inert atmosphere (Ar, He). The arc is then moved to bathe the sample, and the current is increased until the sample melts. When the arc is turned off, the product solidifies as a button. Temperatures higher than 2000°C are easily reached using this method. The whole process takes only 10 seconds to a minute. Therefore, the arc-melting method is a fast and convenient way to synthesize intermetallic compounds. However, because of the enormous temperature changes that occur within a short reaction time, thermodynamic equilibrium is not reached. The products are prone to have more defects and disordered domains. It is typical to anneal arc-melted samples in silica tubes at about 800°C for a week.

Characterization. The chemical compositions of compounds are determined by X-ray fluorescence analysis on a scanning electron microscope (SEM).[75] A high energy electron beam is directed at the sample. Core electrons of the elements in the sample are ejected from the atoms, electrons from outer orbitals then fill the vacant levels, and X-rays with the characteristic energies (or wavelengths) of the particular atoms are emitted. Thus, this technique can qualitatively identify the elements present in the sample. If suitable standards are available, quantitative analysis can also be carried out. The SEM is equipped with an energy-dispersive spectrometer to discriminate X-ray energies. Accordingly, this technique is called energy-dispersive X-ray (EDX) analysis.

If crystals are available, the structures are usually determined using single crystal X-ray diffraction.[71,72,76] Three-dimensional periodic objects diffract radiation of an appropriate wavelength. The wavelength of X-rays (~ 1 Å) is comparable with the interatomic spacing in crystals and, therefore, can be diffracted efficiently by crystals. The directions and intensities (more accurately, structure factors with amplitude and phase) of the diffracted X-ray beams contain all the information about the internal structure of the crystal. Various devices (called diffractometers) have been developed to collect diffraction information. A crystal structure model can be proposed and refined from the diffraction patterns.

Powder X-ray diffraction can be described as a projection of three-dimensional diffraction patterns into a one-dimensional space. It is usually difficult to extract enough information to determine a new structure from powder X-ray diffraction patterns. Nevertheless, powder diffraction is very useful in solid state chemistry research.[71] It is a convenient, and practically the only, way to identify crystalline phases in solid state samples. The detection limits are typically better than 5 percent. Each crystalline phase has its own unique powder diffraction pattern, which is like a fingerprint. These patterns can be generated easily if the crystal structures of compounds are known. In practice, the chemist can identify known phases and discover new phases in the reaction product by comparing the powder diffraction pattern against a library of patterns for known compounds. Usually, isostructural compounds will generate similar powder diffraction patterns. The structures of new compounds may be identified if they adopt a known structure type. Then the cell parameters of the new compounds can be measured

accurately by indexing their powder diffraction patterns, and structural parameters can be refined by the Rietveld method[77] using data from a powder X-ray diffractometer.

Band Structure. Semi-empirical extended Hückel tight binding (EHTB) calculations have been used for almost 40 years to analyze the electronic structures of molecules, solids, and surfaces.[78] The orbital interactions, which can be deduced easily from EHTB calculations, provide chemists with a simple tool for understanding structures, bonding, and reactions. In EHTB calculations, only valence electrons are considered. One-electron crystal orbitals are linear combinations of Slater-type valence orbitals (STOs) with exponents obtained from first principle calculations. The Hamiltonian matrix is constructed semi-empirically using the valence state ionization potentials (VSIPs) of the atoms. Despite its limitations, the EHTB method provides a simple and fast way to calculate the band structures of solids. Chemists have successfully used EHTB calculations to interpret chemical bonding and to examine trends in structural chemistry. The density of states (DOS) and detailed band dispersion analysis can provide great insight into a material's physical properties. EHTB calculations are used extensively to interpret chemical bonding interactions in this research.

Table 1-1. Known Ternary Compounds in the (Zr, Hf)–(Ni, Pd, Pt)–(P, As, Sb) Systems. Structure types are given in parentheses.

P		As		Sb	
$ZrNi_{0.75}P_2$ [25]	($ZrCuSi_2$)	$ZrNi_{0.75}As_2$ [25]	($ZrCuSi_2$)		
$ZrNi_2P_2$ [26]	($ThCr_2Si_2$)				
$Zr_2Ni_3P_3$ [27]	($Zr_2Ni_3P_3$)	$Zr_2Ni_3As_3$ [27]	($Zr_2Ni_3P_3$)		
ZrNiP [28]	(Ni_2In)	ZrNiAs [41]	(Co_2Si)	ZrNiSb [42]	(Co_2Si)
$ZrNi_4P_2$ [29]	($ZrFe_4Si_2$)	$ZrNi_4As_2$ [29]	($ZrFe_4Si_2$)	$ZrNi_2Sb$ [43]	(YPt_2In)
Zr_2NiP_2 [30]	(Be_3N_2)	Zr_2NiAs_2 [30]	(Be_3N_2)	$Zr_3Ni_3Sb_4$ [44]	($Y_3Au_3Sb_4$)
$Zr_2Ni_{12}P_7$ [31]	($Zr_2Fe_{12}P_7$)			Zr_5NiSb_3 [45]	(Ti_5Ga_4)
$Zr_2Ni_{1-x}P$ [32]	($Zr_2Ni_{1-x}P$)			$Zr_5Ni_{0.5}Sb_{2.5}$ [46]	(Mn_5Si_3)
Zr_4NiP [33]	(Nb_4CoSi)			Zr_6NiSb_2 [47]	(Fe_2P)
$Zr_6Ni_{20}P_{13}$ [31]	($Zr_6Ni_{20}P_{13}$)				
$Zr_9Ni_2P_4$ [34]	($Zr_9Ni_2P_4$)				
		$HfNi_{0.75}As_2$ [25]	($ZrCuSi_2$)		
$Hf_2Ni_3P_3$ [27]	($Zr_2Ni_3P_3$)	$Hf_2Ni_3As_3$ [27]	($Zr_2Ni_3P_3$)		
HfNiP [35]	(Co_2Si)	HfNiAs [41]	(Co_2Si)	HfNiSb [42]	(Co_2Si)
$HfNi_4P_2$ [29]	($ZrFe_4Si_2$)	$HfNi_4As_2$ [29]	($ZrFe_4Si_2$)	$HfNi_2Sb$ [43]	(YPt_2In)
$HfNi_xP$ [36]	(Be_3N_2)			$Hf_3Ni_3Sb_4$ [44]	($Y_3Au_3Sb_4$)
Hf_2NiP [37]	(Hf_2NiP)			Hf_5NiSb_3 [48]	(Ti_5Ga_4)
Hf_4NiP [33]	(Nb_4CoSi)			$Hf_{10}Ni_xSb_{6-x}$ [49]	(W_5Si_3)
$Hf_5Ni_{1+x}P_3$ [38]	($Hf_5Ni_{1+x}P_3$)			Hf_6NiSb_2 [47,50]	(Fe_2P)
$Zr_3Pd_4P_3$ [39]	($Zr_3Pd_4P_3$)	ZrPdAs [40]	(NbCoB)	ZrPdSb [40]	(Co_2Si)
$Zr_5Pd_9P_7$ [40]	($Zr_5Pd_9P_7$)				
$Hf_3Pd_4P_3$ [39]	($Zr_3Pd_4P_3$)			HfPdSb [39]	(Co_2Si)
$Hf_5Pd_9P_7$ [40]	($Zr_5Pd_9P_7$)				
				$Zr_3Pt_3Sb_4$ [44]	($Y_3Au_3Sb_4$)

Table 1-2. Known Ternary Compounds in the (Nb, Ta)–(Ni, Pd, Pt)–(P, As, Sb) Systems. Structure types are given in parentheses.

P		As		Sb
$NbNiP_2$ [51]	($UMoC_2$)	$NbNiAs_2$ [59]	($UMoC_2$)	$Nb_{28}Ni_{33.5}Sb_{12.5}$ [63] (X-phase)
NbNiP [52]	(Co_2Si)	NbNiAs [60]	(Co_2Si)	
$Nb_2Ni_2P_3$ [53]	($Nb_2Ni_2P_3$)			
Nb_2Ni_9P [54]	($AuBe_5$)			
Nb_3Ni_2P [54]	(U_3Si_2)			
Nb_4NiP [55]	(Nb_4CoSi)			
$Nb_5Ni_4P_4$ [56]	($Nb_5Cu_4Si_4$)			
$Nb_{17}Ni_{50}P_{33}$ [54]	(Fe_2P)			
$TaNiP_2$ [57]	($UMoC_2$)			
TaNiP [58]	(Co_2Si)	TaNiAs [60]	(Co_2Si)	
Ta_4NiP [33]	(Nb_4CoSi)			
$Ta_5Ni_4P_4$ [56]	($Nb_5Cu_4Si_4$)			
$Nb_5Pd_4P_4$ [39]	($Nb_5Cu_4Si_4$)	$Nb_5Pd_4As_4$ [61]	($Nb_5Cu_4Si_4$)	
		Nb_9PdAs_7 [62]	(Nb_9PdAs_7)	

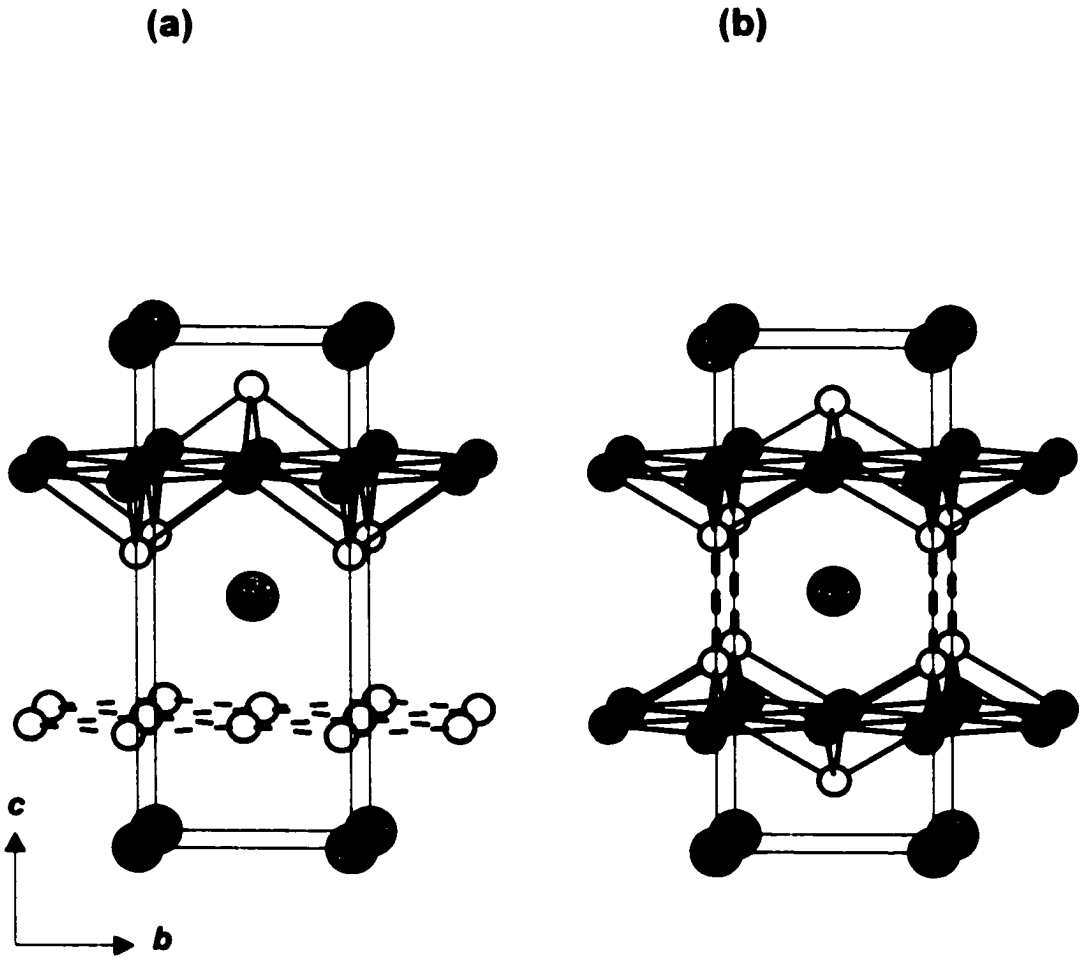

Figure 1-1. Structures of (a) $ZrNi_{0.75}P_2$ ($ZrCuSi_2$-type) with origin shift (0, 0.5, –0.2412) and (b) $ZrNi_2P_2$ ($ThCr_2Si_2$-type). The large lightly shaded circles are Zr atoms, the medium solid circles are Ni atoms, and the small open circles are P atoms.

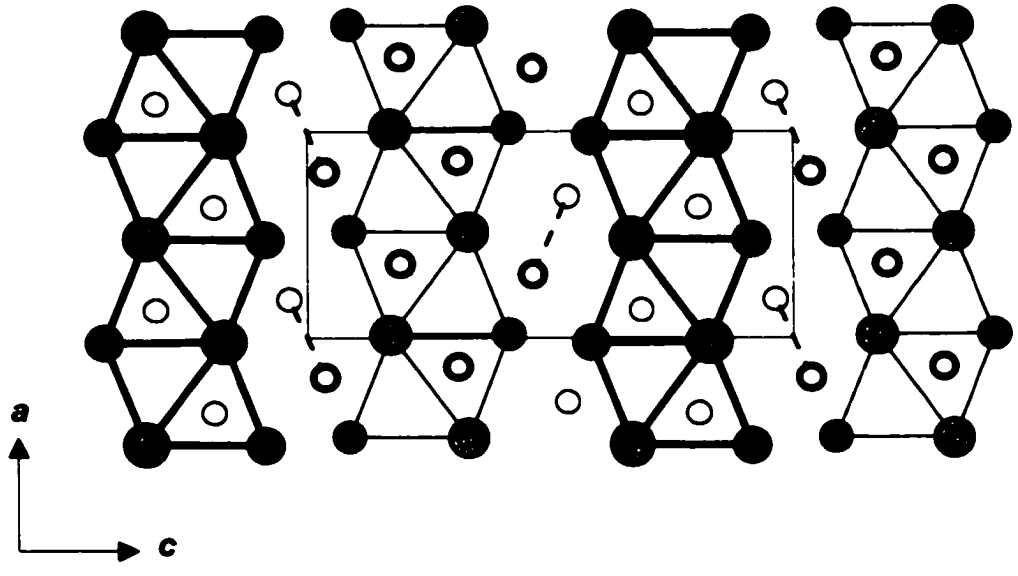

Figure 1-2. Structure of $NbNiP_2$ ($UMoC_2$-type) viewed in projection down the *b* axis. The large lightly shaded circles are Nb atoms, the medium solid circles are Ni atoms, and the small open circles are P atoms. Light and heavy lines indicate a displacement by 1/2 the repeat along the projection axis.

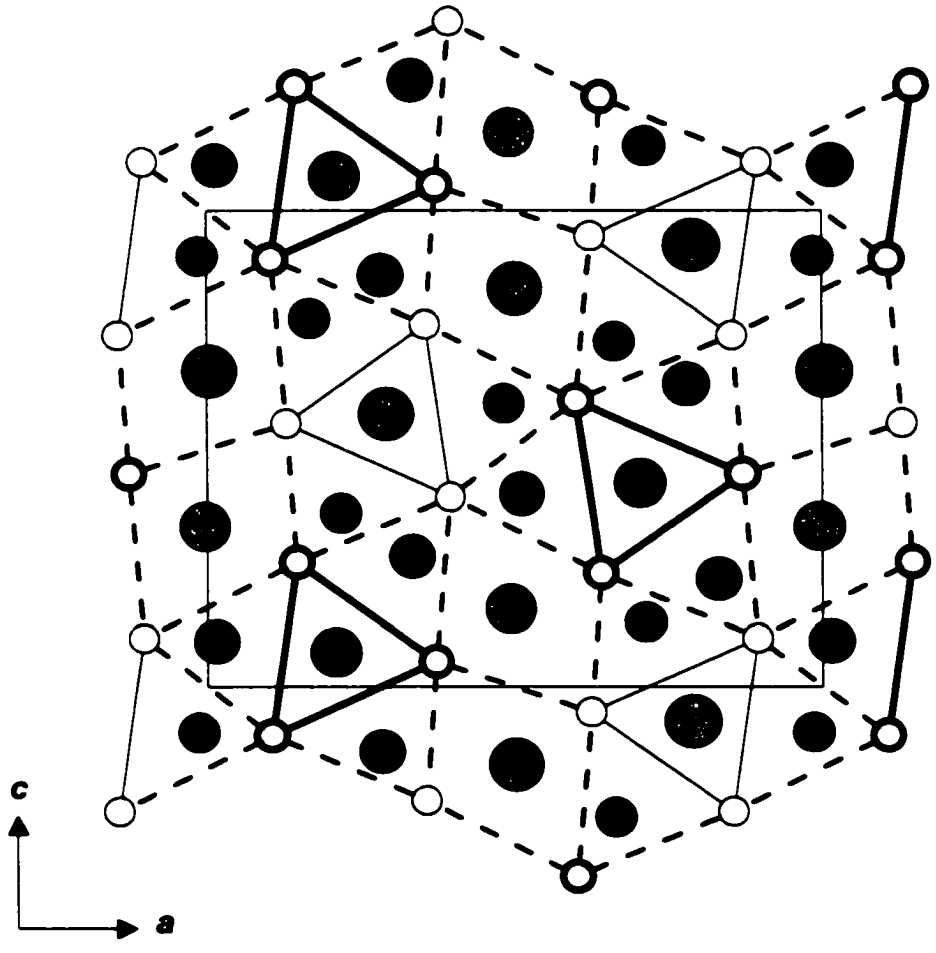

Figure 1-3. Structure of $Zr_2Ni_3P_3$ ($Zr_2Ni_3P_3$-type) viewed in projection down the *b* axis. The large lightly shaded circles are Zr atoms, the medium solid circles are Ni atoms, and the small open circles are P atoms. Light and heavy lines indicate a displacement by 1/2 the repeat along the projection axis, and dashed lines connect atoms at different altitudes along the projection axis.

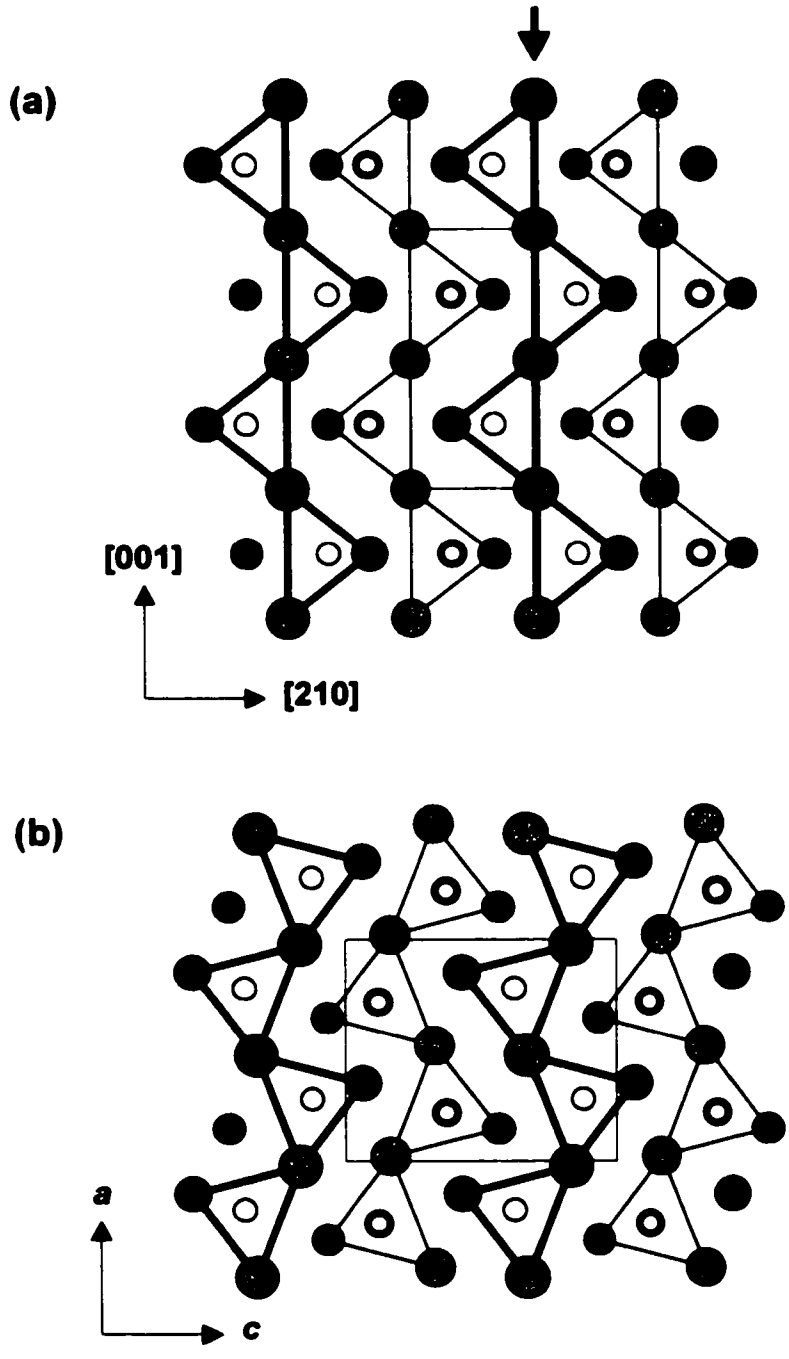

Figure 1-4. Structures of (a) ZrNiP (Ni_2In-type) and (b) HfNiP (Co_2Si-type) viewed in projection down the *b* axis. The large lightly shaded circles are Zr or Hf atoms, the medium solid circles are Ni atoms, and the small open circles are P atoms. Light and heavy lines indicate a displacement by 1/2 the repeat along the projection axis.

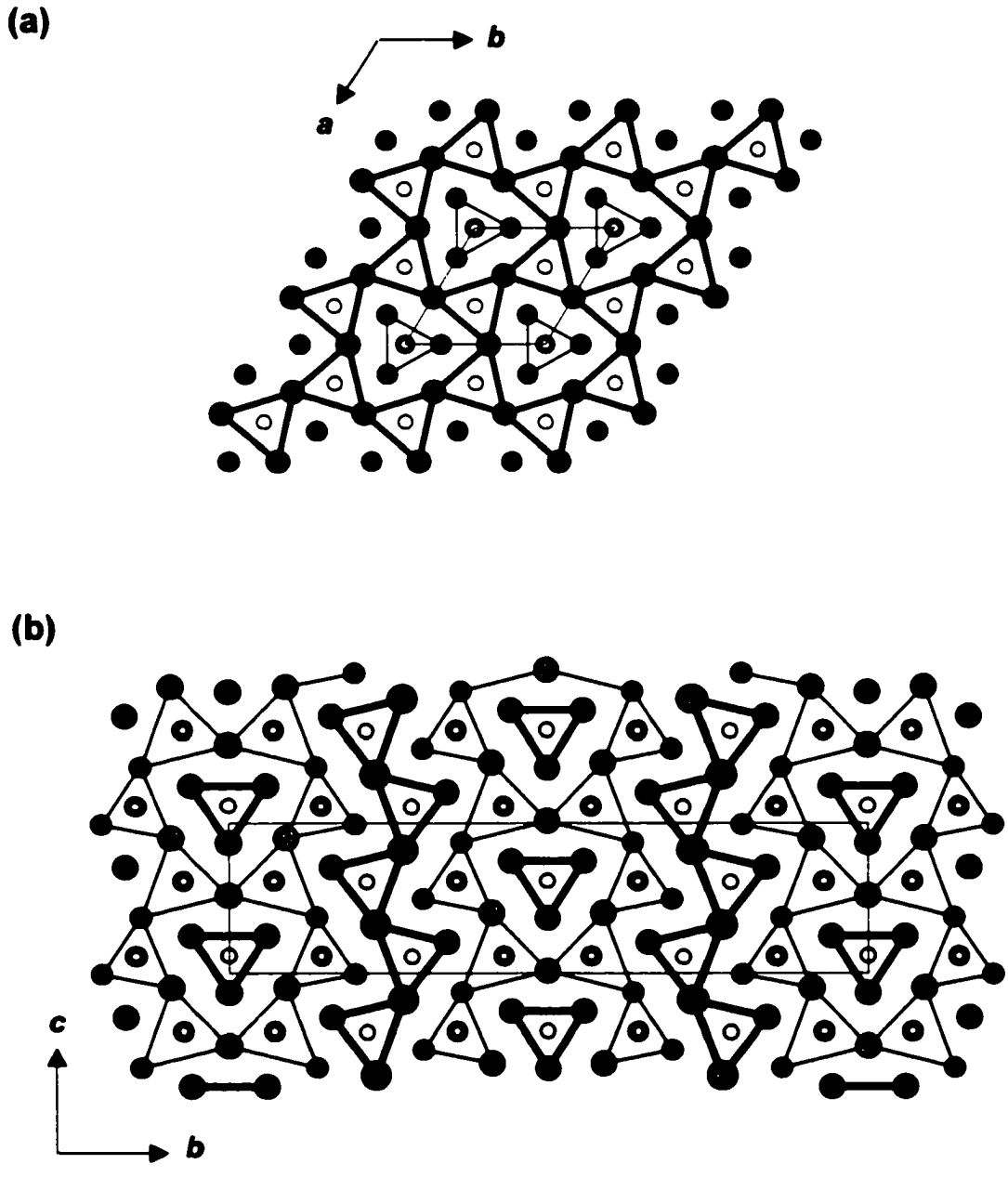

Figure 1-5. Structures of (a) Fe_2P (Fe_2P-type) and (b) $Zr_5Pd_9P_7$ ($Zr_5Pd_9P_7$-type). The large lightly shaded circles are Zr atoms, the medium solid circles are Fe or Ni atoms, and the small open circles are P atoms. Light and heavy lines indicate a displacement by 1/2 the repeat along the projection axis.

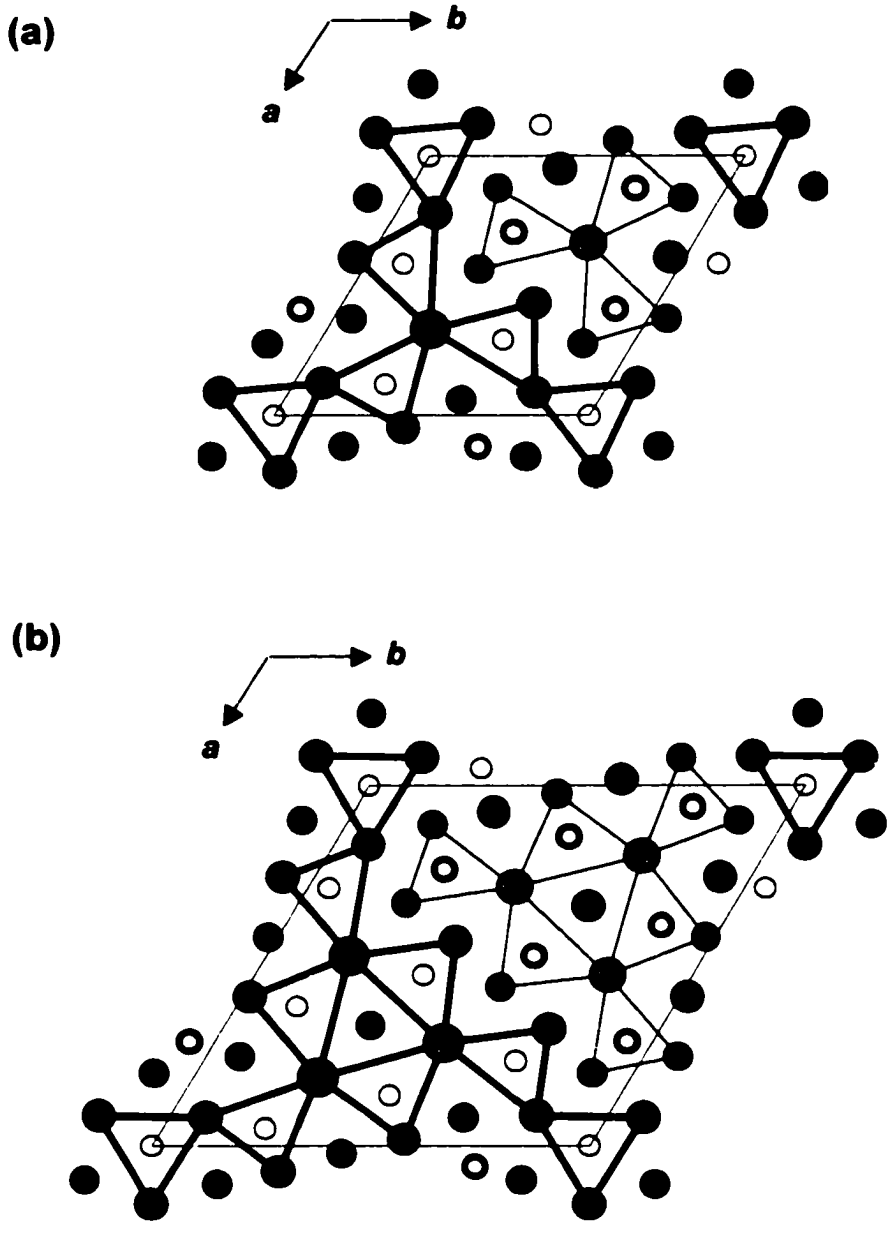

Figure 1-6. Structures of (a) $Zr_2Ni_{12}P_7$ ($Zr_2Fe_{12}P_7$-type) and (b) $Zr_6Ni_{20}P_{13}$ ($Zr_6Ni_{20}P_{13}$-type) viewed in projection down the *c* axis. The large lightly shaded circles are Zr atoms, the medium solid circles are Ni atoms, and the small open circles are P atoms. Light and heavy lines indicate a displacement by 1/2 the repeat along the projection axis.

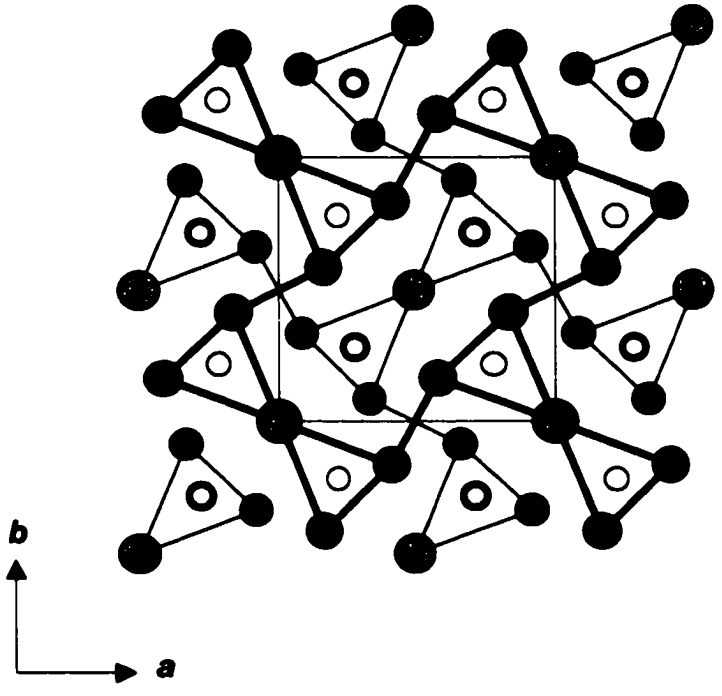

Figure 1-7. Structures of $ZrNi_4P_2$ ($ZrFe_4Si_2$-type) viewed in projection down the *c* axis. The large lightly shaded circles are Zr atoms, the medium solid circles are Ni atoms, and the small open circles are P atoms. Light and heavy lines indicate a displacement by 1/2 the repeat along the projection axis.

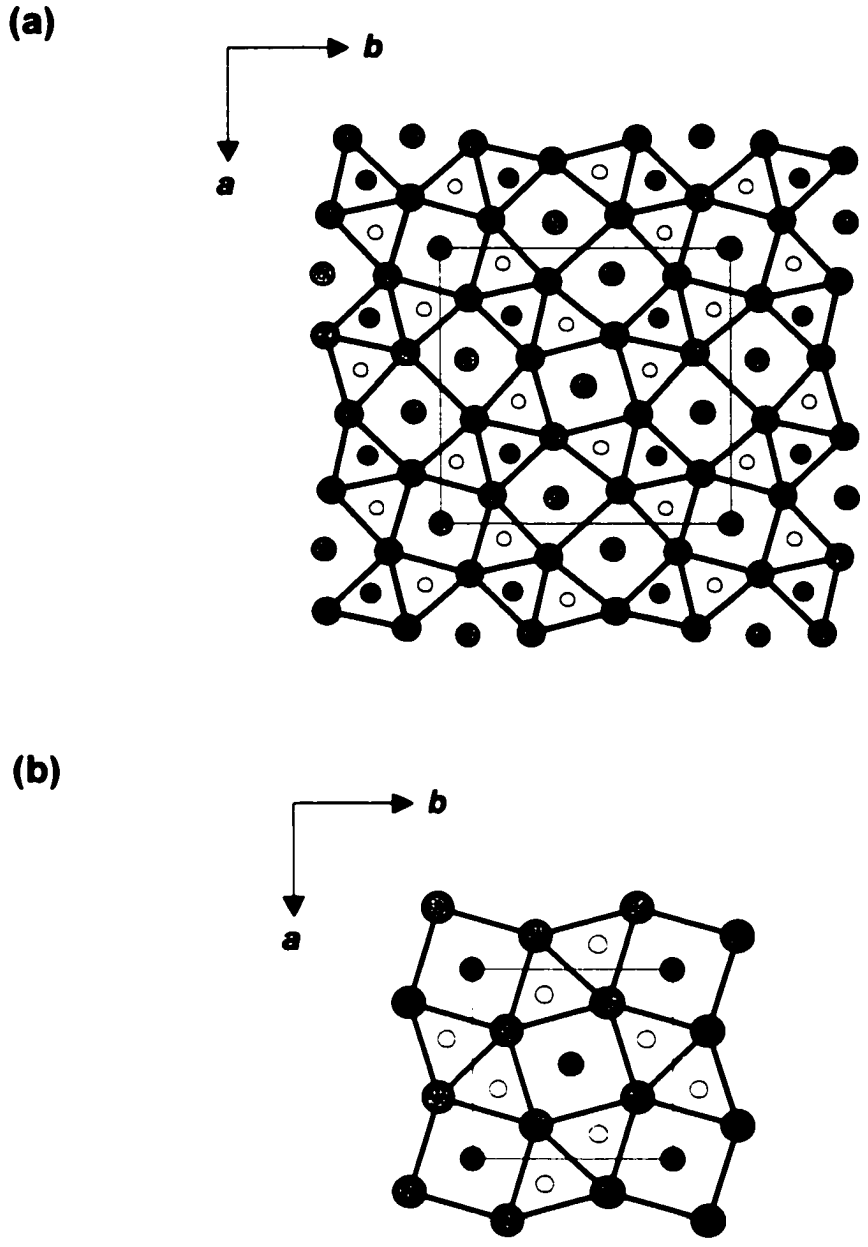

Figure 1-8. Structure of (a) $Zr_9Ni_2P_4$ ($Zr_9Ni_2P_4$-type) and (b) Nb_3Ni_2P (U_3Si_2-type) viewed in projection down the *c* axis. The large lightly shaded circles are Zr or Nb atoms, the medium solid circles are Ni atoms in (a) and 50%Nb+50%Ni atoms in (b), and the small open circles are P atoms in (a) and 57%Ni+43%P atoms in (b). Light and heavy lines indicate a displacement by 1/2 the repeat along the projection axis.

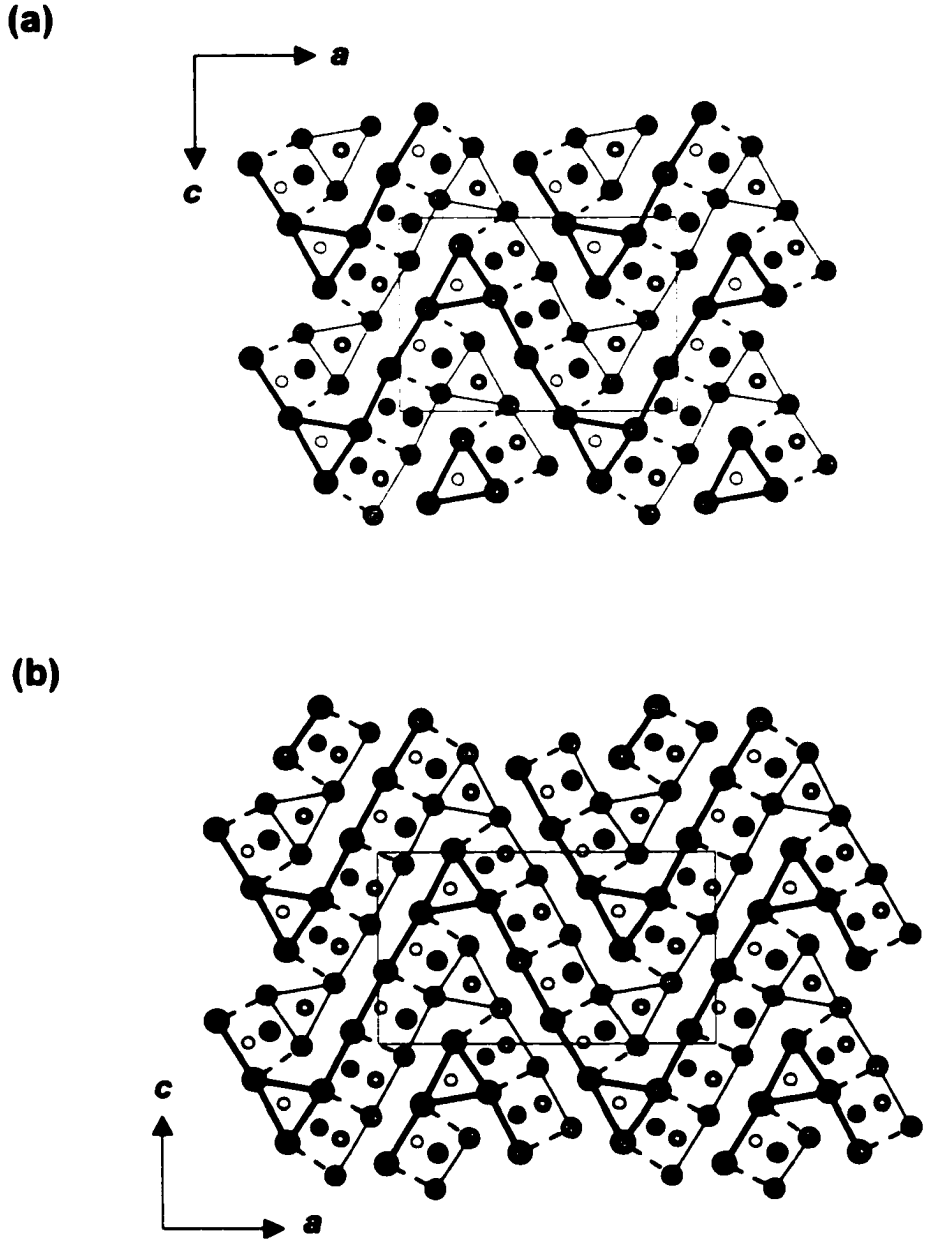

Figure 1-9. Structures of (a) $Zr_2Ni_{1-x}P$ ($Zr_2Ni_{1-x}P$-type) and (b) $Hf_5Ni_{1+x}P_3$ (filled Hf_5CoP_3-type) viewed in projection along the *b* axis. The large lightly shaded circles are Zr or Hf atoms, the medium solid circles are Ni atoms, and the small open circles are P atoms. Light and heavy lines indicate a displacement by 1/2 the repeat along the projection axis, and dashed lines connect atoms at different altitudes along the projection axis.

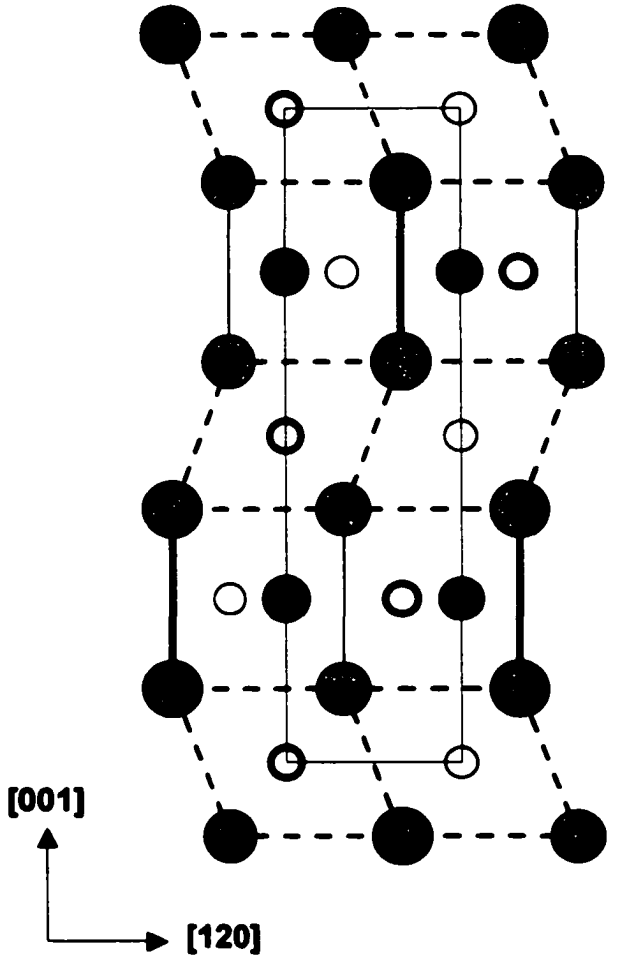

Figure 1-10. Structures of Zr_2NiP_2 (Be_3N_2-type) viewed in projection down the *a* axis. The large lightly shaded circles are Zr atoms, the medium solid circles are Ni atoms, and the small open circles are P atoms. Light and heavy lines indicate a displacement by 1/2 the repeat along the projection axis, and dashed lines connect atoms at different altitudes along the projection axis.

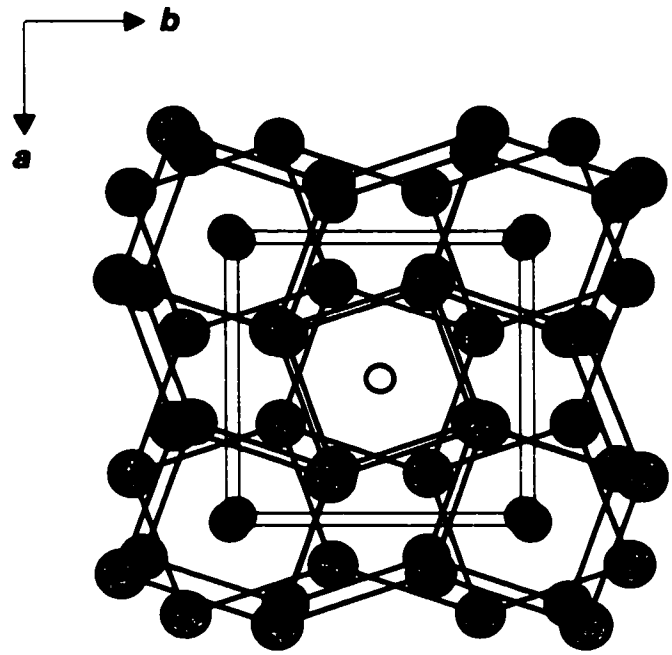

Figure 1-11. A Perspective view of Zr_4NiP (Nb_4CoSi-type) structure along the *c* axis. The large lightly shaded circles are Zr atoms, the medium solid circles are Ni atoms, and the small open circles are P atoms.

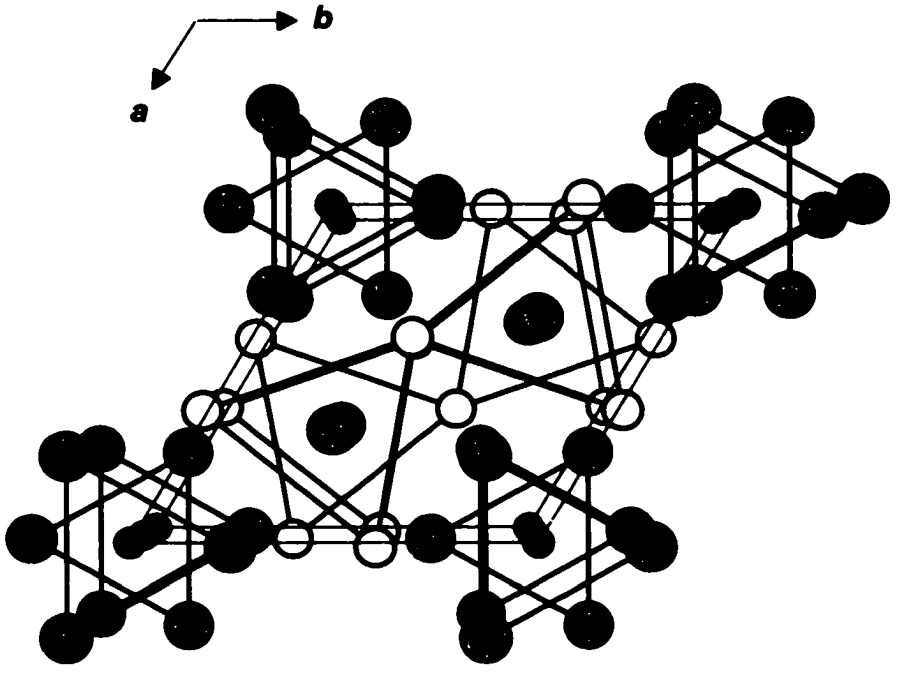

Figure 1-12. A perspective view of Zr_5NiSb_3 (Ti_5Ga_4-type) structure along the *c* axis. The large lightly shaded circles are Zr atoms, the medium solid circles are Ni atoms, and the small open circles are P atoms.

References

(1) (a) *Intermetallic Compounds*; Westbrook, J. H., Ed.; Wiley: New York, 1967. (b) *Intermetallic Compounds: Principles and Practice*, Vol. 1 and 2; Westbrook, J. H.; Fleischer, R. L., Eds.; Wiley: New York, 1995.

(2) *Gmelins Handbuch der Anorganishen Chemie*, Vol. 60A, I: Kupfer; Gmelin-Institut, Eds.; Verlag Chemie: Weinheim, 1955; p 5.

(3) Westbrook, J. H. *Metall. Trans. A* **1977**, *8*, 1327.

(4) Waterstrat, R. M. *J. Met.* **1990**, *42(3)*, 8.

(5) Sauthoff, G. *Intermetallics*; VCH Publishers: New York, 1995; p 14.

(6) Nagamatsu, J.; Nakagawa, N.; Muranaka, T.; Zenitani, Y.; Akimitsu, J. *Nature* **2001**, *410*, 63.

(7) Yamamoto, T. In *The Developments of Sendust and Other Ferromagnetic Alloys*; Yamamoto, T., Ed.; Committee of Academic Achievements: Chiba, 1980; p 1.

(8) Stadelmaier, H. H.; Henig, E.-T.; Petzow, G. *Z. Metallkd.* **1991**, *82*, 163.

(9) Sales, B. C.; Mandrus, D.; Williams, R. K. *Science* **1996**, *272*, 1325.

(10) Jones, C. D. W.; Regan, K. A.; DiSalvo, F. J. *Phys. Rev. B: Condens. Matter* **1998**, *58*, 16057.

(11) Schubert, K. *Kristallstrukturen zweikomponentiger Phasen*; Springer-Verlag: Berlin, 1964.

(12) Pearson, W. B. *The Crystal Chemistry and Physics of Metals and Alloys*; Wiley: New York, 1972.

(13) Villars, P. *Pearson's Handbook, Desk Edition*; ASM International: Materials Park, OH, 1997.

(14) Nesper, R. *Angew. Chem. Int. Ed. Engl.* **1991**, *30*, 789.

(15) Franzen, H. F. Prog. *Solid State Chem.* **1978**, *12*, 1.

(16) Simon, A. *Angew. Chem. Int. Ed. Engl.* **1981**, *20*, 1.

(17) Simon, A. *Angew. Chem. Int. Ed. Engl.* **1988**, *27*, 159.

(18) Simon, A.; Mattausch, Hj.; Miller, G. J.; Bauhofer, W.; Kremer, R. K. In *Handbook on the Physics and Chemistry of Rare Earths*; Gschneidner, K. A., Jr.; Eyring, L., Eds.; Elservier: Amsterdam, 1991; Vol. 15; p 191.

(19) Corbett, J. D. *J. Alloys Compd.* **1995**, *229*, 10.

(20) Hughbanks, T. *J. Alloys Compd.* **1995**, *229*, 40.

(21) Tremel, W.; Kleinke, H.; Derstroff, V.; Reisner, C. *J. Alloys Compd.* **1995**, *219*, 73.

(22) Niewa, R.; DiSalvo, F. J. *Chem. Mater.* **1998**, *10*, 2733.

(23) Marking, G. A.; Franzen, H. F. *Chem. Mater.* **1993**, *5*, 678.

(24) Franzen, H. F.; Köckerling, M. *Prog. Solid State Chem.* **1995**, *23*, 265.

(25) $ZrNi_{0.75}P_2$, $ZrNi_{0.75}As_2$, $HfNi_{0.75}As_2$: El Ghadraoui, E. H.; Pivan, J. Y.; Guérin, R. *J. Less-Common Met.* **1988**, *136*, 303.

(26) $ZrNi_2P_2$: Lomnitskaya, Ya. F.; Kuz'ma, Yu. B. *Russ. J. Inorg. Chem. (Engl. Transl.)* **1986**, *31*, 1390.

(27) $Zr_2Ni_3P_3$, $Hf_2Ni_3P_3$, $Zr_2Ni_3As_3$, $Hf_2Ni_3As_3$: El Ghadraoui, E. H.; Pivan, J. Y.; Guérin, R.; Padiou, J.; Sergent, M. *J. Less-Common Met.* **1985**, *105*, 187.

(28) ZrNiP: Kuz'ma, Yu. B.; Paltii, Ya. F. *Russ. J. Inorg. Chem. (Engl. Transl.)* **1979**, *24*, 1421.

(29) $ZrNi_4P_2$, $HfNi_4P_2$, $ZrNi_4As_2$, $HfNi_4As_2$: Pivan, J. Y.; Guérin, R.; El Ghadraoui, E. H.; Rafiq, M. *J. Less-Common Met.* **1989**, *153*, 285.

(30) Zr_2NiP_2, Zr_2NiAs_2: El Ghadraoui, E. H.; Pivan, J. Y.; Guérin, R.; Sergent, M. *Mater. Res. Bull.* **1988**, *23*, 891.

(31) $Zr_2Ni_{12}P_7$, $Zr_6Ni_{20}P_{13}$: Guérin, R.; El Ghadraoui, E. H.; Pivan, J. Y.; Padiou, J.; Sergent, M. *Mater. Res. Bull.* **1984**, *19*, 1257.

(32) $Zr_2Ni_{1-x}P$: Bruskov, V. A.; Lomnitskaya, Ya. F.; Kuz'ma, Yu. B. *Sov. Phys. Crystallogr. (Engl. Transl.)* **1988**, *33*, 199.

(33) Zr_4NiP, Hf_4NiP, Ta_4NiP: Lomnitskaya, Ya. F.; Kuz'ma, Yu. B. *Inorg. Mater. (Engl. Transl.)* **1980**, *16*, 705.

(34) $Zr_9Ni_2P_4$: Kleinke, H.; Franzen, H. F. *Inorg. Chem.* **1996**, *35*, 5272.

(35) HfNiP: Kleinke, H.; Franzen, H. F. *Z. Anorg. Allg.Chem.* **1996**, *622*, 1893.

(36) $HfNi_xP$: Kleinke, H.; Franzen, H. F. *Z. Anorg. Allg. Chem.* **1996**, *622*, 1342.

(37) Hf_2NiP: Kleinke, H.; Franzen, H. F. *Angew. Chem. Int. Ed. Engl.* **1997**, *36*, 513.

(38) $Hf_5Ni_{1+x}P_3$: Kleinke, H.; Franzen, H. F. *Chem. Mater.* **1997**, *9*, 1030.

(39) $Zr_3Pd_4P_3$, $Hf_3Pd_4P_3$, HfPdSb, $Nb_5Pd_4P_4$: Wang, M.; McDonald, R.; Mar, A. *Inorg. Chem.* **2000**, *39*, 4936.

(40) $Zr_5Pd_9P_7$, $Hf_5Pd_9P_7$, ZrPdAs, ZrPdSb: Heerdmann, A.; Johrendt, D.; Mewis, A. *Z. Anorg. Allg. Chem.* **2000**, *626*, 1393.

(41) ZrNiAs, HfNiAs: Kleinke, H.; Franzen, H. F. *Z. Anorg. Allg. Chem.* **1998**, *624*, 51.

(42) ZrNiSb, HfNiSb: Kleinke, H. *Z. Anorg. Allg. Chem.* **1998**, *624*, 1272.

(43) $ZrNi_2Sb$, $HfNi_2Sb$: Dwight, A. E. *Mater Res. Bull.* **1987**, *22*, 201.

(44) $Zr_3Ni_3Sb_4$, $Hf_3Ni_3Sb_4$, $Zr_3Pt_3Sb_4$: Wang, M.; McDonald, R.; Mar, A. *Inorg. Chem.* **1999**, *38*, 3435.

(45) Zr_5NiSb_3: Garcia, E.; Corbett, J. D. *Inorg. Chem.* **1990**, *29*, 3274.

(46) $Zr_5Ni_{0.5}Sb_{2.5}$: Kwon, Y.-U.; Sevov, S. C.; Corbett, J. D. *Chem. Mater.* **1990**, *2*, 550.

(47) Zr_6NiSb_2, Hf_6NiSb_2, Zr_6NiBi_2, Hf_6NiBi_2: Melnyk, G.; Bauer, E.; Rogl, P.; Skolozdra, R.; Seidl, E. *J. Alloys Compd.* **2000**, *296*, 235.

(48) Hf_5NiSb_3: Rieger, W.; Parthé, E. *Acta Crystallogr., Sect. B: Struct. Crystallogr. Cryst. Chem.* **1968**, *24*, 456.

(49) $Hf_{10}Ni_xSb_{6-x}$: Kleinke, H.; Ruckert, C.; Felser, C. *Eur. J. Inorg. Chem.* **2000**, 315.

(50) $Hf_6Ni_{1-x}Sb_{2+x}$: Kleinke, H. *J. Alloys Compd.* **1998**, *270*, 136.

(51) $NbNiP_2$: Kotur, B. Ya.; Lomnitskaya, Ya. F.; Kuz'ma, Yu. B. *Sov. Phys. Crystallogr. (Engl. Transl.)* **1983**, *28*, 348.

(52) NbNiP: Chaichit, N.; Chalugune, P.; Rukvichai, S.; Choosang, P.; Kaewchansilp, V.; Pontchour, C.-O.; Phavanantha, P.; Pramatus, S. *Acta. Chem. Scand. Ser. A.* **1978**, *32*, 309.

(53) $Nb_2Ni_2P_3$: Guérin, R.; Potel, M.; Sergent, M. *J. Less-Common Met.* **1981**, *78*, 177.

(54) Nb_2Ni_9P, Nb_3Ni_2P, $Nb_{17}Ni_{50}P_{33}$: Lomnitskaya, Ya. F.; Kuz'ma, Yu. B. *Inorg. Mater. (Engl. Transl.)* **1983**, *19*, 1191.

(55) Nb_4NiP: Paltii, Ya. F.; Kuz'ma, Yu. B. *Dopov. Akad. Nauk Ukr. RSR, Ser. A: Fiz.-Mat. Tekh. Nauki* **1977**, *39*, 262.

(56) $Nb_5Ni_4P_4$, $Ta_5Ni_4P_4$: Berger, R.; Phavanantha, P.; Mongkolsuk, M. *Acta. Chem. Scand., Ser. A* **1980**, *34*, 77.

(57) $TaNiP_2$: El Ghadraoui, E. H.; Guérin, R.; Potel, M.; Sergent, M. *Mater. Res. Bull.* **1981**, *16*, 933.

(58) TaNiP: Rundqvist, S.; Nawapong, P. C. *Acta Chem. Scand.* **1966**, *20*, 2250.

(59) $NbNiAs_2$: El Ghadraoui, E. H.; Guérin, R.; Padiou, J.; Sergent, M. *C. R. Séances Acad. Sci., Sér. 2* **1983**, *296*, 617.

(60) NbNiAs, TaNiAs: Rundqvist, S.; Tansuriwongs, P. *Acta Chem. Scand.* **1967**, *21*, 813.

(61) $Nb_5Pd_4As_4$: Wang, M.; Mar, A. Unpublished results.

(62) Nb_9PdAs_7: Wang, M.; Mar, A. *Inorg. Chem.* In press.

(63) $Nb_{28}Ni_{33.5}Sb_{12.5}$: Wang, M.; Mar, A. *J. Solid State Chem.* In press.

(64) Brewer, L.; Wengert, P. R. *Metall. Trans.* **1973**, *4*, 83.

(65) Guo, Q.; Kleppa, O. J. *J. Alloys Compd.* **2001**, *321*, 169.

(66) Pauling, L. *The Nature of the Chemical Bond*, 3rd ed.; Cornell University Press: Ithaca, NY, 1960.

(67) Kuz'ma, Yu. B.; Bilonizhko, N. S. *Dopov. Akad. Nauk Ukr. RSR, Ser. A: Fiz.-Mat. Tekh. Nauki* **1978**, 275.

(68) Miller, G. J. In *Chemistry, Structure, and Bonding of Zintl Phases and Ions*; Kauzlarich, S. M., Ed.; VCH Publishers: New York, 1996; p 1.

(69) Wang, M.; Mar, A. Unpublished calculations.

(70) Schubert, U.; Hüsing, N. *Synthesis of Inorganic Materials*; Wiley-VCH: New York, 2000.

(71) *Solid State Chemistry: Techniques*; Cheetham, A. K.; Day, P., Eds.; Oxford University Press: Oxford, 1987.

(72) Rao, C. N. R.; Gopalakrishnan, J. *New Directions in Solid State Chemistry*, 2nd ed.; Cambridge University Press: Cambridge, 1997.

(73) (a) Sunshine, S. A.; Kang, D.; Ibers, J. A. *J. Am. Chem. Soc.* **1987**, *109*, 6202. (b) Kanatzidis, M. G. *Chem. Mater.* **1990**, *2*, 353. (c) Kanatzidis, M. G.; Sutorik, A. C. *Prog. Inorg. Chem.* **1995**, *43*, 151.

(74) Xie, Y.; Su, H. L.; Qian, X. F.; Liu, X. M.; Qian, Y. T. *J. Solid State Chem.* **2000**, *149*, 88.

(75) Flewitt, P. E. J.; Wild, R. K. *Physical Methods for Materials Characterization*; Institute of Physics Publishing: Bristol, 1994.

(76) Stout, G. H.; Jensen, L. H. *X-ray Structure Determination: A Practical Guide*, 2nd ed.; John Wiley and Sons: New York, 1989.

(77) *The Rietveld Method*; Young, R. A., Ed.; International Union of Crystallography and Oxford University Press: Oxford, 1993.

(78) Hoffmann, R. *Solids and Surfaces: A Chemist's View of Bonding in Extended Structures*; VCH Publishers: New York, 1988.

Chapter 2

Ternary Early-Transition-Metal Palladium Pnictides $Zr_3Pd_4P_3$, $Hf_3Pd_4P_3$, HfPdSb, and $Nb_5Pd_4P_4$ †

Introduction

While many examples are now known of metal-rich binary and ternary transition-metal pnictides where the ratio of metal to nonmetal is equal or close to 2:1,[1] by no means have they been exhaustively investigated, as demonstrated by the recent discovery of Hf_7P_4, for instance.[2] Their structures typically feature the pnicogen atoms coordinated in a trigonal prismatic fashion by the transition-metal atoms. The trigonal prisms may then be further capped on their quadrilateral faces by additional transition-metal atoms, leading to differentiation in structure types: monocapped in MoP_2-type, tricapped in TiNiSi-type, tetracapped in Co_2Si-type, and pentacapped in Ni_2In-type.[3] (A quadrilateral face can be capped by more than one atom, as occurs in the latter two cases.) There is extensive metal-pnicogen and metal-metal bonding in these structures, but no pnicogen-pnicogen bonding. In ternary transition-metal pnictides containing a combination of an early and a late transition metal, metal-metal bonding can be understood in terms of a Lewis acid-base stabilization afforded by donation of electron density by the latter to the

† A version of this chapter has been published. Wang, M.; McDonald, R.; Mar, A. *Inorg. Chem.* **2000**, *39*, 4936. Copyright 2000 American Chemical Society.

former.[4]

Among ternary pnictides $M_xM'_yPn_z$ (where M = Zr, Hf, Nb, Ta; M' = Ni, Pd, Pt; Pn = P, As, Sb), there are numerous examples containing Ni,[5] but only recently have a few containing Pd ($Zr_5Pd_9P_7$, $Hf_5Pd_9P_7$, ZrPdAs, ZrPdSb)[6] been reported and to date none are known with Pt. Paralleling these contrasts, the binary Ni and Pd phosphides share little in common: the only isostructural members are the phosphorus-rich compounds NiP_3 and PdP_3.[7,8] Besides these, Ni forms other phosphorus-rich compounds such as NiP_2 [9] as well as metal-rich compounds (NiP,[9] Ni_2P (Fe_2P- and Ni_2P-type),[10,11] Ni_3P,[12] Ni_5P_2,[13] Ni_5P_4,[14] Ni_8P_3,[15] $Ni_{12}P_5$ [16]), while Pd only forms other metal-rich compounds (Pd_3P (Fe_3C-type),[17] Pd_6P,[18] Pd_9P_2,[19] $Pd_{15}P_2$,[20] Pd_7P_3 [21]). More striking is the frequent lack of isotypy between the structures of ternary pnictides of Zr and Hf, ostensibly the two most similar elements in the periodic table. Differences in metal-metal bond strengths have been argued as the reason behind this observation,[22] although perhaps in some cases, obtaining the desired phase may just be a matter of optimizing synthetic conditions.

In view of the surfeit of ternary nickel phosphides relative to the scarcity of ternary palladium phosphides, the metal-rich regions of the Zr, Hf, Nb, Ta / Pd / P systems were explored. The compounds $Zr_3Pd_4P_3$ and $Hf_3Pd_4P_3$ augment the recent discovery of $Zr_5Pd_9P_7$ and $Hf_5Pd_9P_7$,[6] while $Nb_5Pd_4P_4$ is the first compound found in this system. As well, the compound HfPdSb, isotypic with ZrPdSb,[6] has now been prepared.

Experimental Section

Synthesis. Binary transition-metal pnictides were first prepared by direct reaction of stoichiometric amounts of the elemental powders (Zr, 99.7%, Cerac; Hf, 99.8%, Cerac; Nb, 99.8%, Cerac; P, 99.995%, Cerac; Sb, 99.995%, Aldrich) in evacuated fused-silica tubes (3 d at 800 °C for ZrP and HfP, 3 d at 1000 °C for NbP, or 5 d at 650 °C for $HfSb_2$). Arc-melting reactions were then carried out on a 0.25-g scale on pressed pellets of mixtures of elemental Pd (99.95%, Cerac) and binary transition-metal pnictides, with the use of a Centorr 5TA tri-arc furnace under argon (gettered by melting a titanium pellet). Elemental compositions were determined by EDX (energy-dispersive X-ray) analysis on a Hitachi S-2700 scanning electron microscope. Powder X-ray diffraction patterns were obtained on an Enraf-Nonius FR552 Guinier camera (Cu $K\alpha_1$ radiation; Si standard) and analyzed with the Filmscan and Jade 3.1 software packages.[23]

Small black needle-shaped crystals of $Zr_3Pd_4P_3$ were originally obtained from the reaction ZrP + 2 Pd. EDX analysis revealed the presence of all three elements in the atomic proportions 27% Zr, 43% Pd, and 30% P in these crystals, one of which was selected for the structure determination. With a knowledge of the correct composition, $Zr_3Pd_4P_3$ was prepared with only trace amounts of unidentified impurity from the reaction 3 ZrP + 4 Pd. The analogous reaction 3 HfP + 4 Pd also afforded small black needle-shaped crystals of $Hf_3Pd_4P_3$, but contaminated with ~30% binary impurities such as HfP. Similarly, small black plate-shaped crystals of $Nb_5Pd_4P_4$ were originally obtained from the reaction NbP + 2 Pd. EDX analysis revealed the presence of all three elements in the atomic proportions 35% Nb, 35% Pd, and 30% P in these crystals, one of which was selected for the structure determination. The reaction Nb + 4 NbP + 4 Pd produced only

about 50% $Nb_5Pd_4P_4$. Finally, the reaction Hf + 2 Pd + $HfSb_2$ produced a black powder which was identified by X-ray diffraction to be ~80% HfPdSb, isostructural to ZrPdSb. Table 2-1 lists observed and calculated interplanar distances and intensities for HfPdSb.

Structure Determination. All crystals were pre-screened by EDX analysis and Weissenberg photography. Intensity data were obtained at 22 °C on a Bruker P4/RA/SMART 1000 CCD diffractometer using a combination of ϕ rotations (0.3°) and ω scans (0.3°) in the range $4° \leq 2\theta(\text{Mo } K\alpha) \leq 65°$ for $Zr_3Pd_4P_3$, $4° \leq 2\theta(\text{Mo } K\alpha) \leq 50°$ for $Hf_3Pd_4P_3$, and $5° \leq 2\theta(\text{Mo } K\alpha) \leq 65°$ for $Nb_5Pd_4P_4$. Crystal data and further details of the data collections are given in Table 2-2. All calculations were carried out using the SHELXTL (Version 5.1) package.[24] Conventional atomic scattering factors and anomalous dispersion corrections were used.[25] Intensity data were processed, and face-indexed numerical absorption corrections were applied in XPREP. Initial atomic positions were found by direct methods using XS, and refinements were performed by least-squares methods using XL.

Weissenberg photographs of $Zr_3Pd_4P_3$ and $Hf_3Pd_4P_3$ revealed Laue symmetry *mmm* and systematic extinctions ($0kl$: $k + l = 2n + 1$; $hk0$: $h = 2n + 1$) consistent with the orthorhombic space groups *Pnma* and $Pn2_1a$. The centrosymmetric space group *Pnma* was chosen on the basis of the successful structure solution and refinement, which proceeded satisfactorily. Refinements on occupancy factors confirm that all sites are fully occupied. While the structure determination of $Zr_3Pd_4P_3$ was straightforward, data collection for $Hf_3Pd_4P_3$ proved to be more challenging. Crystals that were singular (as revealed by Weissenberg photographs) and of suitable size were difficult to find; we made do with a small crystal of $Hf_3Pd_4P_3$ (0.03 × 0.005 × 0.004 mm) that had an even

smaller fragment of HfP attached to it. Errors arising from the contribution of HfP to the collected intensities of $Hf_3Pd_4P_3$ were not serious because incidences of accidental overlap of reciprocal lattice points were low. The displacement parameters for the P atoms were refined isotropically; these were sensitive to absorption corrections, which are important even for such a small crystal because of the large absorption coefficient (μ(Mo $K\alpha$) = 624 cm^{-1}) but were difficult to apply because of imprecision in measuring the very small dimensions of the crystal. Final refinements led to satisfactory residuals (Table 2-2) and to featureless difference electron density maps ($\Delta\rho_{max}$ = 2.50, $\Delta\rho_{min}$ = –2.87 $e^- Å^{-3}$ for $Zr_3Pd_4P_3$ and $\Delta\rho_{max}$ = 3.43, $\Delta\rho_{min}$ = –3.52 $e^- Å^{-3}$ for $Hf_3Pd_4P_3$).

The possible space groups for $Nb_5Pd_4P_4$ consistent with its Laue symmetry $4/m$ and systematic extinctions indicating only body centering (hkl: $h + k + l = 2n + 1$) are $I4$, $I\bar{4}$, and $I4/m$. The centrosymmetric space group $I4/m$ was chosen on the basis of its isotypy with $Nb_5Cu_4Si_4$ and the successful refinement (Table 2-2). The final difference electron map is featureless ($\Delta\rho_{max}$ = 2.37, $\Delta\rho_{min}$ = –2.03 $e^- Å^{-3}$).

The atomic positions of $Zr_3Pd_4P_3$, $Hf_3Pd_4P_3$, and $Nb_5Pd_4P_4$ were standardized with the program STRUCTURE TIDY.[26] Final values of the positional and displacement parameters are given in Table 2-3. Interatomic distances are listed in Table 2-4. Anisotropic displacement parameters are listed in Table C-1.

Band Structure. One electron band structure calculations on $Zr_3Pd_4P_3$ were performed using the EHMACC suite of programs.[27,28] Extended Hückel parameters were taken from literature values and are listed in Table 2-5. Properties were extracted from the band structure using 120 k points in the irreducible portion of the Brillouin zone.

Results and Discussion

Structures. Although there are numerous ternary zirconium and hafnium nickel phosphides,[5a-n] none is isostructural to $Zr_3Pd_4P_3$ and $Hf_3Pd_4P_3$, which, along with the recently reported $Zr_5Pd_9P_7$ and $Hf_5Pd_9P_7$,[6] are the few examples of ternary zirconium and hafnium palladium phosphides known to date. $M_3Pd_4P_3$ (M = Zr, Hf) crystallizes in a new structure type; for concreteness we will take M = Zr in the following description. As in most ternary metal-rich phosphides, the unit cell has a short axis between 3 and 4 Å. A view of the structure down the short b axis is given in Figure 2-1. All atoms are located on mirror planes perpendicular to b, alternately on (x, ¼ , z) or (x, ¾, z), as distinguished by the light or heavy lines. This representation emphasizes the description of the structure in terms of the stacking of two-dimensional nets consisting of triangles, distorted squares ("quadrangles"), and pentagons. These nets are self-dual,[29] with the vertices of one net centering the polygons of the other net, and vice versa.

The Zr atoms occupy three crystallographically inequivalent sites, all having pentagonal prismatic coordination with each of the five quadrilateral faces further capped. This CN15 coordination is achieved by 2 Zr, 9 Pd, and 4 P atoms surrounding Zr(1) and by 4 Zr, 6 Pd, and 5 P atoms surrounding Zr(2) or Zr(3). The four Pd sites have similar tetracapped distorted tetragonal prismatic coordination geometries (CN12), with Pd(1) showing the least severe distortion. Pd(1) is surrounded by 5 Zr, 4 Pd, and 3 P; Pd(2) by 4 Zr, 5 Pd, and 3 P; Pd(3) by 6 Zr, 3 Pd, and 3 P; and Pd(4) by 6 Zr, 2 Pd, and 4 P. If only Pd–P bonds are considered, then Pd(4) is found to be coordinated in a distorted tetrahedron of P atoms while the other Pd atoms are bonded to three P atoms, in a T-shape (Pd(1)) or in a trigonal pyramid (Pd(2), Pd(3)). All P atoms reside at the

centers of tricapped trigonal prisms. The CN9 coordination is completed by 5 Zr and 4 Pd around P(1) or P(2), and by 4 Zr and 5 Pd around P(3). The axial directions of the pentagonal, tetragonal, and trigonal prisms around Zr, Pd, and P atoms, respectively, are all oriented parallel to the *b* axis.

The structures of most metal-rich transition-metal pnictides can be built up by considering pnicogen-centered trigonal prisms as building blocks. In $Zr_3Pd_4P_3$, each P-centered trigonal prism has four Zr and two Pd atoms at the vertices, and is linked with adjacent prisms through the two Zr–Zr edges to form a one-dimensional chain extending along the *a* direction, as shown in Figure 2-2(a). Each trigonal prism also shares its two trigonal faces with adjacent prisms above and below along the *b* direction so that a two-dimensional corrugated sheet parallel to (001) results. Neighbouring sheets are then translated by ½ the *b* unit repeat, with the "notches" of one sheet fitting onto the "grooves" of the next sheet.

In a similar manner, Figure 2-2(b) shows that the structure of HfPdSb, isotypic with ZrPdSb,[6] also consists of chains of pnicogen-centered trigonal prisms, each having four Hf and two Pd atoms at the vertices. (The coordination geometries around the other atoms in HfPdSb are also similar to those in $Zr_3Pd_4P_3$, with Hf atoms in pentacapped pentagonal prisms and Pd atoms in tetracapped distorted tetragonal prisms.) When the Sb-centered trigonal prisms are tricapped, as they are here, by additional metal atoms from adjacent chains, this is known as the TiNiSi-type structure,[30] an extremely common one. It is interesting that among the ternary metal-rich pnictides $(M,M')_2Pn$, occasionally the structures are the same when a congeneric early transition metal is substituted (*e.g.*, ZrPdSb (TiNiSi-type) *vs.* HfPdSb (TiNiSi-type)[6]) but more frequently they differ subtly

(*e.g.*, ZrNiP (Ni_2In-type with pentacapped trigonal prisms)[5a] *vs.* HfNiP (TiNiSi-type)[5k]). The number of capping atoms around the trigonal prisms has been correlated with the height/base ratio of the trigonal prisms,[3] and for *M*PdSb and $M_3Pd_4P_3$ (*M* = Zr, Hf), these values (~1.2) are consistent with the presence of tricapped trigonal prisms, as indeed observed in their structures. In both structures, the trigonal prisms are linked exclusively through the edges containing the early transition metal (*M*–*M*) instead of the Pd–Pd edges to form the one-dimensional chains. It is apparent that even with these restrictions there are numerous possibilities for connecting these trigonal prisms to form different topologies and therefore different structures. In the case of $Zr_3Pd_4P_3$, whose metal-to-nonmetal ratio is close to 2:1, the trigonal prisms are connected in such a way as to create a new tetragonal prismatic site (Figure 2-2(a)) not present in $(M,M')_2Pn$ structures which is occupied by an extra Pd atom.

In contrast with the ternary palladium phosphides ($Zr_3Pd_4P_3$, $Zr_5Pd_9P_7$) mentioned above, which find no counterparts in ternary nickel phosphides, the compound $Nb_5Pd_4P_4$ does turn out to be isostructural with the nickel analogues $Nb_5Ni_4P_4$ and $Ta_5Ni_4P_4$.[5t] (We have been unable to prepare "$Ta_5Pd_4P_4$" to date.) $Nb_5Pd_4P_4$ is the first ternary niobium palladium phosphide, and it adopts the $Nb_5Cu_4Si_4$-type structure,[31] an interesting one which has been discussed widely.[32,33] The conventional description involves the condensation of Nb_6P_8 face-capped octahedral clusters through opposite vertices to form one-dimensional chains which are linked via chains of edge-sharing tetrahedral Pd_4 clusters. However, as shown in Figure 2-3, the alternative description in terms of pnicogen-centered trigonal prisms emphasizes the close relationship with other ternary pnictides. Similar to the previous structures described, each P-centered trigonal prism

has four Nb and two Pd atoms at the vertices, with three additional capping atoms to form a tricapped trigonal prism. Four trigonal prisms are linked through Nb–Nb edges to form a tetrameric star-shaped cluster, generating a tetracapped tetragonal prismatic site occupied by Nb(1) (analogous to the tetragonal prismatic site occupied by Pd in $Zr_3Pd_4P_3$). Nb(2) resides in a pentacapped pentagonal prismatic site and Pd resides in a tetracapped distorted tetragonal prismatic site, as in the previous structures.

Bonding. While the use of pnicogen-centered trigonal prismatic building blocks clarifies structural relationships, little is implied about the relative importance of various bonding interactions other than the absence of pnicogen-pnicogen bonds in these structures. In all cases, metal-metal bonds, both homoatomic and heteroatomic, are undoubtedly important contributions in addition to metal-pnicogen bonds. These bonds extend in all three dimensions notwithstanding the portrayal of the structures in Figure 2-2; in fact, the interchain metal-metal bonds are shorter than the intrachain ones. The band structure for $Zr_3Pd_4P_3$ was therefore determined to assess these interactions. The density of states (DOS) curve (Figure 2-4) shows that while most of the Zr 4d states are above the Fermi level (ε_f = –9.55 eV), a substantial portion is found to be mixing with Pd 4d and P 3p states in bonding levels below ε_f. Most of the Pd 4d states are found in the narrow peak between –11 and –13 eV, implying a d^{10} configuration for Pd. The calculated charges are +0.73 for Zr, –0.13 for Pd, and –0.56 for P. The Zr–P distances range from 2.680(3) to 2.814(3) Å, similar to those in Zr_2P (avg. 2.72 Å)[34] and $Zr_5Pd_9P_7$ (2.605(3)–2.803(3) Å)),[6] while the Pd–P distances range from 2.410(4) to 2.585(4) Å, similar to those in Pd_7P_3 (avg. 2.47 Å)[21] and $Zr_5Pd_9P_7$ (2.403(4)–2.684(5) Å).[6] Correspondingly, the crystal orbital overlap population (COOP)[35] curves (Figure 2-5(a))

confirm that the Zr–P bonding is optimized with all bonding levels and no antibonding levels occupied (Mulliken overlap population (MOP) of 0.396), while the Pd–P bonding is moderately strong with some antibonding levels occupied (MOP of 0.148). The Zr–Zr distances range from 3.282(2) to 3.462(2) Å, slightly greater than those in elemental Zr (3.179–3.232 Å),[36] and the Pd–Pd distances range from 2.812(1) to 2.943(2) Å, longer than that in elemental Pd (2.751 Å).[36] The Zr–Pd distances of 2.896(2) to 3.168(2) Å are comparable to those in Zr_3Pd_4 (2.774–3.059 Å)[37] and $Zr_5Pd_9P_7$ (2.898(2)–3.102(1) Å).[6] The COOP curves for these metal-metal interactions are shown in Figure 2-5(b). Consistent with the reduced state of Zr, there is considerable Zr–Zr bonding with most of the bonding levels occupied and an MOP of 0.137. The small but positive MOP of 0.027 for the Pd–Pd contacts corresponds to a weak d^{10}-d^{10} interaction in which mixing with Pd 5s and 5p states stabilizes bonding levels more even though antibonding levels are occupied.[38] There may be other sources, such as dispersion, for this type of interaction, but the extended Hückel model suggests that such hybridization effects are important. Finally, the Zr–Pd bonding is essentially optimized with an MOP of 0.072, consistent with a Lewis acid-base stabilization implicit in interactions between early and late transition metals.

Whether the conclusions of the band structure calculation can be extrapolated to explain the absence of a "$Zr_3Ni_4P_3$" compound is questionable. Certainly d^{10}-d^{10} interactions will change on going to Ni, but covalent energies represent only one factor. The variety of ways that trigonal prisms can be connected to form different topologies suggests that energy differences between these structures may be quite small and subject to steric or matrix influences. As demonstrated in the synthesis of HfPdSb, which

requires a higher temperature than that of ZrPdSb, the reason may be quite pedestrian: one simply has to try looking harder.

Table 2-1. X-ray Powder Diffraction Data for HfPdSb [a]

h k l	$2\theta_{obs}$	d_{calc} (Å)	d_{obs} (Å)	I_c [b]	I_o
0 0 2	22.94	3.8506	3.8737	2	2
0 1 1	23.96	3.6898	3.7109	5	3
1 0 2	26.50	3.3452	3.3608	2	6
1 1 1	27.40	3.2381	3.2525	1	5
2 1 0	33.99	2.6328	2.6352	16	31
1 1 2	34.18	2.6175	2.6209	45	32
2 0 2	35.25	2.5390	2.5442	29	31
2 1 1	36.02	2.4912	2.4910	100	100
1 0 3	37.38	2.3996	2.4034	18	16
0 1 3	41.13	2.1909	2.1929	49	45
3 0 1	41.69	2.1610	2.1646	13	14
0 2 0	42.90	2.1018	2.1060	36	39
1 1 3	43.31	2.0840	2.0873	8	8
2 0 3	44.23	2.0437	2.0462	5	3
3 0 2	46.66	1.9436	1.9451	10	11
3 1 1	47.20	1.9219	1.9238	5	8
0 2 2	49.31	1.8449	1.8464	1	3
2 1 3	49.55	1.8380	1.8382	1	2
1 2 2	51.24	1.7797	1.7814	1	1
1 1 4	}54.15	1.6944	}1.6923	5	}6
3 0 3		1.6926		3	
4 0 0	54.23	1.6886	1.6901	4	6

Table 2-1. X-ray Powder Diffraction Data for HfPdSb (continued)

2 0 4	54.88	1.6726	1.6716	5	5
4 0 1	55.71	1.6494	1.6486	2	1
2 2 2	56.83	1.6191	1.6187	12	13
1 2 3	58.32	1.5811	1.5807	8	8
4 0 2	59.78	1.5464	1.5456	3	3
4 1 1	60.23	1.5354	1.5351	3	4
3 2 1	61.52	1.5067	1.5061	6	12
1 0 5	61.72	1.5017	1.5017	6	5
2 2 3	63.43	1.4652	1.4652	3	3
4 1 2	64.13	1.4513	1.4508	3	2
3 2 2	65.36	1.4270	1.4266	6	8
0 2 4	65.68	1.4197	1.4203	1	1
3 1 4	67.78	1.3819	1.3813	12	15
4 1 3	70.37	1.3374	1.3367	2	4
3 2 3	} 71.63	1.3183	} 1.3163	2	} 8
4 2 0		1.3164		3	
2 2 4	72.13	1.3088	1.3084	3	5
4 2 1	72.87	1.2976	1.2969	1	6
2 3 0	} 73.11	1.2942	} 1.2933	1	} 3
1 3 2		1.2924		3	
2 3 1	} 74.28	1.2763	} 1.2758	8	} 16
5 0 2		1.2747		1	
5 1 1	74.84	1.2685	1.2676	5	9
4 2 2	76.46	1.2456	1.2447	3	5

Table 2-1. X-ray Powder Diffraction Data for HfPdSb (continued)

0 3 3	77.60	1.2299	1.2292	5	5
1 2 5	}78.33	1.2219	}1.2196	5	}11
5 1 2		1.2198		2	
3 1 5	78.62	1.2168	1.2158	4	5
1 1 6	79.37	1.2078	1.2062	4	6

[a] The orthorhombic cell parameters refined from the powder pattern, obtained on a Guinier camera at room temperature with the use of the program POLSQ (Program for least-squares unit cell refinement. Modified by Cahen, D. and Keszler, D., Northwestern University, 1983.), are: a = 6.754(1), b = 4.204(1), c = 7.701(2) Å, and V = 218.66(8) Å^3.

[b] The intensities were calculated based on positional parameters from the crystal structure of ZrPdSb (Heerdmann, A.; Johrendt, D.; Mewis, A. *Z. Anorg. Allg. Chem.* **2000**, *626*, 1393) with the use of the program ATOMS (Dowty, E. Shape Software: Kingsport, TN, 1999).

Table 2-2. Crystallographic Data for $Zr_3Pd_4P_3$, $Hf_3Pd_4P_3$, and $Nb_5Pd_4P_4$

Formula	$Zr_3Pd_4P_3$	$Hf_3Pd_4P_3$	$Nb_5Pd_4P_4$
Formula mass (amu)	792.18	1053.98	1014.03
Space group	D_{2h}^{16}–*Pnma* (No. 62)	D_{2h}^{16}–*Pnma* (No. 62)	C_{4h}^{5}–*I*4/*m* (No. 87)
a (Å)	16.387(2) [a]	16.340(2) [a]	10.306(1) [b]
b (Å)	3.8258(5) [a]	3.7867(3) [a]	10.306(1) [b]
c (Å)	9.979(1) [a]	9.954(1) [a]	3.6372(5) [b]
V (Å^3)	625.6(2)	615.9(1)	386.31(8)
Z	4	4	2
T (°C)	22	22	22
Diffractometer	Bruker P4/RA/SMART–1000 CCD		
ρ_{calc} (g cm^{-3})	8.410	11.367	8.717
Crystal dimensions (mm)	Needle, 0.030 × 0.005 × 0.004	Needle, 0.030 × 0.005 × 0.004	Plate, 0.024 × 0.022 × 0.002
Radiation	Graphite-monochromated Mo *K*α, λ = 0.71073 Å		
μ(Mo *K*α) (cm^{-1})	166.75	623.96	169.45
Transmission factors [c]	0.896–0.938	0.667–0.787	0.728–0.966
Scan type	Mixture of ϕ rotations (0.3°) and ω scans (0.3°)		
2θ limits	4° ≤ 2θ(Mo *K*α) ≤ 65°	4° ≤ 2θ(Mo *K*α) ≤ 50°	4° ≤ 2θ(Mo *K*α) ≤ 65°
Data collected	$-24 \le h \le 23$, $-5 \le k \le 2$, $-15 \le l \le 14$	$-18 \le h \le 19$, $-4 \le k \le 4$, $-11 \le l \le 11$	$-10 \le h \le 15$, $-10 \le k \le 15$, $-5 \le l \le 5$
No. of data collected	4896	4157	1609
No. of unique data, including $F_o^2 < 0$	1250 (R_{int} = 0.104)	636 (R_{int} = 0.174)	395 (R_{int} = 0.077)

Table 2-2. Crystallographic Data for $Zr_3Pd_4P_3$, $Hf_3Pd_4P_3$, and $Nb_5Pd_4P_4$ (continued)

No. of unique data, with $F_o^2 > 2\sigma(F_o^2)$	756	421	281
No. of variables [d]	62	53	22
$R(F)$ for $F_o^2 > 2\sigma(F_o^2)$ [e]	0.044	0.049	0.039
$R_w(F_o^2)$ [f]	0.081	0.079	0.070
Goodness of fit [g]	0.853	0.915	0.879
$\Delta\rho_{max}$, $\Delta\rho_{min}$ (e Å^{-3})	2.50, −2.87	3.43, −3.52	2.37, −2.03

[a] Obtained from a refinement constrained so that $\alpha = \beta = \gamma = 90°$.

[b] Obtained from a refinement constrained so that $a = b$ and $\alpha = \beta = \gamma = 90°$.

[c] A numerical face-indexed absorption correction was applied, with the use of programs in the SHELXTL package (Sheldrick, G. M. *SHELXTL Version 5.1*; Bruker Analytical X-ray Systems: Madison, WI, 1997).

[d] Including an extinction coefficient.

[e] $R(F) = \sum \left| |F_o| - |F_c| \right| / \sum |F_o|$.

[f] $R_w(F_o^2) = \left[\sum \left[w(F_o^2 - F_c^2)^2\right] / \sum wF_o^4\right]^{1/2}$; $w^{-1} = \left[\sigma^2(F_o^2) + (aP)^2 + bP\right]$ where $P = \left[\max(F_o^2, 0) + 2F_c^2\right]/3$. For $Zr_3Pd_4P_3$, $a = 0.0223$, $b = 0.0000$; for $Hf_3Pd_4P_3$, $a = 0.0135$, $b = 0.0000$; for $Nb_5Pd_4P_4$, $a = 0.0238$, $b = 0.0000$.

[g] $GooF = \left[\sum \left[w(F_o^2 - F_c^2)^2\right] / (n - p)\right]^{1/2}$ where n is the number of reflections and p is the total number of parameters refined.

Table 2-3. Positional and Equivalent Isotropic Displacement Parameters for $Zr_3Pd_4P_3$, $Hf_3Pd_4P_3$, and $Nb_5Pd_4P_4$

atom	Wyckoff position	x	y	z	U_{eq} (Å^2) [a]
			$Zr_3Pd_4P_3$		
Zr(1)	4*c*	0.26016(9)	1/4	0.0244(2)	0.0051(3)
Zr(2)	4*c*	0.45161(9)	1/4	0.8825(2)	0.0050(3)
Zr(3)	4*c*	0.56056(9)	1/4	0.5893(2)	0.0050(3)
Pd(1)	4*c*	0.17653(7)	1/4	0.3107(1)	0.0066(3)
Pd(2)	4*c*	0.20644(7)	1/4	0.7352(1)	0.0064(3)
Pd(3)	4*c*	0.37095(7)	1/4	0.6170(1)	0.0061(2)
Pd(4)	4*c*	0.41869(7)	1/4	0.1833(1)	0.0063(3)
P(1)	4*c*	0.0448(2)	1/4	0.1795(4)	0.0056(7)
P(2)	4*c*	0.1141(2)	1/4	0.5366(4)	0.0055(8)
P(3)	4*c*	0.3227(2)	1/4	0.3888(4)	0.0065(8)
			$Hf_3Pd_4P_3$		
Hf(1)	4*c*	0.2602(1)	1/4	0.0229(2)	0.0044(5)
Hf(2)	4*c*	0.4522(1)	1/4	0.8810(2)	0.0061(5)
Hf(3)	4*c*	0.5605(1)	1/4	0.5880(2)	0.0093(5)
Pd(1)	4*c*	0.1765(2)	1/4	0.3104(4)	0.0041(8)
Pd(2)	4*c*	0.2058(2)	1/4	0.7310(4)	0.0023(7)
Pd(3)	4*c*	0.3703(2)	1/4	0.6176(4)	0.0041(7)
Pd(4)	4*c*	0.4194(2)	1/4	0.1825(4)	0.0051(8)
P(1)	4*c*	0.0428(6)	1/4	0.1801(12)	0.003(2)

Table 2-3. Positional and Equivalent Isotropic Displacement Parameters for $Zr_3Pd_4P_3$, $Hf_3Pd_4P_3$, and $Nb_5Pd_4P_4$ (continued)

P(2)	4*c*	0.1134(6)	1/4	0.5342(13)	0.007(3)
P(3)	4*c*	0.3233(6)	1/4	0.3883(12)	0.004(2)
			$Nb_5Pd_4P_4$		
Nb(1)	2*a*	0	0	0	0.0057(4)
Nb(2)	8*h*	0.3104(1)	0.3722(1)	0	0.0065(3)
Pd	8*h*	0.40535(8)	0.11385(9)	0	0.0073(2)
P	8*h*	0.0608(3)	0.2434(3)	0	0.0071(6)

[a] U_{eq} is defined as one-third of the trace of the orthogonalized $\mathbf{U}_{ij}$ tensor.

Table 2-4. Selected Interatomic Distances (Å) for $Zr_3Pd_4P_3$, $Hf_3Pd_4P_3$, and $Nb_5Pd_4P_4$

$Zr_3Pd_4P_3$		$Hf_3Pd_4P_3$	
Zr(1)–P(2)	2.814(3) (×2)	Hf(1)–P(2)	2.804(8) (×2)
Zr(1)–P(3)	2.708(3) (×2)	Hf(1)–P(3)	2.691(8) (×2)
Zr(1)–Pd(1)	3.047(2) (×2)	Hf(1)–Pd(1)	3.021(3) (×2)
Zr(1)–Pd(1)	3.168(2)	Hf(1)–Pd(1)	3.171(4)
Zr(1)–Pd(2)	2.896(2) (×2)	Hf(1)–Pd(2)	2.861(3) (×2)
Zr(1)–Pd(2)	3.017(2)	Hf(1)–Pd(2)	3.038(4)
Zr(1)–Pd(3)	3.022(2) (×2)	Hf(1)–Pd(3)	3.003(3) (×2)
Zr(1)–Pd(4)	3.044(2)	Hf(1)–Pd(4)	3.048(4)
Zr(1)–Zr(2)	3.442(2)	Hf(1)–Hf(2)	3.442(3)
Zr(1)–Zr(3)	3.462(2)	Hf(1)–Hf(3)	3.443(3)
Zr(2)–P(1)	2.787(3) (×2)	Hf(2)–P(1)	2.755(9) (×2)
Zr(2)–P(2)	2.680(3) (×2)	Hf(2)–P(2)	2.657(8) (×2)
Zr(2)–P(2)	2.782(4)	Hf(2)–P(2)	2.766(11)
Zr(2)–Pd(1)	2.930(2) (×2)	Hf(2)–Pd(1)	2.916(3) (×2)
Zr(2)–Pd(3)	2.961(2)	Hf(2)–Pd(3)	2.943(4)
Zr(2)–Pd(4)	2.934(2) (×2)	Hf(2)–Pd(4)	2.896(3) (×2)
Zr(2)–Pd(4)	3.050(2)	Hf(2)–Pd(4)	3.049(4)
Zr(2)–Zr(2)	3.416(3) (×2)	Hf(2)–Hf(2)	3.411(3) (×2)
Zr(2)–Zr(3)	3.428(2)	Hf(2)–Hf(3)	3.411(3)
Zr(3)–P(1)	2.695(5)	Hf(3)–P(1)	2.685(12)
Zr(3)–P(1)	2.730(3) (×2)	Hf(3)–P(1)	2.697(8) (×2)
Zr(3)–P(3)	2.714(3) (×2)	Hf(3)–P(3)	2.691(7) (×2)

Table 2-4. Selected Interatomic Distances (Å) for $Zr_3Pd_4P_3$, $Hf_3Pd_4P_3$, and $Nb_5Pd_4P_4$ (continued)

Zr(3)–Pd(2)	2.963(2)	Hf(3)–Pd(2)	2.979(4)
Zr(3)–Pd(3)	3.026(2) (×2)	Hf(3)–Pd(3)	3.009(3) (×2)
Zr(3)–Pd(3)	3.120(2)	Hf(3)–Pd(3)	3.122(4)
Zr(3)–Pd(4)	2.987(2) (×2)	Hf(3)–Pd(4)	2.985(3) (×2)
Zr(3)–Zr(3)	3.282(2) (×2)	Hf(3)–Hf(3)	3.251(3) (×2)
Pd(1)–P(1)	2.524(4)	Pd(1)–P(1)	2.542(11)
Pd(1)–P(2)	2.476(5)	Pd(1)–P(2)	2.454(13)
Pd(1)–P(3)	2.519(4)	Pd(1)–P(3)	2.520(10)
Pd(1)–Pd(2)	2.812(1) (×2)	Pd(1)–Pd(2)	2.812(4) (×2)
Pd(1)–Pd(3)	2.828(1) (×2)	Pd(1)–Pd(3)	2.802(4) (×2)
Pd(2)–P(2)	2.493(4)	Pd(2)–P(2)	2.473(12)
Pd(2)–P(3)	2.497(3) (×2)	Pd(2)–P(3)	2.502(8) (×2)
Pd(2)–Pd(3)	2.943(2)	Pd(2)–Pd(3)	2.916(5)
Pd(2)–Pd(4)	2.852(1) (×2)	Pd(2)–Pd(4)	2.829(3) (×2)
Pd(3)–P(1)	2.440(3) (×2)	Pd(3)–P(1)	2.447(7) (×2)
Pd(3)–P(3)	2.410(4)	Pd(3)–P(3)	2.409(12)
Pd(4)–P(1)	2.479(4)	Pd(4)–P(1)	2.436(11)
Pd(4)–P(2)	2.468(3) (×2)	Pd(4)–P(2)	2.460(8) (×2)
Pd(4)–P(3)	2.585(4)	Pd(4)–P(3)	2.580(12)

$Nb_5Pd_4P_4$

Nb(1)–P	2.585(3) (×4)	Nb(2)–Nb(1)	2.9541(9) (×2)
Nb(1)–Nb(2)	2.9541(9) (×8)	Nb(2)–Nb(2)	3.292(2) (×2)

Table 2-4. Selected Interatomic Distances (Å) for $Zr_3Pd_4P_3$, $Hf_3Pd_4P_3$, and $Nb_5Pd_4P_4$ (continued)

Nb(2)–P	2.572(2) (×2)	Nb(2)–Nb(2)	3.425(2) (×2)
Nb(2)–P	2.682(2) (×2)	Pd–P	2.365(2) (×2)
Nb(2)–P	2.919(3)	Pd–P	2.455(3)
Nb(2)–Pd	2.874(1) (×2)	Pd–Pd	2.822(1) (×4)
Nb(2)–Pd	2.885(1)	Pd–Pd	3.052(2)
Nb(2)–Pd	3.021(1)		

Table 2-5. Extended Hückel Parameters

atom	orbital	H_{ii} (eV)	ζ_{i1}	c_1	ζ_{i2}	c_2
Zr	5s	−8.93	1.82			
	5p	−5.29	1.78			
	4d	−9.24	3.84	0.6213	1.505	0.5798
Pd	5s	−7.51	2.19			
	5p	−3.86	2.15			
	4d	−12.53	5.98	0.55	2.61	0.67
P	3s	−18.60	1.88			
	3p	−12.50	1.63			

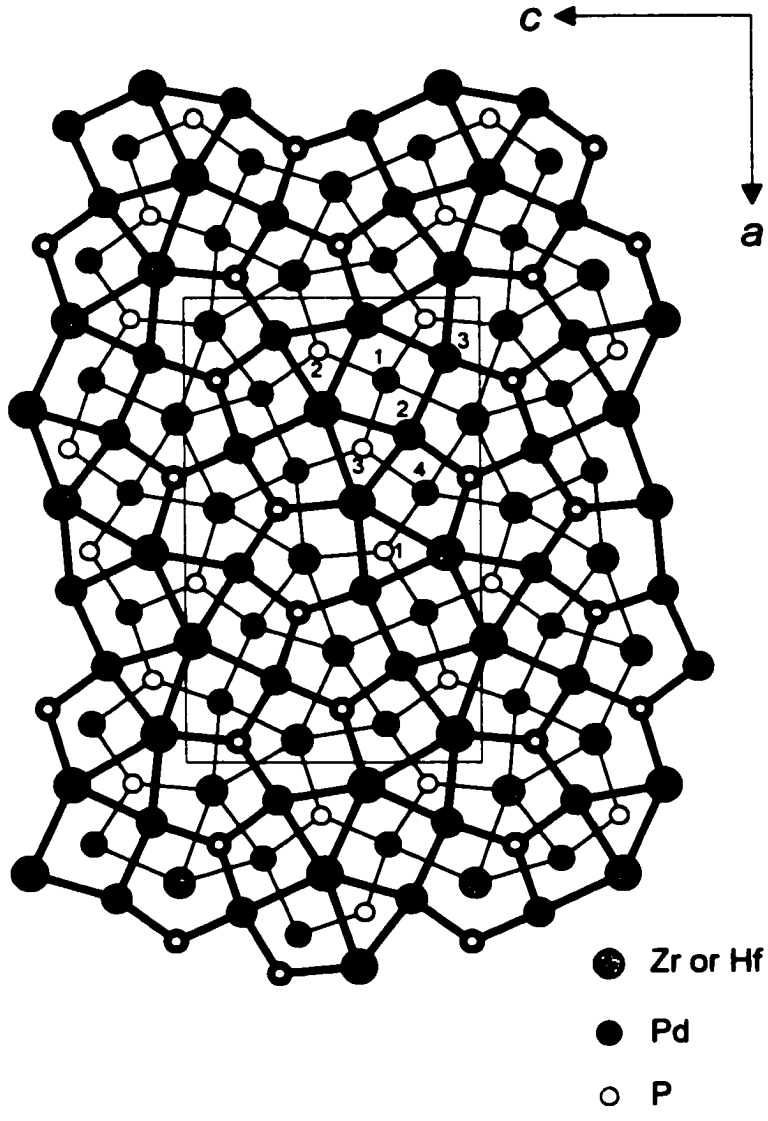

Figure 2-1. View of $Zr_3Pd_4P_3$ or $Hf_3Pd_4P_3$ in terms of two-dimensional nets stacked along the *b* axis at $y = 1/4$ (light lines) or $y = 3/4$ (heavy lines). The large lightly shaded circles are Zr or Hf atoms, the medium solid circles are Pd atoms, and the small open circles are P atoms.

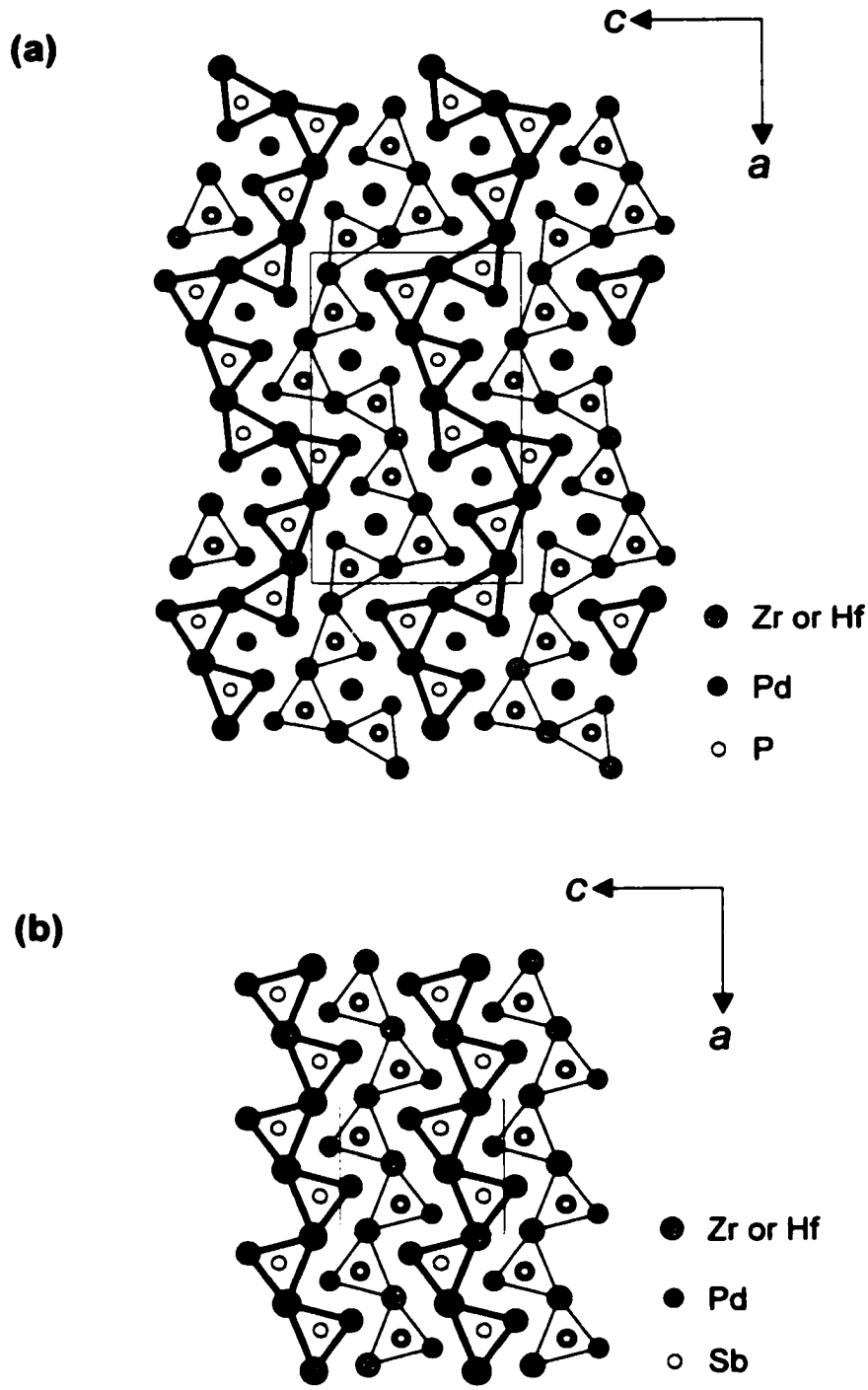

Figure 2-2. Comparison of the structures of (a) $Zr_3Pd_4P_3$ or $Hf_3Pd_4P_3$ and (b) ZrPdSb or HfPdSb, in terms of pnicogen-filled trigonal prisms, shown in projection down the *b* axis. Light and heavy lines indicate a displacement by ½ the *b* unit repeat.

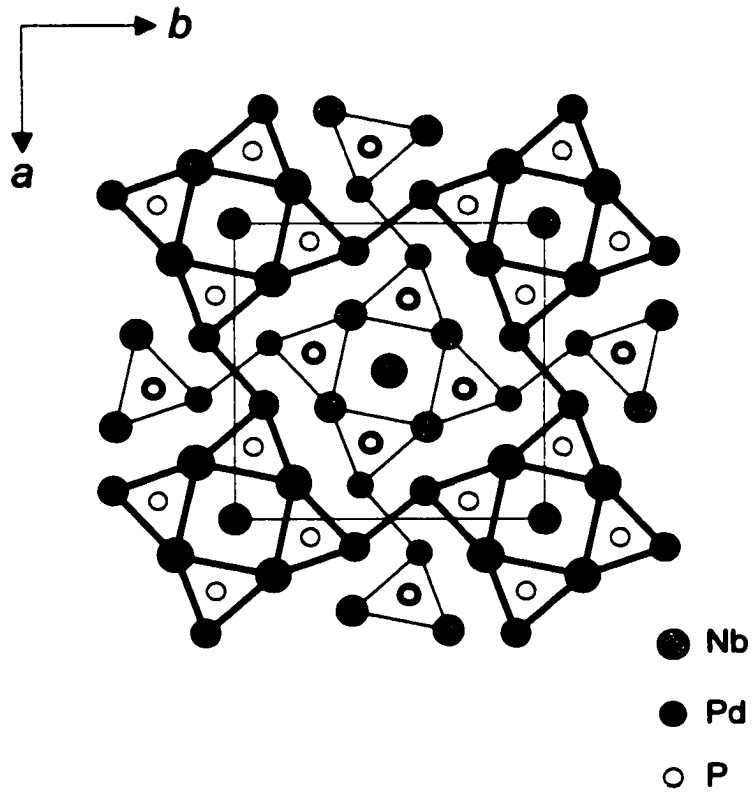

Figure 2-3. Structure of $Nb_5Pd_4P_4$ in terms of pnicogen-filled trigonal prisms, viewed in projection down the *c* axis. Light and heavy lines indicate a displacement by ½ the *c* unit repeat.

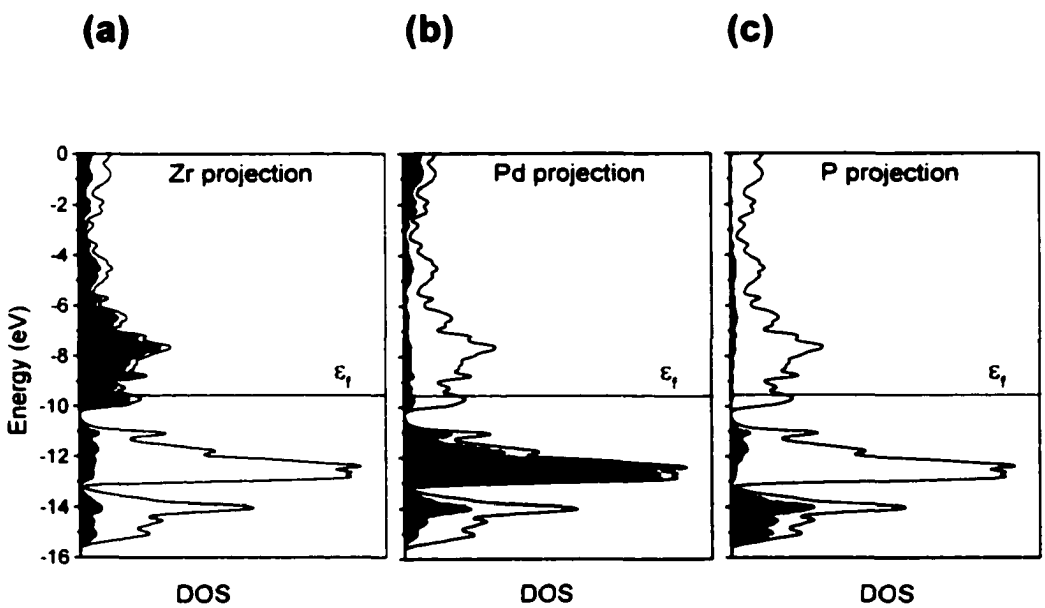

Figure 2-4. Contributions of (a) Zr, (b) Pd, and (c) P (shaded regions) to the total density of states (DOS) (line) for $Zr_3Pd_4P_3$. The Fermi level, ε_f, is at –9.55 eV.

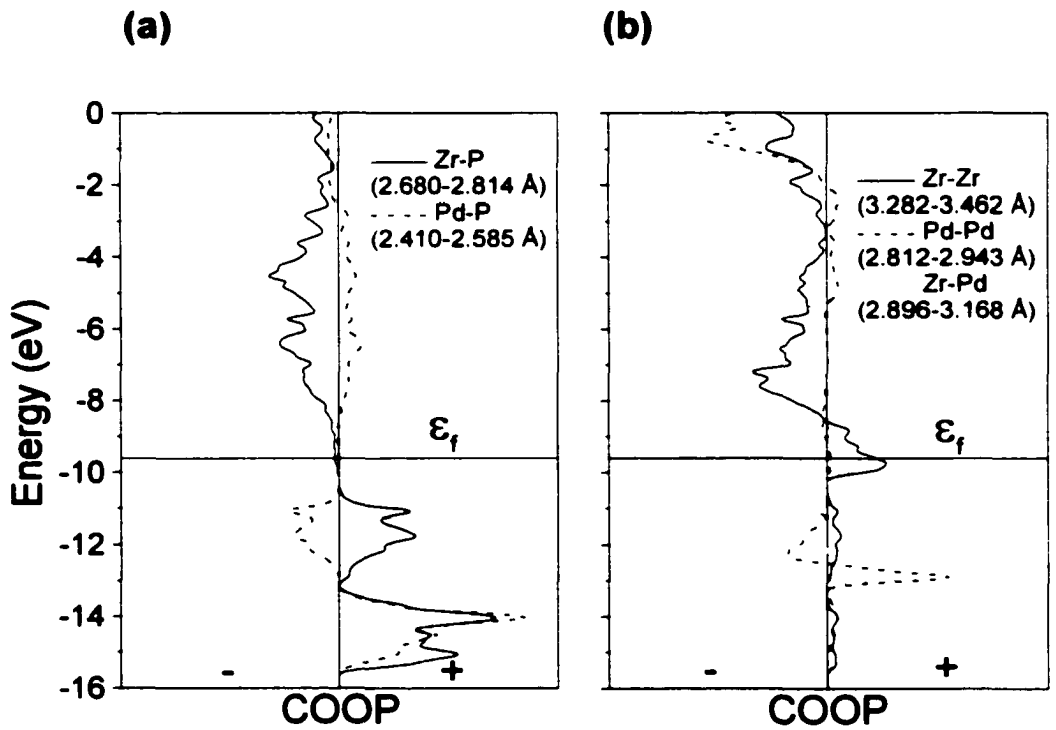

Figure 2-5. Crystal orbital overlap population (COOP) curves for the indicated (a) metal–P and (b) metal-metal contacts in $Zr_3Pd_4P_3$.

References

(1) Villars, P. *Pearson's Handbook, Desk Edition*; ASM International: Materials Park, OH, 1997.

(2) Kleinke, H.; Franzen, H. F. *Angew. Chem. Int. Ed. Engl.* **1996**, *35*, 1934.

(3) Hyde, B. G.; Andersson, S. *Inorganic Crystal Structures*; Wiley: New York, 1989.

(4) Kleinke, H. *Z. Anorg. Allg. Chem.* **1998**, *624*, 1771.

(5) (a) ZrNiP: Kuz'ma, Yu. B.; Paltii, Ya. F. *Russ. J. Inorg. Chem. (Engl. Transl.)* **1979**, *24*, 1421. (b) $ZrNiP_2$: El Ghadraoui, E. H.; Pivan, J. Y.; Guérin, R. *J. Less-Common Met.* **1988**, *136*, 303. (c) Zr_2NiP_2: El Ghadraoui, E. H.; Pivan, J. Y.; Guérin, R.; Sergent, M. *Mater. Res. Bull.* **1988**, *23*, 891. (d) Zr_4NiP_2: Bruskov, V. A.; Lomnitskaya, Ya. F.; Kuz'ma, Yu. B. *Sov. Phys. Crystallogr. (Engl. Transl.)* **1988**, *33*, 199. (e) $ZrNi_2P_2$: Lomnitskaya, Ya. F.; Kuz'ma, Yu. B. *Russ. J. Inorg. Chem. (Engl. Transl.)* **1986**, *31*, 1390. (f) $Zr_9Ni_2P_4$: Kleinke, H.; Franzen, H. F. *Inorg. Chem.* **1996**, *35*, 5272. (g) $Zr_2Ni_3P_3$, $Hf_2Ni_3P_3$: El Ghadraoui, E. H.; Pivan, J. Y.; Guérin, R.; Padiou, J.; Sergent, M. *J. Less-Common Met.* **1985**, *105*, 187. (h) $ZrNi_4P_2$, $HfNi_4P_2$: Pivan, J. Y.; Guérin, R.; El Ghadraoui, E. H.; Rafiq, M. *J. Less-Common Met.* **1989**, *153*, 285. (i) $Zr_2Ni_{12}P_7$, $Zr_6Ni_{20}P_{13}$: Guérin, R.; El Ghadraoui, E. H.; Pivan, J. Y.; Padiou, J.; Sergent, M. *Mater. Res. Bull.* **1984**, *19*, 1257. (j) $Zr_{66}Ni_{17}P_{17}$, $Hf_{66}Ni_{17}P_{17}$, $Ta_{66}Ni_{17}P_{17}$: Lomnitskaya, Ya. F.; Kuz'ma, Yu. B. *Inorg. Mater. (Engl. Transl.)* **1980**, *16*, 705. (k) HfNiP: Kleinke, H.; Franzen, H. F. *Z. Anorg. Allg.Chem.* **1996**, *622*, 1893. (l) $HfNi_xP$: Kleinke, H.; Franzen, H. F. *Z. Anorg. Allg. Chem.* **1996**, *622*,

1342. (m) Hf_2NiP: Kleinke, H.; Franzen, H. F. *Angew. Chem. Int. Ed. Engl.* **1997**, *36*, 513. (n) Hf_5NiP_3: Kleinke, H.; Franzen, H. F. *Chem. Mater.* **1997**, *9*, 1030. (o) NbNiP: Chaichit, N.; Chalugune, P.; Rukvichai, S.; Choosang, P.; Kaewchansilp, V.; Pontchour, C.-O.; Phavanantha, P.; Pramatus, S. *Acta. Chem. Scand, Ser. A.* **1978**, *32*, 309. (p) $NbNiP_2$: Kotur, B. Ya.; Lomnitskaya, Ya. F.; Kuz'ma, Yu. B. *Sov. Phys. Crystallogr. (Engl. Transl.)* **1983**, *28*, 348. (q) $Nb_2Ni_2P_3$: Guérin, R.; Potel, M.; Sergent, M. *J. Less-Common Met.* **1981**, *78*, 177. (r) Nb_2Ni_9P, Nb_3Ni_2P, $Nb_{17}Ni_{50}P_{33}$: Lomnitskaya, Ya. F.; Kuz'ma, Yu. B. *Inorg. Mater. (Engl. Transl.)* **1983**, *19*, 1191. (s) Nb_4NiP: Paltii, Ya. F.; Kuz'ma, Yu. B. *Dopov. Akad. Nauk Ukr. RSR, Ser. A: Fiz.-Mat. Tekh. Nauki* **1977**, *39*, 262. (t) $Nb_5Ni_4P_4$, $Ta_5Ni_4P_4$: Berger, R.; Phavanantha, P.; Mongkolsuk, M. *Acta. Chem. Scand., Ser. A* **1980**, *34*, 77. (u) TaNiP: Rundqvist, S.; Nawapong, P. C. *Acta Chem. Scand.* **1966**, *20*, 2250. (v) $TaNiP_2$: El Ghadraoui, E. H.; Guérin, R.; Potel, M.; Sergent, M. *Mater. Res. Bull.* **1981**, *16*, 933.

(6) Heerdmann, A.; Johrendt, D.; Mewis, A. *Z. Anorg. Allg. Chem.* **2000**, *626*, 1393.

(7) Rundqvist, S.; Ersson, N.-O. *Ark. Kemi* **1968**, *30*, 103.

(8) Rundqvist, S. *Nature (London)* **1960**, *185*, 31.

(9) Larsson, E. *Ark. Kemi* **1965**, *23*, 335.

(10) Rundqvist, S. *Acta Chem. Scand.* **1962**, *16*, 992.

(11) Nowotny, H.; Henglein, E. *Z. Phys. Chem., Abt. B* **1938**, *40*, 281.

(12) Rundqvist, S.; Hassler, E.; Lundvik, L. *Acta Chem. Scand.* **1962**, *16*, 242.

(13) Chikhrii, S. I.; Kuz'ma, Yu. B. *Russ. J. Inorg. Chem. (Engl. Transl.)* **1990**, *35*,

1821.

(14) Elfström, M. *Acta Chem. Scand.* **1965**, *19*, 1694.

(15) Il'nitskaya, O. N.; Aksel'rud, L. G.; Mikhalenko, S. I.; Kuz'ma, Yu. B. *Sov. Phys. Crystallogr. (Engl. Transl.)* **1987**, *32*, 26.

(16) Rundqvist, S.; Larsson, E. *Acta Chem. Scand.* **1959**, *13*, 551.

(17) Andersson, Y.; Rundqvist, S.; Tellgren, R.; Thomas, J. O.; Flanagan, T. B. *J. Solid State Chem.* **1980**, *32*, 321.

(18) (a) Andersson, Y.; Kaewchansilp, V.; del Rosario Casteleiro Soto, M.; Rundqvist, S. *Acta Chem. Scand., Ser. A* **1974**, *28*, 797. (b) Andersson, Y.; Rundqvist, S.; Tellgren, R.; Thomas, J. O.; Flanagan, T. B. *Acta Crystallogr., Sect. B: Struct. Crystallogr. Cryst. Chem.* **1981**, *37*, 1965.

(19) Sellberg, B. *Acta Chem. Scand.* **1966**, *20*, 2179.

(20) Andersson, Y. *Acta Chem. Scand., Ser. A* **1977**, *31*, 354.

(21) Matkovic, T.; Schubert, K. *J. Less-Common Met.* **1977**, *55*, 177.

(22) Kleinke, H.; Felser, C. *J. Alloys Comp.* **1999**, *291*, 73.

(23) Filmscan and Jade 3.1; Materials Data Inc.: Livermore, CA, 1996.

(24) Sheldrick, G. M. *SHELXTL* Version 5.1; Bruker Analytical X-ray Systems, Inc.: Madison, WI, 1997.

(25) *International Tables for X-ray Crystallography*; Wilson, A. J. C., Ed.; Kluwer: Dordrecht, The Netherlands, 1992; Vol. C.

(26) Gelato, L. M.; Parthé, E. *J. Appl. Crystallogr.* **1987**, *20*, 139.

(27) Whangbo, M.-H.; Hoffmann, R. *J. Am. Chem. Soc.* **1978**, *100*, 6093.

(28) Hoffmann, R. *Solids and Surfaces: A Chemist's View of Bonding in Extended*

Structures; VCH Publishers: New York, 1988.

(29) O'Keeffe, M.; Hyde, B. G. *Crystal Structures I. Patterns and Symmetry*; Mineralogical Society of America: Washington, DC, 1996.

(30) Shoemaker, C. B.; Shoemaker, D. P. *Acta Crystallogr.* **1965**, *18*, 900.

(31) Ganglberger, E. *Monatsh. Chem.* **1968**, *99*, 549.

(32) Simon, A. *Angew. Chem. Int. Ed. Engl.* **1981**, *20*, 1.

(33) Simon, A. *Ann. Chim. (Paris)* **1982**, *7*, 539.

(34) Ahlzén, P.-J.; Rundqvist, S. *Z. Kristallogr.* **1989**, *189*, 117.

(35) Hughbanks, T.; Hoffmann, R. *J. Am. Chem. Soc.* **1983**, *105*, 3528.

(36) Donohue, J. *The Structures of the Elements*; Wiley: New York, 1974.

(37) Bendersky, L. A.; Stalick, J. K.; Waterstrat, R. M. *J. Alloys. Comp.* **1993**, *201*, 121.

(38) (a) Pyykkö, P. *Chem. Rev.* **1997**, *97*, 597. (b) Dedieu, A.; Hoffmann, R. *J. Am. Chem. Soc.* **1978**, *100*, 2074. (c) Mehrotra, P. K.; Hoffmann, R. *Inorg. Chem.* **1978**, *17*, 2187.

Chapter 3

Nb_9PdAs_7: A Unique Arrangement in the $M_{n^2+3n+2}X_{n^2+n}Y$ Family of Hexagonal Structures †

Introduction

Binary transition metal-pnicogen (*M–Pn*) compounds have been studied extensively and can be classified into pnicogen-rich or metal-rich phases.[1,2] The structures of most pnicogen-rich phases, which may involve substantial nonmetal-nonmetal bonding in nonclassical patterns, can be interpreted surprisingly well by the simple Zintl concept.[3] Our understanding of metal-rich phases remains poor, although it is apparent that homoatomic metal-metal bonding, in addition to the strong metal-pnicogen bonding component, plays an important role in stabilizing these compounds.

There is now a growing body of examples of ternary pnictides containing two transition metals. For combinations of early (*EM*) and late transition metals (*LM*), the vast majority of these contain Ni.[4] In pnicogen-rich ternary compounds such as MNiPn_2 (M = Zr, Hf; Pn = P, As),[4a,d] ordered structures are observed because *EM* and *LM* prefer different coordination environments; the same principle is operative in the structures of many ternary chalcogenides[5] or halides.[6] In metal-rich ternary compounds such as

† A version of this chapter has been accepted for publication. Wang, M.; Mar, A. *Inorg. Chem.*

$M_3Pd_4P_3$ (M = Zr, Hf) or $M_5Pd_9P_7$,[4a,b] metal-metal interactions become increasingly important so that ordered structures are equally found not only because of the different coordination preferences, but also because of the drive to maximize the Lewis acid-base stabilization derived from strong heteroatomic *EM–LM* interactions (involving donation of electron density to *EM* from *LM*)[7] that can be supplemented by homoatomic *EM–EM* and *LM–LM* interactions as well. For combinations of two *EM*, it might not be thought that new structure types or ordered structures would result from metals with similar coordination preferences. Nevertheless, such compounds as $Zr_{6.45}Nb_{4.55}P_4$ [8] adopt structures not found in the corresponding binary phases and display differential fractional site occupancy (DFSO).[9]

Our primary interest is in the metal-rich regions of the ternary systems (Zr, Hf, Nb, Ta)–(Ni, Pd, Pt)–(P, As, Sb).[4] The systems containing a group 4 metal have been studied fairly comprehensively, although compounds with new structure types such as $Zr_9Ni_2P_4$,[10] Hf_5NiP_3,[11] $M_3Pd_4P_3$ (M = Zr, Hf),[4a] and $M_5Pd_9P_7$ (M = Zr, Hf)[4b] are still being found. The systems containing a group 5 metal have been most well studied in conjunction with Ni. There are thirteen compounds found in the (Nb, Ta)–Ni–P system and three compounds in the (Nb, Ta)–Ni–As system.[4] All of them are metal-rich, containing substantial metal-metal bonding in their structures but no *Pn–Pn* bonding (except in $NbNiP_2$, $TaNiP_2$, and $NbNiAs_2$,[4i] possessing the $UMoC_2$-type structure, which have weak ~2.79 Å P–P or ~2.95 Å As–As bonds). Recently discovered $Nb_{28}Ni_{33.5}Sb_{12.5}$ is the first compound found in the (Nb, Ta)–Ni–Sb system.[4s] To our knowledge, so far $Nb_5Pd_4P_4$ [4a] has been the only compound found in the (Nb, Ta)–Pd–(P, As, Sb) systems and none has been found in the (Nb, Ta)–Pt–(P, As, Sb) systems.

Reported here are the preparation, structure, bonding, and resistivity of Nb_9PdAs_7, the first compound found in the (Nb, Ta)–Pd–As system. Like many other ternary pnictides, pnicogen-centred trigonal prisms serve as the building blocks, but the arrangement is quite unusual in Nb_9PdAs_7 and its structure type, which is new, belongs to a missing member of a family of hexagonal structures with the general formula $M_{n^2+3n+2}X_{n^2+n}Y$.[12]

Experimental Section

Synthesis. Binary NbAs was first prepared by direct reaction of stoichiometric amounts of the elemental powders (Nb, 99.8%, Cerac; As, 99.99%, Alfa-Aesar) in an evacuated fused-silica tube heated at 500 °C for 2 days and 1000 °C for 3 days. A 0.25-g mixture of Pd (99.95%, Alfa-Aesar) and NbAs in a 1:1 molar ratio was pressed into a pellet and arc-melted in a Centorr 5TA tri-arc furnace under argon (gettered by melting a titanium pellet). Some needle-shaped crystals were found which contained all three elements on the basis of EDX (energy-dispersive X-ray) analysis on a Hitachi S-2700 scanning electron microscope. Because these crystals were rather small, insufficient X-ray diffraction intensity prevented satisfactory completion of a structure refinement. Nevertheless, a preliminary structure determination suggested two reasonable possibilities for the composition: "$Nb_{27}Pd_3As_{21}$ (Nb_9PdAs_7)" or "$Nb_{24}Pd_6As_{21}$ ($Nb_8Pd_2As_7$)".

To promote better crystal growth, a few grains of iodine were added in two reactions of Nb, Pd, and As in 27:3:21 and 24:6:24 molar ratios carried out in fused-silica tubes in a two-zone furnace heated in a temperature gradient of 1000/1050 °C (charge in

cool zone) for 3 days. Both reactions now gave larger crystals which contained 56% Nb, 4% Pd, and 40% As (avg. of 11 crystals) as determined from EDX analysis. One of these crystals was chosen for the ultimate structure determination.

Finally, the three reactions (i) 27 Nb + 3 Pd + 21 As, (ii) 24 Nb + 6 Pd + 21 As, and (iii) 30 Nb + 21 As were carried out in alumina tubes jacketed by fused-silica tubes heated at 1000 °C for 3 days. On the basis of X-ray powder diffraction patterns obtained on an Enraf-Nonius FR552 Guinier camera (Cu $K\alpha_1$ radiation), reaction (i) produced the desired hexagonal phase essentially quantitatively, reaction (ii) produced the desired hexagonal phase as well as other binary phases, and reaction (iii) produced only binary NbAs and Nb_5As_3. The EDX analysis, the results of these reactions, and the single-crystal structure determination strongly support the conclusion that the correct composition of the hexagonal phase is $Nb_{27}Pd_3As_{21}$ (or Nb_9PdAs_7) and that it is not another new binary Nb–As phase.

Structure Determination. Weissenberg photography confirmed the singularity of the selected needle-shaped crystal and gave preliminary cell parameters. X-ray diffraction data were collected on a Bruker Platform/SMART 1000 CCD diffractometer at room temperature (22°C) using ω scans (0.2°) in the range $2.82° \leq 2\theta$ (Mo $K\alpha$) $\leq$ 65.14°. Final cell parameters were refined from least-squares analysis of 3161 reflections. Crystal data and further details of the data collection are given in Table 3-1. All calculations were carried out with use of the SHELXTL (version 5.1) package.[13] Conventional atomic scattering factors and anomalous dispersion corrections were used.[14] Intensity data were processed, and face-indexed numerical absorption corrections were applied in XPREP.

Possible space groups to be considered were those in Laue class $6/m$. The centrosymmetric space group $P6_3/m$ was chosen first because it is the most common one adopted by many related hexagonal structures built up of centred trigonal prisms. A model determined by direct methods could be refined with well-behaved anisotropic displacement parameters for all atoms, but only to $R(F) = 0.12$. The sites at (0, 0, ¼) and (0, 0, ¾) are partially occupied by As atoms, each coordinated by nine (symmetry-equivalent) metal atoms in a tricapped trigonal prism. Because the distance between these sites is 1.7791(1) Å, equal to half the c parameter, the occupancy must be 50% (or less) to preclude unreasonable As–As contacts. On a local level, when an As atom occupies one of these sites, the three neighbouring metal atoms capping the trigonal prism (i.e., "waist contact" atoms) are displaced away whereas the six metal atoms at the corners of the trigonal prism move closer to attain reasonable metal–As bond distances. An additional disorder is thus introduced in which the position of the metal atoms forming the tricapped trigonal prism is split into two closely spaced sites each occupied at 50%, as is frequently observed in related structures such as $Cr_{12}P_7$.[15]

In space group $P6_3/m$, the symmetry equivalence of (0, 0, ¼) and (0, 0, ¾) (Wyckoff position $2a$) obliges the occupying As atoms to be disordered over these sites. Transformation to the lower symmetry space group $P\bar{6}$ (through the group-subgroup relation $P6_3/m \xrightarrow{t2,\ \text{origin shift}\ +0,0,1/4} P\bar{6}$) allows an ordered model to be proposed because the As atoms can fully occupy either (0, 0, 0) (Wyckoff position $1a$) or (0, 0, ½) (Wyckoff position $1b$), which are independent sites. It is well recognized that this space group ambiguity plagues the accurate determination of many related hexagonal structures.[16] Refinements in $P\bar{6}$ clearly supported an ordered model in which only the

(0, 0, ½) site is occupied by the As(9) atom, which centres a tricapped trigonal prism as mentioned earlier. Moreover, the corners of the trigonal prism, assigned as Nb(7), are distinguishable from the capping atoms, assigned as Pd. In accordance with the calculated Flack parameter of 0.45(3), the structure was refined as a racemic twin.

The final refinement gave $R(F)$ = 0.0328 and $R_w(F_o^2)$ = 0.0728 with reasonable anisotropic displacement parameters for all atoms. The two twin domains are present at 47(2) and 53%. The final difference electron map is featureless ($\Delta\rho_{max}$ = 2.16, $\Delta\rho_{min}$ = –1.99 e^- $Å^{-3}$). The atomic positions of Nb_9PdSb_7 were standardized with the program STRUCTURE TIDY.[17] Final values of the positional and displacement parameters are given in Table 3-2. Selected interatomic distances are listed in Table 3-3. Anisotropic displacement parameters are listed in Table C-2.

Electrical Resistivity. A single crystal of dimensions 0.025 × 0.0025 × 0.0025 cm was mounted in a two-probe configuration for an ac resistivity measurement along the crystallographic *c* (needle) axis between 2 and 300 K on a Quantum Design PPMS system equipped with an ac-transport controller (Model 7100). A current of 0.1 mA and a frequency of 16 Hz were used.

Band Structure. A tight-binding extended Hückel band structure calculation was performed on Nb_9PdAs_7 with use of the EHMACC suite of programs.[18,19] The atomic parameters were taken from literature values and are listed in Table 3-4. Properties were extracted from the band structure using 80 *k* points in the irreducible portion of the Brillouin zone.

Results and Discussion

Structure. About 18 compounds have been discovered to date in the (Nb, Ta)–(Ni, Pd, Pt)–(P, As, Sb) systems,[4] but Nb_9PdAs_7 is the first ternary niobium palladium arsenide and is isostructural to none of them. Its structure type is new. In common with most ternary metal-rich phosphides and arsenides, it is characterized by a short axis between 3 and 4 Å in the unit cell (c = 3.5582(1) Å) and the use of pnicogen-centred trigonal prisms as structural building blocks. A projection of the structure viewed along the short c axis is shown in Figure 3-1. All atoms are located either on $z = 0$ (light lines) or $z = ½$ planes (heavy lines). The As-centred trigonal prisms share corners within the ab plane to form larger triangular assemblies and share faces along the c direction to form infinite columns $^{1}_{\infty}[Nb_{15}As_{10}]$ and $^{1}_{\infty}[Nb_{12}Pd_3As_{10}]$. Neighbouring columns are displaced relative to each other by $\frac{1}{2}\vec{c}$. Additional As atoms (As(9)) occupy tricapped trigonal prismatic sites generated along the c axis. The representation in Figure 3-1 emphasizes the As-centred trigonal prismatic building blocks and shows only the metal-metal contacts that make up their edges (the dashed lines indicate Nb–Nb contacts longer than 3.5 Å). There are metal-As and metal-metal bonds within and between the columnar assemblies that are also important but not shown. Along the c direction, each atom is 3.5582(1) Å away from its symmetry equivalent above and below; this distance is too far to be considered bonding even for Nb atoms (the largest among Nb, Pd, and As). In the following discussion, we consider only those Nb–Nb contacts shorter than 3.5 Å to be bonding.

While similar, the two types of columns $^{1}_{\infty}[Nb_{15}As_{10}]$ and $^{1}_{\infty}[Nb_{12}Pd_3As_{10}]$ are chemically distinguishable in that Pd atoms preferentially occupy the corners of the

triangular assembly in the latter. Between corresponding atoms in these two types of columns, the metrical details are comparable for atoms in the interior, but they deviate significantly for atoms at the periphery and especially at the corners. Although the interatomic distances are generally unexceptional (Table 3-3), there are important distortions for bonds involving atoms near the *c* axis. Representative coordination polyhedra are shown in Figure 3-2.

The Nb atoms occupy nine crystallographically inequivalent sites. They can be classified into three categories: (i) "interior" Nb(3) and Nb(8), (ii) "peripheral" Nb(1), Nb(2), Nb(4), Nb(5), Nb(6), and Nb(9), and (iii) "corner" Nb(7) atoms. Figure 3-2(a) shows that the coordination of an "interior" atom such as Nb(3) is anticuboctahedral (CN12) with three As atoms above, three As atoms below, and six Nb atoms in the same plane in an *hcp* arrangement. The slip of the $^{1}_{\infty}[Nb_{15}As_{10}]$ and $^{1}_{\infty}[Nb_{12}Pd_3As_{10}]$ columns by $\frac{1}{2}\vec{c}$ causes the "peripheral" atoms to attain CN13. Each such Nb atom is surrounded by five As atoms (arranged in a square pyramid) and eight metal atoms among which are zero, one, or two Pd atoms (Figures 3-2(b)–(d)). Nb(9) is distinctly different in that one of the coordinating atoms (Nb(7), plotted as a broken circle in Figure 3-2(e)) is significantly further away (3.616(2) Å, shown as a dashed line in Figure 3-1). This arises because Nb(7) must be displaced towards As(9) on the *c* axis to form reasonable Nb(7)–As(9) bonds (2.756(1) Å). Finally, the "corner" Nb(7) atom itself has quite a different coordination from the others; it is surrounded by five As, four Pd, and three (and one more distant) Nb atoms, giving CN12+1 (Figure 3-2(f)).

The Pd atoms at the corners of the $^{1}_{\infty}[Nb_{12}Pd_3As_{10}]$ columns are located at the only sites in the structure where a tetrahedral environment of As atoms is available

(Figure 3-2(g)), consistent with the coordination preference of essentially zero-valent palladium (d^{10}). Eight more distant Nb atoms complete the CN12 coordination of Pd.

All As atoms occupy centres of trigonal prisms that have metal atoms at the vertices and that are capped by zero to three additional metal atoms on their quadrilateral faces to give CNs ranging from 6 to 9 (Figures 3-2(h)–(l)).

Structural Relationships. The hexagonal structure adopted by Nb_9PdAs_7 resembles those of a large family of metal-rich compounds, generally silicides, phosphides, and arsenides, composed of differently sized triangular columns of trigonal prisms.[12b,20] Nb_9PdAs_7 belongs to a structural series of general formula $M_{n^2+3n+2}X_{n^2+n}Y$, where typically M is a transition or rare-earth metal and X, Y are nonmetals or metalloids.[12] M resides at the corners of trigonal prisms, X at the centre of trigonal prisms, and Y at the centre of tricapped trigonal prisms, octahedra, or some irregular coordination polyhedra depending on where it is located along (0, 0, z). In our discussion, X and Y are the same element (Si, P, or As). The index n indicates the number of joined trigonal prisms along a basal edge of the triangular columns. Previously only the three members corresponding to n = 1 (Fe_2P-type),[21] 2 ($Cr_{12}P_7$-type),[15] and 3 ($Rh_{20}Si_{13}$-type)[12a] were known. Nb_9PdAs_7 is the first member discovered with n = 4 ($M_{30}X_{20}Y \rightarrow (Nb_{27}Pd_3)As_{20}As = Nb_9PdAs_7 \times 3$) having triangular columns with the longest edge so far (other than $n = \infty$, corresponding to the WC-type structure)[22] in this series. The structures with n = 1, 2, 3, and 4 are shown in Figure 3-3.

The positions of the Y atoms differ in these four structures. For ease of comparison, origin shifts were applied so that tricapped trigonal prismatic sites are located at (0, 0, ¼) or (0, 0, ¾) and octahedral sites at (0, 0, 0) or (0, 0, ½). In Fe_2P

($P\bar{6}2m$),[21] the two tricapped trigonal prismatic sites are crystallographically inequivalent and only one of these is occupied by P atoms (Figure 3-3(a)). In $Cr_{12}P_7$ ($P6_3/m$),[15] the two tricapped trigonal prismatic sites are crystallographically equivalent and are only 50% occupied by P atoms to preclude unrealistically short P–P contacts of ~1.65 Å. Depending on which of these sites is occupied on a local level, the surrounding Cr atoms will adjust their positions so that the three capping or waist atoms are pushed away and the six atoms at the corners of the trigonal prism are drawn towards the P centre. Thus the $Cr_{12}P_7$ structure, when refined in space group $P6_3/m$, is portrayed as an averaged structure (Figure 3-3(b)). In $Rh_{20}Si_{13}$ ($P6_3/m$),[12a] the two octahedral sites are crystallographically equivalent and are also only 50% occupied by Si atoms (Figure 3-3(c)). Unlike the case of $Cr_{12}P_7$, however, there is no need for a distortion involving the positions of Rh atoms coordinating the Si atoms because the Rh–Si contacts are already reasonable. More complicated situations arise in which both the tricapped trigonal prismatic and octahedral sites are partially occupied in a random manner, such as occurs in $Rh_{12}As_7$.[23] In Nb_9PdAs_7 ($P\bar{6}$), only the tricapped trigonal prismatic site at (0, 0, ¼) is occupied by As atoms (Figure 3-3(d)). The difference in the capping atoms (Pd) and the atoms at the corners of the trigonal prism (Nb(7)) of this tricapped trigonal prismatic site is a unique feature of Nb_9PdAs_7. This arrangement anchors the position of the As atom so that an ordered structure can be refined in space group $P\bar{6}$. As a consequence, one of the large triangular columns $^{1}_{\infty}[Nb_{12}Pd_3As_{10}]$ has Pd atoms at the corners whereas the other column $^{1}_{\infty}[Nb_{15}As_{10}]$ does not. The extreme case of $n = \infty$ in the $M_{n+3n+2}X_{n+n}Y$ series gives the WC structure with C atoms occupying the centres of half the trigonal prisms made up of W atoms at the corners (or vice versa).

In the $M_{n^2+3n+2}X_{n^2+n}Y$ series, only half of the trigonal prisms are filled and only half of the tricapped trigonal prismatic or octahedral sites along (0, 0, z) are filled. Filling all these sites generates another structural series with general formula $M_{n^2+3n+2}X_{2n^2}Y_2$,[12b] adopted mostly by *RE*–Ni–Si phases such as $Ce_6Ni_2Si_3$ (n = 2), $La_5Ni_2Si_3$ (n = 3), $La_{15}Ni_7Si_{10}$ (n = 4), and $La_{21}Ni_{11}Si_{15}$ (n = 5);[24,25] the AlB_2 structure ($n = \infty$) corresponds to the extreme case. Whether other members of the $M_{n^2+3n+2}X_{n^2+n}Y$ series can be synthesized remains an open question. The next largest member (n = 5) with hypothetical formula $M_{42}X_{30}Y$ is worth targeting. There do exist related hexagonal structures containing even larger triangular columns with six ($Ho_{20}Ni_{66}P_{43}$)[26] or seven ($La_{18}Rh_{96}P_{51}$)[27] joined trigonal prisms along a basal edge. They have complicated atomic arrangements that cannot be fit into a general formula.

Bonding. There are strong metal–metal and metal–As but no As–As bonding interactions in the structure. Because all As atoms are isolated and are surrounded only by more electropositive Nb atoms, they can be assigned a formal oxidation state of –3 according to the Zintl concept. If we assume a d^{10} configuration for the Pd atoms, we arrive at the formulation $[(Nb^{2.33+})_9(Pd^0)(As^{3-})_7]$. In this crude approximation, each Nb atom donates 2.33 valence electrons to form strong Nb–As bonds. The remaining 2.67 valence electrons on each Nb atom are then available for forming metal–metal bonds (mostly Nb–Nb but also some Nb–Pd), consistent with the extended network of Nb–Nb contacts of 3.029(2)–3.429(2) Å observed in the structure of Nb_9PdAs_7. These metal–metal bonds are crucial in stabilizing the structure.

To analyze the bonding in more detail, the band structure of Nb_9PdAs_7 was calculated. The density of states (DOS) is plotted in Figure 3-4. As expected for this

metal-rich compound, there is no band gap at the Fermi level (ε_f = –9.50 eV) which is also consistent with the metallic behaviour of Nb_9PdAs_7 (ρ_{300} = 1.17 × 10^{-3} Ω cm; ρ_{300}/ρ_2 = 1.24) seen in the resistivity plot in Figure 3-5. The states around the Fermi level are dominated by Nb 4d contributions (Figure 3-4(a)), implying that electronic conduction occurs largely through the extended network of metal–metal bonded Nb atoms. The Nb 4d states are broadly dispersed and can be roughly divided into three regions, separated by local minima: **I.** –16.0 to –11.4 eV; **II.** –11.4 to –9.5 eV; **III.** above –9.5 eV. Most of the As 4p states lie between –16.0 and –11.4 eV (Figure 3-4(b)), which overlaps with region **I** of the Nb 4d states. The substantial mixing of Nb and As states in this region leads to strong Nb–As covalent bonds. This expectation is confirmed by the crystal orbital overlap population (COOP)[28] curve in Figure 3-6(a), which shows that Nb–As bonding is optimized with all bonding levels and no antibonding levels occupied (Mulliken overlap population (MOP) of 0.393). The Nb–As bond distances of 2.600(1)–2.818(2) Å in Nb_9PdAs_7 are similar to those in $NbAs_2$ (2.53–2.82 Å)[29] and Nb_4As_3 (2.545(2)–2.752(2) Å).[30]

Between –11 and –7 eV, the DOS is dominated by Nb 4d states, with a local minimum near the Fermi level separating regions **II** and **III**. Region **II** is associated with Nb–Nb bonding levels and region **III** with Nb–Nb antibonding levels, as verified by inspection of the Nb–Nb COOP curve (Figure 3-6(b)). Most of the Nb–Nb distances *between* the large triangular columns (3.029(2)–3.091(2) Å) are actually shorter than those *within* columns (3.212(2)–3.429(2) Å), notwithstanding the portrayal in Figure 3-1. The intercolumn Nb–Nb bonds are exactly optimized, with the Nb–Nb bonding levels completely filled and the Nb–Nb antibonding levels completely empty (solid line in

Figure 3-6(b)); the MOP of 0.21 represents fairly strong metal–metal interactions. The intracolumn Nb–Nb bonds are also nearly optimized with only a small portion of the antibonding levels occupied (dashed line in Figure 3-6(b)); the slightly smaller MOP of 0.13 indicates weaker but still substantial metal–metal interactions. All Nb–Nb bonds found in Nb_9PdAs_7 are greater than the 2.86 Å bond found in elemental Nb (which also has longer 3.30 Å contacts)[31] but are comparable to those in other Nb-rich arsenides such as Nb_4As_3 (2.905(1)–3.487(2) Å).[30]

The oxidation state formulation $[(Nb^{2.33+})_9(Pd^0)(As^{3-})_7]$ suggests that per unit cell ($Z = 3$), 198 valence electrons ($10 \times 1 \times 3 + 8 \times 7 \times 3 = 198$) are needed to fill up metal–As bonding levels and the remaining 72 valence electrons ($2.67 \times 9 \times 3 = 72$) will then be used to fill up Nb–Nb bonding levels. This crude analysis is nicely validated by the band structure calculation. At a count of 198 electrons, the DOS curve is filled up to −11.39 eV, precisely at the local minimum separating region **I** (Nb–As bonding) from regions **II** (Nb–Nb bonding) and **III** (Nb–Nb antibonding) in the Nb d-block (Figure 3-4(a)).

The contribution of the Pd 4d states falls essentially in the narrow peak below the Fermi level between −12 and −13 eV (Figure 3-4(c)), which is also consistent with the d^{10} configuration proposed in the oxidation state formulation above. An MOP of 0.069 reveals weak heteroatomic Nb–Pd bonds (Figure 3-6(c)) of 2.940(2)–2.981(2) Å, which is longer than the sum of Pauling single-bond radii ($r_{Nb} + r_{Pd} = 1.342 + 1.278$ Å $= 2.620$ Å).[32] As expected for a closed shell d^{10} configuration for Pd, some Pd–As antibonding levels are located below the Fermi level. Although small, the cumulative MOP of 0.12 represents normal Pd–As interactions. The observed Pd–As bond distances of 2.538(1)–2.662(2) Å are comparable with those in $PdAs_2$ (2.50 Å)[33] and in Pd_2As (2.39–2.70 Å).[34]

In conclusion, the first and rather unique ternary niobium palladium arsenide has been synthesized. The structure of Nb_9PdAs_7 not only extends the $M_{n^2+3n+2}X_{n^2+n}Y$ family of WC-related hexagonal structures to $n = 4$, but also exhibits some features that are not observed in the other members in the same family. In particular, ordering of different metal atoms can occur even within these very large triangular columns of linked trigonal prisms, so that the Pd atoms prefer sites of tetrahedral As coordination. Other related members with smaller or larger triangular assemblies should be feasible to target. The band structure calculation shows that the bonding of even metal-rich compounds can be understood to a first approximation by simple chemical ideas such as the Zintl concept.

Table 3-1. Crystallographic Data for Nb_9PdAs_7

Formula	Nb_9PdAs_7
Formula mass (amu)	1467.03
Space group	$C_{3h}^1 - P\bar{6}$ (No. 174)
a (Å)	16.6955(6) [a]
c (Å)	3.5582(1) [a]
V (Å^3)	858.93(5)
Z	3
T (°C)	22
Diffractometer	Bruker PLATFORM/SMART–1000 CCD
ρ_{calc} (g cm^{-3})	8.508
Crystal dimensions (mm)	Needle, 0.088 × 0.014 × 0.014
Radiation	Graphite-monochromated Mo $K\alpha$, λ = 0.71073 Å
μ(Mo $K\alpha$) (cm^{-1})	302.01
Transmission factors [b]	0.351–0.699
Scan type	ω scans (0.2°)
2θ limits	$2° \leq 2\theta(\text{Mo } K\alpha) \leq 66°$
Data collected	$-15 \leq h \leq 25$, $-25 \leq k \leq 24$, $-5 \leq l \leq 5$
No. of data collected	6881
No. of unique data, including $F_o^2 < 0$	2353 (R_{int} = 0.052)
No. of unique data, with $F_o^2 > 2\sigma(F_o^2)$	1760
No. of variables [c]	105
Flack parameter [d]	0.47(2)

Table 3-1. Crystallographic Data for Nb_9PdAs_7 (continued)

$R(F)$ for $F_o^2 > 2\sigma(F_o^2)$ [e]	0.033
$R_w(F_o^2)$ [f]	0.073
Goodness of fit [g]	1.017
$\Delta\rho_{max}$, $\Delta\rho_{min}$ (e Å^{-3})	2.16, −1.99

[a] Obtained from a refinement constrained so that $a = b$, $\alpha = \beta = 90°$, and $\gamma = 120°$.

[b] A numerical face-indexed absorption correction was applied, with the use of programs in the SHELXTL package (Sheldrick, G. M. *SHELXTL Version 5.1*; Bruker Analytical X-ray Systems: Madison, WI, 1997).

[c] Including an extinction coefficient.

[d] Flack, H. D. *Acta Crystallogr. Sect. A: Found. Crystallogr.* **1983**, *39*, 876.

[e] $R(F) = \sum \left| |F_o| - |F_c| \right| / \sum |F_o|$.

[f] $R_w(F_o^2) = \left[\sum \left[w(F_o^2 - F_c^2)^2\right] / \sum wF_o^4\right]^{1/2}$; $w^{-1} = \left[\sigma^2(F_o^2) + (0.0208P)^2 + 0.3365P\right]$ where $P = \left[\max(F_o^2, 0) + 2F_c^2\right]/3$.

[g] $GooF = \left[\sum \left[w(F_o^2 - F_c^2)^2\right] / (n - p)\right]^{1/2}$ where n is the number of reflections and p is the total number of parameters refined.

Table 3-2. Positional and Equivalent Isotropic Displacement Parameters for Nb_9PdAs_7

atom	Wyckoff position	x	y	z	U_{eq} (Å^2) [a]
Nb(1)	3*k*	0.31536(10)	0.20192(9)	½	0.0030(3)
Nb(2)	3*k*	0.35787(9)	0.02973(9)	½	0.0037(3)
Nb(3)	3*k*	0.53364(9)	0.24556(9)	½	0.0033(3)
Nb(4)	3*k*	0.57828(10)	0.07225(10)	½	0.0032(3)
Nb(5)	3*j*	0.07269(10)	0.49636(10)	0	0.0029(3)
Nb(6)	3*j*	0.11658(9)	0.31844(9)	0	0.0036(3)
Nb(7)	3*j*	0.13091(9)	0.12059(9)	0	0.0065(3)
Nb(8)	3*j*	0.28785(9)	0.53367(9)	0	0.0025(3)
Nb(9)	3*j*	0.32442(9)	0.35451(9)	0	0.0028(3)
Pd	3*k*	0.01025(8)	0.15826(8)	½	0.0095(2)
As(1)	3*k*	0.15675(11)	0.44785(11)	½	0.0031(3)
As(2)	3*k*	0.19388(11)	0.26140(10)	½	0.0034(3)
As(3)	3*k*	0.37261(11)	0.48689(11)	½	0.0028(3)
As(4)	3*j*	0.27065(11)	0.07280(10)	0	0.0055(3)
As(5)	3*j*	0.44670(11)	0.28996(10)	0	0.0037(3)
As(6)	3*j*	0.48934(10)	0.11474(10)	0	0.0039(3)
As(7)	1*e*	⅔	⅓	0	0.0037(6)
As(8)	1*d*	⅓	⅔	½	0.0026(6)
As(9)	1*b*	0	0	½	0.0065(5)

[a] U_{eq} is defined as one-third of the trace of the orthogonalized $\mathbf{U}_{ij}$ tensor.

Table 3-3. Selected Interatomic Distances (Å) for Nb_9PdAs_7

Nb(1)–As(4)	2.600(1) (×2)	Nb(6)–As(1)	2.614(1) (×2)
Nb(1)–As(5)	2.629(2) (×2)	Nb(6)–As(2)	2.639(2) (×2)
Nb(1)–As(2)	2.667(2)	Nb(6)–As(4)	2.772(2)
Nb(1)–Nb(9)	3.048(2) (×2)	Nb(6)–Nb(2)	3.091(2) (×2)
Nb(1)–Nb(7)	3.211(2) (×2)	Nb(6)–Nb(9)	3.212(2)
Nb(1)–Nb(2)	3.288(2)	Nb(6)–Nb(8)	3.289(2)
Nb(1)–Nb(3)	3.340(2)	Nb(6)–Nb(5)	3.397(2)
Nb(1)–Nb(4)	3.379(2)	Nb(6)–Nb(7)	3.429(2)
Nb(1)–Pd	3.234(2)	Nb(6)–Pd	2.953(2) (×2)
Nb(2)–As(4)	2.617(2) (×2)	Nb(7)–As(2)	2.707(2) (×2)
Nb(2)–As(6)	2.623(1) (×2)	Nb(7)–As(9)	2.756(1) (×2)
Nb(2)–As(1)	2.732(2)	Nb(7)–As(4)	2.818(2)
Nb(2)–Nb(5)	3.029(2) (×2)	Nb(7)–Nb(1)	3.211(2) (×2)
Nb(2)–Nb(6)	3.091(2) (×2)	Nb(7)–Nb(6)	3.429(2)
Nb(2)–Nb(1)	3.288(2)	Nb(7)–Nb(9)	3.616(2)
Nb(2)–Nb(3)	3.320(2)	Nb(7)–Nb(7)	3.646(2) (×2)
Nb(2)–Nb(4)	3.381(2)	Nb(7)–Pd	2.940(2) (×2)
Nb(2)–Pd	3.222(2)	Nb(7)–Pd	2.981(2) (×2)
Nb(3)–As(6)	2.621(1) (×2)	Nb(8)–As(1)	2.622(2) (×2)
Nb(3)–As(5)	2.626(2) (×2)	Nb(8)–As(3)	2.624(1) (×2)
Nb(3)–As(7)	2.644(1) (×2)	Nb(8)–As(8)	2.643(1) (×2)

Table 3-3. Selected Interatomic Distances (Å) for Nb_9PdAs_7 (continued)

Nb(3)–Nb(2)	3.320(2)	Nb(8)–Nb(6)	3.289(2)
Nb(3)–Nb(4)	3.322(2)	Nb(8)–Nb(5)	3.305(2)
Nb(3)–Nb(4)	3.329(2)	Nb(8)–Nb(5)	3.325(2)
Nb(3)–Nb(1)	3.340(2)	Nb(8)–Nb(9)	3.339(2)
Nb(3)–Nb(3)	3.388(2) (×2)	Nb(8)–Nb(8)	3.386(2) (×2)
Nb(4)–As(5)	2.625(2) (×2)	Nb(9)–As(3)	2.630(1) (×2)
Nb(4)–As(6)	2.632(2) (×2)	Nb(9)–As(2)	2.635(2) (×2)
Nb(4)–As(3)	2.737(2)	Nb(9)–As(5)	2.744(2)
Nb(4)–Nb(9)	3.043(1) (×2)	Nb(9)–Nb(4)	3.043(1) (×2)
Nb(4)–Nb(5)	3.072(1) (×2)	Nb(9)- Nb(1)	3.048(2) (×2)
Nb(4)–Nb(3)	3.322(2)	Nb(9)–Nb(6)	3.212(2)
Nb(4)–Nb(3)	3.329(2)	Nb(9)–Nb(8)	3.339(2)
Nb(4)–Nb(1)	3.379(2)	Nb(9)–Nb(5)	3.404(2)
Nb(4)–Nb(2)	3.381(2)	Nb(9)–Nb(7)	3.616(2)
Nb(5)–As(3)	2.630(1) (×2)	Pd–As(4)	2.538(1) (×2)
Nb(5)–As(1)	2.632(2) (×2)	Pd–As(9)	2.561(1)
Nb(5)–As(6)	2.750(2)	Pd–As(2)	2.662(2)
Nb(5)–Nb(2)	3.029(2) (×2)	Pd–Nb(7)	2.940(2) (×2)
Nb(5)–Nb(4)	3.072(1) (×2)	Pd–Nb(6)	2.953(2) (×2)
Nb(5)–Nb(8)	3.305(2)	Pd–Nb(7)	2.981(2) (×2)
Nb(5)–Nb(8)	3.325(2)	Pd–Nb(2)	3.222(2)

Table 3-3. Selected Interatomic Distances (Å) for Nb_9PdAs_7 (continued)

Nb(5)–Nb(6)	3.397(2)	Pd–Nb(1)	3.234(2)
Nb(5)–Nb(9)	3.404(2)		

Table 3-4. Extended Hückel Parameters

atom	orbital	H_{ii} (eV)	ζ_{i1}	c_1	ζ_{i2}	c_2
Nb	5s	−9.04	1.89			
	5p	−5.13	1.85			
	4d	−9.94	4.08	0.6401	1.64	0.5516
Pd	5s	−7.51	2.19			
	5p	−3.86	2.15			
	4d	−12.53	5.98	0.55	2.61	0.67
As	4s	−16.22	2.23			
	4p	−12.16	1.89			

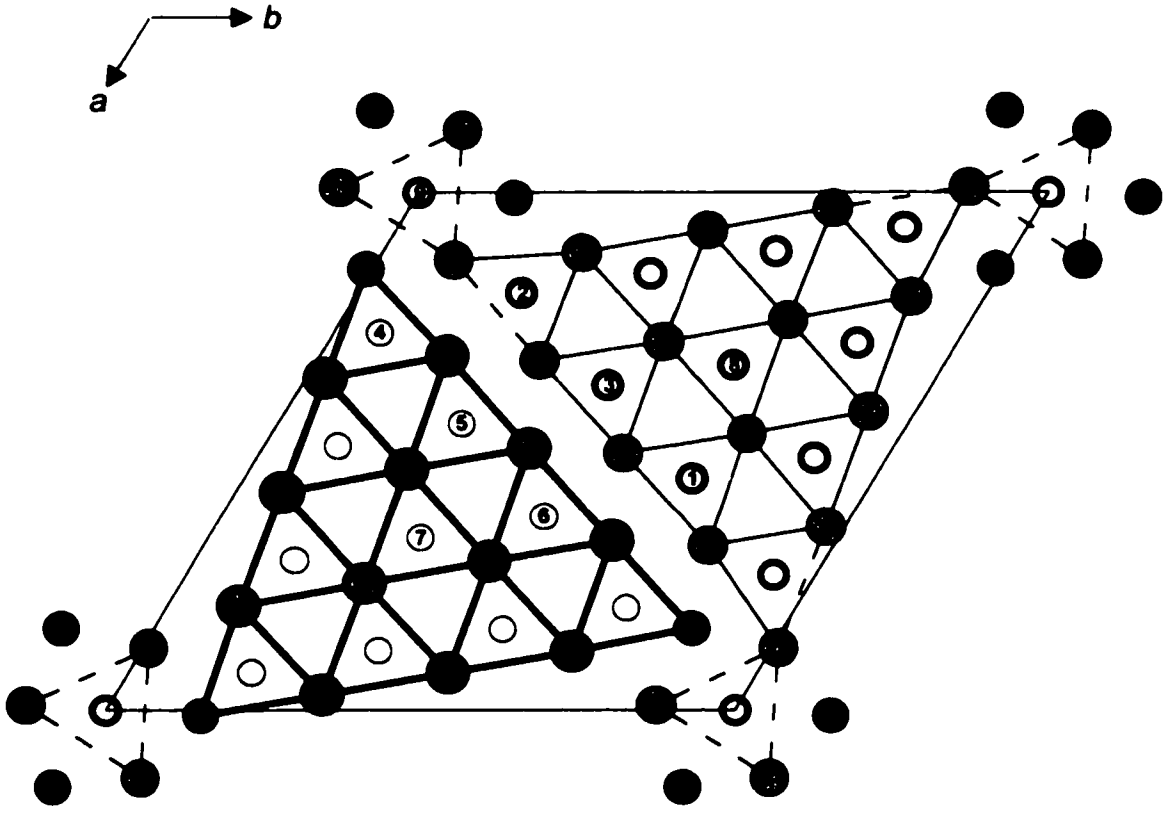

Figure 3-1. Structure of Nb_9PdAs_7 viewed in projection down the *c* axis. The large lightly shaded circles are Nb atoms, the medium solid circles are Pd atoms, and the small open circles are As atoms. Atoms at $z = 0$ have thin rims and those at $z = ½$ have thick rims. The dashed lines are Nb–Nb contacts longer than 3.5 Å.

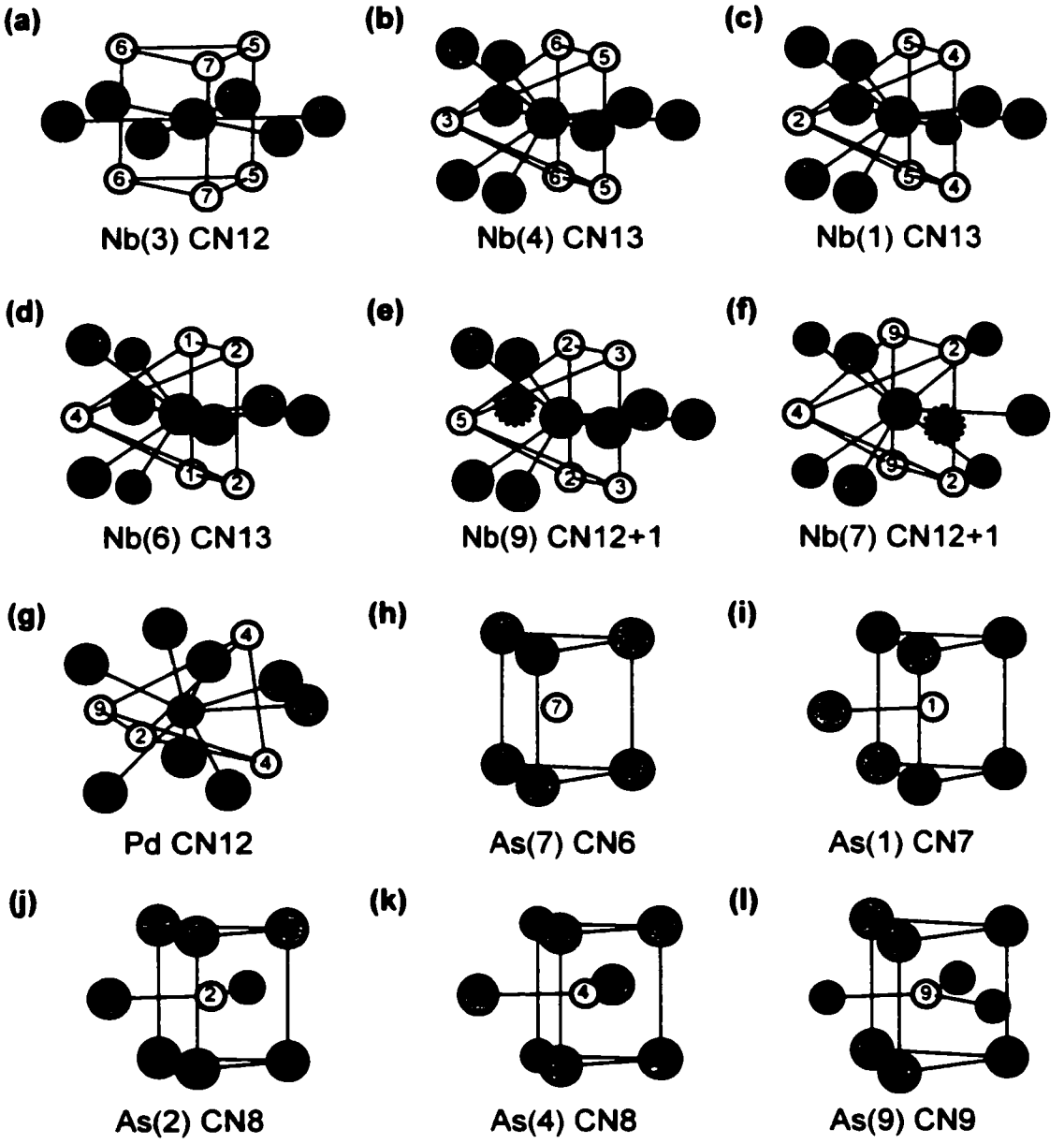

Figure 3-2. Representative coordination polyhedra in Nb_9PdAs_7. The large lightly shaded circles are Nb atoms, the medium solid circles are Pd atoms, and the small open circles are As atoms. The broken circle in (e) and (f) indicates a Nb atom further than 3.5 Å away from the coordination centre.

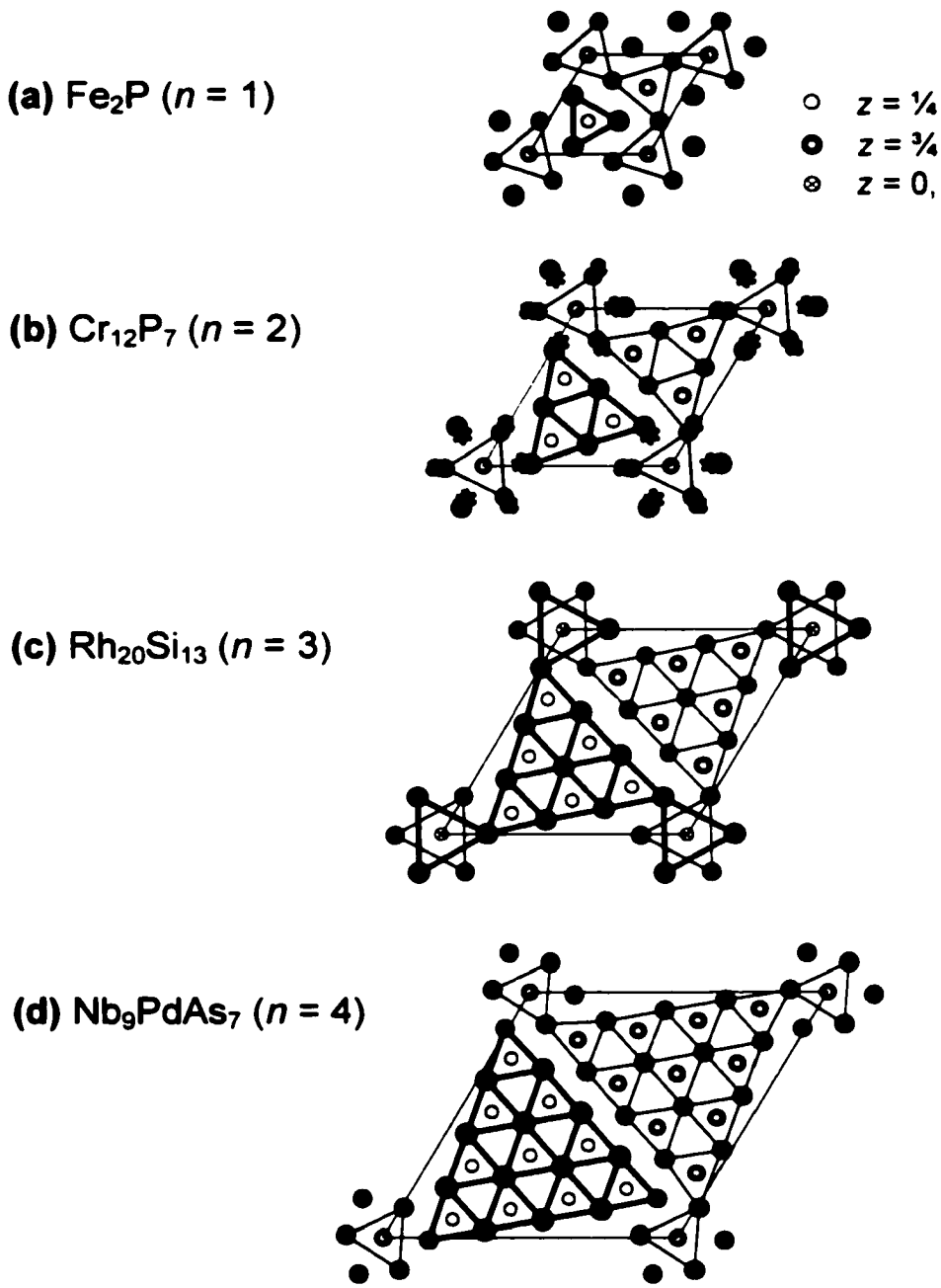

Figure 3-3. Comparison of members in the $M_{n^2+3n+2}X_{n^2+n}Y$ family, where transition metal atoms M are shown as shaded circles and nonmetal or metalloid atoms X, Y = Si, P, As are shown as open circles. M atoms form trigonal prisms centred by X atoms; Y atoms are found along the c axis. Shown are the structures of (a) Fe_2P (origin shifted by (⅓ , −⅓ , −¼)), (b) $Cr_{12}P_7$ (origin shifted by (0, 0, ½)) (the arrangement of Cr atoms when P is at (0, 0, ¾) is highlighted; broken circles are the corresponding Cr positions when P is at (0, 0, ¼)), (c) $Rh_{20}Si_{13}$, and (d) Nb_9PdAs_7 (origin shifted by (0, 0, ¼)).

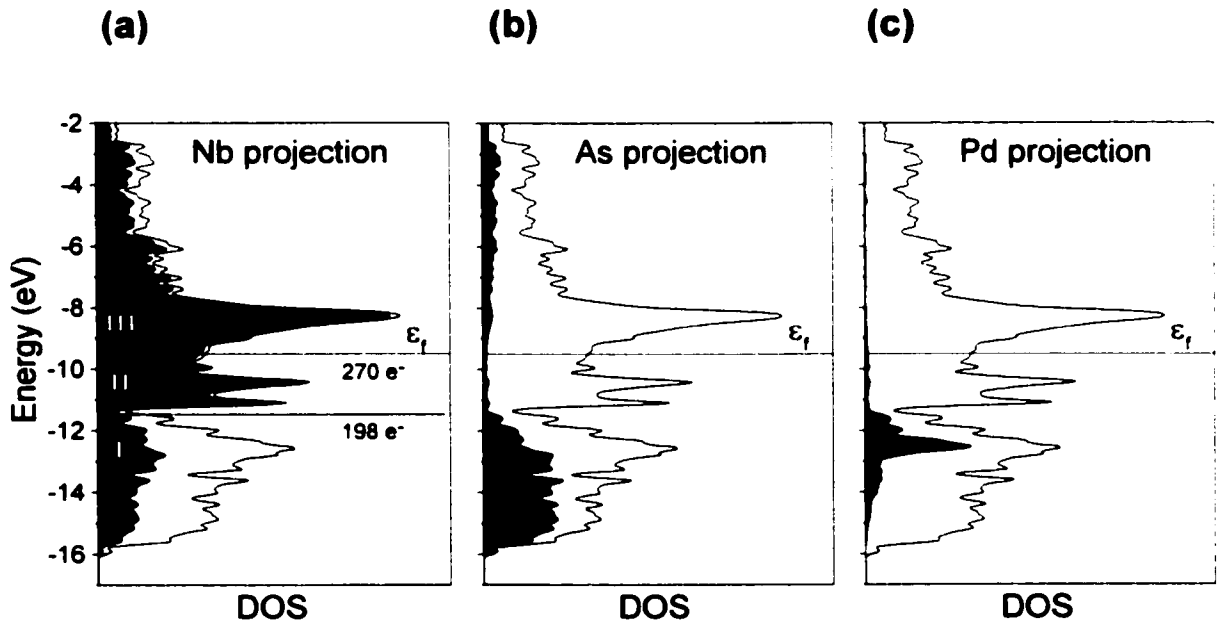

Figure 3-4. Contributions of (a) Nb, (b) As, and (c) Pd (shaded regions) to the total density of states (DOS) (line) for Nb_9PdAs_7. See text for discussion of regions **I**, **II**, and **III** and electron count shown in (a). The Fermi level, ε_f, lies at –9.5 eV, at an count of 270 e^- per unit cell.

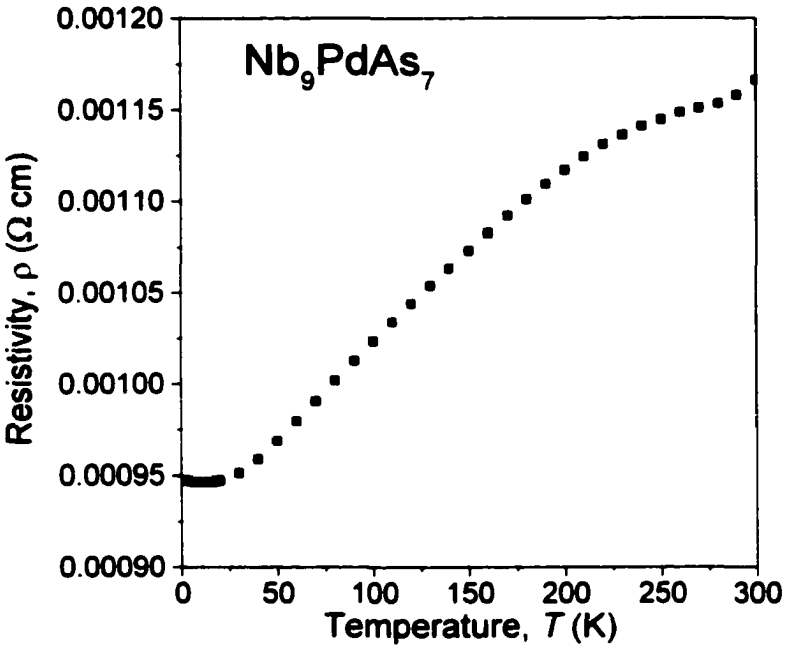

Figure 3-5. Temperature dependence of the resistivity along the needle axis *c* of a single crystal of Nb_9PdAs_7.

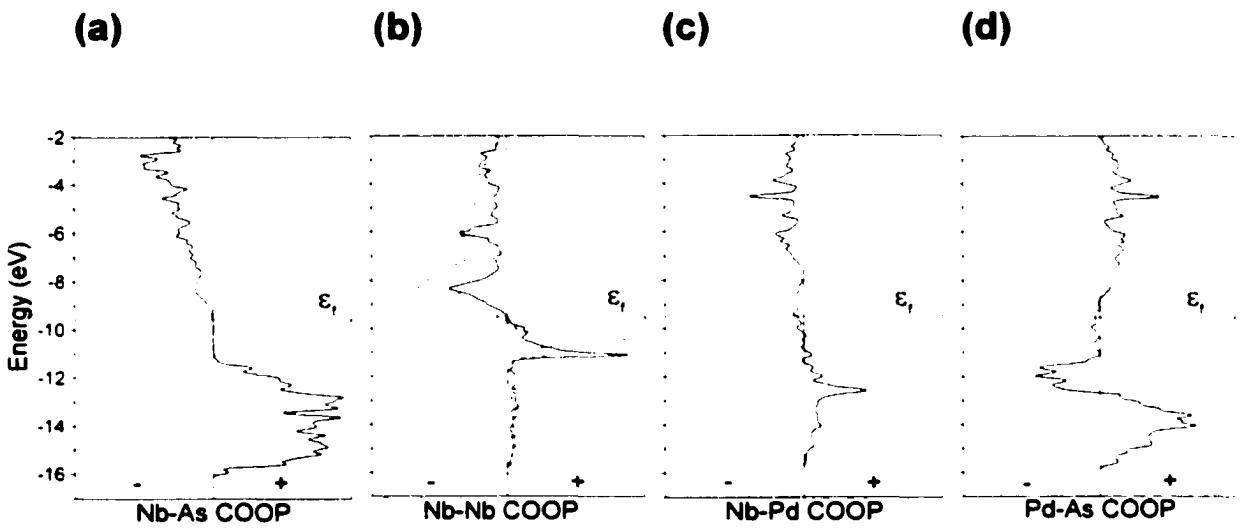

Figure 3-6. Crystal orbital overlap population (COOP) curves for (a) Nb–As, (b) Nb–Nb (solid line, 3.029(2)–3.091(2) Å; dashed line, 3.212(2)–3.429(2) Å), (c) Nb–Pd, and (d) Pd–As interactions in Nb_9PdAs_7.

References

(1) Hulliger, F. In *Structure and Bonding*; Jørgensen, C. K.; Neilands, J. B.; Nyholm, R. S.; Reinen, D.; Williams, R. J. P., Eds., Springer-Verlag: New York, 1968; Vol. 4, p. 83.

(2) Villars, P. *Pearson's Handbook, Desk Edition*; ASM International: Materials Park, OH, 1997.

(3) Papoian, G. A.; Hoffmann, R. *Angew. Chem., Int. Ed.* **2000**, *39*, 2408.

(4) (a) $M_3Pd_4P_3$ (M = Zr, Hf), HfPdSb, $Nb_5Pd_4P_4$: Wang, M.; McDonald, R.; Mar, A. *Inorg. Chem.* **2000**, *39*, 4936. $M_xNi_yP_z$ (M = Zr, Hf, Nb, Ta): See references therein. (b) $M_5Pd_9P_7$ (M = Zr, Hf), ZrPdAs, ZrPdSb: Heerdmann, A.; Johrendt, D.; Mewis, A. *Z. Anorg. Allg. Chem.* **2000**, *626*, 1393. (c) ZrNiAs, HfNiAs: Kleinke, H.; Franzen, H. F. *Z. Anorg. Allg. Chem.* **1998**, *624*, 51. (d) $ZrNi_{0.75}As_2$, $HfNi_{0.75}As_2$: El Ghadraoui, E. H.; Pivan, J. Y.; Guérin, R. *J. Less-Common Met.* **1988**, *136*, 303. (e) Zr_2NiAs_2: El Ghadraoui, E. H.; Pivan, J. Y.; Guérin, R.; Sergent, M. *Mater. Res. Bull.* **1988**, *23*, 891. (f) $ZrNi_4As_2$, $HfNi_4As_2$: Pivan, J. Y.; Guérin, R.; El Ghadraoui, E. H.; Rafiq, M. *J. Less-Common Met.* **1989**, *153*, 285. (g) $Zr_2Ni_3As_3$, $Hf_2Ni_3As_3$: El Ghadraoui, E. H.; Pivan, J. Y.; Guérin, R.; Padiou, J.; Sergent, M. *J. Less-Common Met.* **1985**, *105*, 187. (h) NbNiAs, TaNiAs: Rundqvist, S.; Tansuriwongs, P. *Acta Chem. Scand.* **1967**, *21*, 813. (i) $NbNiAs_2$: El Ghadraoui, E. H.; Guérin, R.; Padiou, J.; Sergent, M. *C. R. Séances Acad. Sci., Sér. 2* **1983**, *296*, 617. (j) ZrNiSb, HfNiSb: Kleinke, H. *Z. Anorg. Allg. Chem.* **1998**, *624*, 1272. (k) $ZrNi_2Sb$, $HfNi_2Sb$: Dwight, A. E. *Mater. Res. Bull.* **1987**, *22*, 201. (l) Zr_5NiSb_3: Garcia, E.;

Corbett, J. D. *Inorg. Chem.* **1990**, *29*, 3274. (m) $Zr_5Ni_{0.5}Sb_{2.5}$: Kwon, Y.-U.; Sevov, S. C.; Corbett, J. D. *Chem. Mater.* **1990**, *2*, 550. (n) $Zr_3Ni_3Sb_4$, $Hf_3Ni_3Sb_4$, $Zr_3Pt_3Sb_4$: Wang, M.; McDonald, R.; Mar, A. *Inorg. Chem.* **1999**, *38*, 3435. (o) Zr_6NiSb_2, Hf_6NiSb_2: Melnyk, G.; Bauer, E.; Rogl, P.; Skolozdra, R.; Seidl, E. *J. Alloys Compd.* **2000**, *296*, 235. (p) Hf_5NiSb_3: Rieger, W.; Parthé, E. *Acta Crystallogr., Sect. B: Struct. Crystallogr. Cryst. Chem.* **1968**, *24*, 456. (q) $Hf_6Ni_{1-x}Sb_{2+x}$: Kleinke, H. *J. Alloys Compd.* **1998**, *270*, 136. (r) $Hf_{10}Ni_xSb_{6-x}$: Kleinke, H.; Ruckert, C.; Felser, C. *Eur. J. Inorg. Chem.* **2000**, 315. (s) $Nb_{28}Ni_{33.5}Sb_{12.5}$: Wang, M.; Mar, A. *J. Solid State Chem.* In press.

(5) Hughbanks, T. *J. Alloys Compd.* **1995**, *229*, 40.

(6) Corbett, J. D. *J. Alloys Compd.* **1995**, *229*, 10.

(7) Brewer, L.; Wengert, P. R. *Metall. Trans.* **1973**, *4*, 83.

(8) Marking, G. A.; Franzen, H. F. *Chem. Mater.* **1993**, *5*, 678.

(9) Franzen, H. F.; Köckerling, M. *Prog. Solid State Chem.* **1995**, *23*, 265.

(10) Kleinke, H.; Franzen, H. F. *Inorg. Chem.* **1996**, *35*, 5272.

(11) Kleinke, H.; Franzen, H. F. *Chem. Mater.* **1997**, *9*, 1030.

(12) (a) Engström, I. *Acta Chem. Scand.* **1965**, *19*, 1924. (b) Hyde, B. G.; Andersson, S. *Inorganic Crystal Structures*; Wiley: New York, 1989.

(13) Sheldrick, G. M. *SHELXTL*, version 5.1; Bruker Analytical X-ray Systems, Inc.: Madison, WI, 1997.

(14) *International Tables for X-ray Crystallography*; Wilson, A. J. C., Ed.; Kluwer: Dordrecht, The Netherlands, 1992; Vol. C.

(15) Chun, H. K.; Carpenter, G. B. *Acta Crystallogr., Sect. B: Struct. Crystallogr.*

Cryst. Chem. **1979**, *35*, 30

(16) Jeitschko, W.; Jakubowski-Ripke, U. *Z. Kristallogr.* **1993**, *207*, 69.

(17) Gelato, L. M.; Parthé, E. *J. Appl. Crystallogr.* **1987**, *20*, 139.

(18) Whangbo, M.-H.; Hoffmann, R. *J. Am. Chem. Soc.* **1978**, *100*, 6093.

(19) Hoffmann, R. *Solids and Surfaces: A Chemist's View of Bonding in Extended Structures*; VCH Publishers: New York, 1988.

(20) Pearson, W. B. *The Crystal Chemistry and Physics of Metals and Alloys*; Wiley: New York, 1972.

(21) Rundqvist, S.; Jellinek, F. *Acta Chem. Scand.* **1959**, *13*, 425.

(22) Butorina, L. N. *Sov. Phys. Crystallogr. (Engl. Transl.)* **1960**, *5*, 216.

(23) (a) Lambert-Andron, B.; Dhahri, E.; Chaudoüet, P.; Madar, R. *J. Less-Common Met.* **1985**, *108*, 353. (b) Pivan, J. Y.; Guérin, R.; Sergent, M. *J. Less-Common Met.* **1985**, *107*, 249.

(24) Bodak, O. I.; Gladyshevskii, E. I.; Kharchenko, O. I. *Sov. Phys. Crystallogr. (Engl. Transl.)* **1974**, *19*, 45.

(25) Prots, Yu. M.; Jeitschko, W. *Z. Kristallogr. Suppl.* **1997**, *12*, 137.

(26) Pivan, J.-Y.; Guérin, R.; Sergent, M. *Mater. Res. Bull.* **1985**, *20*, 887.

(27) Pivan, J.-Y.; Guérin, R.; Pena, O; Padiou, J.; Sergent, M. *Mater. Res. Bull.* **1988**, *23*, 513.

(28) Hughbanks, T.; Hoffmann, R. *J. Am. Chem. Soc.* **1983**, *105*, 3528.

(29) Furuseth, S.; Kjekshus, A. *Acta Crystallogr.* **1965**, *18*, 320.

(30) Carlsson, B.; Rundqvist, S. *Acta Chem. Scand.* **1971**, *25*, 1972.

(31) Donohue, J. *The Structures of the Elements*; Wiley: New York, 1979.

(32) Pauling, L. *The Nature of the Chemical Bond*, 3rd ed.; Cornell University Press: Ithaca, NY, 1960.

(33) Brese, N. E.; von Schnering, H. G. *Z. Anorg. Allg. Chem.* **1994**, *620*, 393.

(34) Bälz, U.; Schubert, K. *J. Less-Common Met.* **1969**, *19*, 300.

Chapter 4

$M_3Ni_3Sb_4$ (M = Zr, Hf) and $Zr_3Pt_3Sb_4$. Ternary Antimonides with the $Y_3Au_3Sb_4$ Structure †

Introduction

Although $Y_3Au_3Sb_4$ was identified more than two decades ago,[1] its claim to fame lies in serving as the structure type adopted by many ternary pnictides $M_3M'_3Pn_4$ (Pn = As, Sb, Bi) and a few stannides $M_3M'_3Sn_4$ which have been the object of recent intense scrutiny because of their interesting electronic properties. The known compounds in this family generally consist of M = f-element and M' = late transition metal (Groups 9–11): $U_3M'_3Sb_4$ (M' = Co, Rh, Ir),[2,3] $U_3Ni_{3-x}As_4$,[4] $M_3Ni_3Sb_4$ (M = U, Th),[2,3,5] $M_3Ni_3Sn_4$ (M = U, Th),[5,6,7] $U_3Pd_3Sb_4$,[2,5] $M_3Pt_3Sb_4$ (M = Ce–Nd, U),[2,5,8-10] $M_3Pt_3Bi_4$ (M = La, Ce),[11-13] $U_3Pt_3Sn_4$,[5] $M_3Cu_3Sb_4$ (M = Y, La–Nd, Sm, Gd–Er, U),[5,14-17] $U_3Cu_3Sn_4$,[5] $M_3Au_3Sb_4$ (M = Y, La–Nd, Sm, Gd–Lu),[1,8,9,18] and $U_3Au_3Sn_4$.[5] Some of these have been found to be Kondo insulators,[8-13] superconductors,[7] magnetoresistive materials,[13] and thermoelectric materials,[10,16] the properties originating from the f-electrons of the M component. Since doping is a common strategy for modifying electronic properties, the occurrence of isostructural compounds expands the range in which this is possible. We report here the

† A version of this chapter has been published. Wang, M.; McDonald, R.; Mar, A. *Inorg. Chem.* **1999**, *38*, 3435. Copyright 1999 American Chemical Society.

preparation of $Zr_3Ni_3Sb_4$, $Hf_3Ni_3Sb_4$, and $Zr_3Pt_3Sb_4$, which represent the first members of this structural family that do *not* contain an *f*-element or Y for the *M* component.

Experimental Section

Synthesis. Reactions were carried out on a ~0.25-g scale by arc-melting mixtures of the elemental powders (Zr, 99.7%; Hf, 99.8%; Ni, 99.9%; Pt, 99.9%; all from Cerac) pressed into pellets. Each pellet was melted twice in a Centorr 5TA tri-arc furnace under argon (gettered by melting a titanium pellet) at slightly greater than atmospheric pressure. Single crystals of $Zr_3Ni_3Sb_4$ were originally found after arc-melting a mixture of Zr, Ni, and Sb in a 1:2:4.5 ratio and annealing in a Ta tube at 1000 °C for 5 days. EDX (energy dispersive X-ray) analysis of these black block-shaped crystals on a Hitachi S-2700 scanning electron microscope confirmed the presence of all three elements in roughly the expected proportions (23(2)% Zr, 34(2)% Ni, 43(2)% Sb). The X-ray powder patterns, obtained on an Enraf-Nonius FR552 Guinier camera (Cu $K\alpha_1$ radiation; Si standard), revealed the presence of $Zr_3Ni_3Sb_4$ as well as NiSb and Sb. A single crystal from this reaction was used for the structure determination described below.

Subsequently $Zr_3Ni_3Sb_4$, $Hf_3Ni_3Sb_4$, and $Zr_3Pt_3Sb_4$ could be prepared by arc-melting mixtures of the elements in the stoichiometric proportions, with 2% excess Sb added to compensate for the weight loss suffered as a result of slight vaporization of Sb (2–4%). We were unable to prepare $Hf_3Pt_3Sb_4$, nor were we successful in substituting *M* = Nb, Ta or *M'* = Co, Pd under these conditions. The cell parameters refined with the use of the program POLSQ[19] are listed in Table 4-1. The observed and calculated interplanar distances and intensities are listed in Table C-3.

Structure Determination. Intensity data were collected at room temperature with the θ–2θ scan technique in the range $11° \leq 2\theta(\text{Mo } K\alpha) \leq 70°$ on an Enraf-Nonius CAD-4 diffractometer. Crystal data and further details of the data collection are given in Table 4-2. Calculations were carried out with the use of the SHELXTL (Version 5.1) package.[20] Conventional atomic scattering factors and anomalous dispersion corrections were used.[21] Intensity data were processed and face-indexed absorption corrections were applied in XPREP. The unique space group consistent with the cubic symmetry and the systematic absences in the intensity data is $I\bar{4}3d$. All atoms were easily found by direct methods, and the structure was refined by least-squares methods. All sites are fully occupied, as confirmed by refinements on the occupancies, which converge to 99(7)% for Zr, 100(7)% for Ni, and 100(7)% for Sb, with reasonable displacement parameters. The Flack parameter converges to –0.04(8), confirming the correct absolute structure. The final cycle of least-squares refinement on F_o^2 of 9 variables (including anisotropic displacement parameters and an isotropic extinction parameter) and 276 averaged reflections (including those having $F_o^2 < 0$) converged to values of $R_w(F_o^2)$ of 0.065 and $R(F)$ (for $F_o^2 > 2\sigma(F_o^2)$) of 0.027. The final difference electron density map is featureless ($\Delta\rho_{max}$ = 1.28; $\Delta\rho_{min}$ = –1.19 e Å^{-3}). Final values of the positional and equivalent isotropic displacement parameters are given in Table 4-3, anisotropic displacement parameters are listed in Table C-4.

Band Structure. Extended Hückel calculations[22,23] were carried out using the EHMACC suite of programs to determine the band structure of $Zr_3Ni_3Sb_4$. The atomic parameters used were taken from those previously applied to ZrNiSb and are listed in Table 4-4.[24] Properties were extracted from the band structure using 40 *k*-points in the

irreducible portion of the Brillouin zone.

Results and Discussion

Crystal Structures. The known ternary zirconium and hafnium nickel antimonides, MNiSb,[24] MNi$_2$Sb,[25,26] M_5NiSb$_3$ (M = Zr, Hf),[27,28] Zr$_5$Ni$_{0.7}$Sb$_{2.3}$,[29] and Hf$_6$Ni$_{1-x}$Sb$_{2+x}$,[30] are all metal-rich phases, and the compounds M_3Ni$_3$Sb$_4$ (M = Zr, Hf) which extend these ternary systems are no exception. To our knowledge, Zr$_3$Pt$_3$Sb$_4$ is the first ternary zirconium platinum antimonide. While the M_3Ni$_3$Sb$_4$ composition is close to being equiatomic, we did not observe the formation of the known MNiSb (M = Zr, Hf)[24] as a competing phase under the synthetic conditions used. In contrast, attempts to substitute Ni with Co resulted in the formation of MCoSb (M = Zr, Hf) with the LiAlSi-type structure.[24,31]

Zr$_3$Ni$_3$Sb$_4$ adopts the Y$_3$Au$_3$Sb$_4$ structure, a filled variant of the more prevalent Th$_3$P$_4$ structure. These are complicated structures which defy a straightforward description.[32,33] As shown in Figure 4-1, the Zr atom is coordinated to eight Sb atoms at 3.1240(6)–3.1488(6) Å in a dodecahedron (or more accurately, a bisdisphenoid (two interpenetrating tetrahedra) because the two sets of Zr–Sb distances are inequivalent), while the Ni atom is coordinated to four Sb atoms at 2.5278(3) Å in a tetrahedron elongated along its $\bar{4}$ axis. The Zr–Sb and Ni–Sb distances are comparable to those found in ZrNiSb (2.9144(7)–3.3212(7) Å and 2.4858(6)–2.617(1) Å, respectively).[24] The "Zr$_3$Sb$_4$" part of Zr$_3$Ni$_3$Sb$_4$ corresponds to the Th$_3$P$_4$ structure, which consists of an array of metal-centered dodecahedra sharing edges and faces in all directions.[33] Filling all the remaining tetrahedral sites between the dodecahedra with Ni atoms results in the space-

filling array of the $Y_3Au_3Sb_4$ structure adopted by $Zr_3Ni_3Sb_4$. Understandably, this traditional structural description of metal-centered polyhedra is difficult to represent clearly in a figure. An alternative description considers the anionic substructure, which consists of two interpenetrating enantiomeric three-connected nets of the nonmetal component.[34] In the present case, because the Sb–Sb distances are all greater than 3.3 Å and are shown to be non-bonding (see below), such a description does not accurately portray the bonding network within the $Zr_3Ni_3Sb_4$ structure. On the other hand, given the short Zr–Ni distances of 2.7746(2) Å, metal-metal bonding is undoubtedly an integral part of this structure. As shown in Figure 4-2, the Zr and Ni atoms are tetrahedrally surrounded by atoms of the other kind to form a four-connected net extending in all three directions, with the tetrahedra sharing edges. This net can be decomposed into chains, one of which is drawn in isolation in the bottom half of Figure 4-2. These chains run along $\bar{4}$ axes, parallel to each of the cubic axes, and form six-membered rings in a twist-boat conformation. The Sb atoms are then located at the centers of highly distorted octahedra (Figure 4-1) whose vertices are the Zr atoms.

Bonding. The synthesis of $Zr_3Ni_3Sb_4$ raises questions about the contribution of metal-metal bonding in $M_3M'_3Pn_4$ compounds. For M = lanthanide or Y, and more so for M = actinide, the M–M' distance can be quite short, certainly within the realm of metal-metal bonding (*e.g.*, d(Nd–Cu) = 2.96 Å in $Nd_3Cu_3Sb_4$,[14] d(Y–Au) = 3.006(1) Å in $Y_3Au_3Sb_4$,[1] and d(U–Ni) = 2.874(1)Å in $U_3Ni_3Sb_4$ [2]). In contrast to the cases above in which the degree of metal-metal bonding or the contribution of f-orbitals *vs.* d-orbitals to bonding can be debated, the Zr–Ni bonding in $Zr_3Ni_3Sb_4$ inarguably has a strong covalent character and necessarily results from overlap of d-orbitals. Given that Zr–Ni distances

of 2.9131(7)–3.138(1) Å in ZrNiSb and 2.6951(8)–2.807(2) Å in $Zr_9Ni_2P_4$ correspond to not insignificant Mulliken overlap populations of 0.05–0.10 and 0.06–0.21, respectively,[24,35] the short distance of 2.7746(2) Å in $Zr_3Ni_3Sb_4$ implies a substantial bonding interaction. It is noteworthy that: (i) except for $U_3Pd_3Sb_4$,[2,5] no other $M_3M'_3Sb_4$ phases have been found with M' = Pd, and (ii) the compound "$Hf_3Pt_3Sb_4$" could not be prepared. This suggests that there may be some optimum degree of metal-metal bonding for the $Y_3Au_3Sb_4$ structure to exist. To test this proposal, we have carried out a band structure calculation on $Zr_3Ni_3Sb_4$.

The total density of states (DOS) curve (Figure 4-3) shows that $Zr_3Ni_3Sb_4$ is predicted to be a semiconductor with a small band gap of 0.57 eV. Although infrared (4000–400 cm^{-1}) diffuse reflectance measurements on a powder sample of $Zr_3Ni_3Sb_4$ did not reveal any absorption that would suggest a band gap, it should be noted that the extended Hückel method is rarely accurate enough to yield correct band gap energies. The presence of impurities can well introduce donor or acceptor levels that mask the intrinsic band gap energy, which would be difficult to measure by optical methods. At best, we can conclude that $Zr_3Ni_3Sb_4$ is a narrow-gap semiconductor or a semimetal. Lack of suitably large single crystals has precluded electrical measurements thus far.

The electron count in $Zr_3Ni_3Sb_4$ (3 x 4 + 3 x 0 + 4 x 5) preserves the value of 32 e^- per formula unit found in many $M_3M'_3Pn_4$ compounds.[14] By analogy with $Th_3Ni_3Sb_4$,[5] an approximation to an oxidation state formalism for $Zr_3Ni_3Sb_4$ would be "$(Zr^{+4})_3(Ni^0)_3(Sb^{-3})_4$." While Sb^{-3} appears to be consistent with the presence of isolated Sb atoms within the structure, clearly Zr^{+4} represents an unrealistic extreme, and a reduced actual charge would be expected for Zr–Ni bonding to occur. Figure 4-3(a)

shows that Zr 4d states contribute largely to the unoccupied conduction band (above –8.5 eV), but there are important contributions to the filled states at lower energy as well. Most of the Ni 3d states contribute to the large narrow peak in the DOS (between –10.5 and –9 eV) (Figure 4-3(b)), which constitutes the valence band, implying a nearly d^{10} configuration for Ni. The bands between –15.5 and –10.5 eV have contributions from all three atom types, with Sb 5p character being dominant (Figure 4-3(c)), and these correspond to strong metal-nonmetal bonding states in $Zr_3Ni_3Sb_4$. The calculated charges are +0.53 for Zr, –0.07 for Ni, and –0.35 for Sb. Importantly, the reduced charge on Zr sets up a situation for metal-metal bonding to occur with Ni.

Crystal orbital overlap population (COOP) curves (Figure 4-4) were analyzed to quantify the degree of bonding in $Zr_3Ni_3Sb_4$. As expected, there are strong Zr–Sb and Ni–Sb bonds, corresponding to large Mulliken overlap populations (MOP) of 0.266 and 0.245, respectively. To provide a reference for Zr–Ni bond strengths, the band structure of the binary intermetallic ZrNi [36] was also determined.[37] The MOP of 0.156 for the Zr–Ni bond (2.7746(2) Å) in $Zr_3Ni_3Sb_4$ is significant, when compared to an MOP of ~0.20 for the Zr–Ni bonds (2.74 Å) in ZrNi. Although Sb–Sb contacts as long as the 3.3875(6) Å distance found in $Zr_3Ni_3Sb_4$ have been implicated as weakly bonding in other antimonides, such as $Zr_2V_6Sb_9$,[38] the MOP of 0.025 here implies negligible, if any, Sb–Sb bonding. $Zr_3Ni_3Sb_4$ provides a useful comparison to ZrNiSb,[24] being close in composition. The key difference seems to be that the modest Zr–Zr bonding (MOP 0.159) in ZrNiSb disappears on going to $Zr_3Ni_3Sb_4$. While Ni–Sb bond strengths are similar in both compounds, the weaker Zr–Sb bonds and the absence of Zr–Zr bonds (all Zr–Zr interatomic distances are greater than 4 Å) in $Zr_3Ni_3Sb_4$ are compensated by the

presence of stronger Zr–Ni bonds.

In conclusion, we have demonstrated that metal-metal bonding (Zr–Ni) is an important feature in $Zr_3Ni_3Sb_4$, and we propose that it may be equally significant, by extension, to other $M_3M'_3Pn_4$ compounds, particularly those with M = U or Th. Since the unusual electronic properties of many $M_3M'_3Pn_4$ compounds are believed to originate from *f*-orbital participation when M is a lanthanide or actinide (particularly Ce and U, which have a stable +4 oxidation state), it will be interesting to see how these properties change when Zr, which only has d electrons available, is partially substituted for these elements.

Table 4-1. Cell Parameters for $M_3M'_3Sb_4$ (M = Zr, Hf; M' = Ni, Pt)

compound	a (Å)	V (Å^3)
$Zr_3Ni_3Sb_4$	9.066(2)	745.1(4)
$Hf_3Ni_3Sb_4$	9.016(1)	732.8(4)
$Zr_3Pt_3Sb_4$	9.359(1)	819.8(4)

Table 4-2. Crystallographic Data for $Zr_3Ni_3Sb_4$

Formula	$Zr_3Ni_3Sb_4$
Formula mass (amu)	936.79
Space group	$T_d^6 - I\bar{4}3d$ (No. 220)
a (Å)	9.0617(6) Å [a]
V (Å^3)	744.10(9)
Z	4
T (°C)	22
Diffractometer	Enraf-Nonius CAD4
ρ_{calc} (g cm^{-3})	8.362
Crystal dimensions (mm)	0.04 × 0.03 × 0.02
Radiation	Graphite-monochromated Mo $K\alpha$, λ = 0.71073 Å
μ(Mo $K\alpha$) (cm^{-1})	255.88
Transmission factors [b]	0.605–0.951
Scan type	θ–2θ
Scan speed (deg. min^{-1})	1.67
Scan range (deg.)	0.60 + 0.344 tanθ
2θ limits	$11° \leq 2\theta$(Mo $K\alpha$) $\leq 70°$
Data collected	$-14 \leq h \leq 14$, $-14 \leq k \leq 14$, $-14 \leq l \leq 14$
No. of data collected	5878
No. of unique data, including $F_o^2 < 0$	276 (R_{int} = 0.246)
No. of unique data, with $F_o^2 > 2\sigma(F_o^2)$	251
No. of variables [c]	9

Table 4-2. Crystallographic Data for $Zr_3Ni_3Sb_4$ (continued)

$R(F)$ for $F_o^2 > 2\sigma(F_o^2)$ [d]	0.027
$R_w(F_o^2)$ [e]	0.065
Goodness of fit [f]	1.091
$\Delta\rho_{max}$, $\Delta\rho_{min}$ (e Å^{-3})	1.28, −1.19

[a] Obtained from a refinement constrained so that $a = b = c$ and $\alpha = \beta = \gamma = 90°$.

[b] A numerical face-indexed absorption correction was applied, with the use of programs in the SHELXTL package (Sheldrick, G. M. *SHELXTL Version 5.1*; Bruker Analytical X-ray Systems: Madison, WI, 1997).

[c] Including an extinction coefficient.

[d] $R(F) = \sum \| F_o | - | F_c \| / \sum | F_o |$.

[e] $R_w(F_o^2) = \left[\sum \left[w(F_o^2 - F_c^2)^2\right] / \sum w F_o^4\right]^{1/2}$; $w^{-1} = \left[\sigma^2(F_o^2) + (0.0000P)^2 + 6.7215P\right]$ where $P = \left[\max(F_o^2, 0) + 2F_c^2\right]/3$.

[f] $GooF = \left[\sum \left[w(F_o^2 - F_c^2)^2\right] / (n - p)\right]^{1/2}$ where n is the number of reflections and p is the total number of parameters refined.

Table 4-3. Positional and Equivalent Isotropic Thermal Parameters (Å^2) for $Zr_3Ni_3Sb_4$

atom	Wyckoff position	x	y	z	U_{eq} [a]
Zr	12*a*	3/8	0	1/4	0.0082(3)
Ni	12*b*	7/8	0	1/4	0.0075(4)
Sb	16*c*	0.08207(6)	0.08207(6)	0.08207(6)	0.0067(2)

[a] U_{eq} is defined as one-third of the trace of the orthogonalized $\mathbf{U}_{ij}$ tensor.

Table 4-4. Extended Hückel Parameters

atom	orbital	H_{ii} (eV)	ζ_{i1}	c_1	ζ_{i2}	c_2
Zr	5s	–8.52	1.82			
	5p	–4.92	1.78			
	4d	–8.63	3.84	0.6213	1.510	0.5798
Ni	4s	–8.03	1.93			
	4p	–3.74	1.93			
	3d	–9.90	5.75	0.5817	2.20	0.5800
Sb	5s	–18.80	2.32			
	5p	–11.70	2.00			

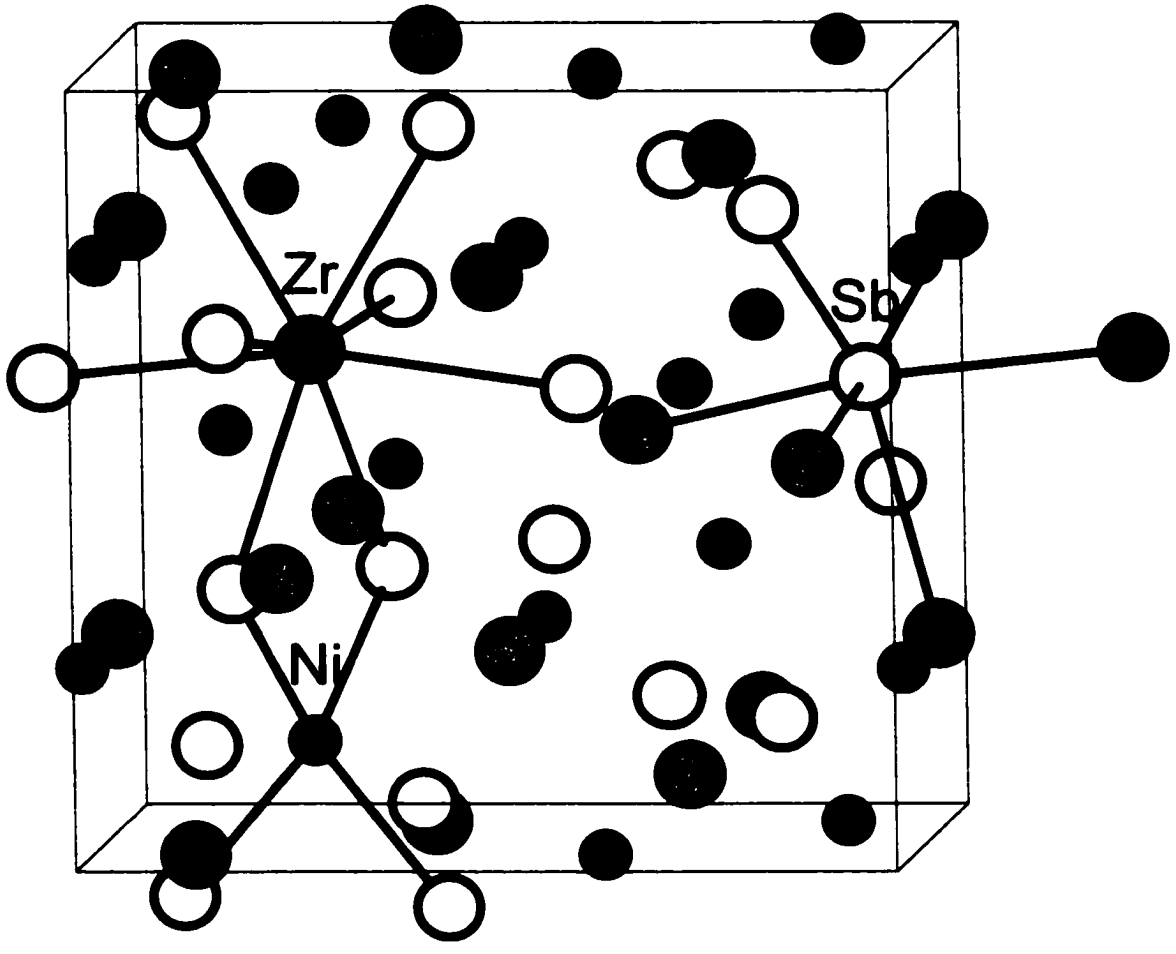

Figure 4-1. View of $Zr_3Ni_3Sb_4$ with the cubic unit cell outlined. The lightly shaded circles are Zr atoms, the small dark spheres are Ni atoms, and the open circles are Sb atoms. A Zr-centered dodecahedron, a Ni-centered tetrahedron, and an Sb-centered octahedron are highlighted.

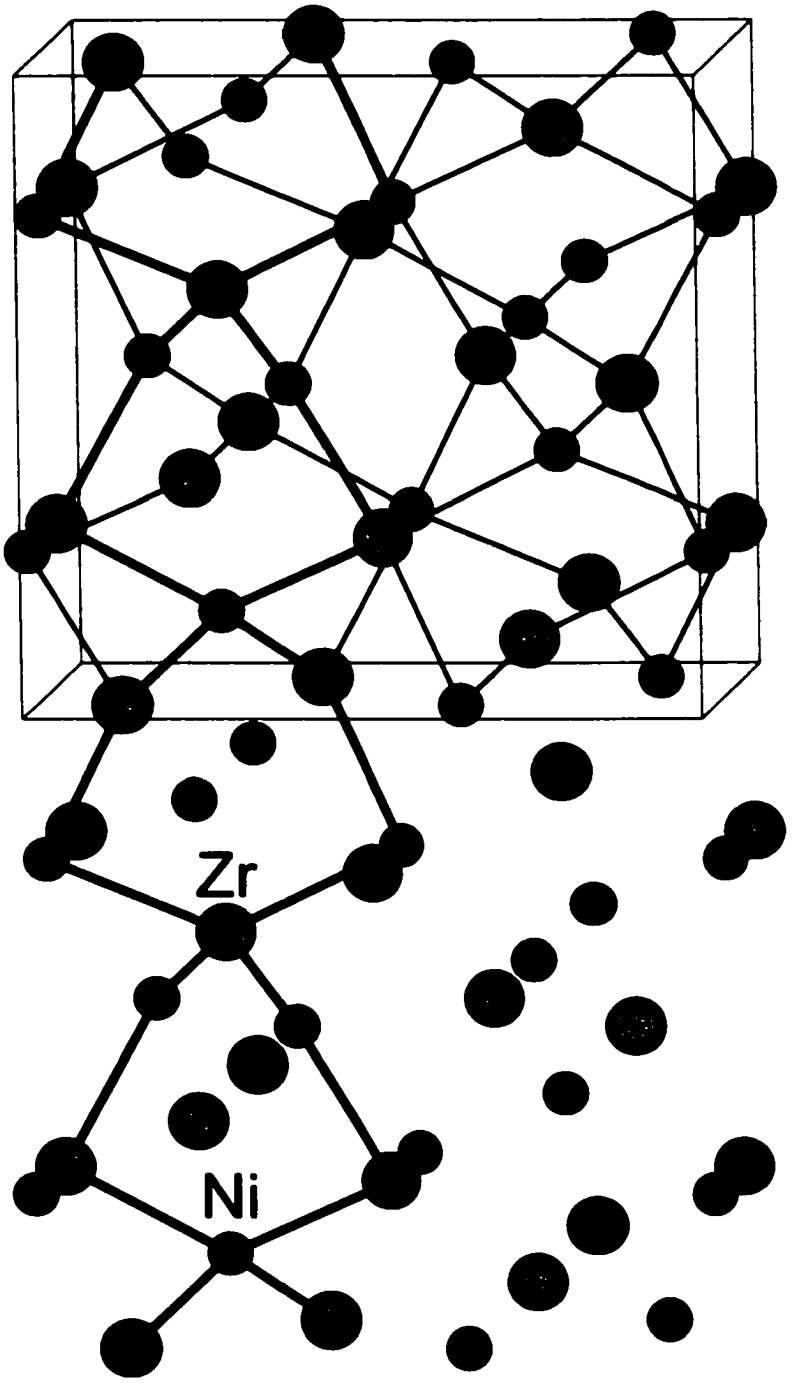

Figure 4-2. View of the Zr–Ni bonding network in $Zr_3Ni_3Sb_4$, with all Sb atoms omitted for clarity. The medium lightly shaded circles are Zr atoms and the small dark circles are Ni atoms. One of the chains of six-membered rings running parallel to a $\bar{4}$ axis is outlined with thicker bonds, extending into the next unit cell.

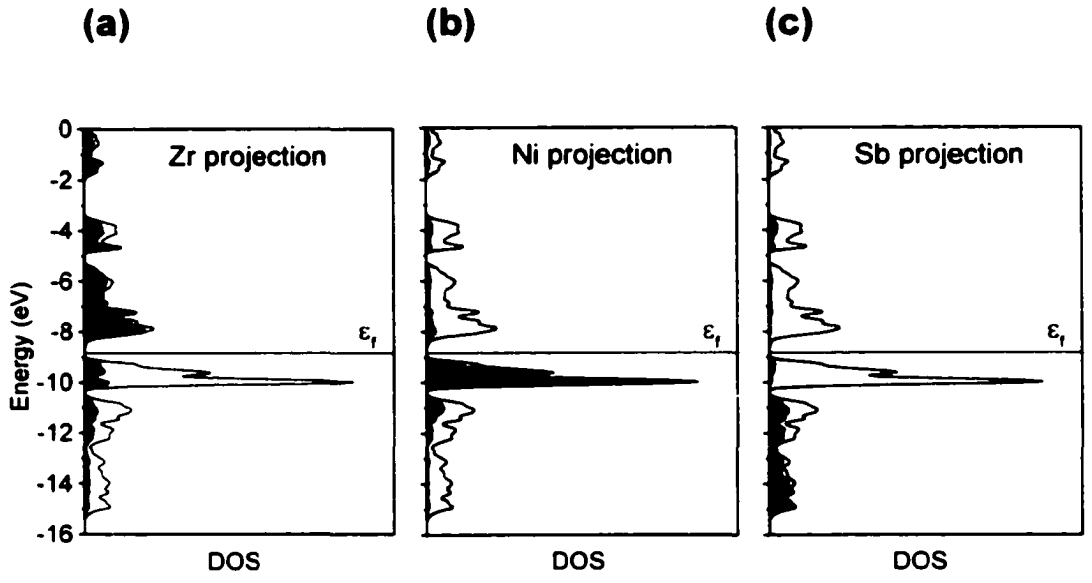

Figure 4-3. Contributions of (a) Zr, (b) Ni, and (c) Sb (shaded regions) to the total density of states (DOS) (line) for $Zr_3Ni_3Sb_4$.

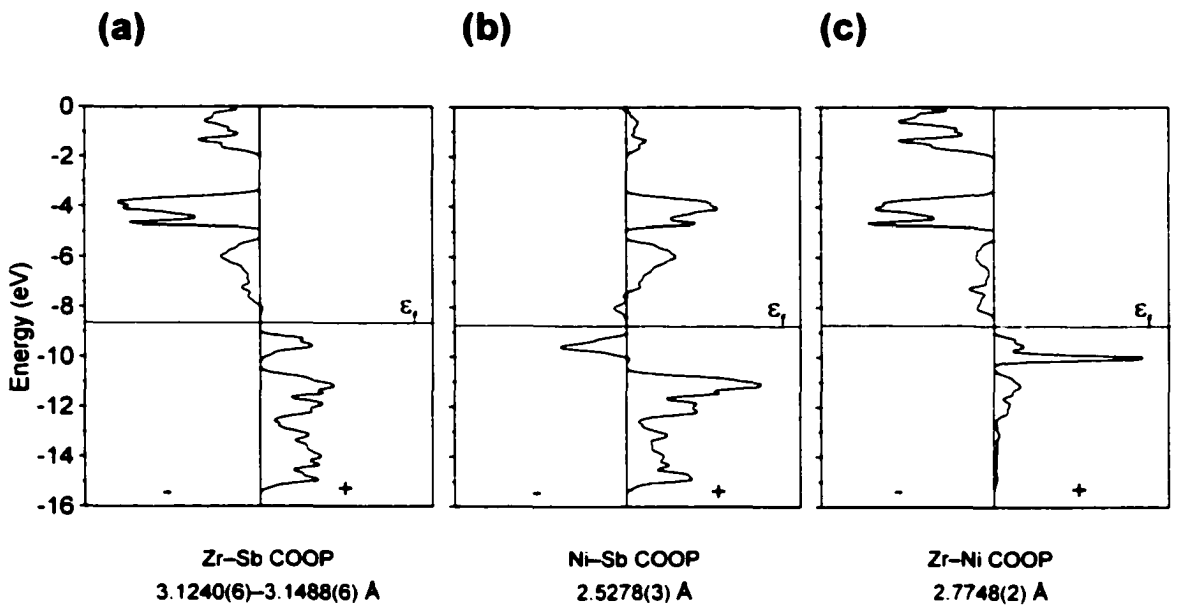

Figure 4-4. Crystal orbital overlap population (COOP) curves for (a) Zr–Sb, (b) Ni–Sb, and (c) Zr–Ni contacts in $Zr_3Ni_3Sb_4$.

References

(1) Dwight, A. E. *Acta Crystallogr. Sect. B: Struct. Crystallogr. Cryst. Chem.* **1977**, *33*, 1579.

(2) Dwight, A. E. *J. Nucl. Mater.* **1979**, *79*, 417.

(3) Buschow, K. H. J.; de Mooij, D. B.; Palstra, T. T. M.; Nieuwenhuys, G. J.; Mydosh, J. A. *Philips J. Res.* **1985**, *40*, 313.

(4) Troc, R.; Kaczorowski, D.; Noël, H.; Guerin, R. *J. Less-Common Met.* **1990**, *157*, L1.

(5) Takabatake, T.; Miyata, S.-I.; Fujii, H.; Aoki, Y.; Suzuki, T.; Fujita, T.; Sakurai, J.; Hiraoka, T. *J. Phys. Soc. Jpn.* **1990**, *59*, 4412.

(6) Yethiraj, M.; Robinson, R. A.; Rhyne, J. J.; Gotaas, J. A.; Buschow, K. H. J. *J. Magn. Magn. Mater.* **1989**, *79*, 355.

(7) Aoki, Y.; Suzuki, T.; Fujita, T.; Takabatake, T.; Miyata, S.-I.; Fujii, H. *J. Phys. Soc. Jpn.* **1992**, *61*, 684.

(8) Kasaya, M.; Katoh, K.; Takegahara, K. *Solid State Commun.* **1991**, *78*, 797.

(9) Kasaya, M.; Katoh, K.; Kohgi, M.; Osakabe, T.; Sato, N. *Physica B* **1994**, *199-200*, 534.

(10) Jones, C. D. W.; Regan, K. A.; DiSalvo, F. J. *Phys. Rev. B: Condens. Matter* **1998**, *58*, 16057.

(11) Hundley, M. F.; Canfield, P. C.; Thompson, J. D.; Fisk, Z.; Lawrence, J. M. *Phys. Rev. B: Condens. Matter* **1990**, *42*, 6842.

(12) Severing, A.; Thompson, J. D.; Canfield, P. C.; Fisk, Z.; Riseborough, P. *Phys. Rev. B: Condens. Matter* **1991**, *44*, 6832.

(13) Hundley, M. F.; Lacerda, A.; Canfield, P. C.; Thompson, J. D.; Fisk, Z. *Physica B* **1993**, *186-188*, 425.

(14) Skolozdra, R. V.; Salamakha, P. S.; Ganzyuk, A. L.; Bodak, O. I. *Izv. Akad. Nauk SSSR, Neorg. Mater.* **1993**, *29*, 25.

(15) Patil, S.; Hossain, Z.; Paulose, P. L.; Nagarajan, R.; Gupta, L. C.; Godart, C. *Solid State Commun.* **1996**, *99*, 419.

(16) Fess, K.; Kaefer, W.; Thurner, Ch.; Friemelt, K.; Kloc, Ch.; Bucher, E. *J. Appl. Phys.* **1998**, *83*, 2568.

(17) Fujii, H.; Miyata, S.; Takabatake, T. *J. Magn. Magn. Mater.* **1992**, *104-107*, 45.

(18) Katoh, K.; Kasaya, M. *Physica B* **1993**, *186-188*, 428.

(19) POLSQ: Program for least-squares unit cell refinement. Modified by D. Cahen and D. Keszler, Northwestern University, 1983.

(20) Sheldrick, G. M. SHELXTL version 5.1; Bruker Analytical X-ray Instruments, Inc.: Madison, WI, 1997.

(21) *International Tables for X-ray Crystallography*; Wilson, A. J. C., Ed.; Kluwer: Dordrecht, The Netherlands, 1992; Vol. C.

(22) Hoffmann, R. *J. Chem. Phys.* **1963**, *39*, 1397.

(23) Whangbo, M.-H.; Hoffmann, R. *J. Am. Chem. Soc.* **1978**, *100*, 6093.

(24) Kleinke, H. *Z. Anorg. Allg. Chem.* **1998**, *624*, 1272.

(25) Soltys, J.; Turek, K. *Acta Phys. Pol. A* **1975**, *47*, 335.

(26) Dwight, A. E. *Mater. Res. Bull.* **1987**, *22*, 201.

(27) Rieger, W.; Parthé, E. *Acta Crystallogr. Sect. B: Struct. Crystallogr. Cryst. Chem.* **1968**, *24*, 456.

(28) Garcia, E.; Corbett, J. D. *Inorg. Chem.* **1990**, *29*, 3274.

(29) Kwon, Y.-U.; Sevov, S. C.; Corbett, J. D. *Chem. Mater.* **1990**, *2*, 550.

(30) Kleinke, H. *J. Alloys Compd.* **1998**, *270*, 136.

(31) Marazza, R.; Ferro, R.; Rambaldi, G. *J. Less-Common Met.* **1975**, *39*, 341.

(32) Pearson, W. B. *The Crystal Chemistry and Physics of Metals and Alloys*; Wiley: New York, 1972.

(33) Hyde, B. G.; Andersson, S. *Inorganic Crystal Structures*; Wiley: New York, 1989.

(34) Heim, H.; Bärnighausen, H. *Acta Crystallogr. Sect. B: Struct. Crystallogr. Cryst. Chem.* **1978**, *34*, 2084.

(35) Kleinke, H.; Franzen, H. F. *Inorg. Chem.* **1996**, *35*, 5272.

(36) Kirkpatrick, M. E.; Bailey, D. M.; Smith, J. F. *Acta Crystallogr.* **1962**, *15*, 252.

(37) Wang, M.; Mar, A. Unpublished results.

(38) Kleinke, H. *Eur. J. Inorg. Chem.* **1998**, 1369.

Chapter 5

$Nb_{28}Ni_{33.5}Sb_{12.5}$, a New Representative of the *X*-phase †

Introduction

Ternary antimonides *RE*–*M'*–Sb containing a rare earth (or Group 3 transition metal) and a late transition metal have attracted attention because of their potential for displaying interesting magnetic properties,[1] and more recently, because of their promising thermoelectric properties, especially in $REFe_{4-x}Co_xSb_{12}$ (RE = La, Ce; $0 < x < 4$) compounds.[2] In contrast, ternary antimonides *M*–*M'*–Sb containing an early (Groups 4–6) and a late transition metal have not been as extensively investigated. In the (Zr, Hf)–(Ni, Pd, Pt)–Sb systems, several compounds have been characterized: *M*NiSb (*M* = Zr, Hf; Co_2Si-type),[3] MNi_2Sb (*M* = Zr, Hf; YPt_2In-type),[4] M_5NiSb_3 (*M* = Zr, Hf; Ti_5Ga_4-type),[5,6] $Zr_5Ni_{0.5}Sb_{2.5}$ (Mn_5Si_3-type),[7] $Hf_{10}Ni_xSb_{6-x}$ (W_5Si_3-type),[8] $Hf_6Ni_{1-x}Sb_{2+x}$ (Fe_2P-type),[9] $M_3Ni_3Sb_4$ (*M* = Zr, Hf),[10] and $Zr_3Pt_3Sb_4$ ($Y_3Au_3Sb_4$-type).[10] In the (Nb, Ta)–(Ni, Pd, Pt)–Sb systems, no ternary compounds have been reported thus far, to our knowledge.

The divergence in the crystal chemistry of Group 4 *vs.* 5 antimonides is also reflected in the binary compounds. For example, the structures of binary Zr *vs.* Nb antimonides are quite different. ZrSb occurs as two phases with FeSi- and ZrSb-type

† A version of this chapter has been accepted for publication. Wang, M.; Mar, A. *J. Solid State Chem.*

structures,[11,12] whereas NbSb crystallizes only in the NiAs-type structure.[13] Two orthorhombic phases of $ZrSb_2$ with Co_2Si- and $ZrSb_2$-type structures are known,[12,14] whereas $NbSb_2$ has a monoclinic structure.[15,16] There are no analogues of Zr_2Sb (La_2Sb-type)[11] and Zr_5Sb_3 (Mn_5Si_3- (LT) and Y_5Bi_3-type (HT))[17] among the Nb antimonides, while Nb_5Sb_4 (Ti_5Te_4-type)[18] finds no counterpart among the Zr antimonides. However, the structure of Zr_3Sb (Ni_3P-type)[19] can be derived from that of Nb_3Sb (Cr_3Si-type),[18,20] which represents a simple example of a *tetrahedrally close-packed structure*.[21-24]

Tetrahedrally close-packed structures (sometimes called topologically close-packed (TCP) or Frank-Kasper structures) are adopted by a large number of intermetallic compounds of the transition metals, and include well-known examples such as the Laves ($MgCu_2$, $MgNi_2$, $MgZn_2$), A15 (Cr_3Si), and σ (FeCr) phases.[21-24] Unlike close-packed structures in which atoms of equal size pack to generate small tetrahedral and large octahedral interstices, TCP structures are realized when two or more types of atoms of slightly different size achieve the best filling of space by packing to form only small, slightly irregular tetrahedral interstices. Moreover, the coordination geometries are limited to four types, with CN 12, 14, 15, and 16. While size considerations are important, the valence electron concentration (VEC) is another factor that controls the structure. For instance, inclusion of main-group elements, especially Si and Al, stabilizes some phases (NbNiAl and Nb_2Ni_3Si are hexagonal Laves phases whereas $NbNi_2$ itself does not exist) and destabilizes others (addition of Al to the Cr–Co system inhibits σ-phase formation).[23]

The *X*-phase is an interesting case of a TCP structure which, up to now, had only a unique representative, a Si-stabilized intermetallic compound $Mn_{45-x}Co_{40+x}Si_{15}$ whose

structure was determined in the early 1970's.[25,26] We describe here the preparation, crystal and electronic structures, and electrical resistivity of $Nb_{28}Ni_{33.5}Sb_{12.5}$, a new Sb-stabilized intermetallic compound. To our knowledge, it is only the second compound to crystallize in the *X*-phase structure, and is the first ternary compound found in the Nb–Ni–Sb system.

Experimental Section

Synthesis. Starting materials were powders of the elements Nb (99.8%, Cerac), Ni (99.9%, Cerac), and Sb (99.995%, Aldrich), and of the binary compound $NbSb_2$ (prepared by direct reaction of Nb and Sb in a 1:2 molar ratio in an evacuated fused-silica tube for 3 days at 800 °C). Reaction of Nb, Ni, and $NbSb_2$ in a 1:6:2 molar ratio was carried out in a Centorr 5TA tri-arc furnace under argon (gettered by melting a titanium pellet), followed by heating in a fused-silica tube in a two-zone furnace with a temperature gradient of 900/950 °C (charge in cool zone) for 3 days in the presence of trace amounts of iodine. Some small needle-shaped crystals were found in the product, which contained (mol%) 35% Nb, 45% Ni, and 19% Sb, as determined from EDX (energy-dispersive X-ray) analyses on a Hitachi S-2700 scanning electron microscope. The reaction is reproducible. One of these crystals was selected for the structure determination.

After a preliminary structure determination (*vide infra*) was made, reactions of varying stoichiometries were attempted to resolve some compositional ambiguities. Mixtures of Nb, Ni, and either $NbSb_2$ or Sb were arc-melted, and the products were characterized by X-ray powder diffraction on an Enraf-Nonius FR552 Guinier camera

(Table 5-1). Although there is evidence for some degree of nonstoichiometry, which is common for many intermetallic compounds, Table 5-1 shows that there is consistently a slight excess of Ni over Nb. In conjunction with the single-crystal structure determination, these results suggest that the average composition is close to $Nb_{28}Ni_{32}Sb_{14}$.

Structure Determination. The singularity of a selected needle-shaped crystal, its Laue symmetry *mmm*, and preliminary cell parameters were revealed by Weissenberg photography. X-ray diffraction data were collected on a Bruker P4/RA/SMART CCD diffractometer at room temperature with a combination of ϕ rotations (0.3°) and ω scans (0.3°) in the range $4° \leq 2\theta(\text{Mo } K\alpha) \leq 65°$. Final cell parameters were refined from least-squares analysis of 5952 reflections. Crystal data and further details of the data collection are given in Table 5-2. All calculations were carried out using the SHELXTL (Version 5.1) package.[27] Conventional atomic scattering factors and anomalous dispersion corrections were used.[28] Intensity data were processed, and face-indexed absorption corrections were applied in XPREP.

Among the possible space groups (*Pnn*2, *Pnnm*) consistent with the orthorhombic symmetry and systematic absences observed, the centrosymmetric space group *Pnnm* was chosen which led to successful structure solution and refinement. An initial model (Model A, "$Nb_{36}Ni_{28}Sb_{10}$") was proposed for the assignment of the 16 independent sites (Table 5-3), all of whose positions were readily located by direct methods. At this stage, we noted its isotypy to the *X*-phase ($Mn_{45-x}Co_{40+x}Si_{15}$),[25,26] in which all four kinds of coordination polyhedra (CN12 (icosahedron), CN14, CN15, CN16) possible in a TCP structure are found. Since main-group atoms normally occupy the CN12 sites in TCP

structures, the assignment of Sb at these locations is reasonable. A broad principle governing the formation of TCP structures is that transition metals to the right of Group 7 prefer the CN12 sites, those to the left of Group 7 prefer the sites of higher CN, and those in Group 7 (Mn, Tc, Re) have no clear preference.[29] Model A conforms well to this principle, except that a CN12 site (site 8) is occupied by Nb and the resulting Nb–Ni distances are generally somewhat shorter than expected. Although refinement on Model A proceeded satisfactorily, resulting in reasonable displacement parameters for all atoms including Nb in site 8, attempts in synthesis at the composition "$Nb_{36}Ni_{28}Sb_{10}$" failed, giving only binary products (Table 5-1). In Model B, site 8 is instead occupied by Ni, in compliance with the CN12 site preference for later transition metals, giving the formula "$Nb_{28}Ni_{36}Sb_{10}$." Although a synthesis based on this composition afforded the ternary Nb–Ni–Sb compound in large amounts, refinement of this model was unsatisfactory, yielding unusually small displacement parameters for site 8. Despite their different sizes, there is precedence for disorder of Ni and Sb, as occurs in the crystal structure of Hf_6NiSb_2, for instance.[9] In Model C, such a disorder was now allowed and occupancies of 50% Ni and 50% Sb were arbitrarily assigned in site 8. The refinement proceeded well and, more convincingly, a synthesis based on the composition "$Nb_{28}Ni_{32}Sb_{14}$" gave the best yield of the ternary phase thus far.

Possible further disorder was next probed in all remaining sites. Up to this stage (Model C), the CN12 (icosahedral) sites are occupied by Ni atoms (sites 1–5), Sb atoms (sites 6, 7, 9), or a mixture of both (site 8), while the CN14, CN15, and CN16 sites (sites 10–16) are occupied by Nb atoms. Since sites 1–5 (Ni) make contacts of ~2.5 Å with sites 6, 7, or 9 (Sb), which are too short for Nb–Sb or Sb–Sb bonds, the possibility of

disorder in sites 1–5 could be ruled out. For sites 6, 7, or 9, we considered models involving either Ni/Sb or Nb/Sb disorder; all refinements resulted in essentially 100% Sb occupancy in sites 6 and 7 but in a 21% Ni, 79% Sb occupancy ratio in site 9. The disorder of Ni and Sb in site 8 has already been discussed above. Finally, refinements allowing disorder of Nb with either Sb or Ni in sites 10–16 resulted in 100% occupancy by Nb. Other refinements did not support models allowing Nb or Sb deficiencies or Nb/Ni disorder. We accept as our final model one in which only sites 8 and 9 feature disorder of Ni and Sb atoms, giving the formula $Nb_{28}Ni_{33.5}Sb_{12.5}$ (Model D), which is very close to "$Nb_{28}Ni_{32}Sb_{14}$" (Model C). The final difference electron density map is featureless ($\Delta\rho_{max}$ = 3.08; $\Delta\rho_{min}$ = –3.40 e Å^{-3}). The atomic positions were standardized with the use of the program STRUCTURE TIDY.[30] Final values of the positional and equivalent isotropic displacement parameters are given in Table 5-4. Anisotropic displacement parameters are listed in Table C-5.

Electrical Resistivity. An ingot of dimensions 1.25 × 0.25 × 0.09 mm, taken from the product of reaction 3 (Table 5-1), was mounted in a four-probe configuration for an ac resistivity measurement between 5 and 300 K on a Quantum Design PPMS system equipped with an AC-transport controller (Model 7100). A current of 0.01 mA and a frequency of 16 Hz were used.

Band Structure. A tight-binding band structure calculation in the extended Hückel approximation was performed on the idealized structure "$Nb_{28}Ni_{32}Sb_{14}$" (Model C) with use of the EHMACC suite of programs.[31,32] The atomic parameters used[3,33] are listed in Table 5-5. Properties were extracted from the band structure using 45 *k*-points in the irreducible portion of the Brillouin zone.

Results and Discussion

Composition. Although the nominal composition "$Nb_{28}Ni_{33.5}Sb_{12.5}$" found from the structure determination is consistent with the EDX analyses and is close to the starting composition of the synthesis, there is evidence for a narrow range of homogeneity. The variability in composition originates from disorder of Ni and Sb in only two sites in the crystal structure. On the basis of synthetic experiments (Table 5-1), the composition of this ternary phase is estimated to be $Nb_{28}Ni_{34\pm2}Sb_{12\pm2}$. Lattice constants range from a = 13.210(8), b = 16.469(9), c = 5.013(3) Å, V = 1090.5(8) Å^3 for the ternary phase synthesized in reaction 3 (loading composition $Nb_{28}Ni_{36}Sb_{10}$) to a = 13.256(6), b = 16.537(7), c = 5.040(2) Å, V = 1104.9(6) Å^3 for that synthesized in reaction 4 (loading composition $Nb_{28}Ni_{32}Sb_{14}$) (Table C-6). The lattice constants for the single crystal of $Nb_{28}Ni_{33.5}Sb_{12.5}$ analyzed (Table 5-2) are intermediate between these values. The variation in cell volume in $Nb_{28}Ni_{34\pm2}Sb_{12\pm2}$ is ~1.3%, comparable to the ~1.5% variation in $Hf_6Ni_{1-x}Sb_{2+x}$ ($0 < x < 0.24$).[9] In contrast to the isotypic $Mn_{45-x}Co_{40+x}Si_{15}$, where two or all three components were proposed to be disordered over 9 of the 16 sites, the greater differentiation in atomic sizes in $Nb_{28}Ni_{34\pm2}Sb_{12\pm2}$ may account for the reduction in disorder.

Crystal Structure. Although a large number of alloys and intermetallic compounds crystallize in TCP structures, which include the ubiquitous Laves phases, to date only about 20 TCP structure *types* are known,[34] despite the prediction of the existence of many more.[21,22] $Nb_{28}Ni_{33.5}Sb_{12.5}$ is only the second representative of the *X*-phase, which is the structure type adopted by $Mn_{45}Co_{40}Si_{15}$ discovered in 1962[35] and characterized independently by two groups in 1970 and 1972.[25,26]

Like most TCP structures, the structure of $Nb_{28}Ni_{33.5}Sb_{12.5}$ can be described in terms of the stacking of two-dimensional nets. Figure 5-1 shows the stacking of these layers projected along the short *c* axis. (For simplicity, the more Ni-rich disordered site *X*(1) is portrayed like a Ni atom (small solid circles), and the more Sb-rich disordered site *X*(2) like an Sb atom (small lightly shaded circles).) The primary or main layers **A** (or **A'**), which lie on the $z = 0$ or $z = ½$ planes, alternate with the secondary layers **B**, which lie on the $z = \sim¼$ or $z = \sim¾$ planes, as shown in Figure 5-2a. Layers **A** and **A'** are related by a two-fold screw axis along *c*. (The standardization of atomic coordinates in the crystal structure of $Nb_{28}Ni_{33.5}Sb_{12.5}$ shifts the origin of the unit cell by $½\vec{c}$ relative to that of $Mn_{45}Co_{40}Si_{15}$ so that the layers **A** and **A'** are interchanged.) Each main layer **A** is constructed from a tessellation of pentagons and triangles whose vertices are Nb, Ni, and Sb atoms and described by the Schäfli symbols $5^3.3 + 5^2.3^2 + 5.3.5.3^2 + 5.3.5.3$, as shown in Figure 5-2b. Each secondary layer **B** is constructed from a tessellation of squares and triangles whose vertices are Ni atoms only and described by the Schäfli symbols $4.3^5 + 4.3^4 + 3^6$, as shown in Figure 5-2c. It should be understood that the stacking of layers is merely a way of describing and classifying structures, and is not meant to make implications about bonding. While the lines shown in the main layer **A** range from 2.5 to 3.3 Å and do imply bonding contacts, those in the secondary layer **B** are all greater than 4.2 Å and therefore cannot represent bonds; on the other hand, there do exist strong bonding interactions between atoms in the **A** and **B** layers even though they are not drawn.

The coordination polyhedra found in $Nb_{28}Ni_{33.5}Sb_{12.5}$ are shown in Figure 5-3, and correspond to the four possible Frank-Kasper polyhedra of CN12, 14, 15, and 16.[29] All

CN12 sites, approximately icosahedral (I_h), are occupied by the Ni and Sb atoms. Three of these, Ni(1), Ni(2), and the Ni-rich disordered site *X*(1), have two opposing vertices that are symmetry equivalents of the central atom. These are also the three sites that make up the secondary **B** layer. If these opposing vertices are considered to be capping atoms of a pentagonal antiprism, then the structure of $Nb_{28}Ni_{33.5}Sb_{12.5}$ can also be regarded as consisting of infinite columns, aligned along the *c* axis, of pentagonal antiprisms centred by these atoms, as can be seen by inspection of Figure 5-1. The CN14 site, occupied by Nb(1), centres a bicapped hexagonal antiprism (approximately D_{6d}) with the six-fold improper rotation axis oriented vertically, and the CN15 site, occupied by Nb(7), centres a so-called "μ-phase polyhedron" (approximately D_{3h}) with the three-fold rotation axis oriented horizontally in Figure 5-3. All CN16 sites, occupied by the remaining Nb atoms, centre Friauf polyhedra (approximately T_d).

Interatomic distances found in $Nb_{28}Ni_{33.5}Sb_{12.5}$ are listed in Table 5-6, to be read downwards so that the number of distances corresponds to the CN in the header row. These distances are generally about ~0.2 Å greater than those in $Mn_{45}Co_{40}Si_{15}$, reflecting the larger atomic sizes of the components in $Nb_{28}Ni_{33.5}Sb_{12.5}$. Most Ni–Ni distances lie in the range of 2.449(1)–2.674(2) Å, consistent with that found in elemental Ni (2.49 Å)[36] or NiSb (2.56 Å).[37] The two somewhat shorter distances of 2.360(2) (Ni(1)–Ni(1)) and 2.410(2) Å (Ni(2)–Ni(2)), close to the sum (2.31 Å) of the Pauling single bond radii[38] and corresponding to the repeat of pentagonal antiprisms in the columns along the *c* axis described earlier, may be a result of matrix effects arising from satisfying the packing requirements of atoms in the other coordination polyhedra. Most Nb–Nb distances lie in the range of 2.736(1)–3.324(1) Å, similar to that found in elemental Nb (2.86 Å) (36) or

Nb_3Sb (2.63–3.22 Å) (18). There is an unusually short distance of 2.488(2) Å (Nb(1)–Nb(1)) which corresponds to the length of the shared edge of two triangles in the main layer **A** (Figure 5-1 or Figure 5-2b). A Nb–Nb distance of 2.58 Å is found in Nb_3Ge,[39] while (multiply-bonding) distances as short as 2.20 Å are seen in organometallic complexes such as $Nb_2(hpp)_4$.[‡,40] The corresponding Mn–Mn distance in $Mn_{45}Co_{40}Si_{15}$ is also much shorter than the other ones and may be more a result of geometrical constraints imposed by the rest of the structure. There are no Sb–Sb contacts present; the short *X*(1)–*X*(1) distances of 2.512(1)–2.522(1) Å can be interpreted as Ni–Sb contacts given that the *X*(1) site consists of a nearly equal mixture of Ni and Sb. The other Ni–Sb distances of 2.449(1)–2.5915(8) Å are similar to that found in NiSb (2.60 Å) (37). The Nb–Sb distances of 2.8786(9)–2.9922(5) Å are similar to those in $NbSb_2$ (2.84–2.97 Å) and the Nb–Ni distances of 2.616(1)–3.038(1) Å are somewhat longer than those in $NbNi_3$ ($TiAl_3$-type) (2.56–2.59 Å).[41]

Although complex, the *X*–phase structure has been related through a "fourling" operation of units of the simpler $MnZn_2$-type structure, one of the three Laves phases.[20,42] Both consist of main layers tessellated by pentagons and triangles, but whereas the secondary layer in the *X*-phase structure is tessellated by squares and triangles, it is only tessellated by triangles in the $MnZn_2$-type structure. Distortion of the squares in the secondary net of the *X*-phase structure (Figure 5-2c) would be necessary to transform it to the 3^6 net found in the $MnZn_2$-type structure.

Electronic Structure. $Nb_{28}Ni_{33.5}Sb_{12.5}$ displays metallic behaviour with a small resistivity ratio ($\rho_{300} = 2.3 \times 10^{-4}$ Ω cm, $\rho_5 = 1.6 \times 10^{-4}$ Ω cm, $\rho_{300}/\rho_5 = 1.4$) typical of

‡ hpp^-: the anion of 1,3,4,6,7,8-hexahydropyrimido[1,2-*a*]pyrimidine (Hhpp).

disordered alloy structures (Figure 5-4). This observation is consistent with the band structure calculation (based on an idealized "$Nb_{28}Ni_{32}Sb_{14}$" model), which reveals a moderate density of states (DOS) at the Fermi level (ε_f = –9.38 eV), as shown in Figure 5-5. The DOS curve can be decomposed into a rather broad Nb d-block, extending from –6 to –12 eV (Figure 5-5a), in which only half of these states are occupied, and a narrow block located just below the Fermi level extending from –10 to –12 eV (Figure 5-5b), which represents filled states composed almost entirely of Ni 3d character. The substantial mixing of Nb and Ni character from –12 eV up to the Fermi level implies a significant degree of Nb–Ni bonding. Lower down in energy (–12.5 to –14 eV) is a region composed largely of Sb 5p character (Figure 5-5c) corresponding to Nb–Sb and Ni–Sb bonding levels.

The strength of the bonding interactions can be quantified by inspection of their crystal orbital overlap population (COOP) curves[43] (Figure 5-6) and their Mulliken overlap populations (MOP) (Table 5-7). (Note that it is valid to compare overlaps only between identical types of contacts.) The regions centred around the two maxima around –7.5 and –9.5 eV in the Nb d-block in the DOS curve (Figure 5-5a) correspond to Nb–Nb bonding and antibonding levels, respectively, as verified by inspection of the COOP curve (Figure 5-6a). With most of the Nb–Nb bonding levels occupied, all Nb–Nb contacts less than 3.4 Å represent fairly strong interactions, as evidenced by a MOP of 0.267. Although most of the Nb–Nb contacts range from 2.9 to 3.4 Å, with a cumulative MOP of 0.245, there are three that are significantly shorter with substantially larger MOP values: 0.550 for the 2.488(2) Å (Nb(1)–Nb(1)) contact, and 0.417 for the 2.736(1) (Nb(1)–Nb(2)) and 2.753(2) Å (Nb(7)–Nb(7)) contacts. The Nb–Ni (Figure 5-6b) and

Nb–Sb interactions (Figure 5-6c) are optimized in the structure, with all bonding levels just filled up to the Fermi level, and MOP values of 0.097 and 0.271, respectively. Consistent with the preference for the icosahedral sites to be occupied by atoms with complete d subshells, the Ni d-block is nearly filled (Figure 5-5b); although filling of Ni–Ni bonding levels is nearly canceled by the filling of Ni–Ni antibonding levels (Figure 5-6d), these apparently d^{10}-d^{10} interactions[44] also include sufficient mixing of Ni 4s and 4p states as well as Sb states to stabilize Ni–Ni bonding levels by a small amount so that there is net bonding, as indicated by the small but positive MOP of 0.050. Finally, there are strong Ni–Sb bonds (MOP 0.222) notwithstanding the occupation of some Ni–Sb antibonding levels (Figure 5-6e).

Although atomic sizes and packing considerations govern the crystal structure adopted by an intermetallic compound, these are not the only factors. The relative atomic sizes in $Nb_{28}Ni_{33.5}Sb_{12.5}$ and $Mn_{45}Co_{40}Si_{15}$ are quite different, and yet they adopt the same structure. The similarity in valence electron concentrations of $Nb_{28}Ni_{33.5}Sb_{12.5}$ (7.26 e^-) and $Mn_{45}Co_{40}Si_{15}$ (7.35 e^-) is quite striking, and suggests that electronic factors are important. A second-moment scaling treatment of the band structure may prove illuminating.[45]

Table 5-1. Reactions in the Nb–Ni–Sb System

Reaction	Nb : Ni : Sb molar ratio	*Identified crystalline phases* [a]
1	36 : 28 : 10	Nb_3Sb (*M*) + other binaries (*m*)
2	32 : 32 : 10	Nb_3Sb (*M*) + other binaries (*m*)
3	28 : 36 : 10	*X*-phase (*M*) + other binaries (*t*)
4	28 : 32 : 14	*X*-phase (*M*) + Nb_3Sb (*t*) + other binaries (*t*)
5	28 : 28 : 18	Nb_3Sb (*M*) + *X*-phase (*m*) + other binaries (*t*)

[a] Designations. *M*: major phase (70–90%); *m*: minor phase (10–30%); *t*: trace (<10%).

Table 5-2. Crystallographic Data for $Nb_{28}Ni_{33.5}Sb_{12.5}$

Formula	$Nb_{28}Ni_{33.5(2)}Sb_{12.5(2)}$
Formula mass (amu)	6090.14
Space group	D_{2h}^{12}–*Pnnm* (No. 58)
a (Å)	13.2334(5) [a]
b (Å)	16.5065(7) [a]
c (Å)	5.0337(2) [a]
V (Å^3)	1099.5(1)
Z	1
T (°C)	22
Diffractometer	Bruker P4/RA/SMART–1000 CCD
ρ_{calc} (g cm^{-3})	9.197
Crystal dimensions (mm)	Needle, 0.24 × 0.04 × 0.02
Radiation	Graphite-monochromated Mo $K\alpha$, λ = 0.71073 Å
μ(Mo $K\alpha$) (cm^{-1})	284.01
Transmission factors [b]	0.241–0.558
Scan type	Mixture of ϕ rotations (0.3°) and ω scans (0.3°)
2θ limits	$4° \leq 2\theta$(Mo $K\alpha$) $\leq 65°$
Data collected	$-18 \leq h \leq 19$, $-24 \leq k \leq 24$, $-7 \leq l \leq 7$
No. of data collected	10904
No. of unique data, including $F_o^2 < 0$	2171 (R_{int} = 0.052)
No. of unique data, with $F_o^2 > 2\sigma(F_o^2)$	1670
No. of variables [c]	109

Table 5-2. Crystallographic Data for $Nb_{28}Ni_{33.5}Sb_{12.5}$ (continued)

$R(F)$ for $F_o^2 > 2\sigma(F_o^2)$ [d]	0.033
$R_w(F_o^2)$ [e]	0.083
Goodness of fit [f]	1.039
$\Delta\rho_{max}$, $\Delta\rho_{min}$ (e Å^{-3})	3.08, −3.40

[a] Obtained from a refinement constrained so that $\alpha = \beta = \gamma = 90°$.

[b] A numerical face-indexed absorption correction was applied, with the use of programs in the SHELXTL package (Sheldrick, G. M. *SHELXTL Version 5.1*; Bruker Analytical X-ray Systems: Madison, WI, 1997).

[c] Including an extinction coefficient.

[d] $R(F) = \sum \left| |F_o| - |F_c| \right| / \sum |F_o|$.

[e] $R_w(F_o^2) = \left[\sum \left[w(F_o^2 - F_c^2)^2\right] / \sum wF_o^4\right]^{1/2}$; $w^{-1} = \left[\sigma^2(F_o^2) + (0.0399P)^2 + 0.0000P\right]$ where $P = \left[\max(F_o^2, 0) + 2F_c^2\right]/3$.

[f] $GooF = \left[\sum \left[w(F_o^2 - F_c^2)^2\right] / (n-p)\right]^{1/2}$ where n is the number of reflections and p is the total number of parameters refined.

Table 5-3. Models in Refinement of *X*-Phase Structure

	Model A	Model B	Model C	Model D
CN12				
Site 1 (8*h*)	Ni	Ni	Ni	Ni(1)
Site 2 (8*h*)	Ni	Ni	Ni	Ni(2)
Site 3 (4*g*)	Ni	Ni	Ni	Ni(3)
Site 4 (4*g*)	Ni	Ni	Ni	Ni(4)
Site 5 (4*g*)	Ni	Ni	Ni	Ni(5)
Site 6 (4*g*)	Sb	Sb	Sb	Sb(1)
Site 7 (2*a*)	Sb	Sb	Sb	Sb(2)
Site 8 (8*h*)	Nb	Ni	50% Ni, 50% Sb	*X*(1) = 59% Ni, 41% Sb
Site 9 (4*g*)	Sb	Sb	Sb	*X*(2) = 21% Ni, 79% Sb
CN14				
Site 10 (4*g*)	Nb	Nb	Nb	Nb(1)
CN15				
Site 11 (4*g*)	Nb	Nb	Nb	Nb(7)
CN16				
Site 12 (4*g*)	Nb	Nb	Nb	Nb(2)
Site 13 (4*g*)	Nb	Nb	Nb	Nb(3)
Site 14 (4*g*)	Nb	Nb	Nb	Nb(4)
Site 15 (4*g*)	Nb	Nb	Nb	Nb(5)
Site 16 (4*g*)	Nb	Nb	Nb	Nb(6)
Formula	$Nb_{36}Ni_{28}Sb_{10}$	$Nb_{28}Ni_{36}Sb_{10}$	$Nb_{28}Ni_{32}Sb_{14}$	$Nb_{28}Ni_{33.5(2)}Sb_{12.5(2)}$
R_1 / wR_2	0.037 / 0.103	0.063 / 0.236	0.038 / 0.104	0.033 / 0.083

Table 5-4. Positional and Equivalent Isotropic Displacement Parameters for $Nb_{28}Ni_{33.5(2)}Sb_{12.5(2)}$

Atom	Wyckoff position	x	y	z	U_{eq} (Å^2) [a]
Nb(1)	4*g*	0.02254(6)	0.57316(4)	0	0.01147(16)
Nb(2)	4*g*	0.08693(6)	0.73064(4)	0	0.00749(15)
Nb(3)	4*g*	0.09989(5)	0.16209(4)	0	0.00659(15)
Nb(4)	4*g*	0.21753(6)	0.44618(4)	0	0.00753(15)
Nb(5)	4*g*	0.27940(5)	0.26523(4)	0	0.00664(15)
Nb(6)	4*g*	0.40087(5)	0.55016(4)	0	0.00597(15)
Nb(7)	4*g*	0.59926(6)	0.02495(4)	0	0.00940(16)
Ni(1)	8*h*	0.09926(6)	0.32456(5)	0.23441(15)	0.00839(16)
Ni(2)	8*h*	0.40816(6)	0.39308(4)	0.23934(15)	0.00885(17)
Ni(3)	4*g*	0.19180(9)	0.00229(6)	0	0.0104(2)
Ni(4)	4*g*	0.44436(8)	0.13723(6)	0	0.0084(2)
Ni(5)	4*g*	0.69464(8)	0.29083(6)	0	0.0096(2)
Sb(1)	4*g*	0.50370(4)	0.28599(3)	0	0.00653(12)
Sb(2)	2*a*	0	0	0	0.00720(16)
X(1) [b]	8*h*	0.28595(4)	0.10484(3)	0.24949(11)	0.00796(19)
X(2) [c]	4*g*	0.75676(5)	0.14668(3)	0	0.00591(19)

[a] U_{eq} is defined as one-third of the trace of the orthogonalized $\mathbf{U}_{ij}$ tensor.

[b] 59(2)% Ni, 41% Sb.

[c] 21(2)% Ni, 79% Sb.

Table 5-5. Extended Hückel Parameters

Atom	Orbital	H_{ii} (eV)	ζ_{i1}	c_1	ζ_{i2}	c_2
Nb	5s	−8.62	1.890			
	5p	−4.79	1.850			
	4d	−9.28	5.750	0.6401	1.640	0.5516
Ni	4s	−8.62	1.930			
	4p	−4.28	1.930			
	3d	−11.06	5.750	0.5862	2.200	0.5845
Sb	5s	−18.79	2.323			
	5p	−11.70	1.999			

Table 5-6. Interatomic Distances (Å) in $Nb_{28}Ni_{33.5(2)}Sb_{12.5(2)}$ [a]

	Ni(1) CN12	Ni(2) CN12	Ni(3) CN12	Ni(4) CN12	Ni(5) CN12	Sb(1) CN12	Sb(2) CN12	*X*(1) CN12	*X*(2) CN12	Nb(1) CN14	Nb(7) CN15	Nb(2) CN16	Nb(3) CN16	Nb(4) CN16	Nb(5) CN16	Nb(6) CN16
Ni(1) CN12	2.360 2.674			2.527 [2]	2.647 [2]	2.592 [2]			2.521 [2]	2.616 [2]	2.821 [2]	2.880 [2]	2.930 [2]	2.806 [2]	2.834 [2]	
Ni(2) CN12		2.410 2.624	2.593 [2]			2.485 [2]	2.513 [4]		2.483 [2]			2.986 [2]	2.998 [2]	2.930 [2]	2.968 [2]	2.861 [2] 2.952 [2]
Ni(3) CN12		2.593					2.538 [2]	2.449	2.551		2.801		2.905	2.938 [2]		2.909 [2]
Ni(4) CN12	2.527					2.578		2.501		2.765 [2]	2.739 2.764	2.980 [2]			3.038	
Ni(5) CN12	2.647					2.528		2.453	2.517			2.912	2.917 [2]		2.907 [2]	2.913
Sb(1) CN12	2.592	2.485		2.578	2.528							2.934 [2]	2.948 [2]		2.988	2.985
Sb(2) CN12		2.513	2.538										2.984			2.957 [2]
X(1) CN12			2.449 [2]	2.501 [2]	2.453 [2]			2.512 2.522		2.879 [2]	2.911 [2]	2.955 [2]	2.921 [2]	2.907 [2]	2.932 [2]	2.918 [2]
X(2) CN12	2.521	2.483	2.551		2.517						2.895	2.895		2.992 [2]	2.922 [2]	
Nb(1) CN14	2.616			2.765 [2]				2.879		2.488	3.093 [2] 3.160 [2]	2.736		3.193 3.324		
Nb(7) CN15	2.821		2.801	2.739 2.764				2.911	2.895	3.093 [2] 3.160 [2]	2.753			3.002 [2]		
Nb(2) CN16	2.880	2.986		2.980 [2]	2.912	2.934 [2]		2.955	2.895	2.736			3.041		3.129 [2]	
Nb(3) CN16	2.930	2.998	2.905		2.917 [2]	2.948 [2]	2.984 [2]	2.921				3.041			2.923	3.122 [2]
Nb(4) CN16	2.806	2.930	2.938 [2]					2.907	2.922 [2]	3.193 3.324	3.002 [2]				3.097	2.972
Nb(5) CN16	2.834	2.968		3.038	2.907 [2]	2.988		2.932	2.922 [2]			3.129 [2]	2.923	3.097		
Nb(6) CN16		2.861 2.952	2.909 [2]		2.913	2.985	2.956 [4]	2.918					3.122 [2]	2.972		3.103

Table 5-6. Interatomic Distances (Å) in $Nb_{28}Ni_{33.5(2)}Sb_{12.5(2)}$ (continued)

[a] Esds range from 0.0005 to 0.0015 Å. When read down, the number of distances listed (superscripts indicate number of times a distance occurs) corresponds to the CN in the header row.

Table 5-7. Mulliken Overlap Populations (MOP) for $Nb_{28}Ni_{33.5}Sb_{12.5}$

Contact	Distances (Å)	MOP
Nb–Nb	2.488(2)	0.550
	2.736(1), 2.753(2)	0.417
	2.923(1)–3.324(1)	0.245
	2.488(2)–3.324(1)	0.267
Nb–Ni	2.616(1)–2.998(1)	0.097
Nb–Sb	2.8786(9)–2.9881(9)	0.271
Ni–Ni	2.360(2)–2.674(2)	0.050
Ni–Sb	2.4833(9)–2.5915(8)	0.222

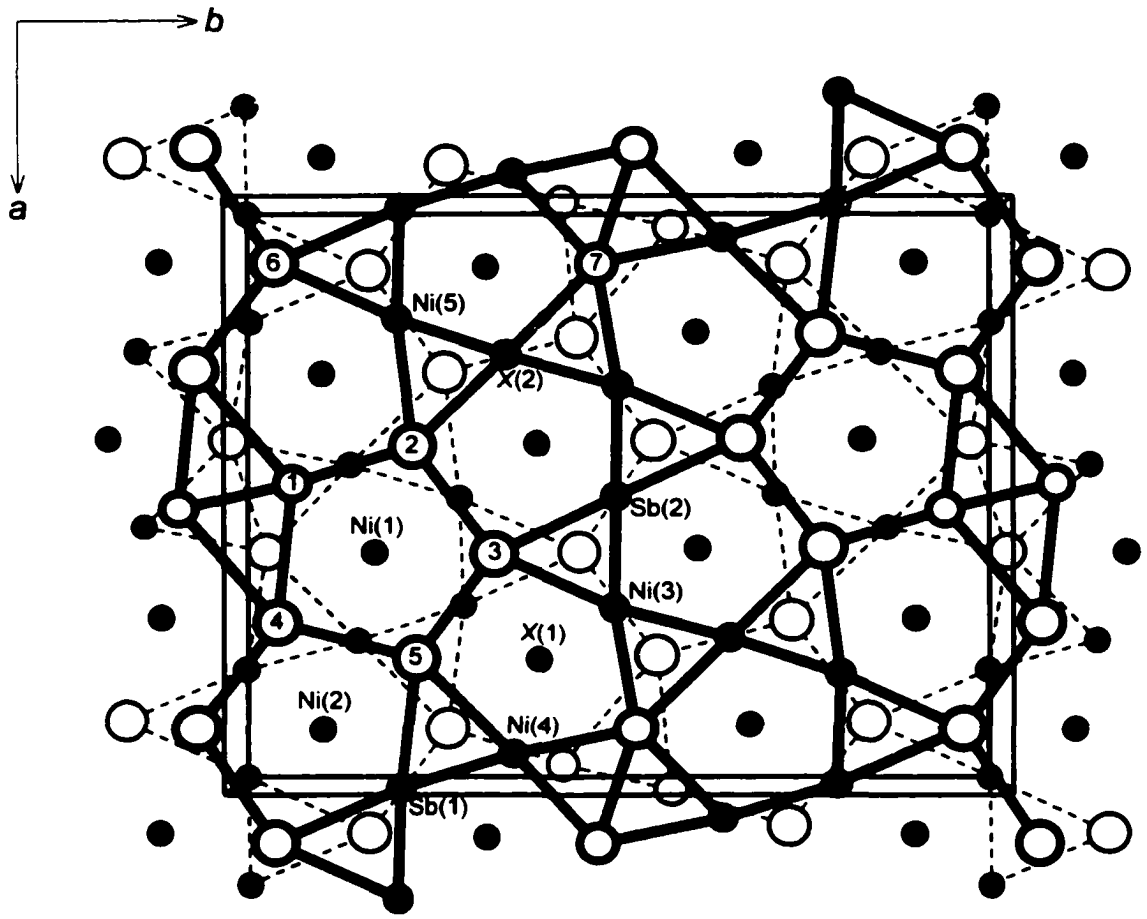

Figure 5-1. View down the *c* axis of the structure of $Nb_{28}Ni_{33.5}Sb_{12.5}$ showing the unit cell outline and the labeling scheme. The open circles are Nb atoms, the solid circles are Ni atoms, and the lightly shaded circles are Sb atoms. For the disordered sites, the more Ni-rich site *X*(1) is portrayed like a Ni atom and the more Sb-rich site *X*(2) like an Sb atom. The size of the circles is proportional to the CN of the site. The main layers **A** lie at $z = 0$ (dashed lines) and $z = ½$ (thick lines), while the secondary layers **B** lie at $z = ~¼$ and $~¾$ (unconnected Ni(1), Ni(2), and *X*(1) sites).

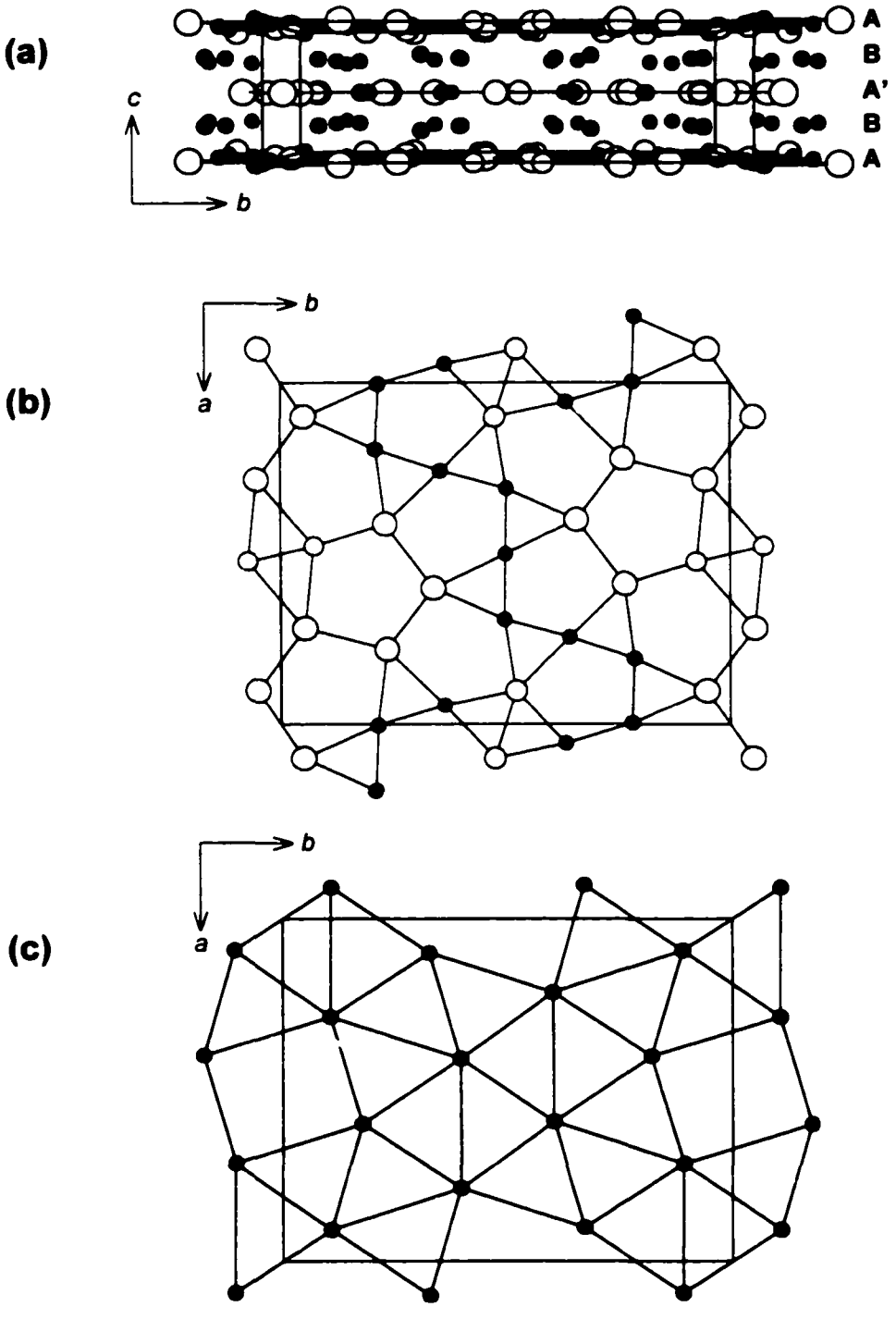

Figure 5-2. (a) View down the *a* axis of $Nb_{28}Ni_{33.5}Sb_{12.5}$ showing the stacking of main (**A** and **A'**) and secondary (**B**) layers. (b) Tessellation of pentagons and triangles in main layer **A**. (c) Tessellation of squares and triangles in secondary layer **B**.

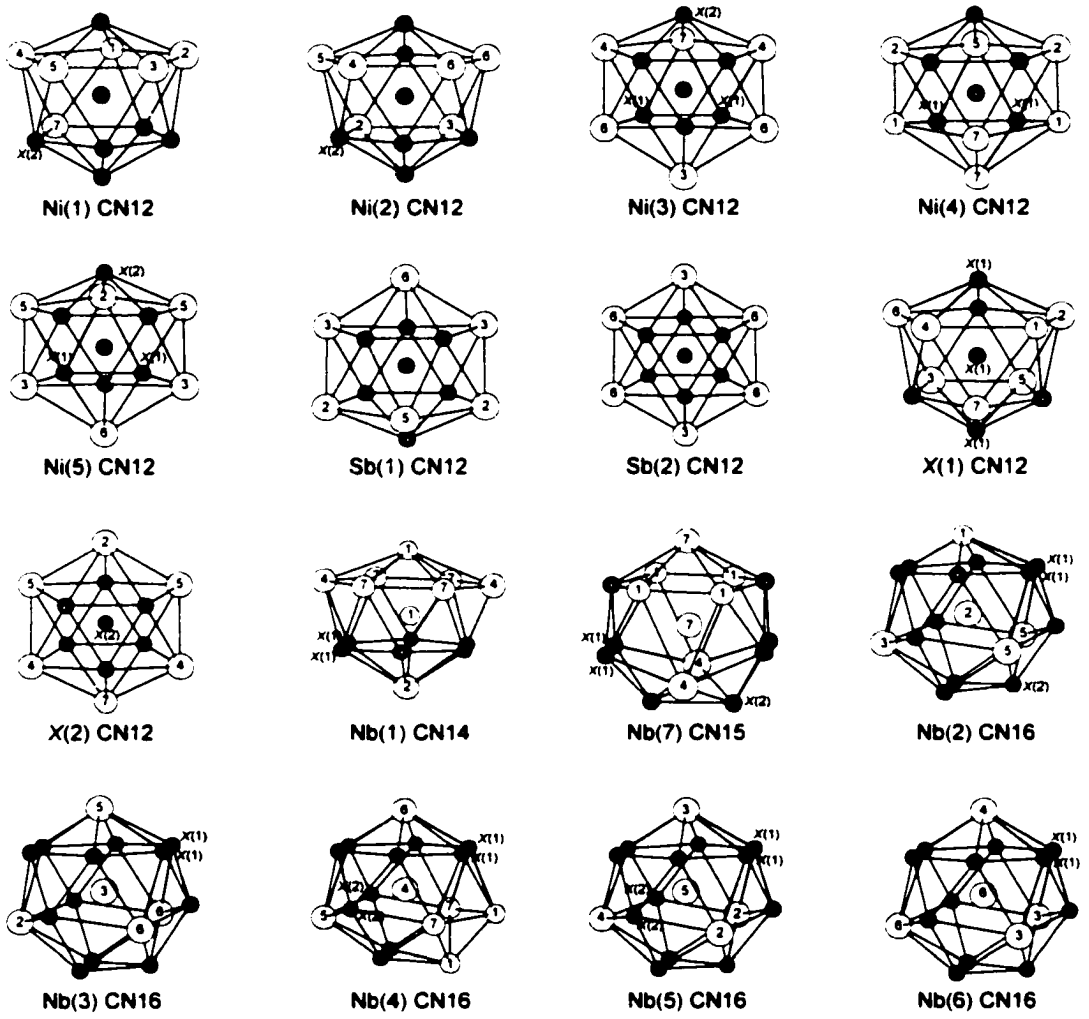

Figure 5-3. Coordination polyhedra in $Nb_{28}Ni_{33.5}Sb_{12.5}$.

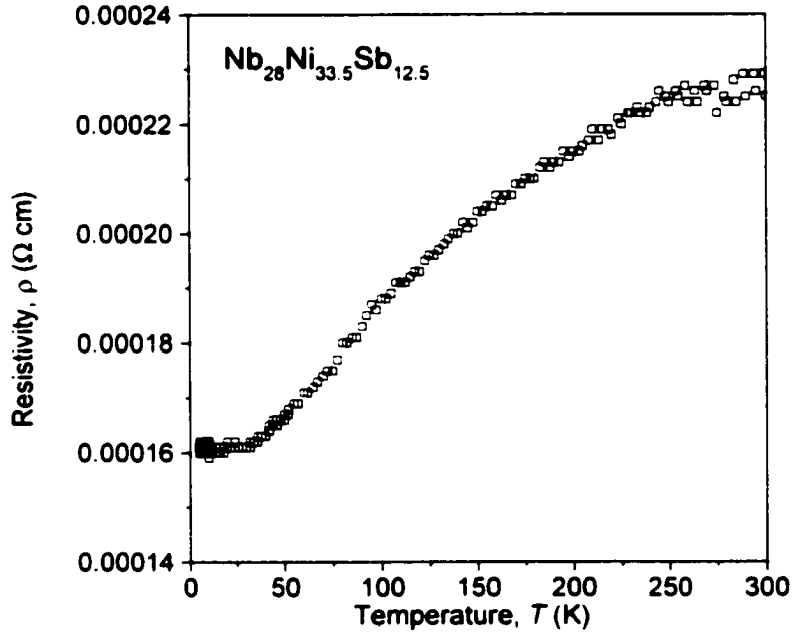

Figure 5-4. Temperature dependence of the resistivity of $Nb_{28}Ni_{33.5}Sb_{12.5}$.

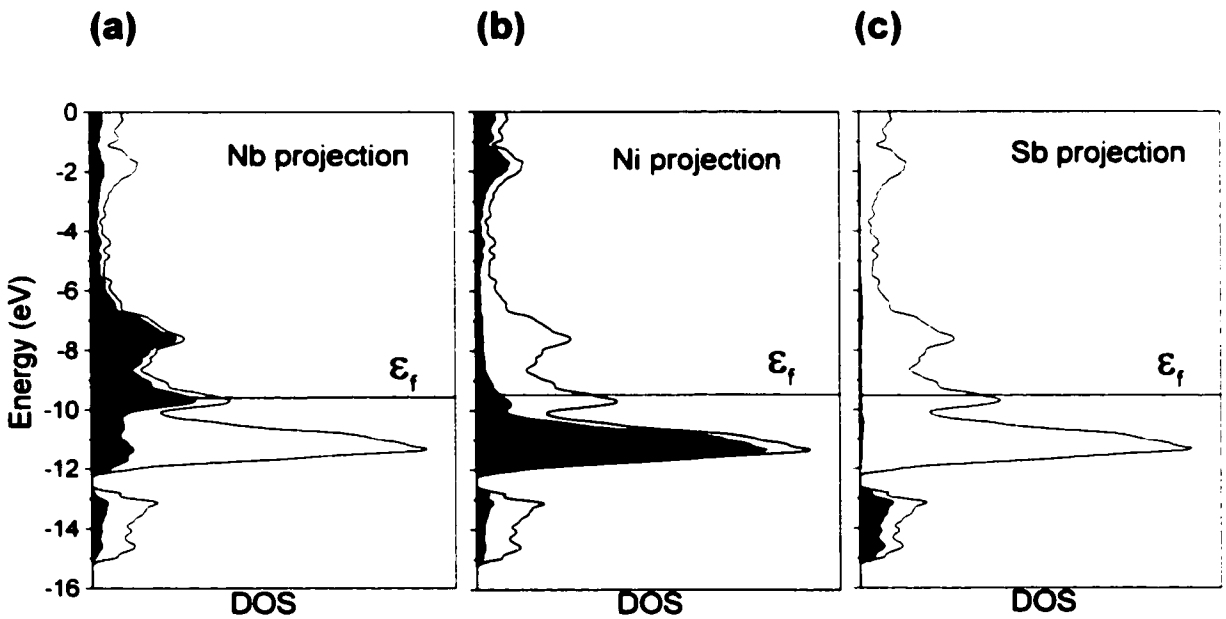

Figure 5-5. Contributions of (a) Nb, (b) Ni, and (c) Sb (shaded regions) to the total density of states (DOS) (line) for $Nb_{28}Ni_{33.5}Sb_{12.5}$ (idealized as "$Nb_{28}Ni_{32}Sb_{14}$"). The Fermi level (ε_f) is at –9.38 eV.

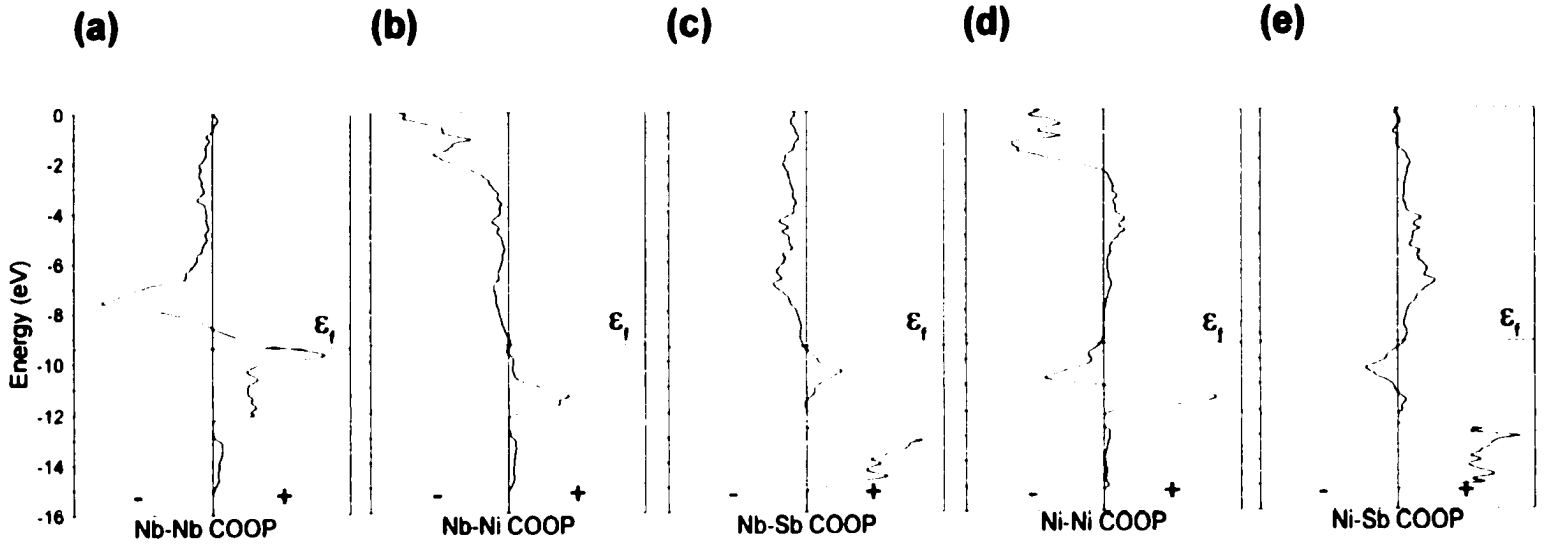

Figure 5-6. Crystal orbital overlap population (COOP) curves for (a) Nb–Nb, (b) Nb–Ni, (c) Nb–Sb, (d) Ni–Ni, and (e) Ni–Sb contacts, within the range of distances listed in Table 7, in $Nb_{28}Ni_{33.5}Sb_{12.5}$ (idealized as "$Nb_{28}Ni_{32}Sb_{14}$").

References

(1) *Handbook of Crystal Structures and Magnetic Properties of Rare Earth Intermetallics*; Szytula, A.; Leciejewicz, J., Eds.; CRC Press: Boca Raton, 1994.

(2) Sales, B. C.; Mandrus, D.; Williams, R. K. *Science* **1996**, *272*, 1325.

(3) Kleinke, H. *Z. Anorg. Allg. Chem.* **1998**, *624*, 1272.

(4) Dwight, A. E. *Mater. Res. Bull.* **1987**, *22*, 201.

(5) Rieger, W.; Parthé, E. *Acta Crystallogr., Sect. B: Struct. Crystallogr. Cryst. Chem.* **1968**, *24*, 456.

(6) Garcia, E.; Corbett, J. D. *Inorg. Chem.* **1990**, *29*, 3274.

(7) Kwon, Y.-U.; Sevov, S. C.; Corbett, J. D. *Chem. Mater.* **1990**, *2*, 550.

(8) Kleinke, H.; Ruckert, C.; Felser, C. *Eur. J. Inorg. Chem.* **2000**, 315.

(9) Kleinke, H. *J. Alloys Compd.* **1998**, *270*, 136.

(10) Wang, M.; McDonald, R.;. Mar, A. *Inorg. Chem.* **1999**, *38*, 3435.

(11) Garcia, E.; Corbett, J. D. *J. Solid State Chem.* **1988**, *73*, 440.

(12) Garcia, E.; Corbett, J. D. *J. Solid State Chem.* **1988**, *73*, 452.

(13) Myzenkova, L. F.; Baron, V. V.; Savitskiy, Ye. M. *Russ. Metall. (Engl. Transl.)* **1966**, 89.

(14) Kjekshus, A. *Acta Chem. Scand.* **1972**, *26*, 1633.

(15) Furuseth, S.; A. Kjekshus, A. *Acta Crystallogr.* **1965**, *18*, 320.

(16) Rehr, A.; Kauzlarich, S. M. *Acta Crystallogr., Sect. C: Cryst. Struct. Commun.* **1994**, *50*, 1177.

(17) Garcia, E.; Corbett, J. D. *Inorg. Chem.* **1988**, *27*, 2353.

(18) Furuseth, S.; Kjekshus, A. *Acta Chem. Scand.* **1964**, *18*, 1180.

(19) Schubert, K.; Raman, A.; Rossteutscher, W. *Naturwissenschaften* **1964**, *51*, 506.

(20) Hyde, B. G.; Andersson, S. *Inorganic Crystal Structures*; Wiley: New York, 1989.

(21) Frank, F. C.; Kasper, J. S. *Acta Crystallogr.* **1958**, *11*, 184.

(22) Frank, F. C.; Kasper, J. S. *Acta Crystallogr.* **1959**, *12*, 483.

(23) Wernick, J. H. In *Intermetallic Compounds*; Westbrook, J. H., Ed.; Wiley: New York, 1967; p 197.

(24) Shoemaker, C. B.; Shoemaker, D. P. In *Developments in the Structural Chemistry of Alloy Phases*; Giessen, B. C., Ed.; Plenum Press: New York, 1969; p 107.

(25) Yarmolyuk, Ya. P.; Kripyakevich, P. I.; Gladyshevskii, E. I. *Sov. Phys. Crystallogr. (Engl. Transl.)* **1970**, *15*, 226.

(26) Manor, P. C.; Shoemaker, C. B.; Shoemaker, D. P. *Acta Crystallogr., Sect. B.: Struct. Crystallogr. Cryst. Chem.* **1972**, *28*, 1211.

(27) Sheldrick, G. M. *SHELXTL*, version 5.1; Bruker Analytical X-ray Systems, Inc.: Madison, WI, 1997.

(28) *International Tables for X-ray Crystallography*; Wilson, A. J. C., Ed.: Kluwer: Dordrecht, 1992; Vol. C.

(29). Kasper, J. S. In *Theory of Alloy Phases*; American Society for Metals: Cleveland, 1956; p. 264.

(30) Gelato, L. M.; Parthé, E. *J. Appl. Crystallogr.* **1987**, *20*, 139.

(31) Whangbo, M.-H.; Hoffmann, R. *J. Am. Chem. Soc.* **1978**, *100*, 6093.

(32) Hoffmann, R. *Solids and Surfaces: A Chemist's View of Bonding in Extended*

Structures; VCH Publishers: New York, 1988.

(33) Kleinke, H.; Franzen, H. F. *J. Am. Chem. Soc.* **1997**, *119*, 12824.

(34) Shoemaker, D. P.; Shoemaker, C. B. *Acta. Crystallogr., Sect. B: Struct. Sci.* **1986**, *42*, 3.

(35) Kuz'ma, Yu. B. *Russ. J. Inorg. Chem. (Engl. Transl.)* **1962**, *7*, 691.

(36) Donohue, J. *The Structures of the Elements*; Wiley: New York, 1974.

(37) A. Kjekshus and K. P. Walseth, *Acta Chem. Scand.* **23**, 2621 (1969).

(38) Pauling, L. *The Nature of the Chemical Bond*, 3rd ed.; Cornell University Press: Ithaca, NY, 1960.

(39) Carpenter, J. H.; Searcy, A. W. *J. Am. Chem. Soc.* **1956**, *78*, 2079.

(40) Cotton, F. A.; Matonic, J. H., Murillo, C. A. *J. Am. Chem. Soc.* **1998**, *120*, 6047.

(41) Kaufman, A.; Hoffman, N. J.; Lipson, H. *Scr. Metall.* **1969**, *3*, 715.

(42) Andersson, S. *J. Solid State Chem.* **1978**, *23*, 191.

(43) Hughbanks, T.; Hoffmann, R. *J. Am. Chem. Soc.* **1983**, *105*, 3528.

(44) Pyykkö, P. *Chem. Rev.* **1997**, *97*, 597.

(45) Lee, S. *J. Am. Chem. Soc.* **1991**, *113*, 101.

Chapter 6

$Nb_4Pd_{0.5}ZSb_2$ (Z = Cr, Fe, Co, Ni, Si): The First Ordered Quaternary Variants of the W_5Si_3–Type Structure †

Introduction

The early transition metals, having few valence electrons in relatively expanded d orbitals, form clusters though multicentre metal-metal bonding in a variety of molecular species and extended structures.[1] Interstitial atoms are often contained within these electron-deficient polyhedra, stabilizing them by supplementing the weak metal-metal bonds with strong metal-interstitial bonds.[1,2] The most frequently observed cluster types are octahedra (or trigonal antiprisms) (**1**), trigonal prisms with capping atoms on one or more quadrilateral faces (**2**), and square antiprisms (**3**). These polyhedra can be centred by a gamut of interstitial atoms, including first-row transition metals, second- and third-row main-group elements, and hydrogen.

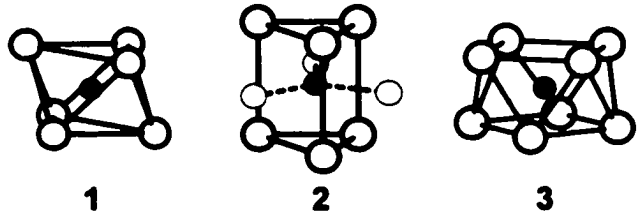

1 **2** **3**

† A version of this chapter has been accepted for publication. Wang, M.; Sheets, W. C.; McDonald, R.; Mar, A. *Inorg. Chem.*

In the past two decades, early transition-metal-rich halides and chalcogenides have been the most exhaustively studied class of cluster compounds with extended structures. In the halides, cluster **1** is the usual basic building block observed,[3] whereas in the chalcogenides, cluster **2** is more prevalent and clusters **1** and **3** are less commonly found.[4,5] In contrast, much less is known about the existence of clusters among early transition-metal-rich pnictides. All three clusters have been identified thus far in the structures of these pnictides. For example, Zr_5NiSb_3 (Ti_5Ga_4-type) contains cluster **1**,[6] Zr_6FeSb_2 (Zr_6CoAl_2-type) contains cluster **2**,[7] and V_4SiSb_2 contains cluster **3**.[8] These clusters can be further condensed by sharing their corners, edges, or faces to give a rich structural chemistry.

The V_4SiSb_2 structure is particularly intriguing in featuring apparently empty channels surrounded by the pnicogen atoms. A recent band structure calculation on the isostructural bismuthides Ti_4ZBi_2 (Z = Cr, Mn, Fe, Co, Ni)[9] implied that electrophilic species could be feasibly intercalated into the tetrahedral voids of these channels, interacting with the lone pairs of the surrounding pnicogen atoms.[10] We were thus interested in the possibility of preparing quaternary early transition-metal-rich pnictide cluster compounds in which these voids are filled by guest atoms while accommodating a wide variety of interstitial atoms Z (Si as well as first-row transition metals) within clusters of type **3**.

Extending our systematic studies of ternary transition-metal-rich pnictides, in which we have discovered the compounds $M_3Pd_4P_3$ (M = Zr, Hf),[11] $Nb_5Pd_4P_4$,[11] $M_3Ni_3Sb_4$ (M = Zr, Hf),[12] $Zr_3Pt_3Sb_4$,[12] and $Nb_{28}Ni_{33.5}Sb_{12.5}$,[13] we report here several members of a new family of quaternary (or pseudoquaternary) transition-metal-rich antimonides

$Nb_4Pd_{0.5}ZSb_2$ (Z = Cr, Fe, Co, Ni, Si). They represent the first examples of a filled V_4SiSb_2-type structure, or a quaternary *ordered* substitutional variant of the W_5Si_3-type structure.[14]

Experimental Section

Synthesis. Reactants used were the elemental powders (Nb, 99.8%, Cerac; Pd, 99.95%, Alfa-Aesar; Cr, 99.95%, Cerac; Fe, 99.9%, Cerac; Co, 99.8%, Cerac; Ni, 99.9%, Cerac; Si, 99.96%, Cerac; Sb, 99.995%, Aldrich). In the course of investigating the ternary Nb–Pd–Sb system, $Nb_4Pd_{0.5}SiSb_2$ was first identified in a direct reaction of Nb, Pd, and Sb in a 1:1:1 molar ratio (total weight 0.25 g) placed in an evacuated fused-silica tube. The reactants were heated at 1100 °C for 12 h and then at 1000 °C for 4 days. The silica tube served as the source of Si in the products. EDX (energy-dispersive X-ray) analysis of several crystals from the above reaction on a Hitachi S-2700 scanning electron microscope suggested an approximate atomic composition of 50% Nb, 8% Pd, 12% Si, and 30% Sb (with typical uncertainties of 1–2%). On this basis, a mixture of Nb, Pd, Si, and Sb in a 5:1:1:3 ratio was reacted at 1000 °C for 3 days. A needle-shaped crystal from this reaction was selected for the structure determination, which revealed the correct composition to be $Nb_4Pd_{0.5}SiSb_2$ (53% Nb, 7% Pd, 13% Si, 27% Sb). A stoichiometric reaction of the elements in the correct ratio at 1000 °C for 3 days afforded a quantitative yield of $Nb_4Pd_{0.5}SiSb_2$, as revealed by X-ray powder diffraction patterns obtained on an Enraf-Nonius FR552 Guinier camera (Cu $K\alpha_1$ radiation).

Since Si can be replaced by some first-row transition metals as an interstitial atom in other cluster structures such as Ta_4ZTe_4,[15] substitution of the Si atoms in $Nb_4Pd_{0.5}SiSb_2$

by Fe was first attempted. Two direct reactions of Nb, Pd, Fe, and Sb in 5:1:1:3 and 4:0.5:1:2 ratios at 1000 °C for 3 days were carried out. The products in both reactions contained more than 50% $Nb_4Pd_{0.5}FeSb_2$, as well as the phases NbFeSb and Nb_3Sb, as determined by X-ray powder diffraction patterns. EDX analyses on several needle-shaped crystals confirmed the presence of all four elements in the atomic proportions 49% Nb, 9% Pd, 12% Fe, and 30% Sb. One crystal from the first reaction (5:1:1:3 ratio) was chosen for the structure determination.

Subsequently, reactions of Nb, Pd, *Z*, and Sb in both 5:1:1:3 and 4:0.5:1:2 ratios were carried out for *Z* = Cr–Zn. For *Z* = Co and Ni, the quaternary compounds were obtained as needle-shaped crystals, as verified by EDX analyses which indicated compositions of 49% Nb, 9% Pd, 13% Co, 29% Sb (avg. of five crystals) and 53% Nb, 7% Pd, 10% Ni, 31% Sb (avg. of six crystals), respectively. For *Z* = Cr, incorporation of Si from the silica tube occurred to give crystals containing *five* elements present in the proportions 49% Nb, 7% Pd, 6% Cr, 9% Si, 29% Sb (avg. of five crystals). We have been unable to prepare an all-Cr compound free from Si incorporation. When the reaction is repeated in an alumina crucible jacketed by a silica tube, the desired phase was not formed, but rather the product consisted predominantly of binary phases such as Nb_3Sb. For *Z* = Mn, Cu, and Zn, no quaternary phases were obtained under any of the synthetic conditions described above.

Structure Determination. All crystals were screened by EDX analysis and Weissenberg photography. Intensity data were collected at room temperature (22 °C) on a Bruker Platform/SMART 1000 CCD diffractometer using ω scans (0.2°) in the range $5.52° \leq 2\theta$ (Mo Kα) $\leq 65.12°$ for $Nb_4Pd_{0.5}Cr_{0.28}Si_{0.72}Sb_2$, $5.50° \leq 2\theta$ (Mo Kα) $\leq 65.10°$

for $Nb_4Pd_{0.5}FeSb_2$, 5.50° ≤ 2θ (Mo Kα) ≤ 65.14° for $Nb_4Pd_{0.5}CoSb_2$, 5.52° ≤ 2θ (Mo Kα) ≤ 65.18° for $Nb_4Pd_{0.5}Ni_{0.78}Sb_2$, and 5.54° ≤ 2θ (Mo Kα) ≤ 52.66° for $Nb_4Pd_{0.5}SiSb_2$. Crystal data and further details of the data collections are given in Table 6-1. All calculations were carried out with use of the SHELXTL (version 5.1) package.[16] Conventional atomic scattering factors and anomalous dispersion corrections were used.[17] Intensity data were processed, and face-indexed numerical absorption corrections were applied in XPREP.

The five compounds are isostructural. Weissenberg photographs revealed tetragonal symmetry in all cases. The Laue symmetry *4/mmm* and the systematic extinctions suggested space groups *I4/mcm*, *I4cm*, and $I\bar{4}c2$. The centrosymmetric space group *I4/mcm* (No. 140) was chosen on the basis of the successful structure solution and refinement. The positions of all atoms were found by direct methods. In the early stages of refinement, the displacement parameter of the Pd site was unusually large, implying that it is partially occupied. For example, when refined, the occupancy of the Pd site converged to 56(2)% in the Fe-containing and 58(2)% in the Si-containing compound. In all compounds, the closest separation between Pd sites is ~2.47–2.50 Å, which would be unusually short for a Pd–Pd bond (cf. 2.56 Å from the sum of two Pauling single-bond metallic radii of Pd [18] or 2.75 Å for the Pd–Pd distance in elemental Pd [19]). Although the possibility that these short Pd–Pd contacts genuinely exist cannot be excluded, we chose the simplest interpretation in which they are precluded by setting the Pd occupancy to 50%.

The subsequent refinements for $Nb_4Pd_{0.5}FeSb_2$, $Nb_4Pd_{0.5}CoSb_2$, and $Nb_4Pd_{0.5}SiSb_2$ proceeded in a straightforward manner, with full occupancies of all sites

other than that of Pd. For the pseudoquaternary compound $Nb_4Pd_{0.5}(Cr_xSi_{1-x})Sb_2$, the Z site was modeled to accommodate a disorder of Cr and Si atoms in proportions that sum to full occupancy. With this constraint, the occupancies refined to 28(3)% Cr and 72% Si. For the Ni-containing compound, the displacement parameter of the Z site remained somewhat large, suggesting a substoichiometry in Ni. Consistent with the lower than expected content of Ni found in the EDX analysis, the occupancy of this site converged to 78(1)% Ni when allowed to refine.

The final refinements for all compounds led to generally well-behaved anisotropic displacement parameters. The thermal ellipsoids of the Sb sites are somewhat elongated along the c-axis, perhaps reflecting the tendency of the Sb atoms to be displaced either slightly above or below the mirror plane (x, y, 0) depending on whether a Pd atom locally occupies the site above or below. Indeed, the Sb atom can be refined with 50% occupancy at two split sites off the mirror plane. For example, in $Nb_4Pd_{0.5}FeSb_2$, the sites are displaced ~0.14 Å off the mirror plane. However, in other cases, the resolution of the split sites is sufficiently poor that correlation between the positional and displacement parameters renders the refinement unstable. We therefore opted to retain the Sb position on the mirror plane with the understanding that the elongation of the thermal ellipsoid is an artifact that results from averaging two closely-spaced split sites. Satisfactory residuals (Table 6-1) and featureless difference electron maps ($\Delta\rho_{max}$ = 2.25, $\Delta\rho_{min}$ = –1.36 e^- $Å^{-3}$ for $Nb_4Pd_{0.5}Cr_{0.28(3)}Si_{0.72}Sb_2$; $\Delta\rho_{max}$ = 2.78, $\Delta\rho_{min}$ = –1.68 e^- $Å^{-3}$ for $Nb_4Pd_{0.5}FeSb_2$; $\Delta\rho_{max}$ = 2.20, $\Delta\rho_{min}$ = –2.04 e^- $Å^{-3}$ for $Nb_4Pd_{0.5}CoSb_2$; $\Delta\rho_{max}$ = 2.60, $\Delta\rho_{min}$ = –1.99 e^- $Å^{-3}$ for $Nb_4Pd_{0.5}Ni_{0.78(1)}Sb_2$; and $\Delta\rho_{max}$ = 2.18, $\Delta\rho_{min}$ = –2.71 e^- $Å^{-3}$ for $Nb_4Pd_{0.5}SiSb_2$) were obtained for all structures. The atomic positions were standardized

with the program STRUCTURE TIDY.[20] Final values of the positional and displacement parameters are given in Table 6-2. Selected interatomic distances are listed in Table 6-3. Anisotropic displacement parameters are listed in Table C-7.

Electrical Resistivity. A pressed pellet of $Nb_4Pd_{0.5}SiSb_2$ with dimensions of 0.53 × 0.30 × 0.05 cm was mounted in a four-probe configuration for an ac resistivity measurement between 2 and 300 K on a Quantum Design PPMS system equipped with an ac-transport controller (Model 7100). A current of 0.1 mA and a frequency of 16 Hz were used. Measurements on the other members could not be performed owing to difficulties in preparing phase-pure material or single crystals of adequate size.

Band Structure. One-electron band structure calculations on $Nb_4Pd_{0.5}FeSb_2$ and $Nb_4Pd_{0.5}SiSb_2$ were performed with use of the EHMACC suite of programs.[21,22] The 50% Pd occupancy was modeled by alternately removing every second Pd atom within each $^{1}_{\infty}[Pd_{0.5}Sb_{4/2}]$ column. Extended Hückel parameters were taken from literature values and are listed in Table 6-4. Properties were extracted from the band structure using 128 *k* points in the irreducible portion of the Brillouin zone.

Results and Discussion

Crystal Structure. The quaternary (or pseudoquaternary, in the case of $Nb_4Pd_{0.5}Cr_{0.28}Si_{0.72}Sb_2$) transition-metal antimonides $Nb_4Pd_{0.5}ZSb_2$ (Z = Cr, Fe, Co, Ni, Si) adopt a three-dimensional structure than can be described by linking one-dimensional $^{1}_{\infty}[Nb_{8/2}Z]$ and $^{1}_{\infty}[Pd_{0.5}Sb_{4/2}]$ columns together, as shown in a projection along the *c* axis in Figure 6-1.

In this view, it is easy to visualize the Nb_8 square antiprismatic clusters centered

by interstitial Z atoms (**3**) whose fourfold axis coincides with the c axis. The Nb–Z distances within the square antiprisms are ~2.63 Å and indicate strong interactions. For example, the Nb–Fe distance (2.6361(7) Å) in $Nb_4Pd_{0.5}FeSb_2$ falls within the range of those in the binary intermetallic μ-phase Nb_6Fe_7 (nearest neighbour Nb–Fe distances of 2.54–2.64 Å),[23] and the Nb–Si distance in $Nb_4Pd_{0.5}SiSb_2$ (2.624(2) Å) is comparable to those in binary niobium silicides (e.g., Nb–Si distance of 2.59 Å in Nb_5Si_3 [24] or 2.62 Å in $NbSi_2$ [25]). The Z-centered Nb_8 square antiprisms then share opposite square faces to form the one-dimensional $^1_\infty[Nb_{8/2}Z]$ columns that run along the c direction. The resulting Z–Z distances (e.g., 2.4772(1) Å for Fe–Fe; 2.4817(2) Å for Si–Si), which are equal to half the c parameter, are short (cf. 2.48 Å for Fe–Fe in elemental Fe; 2.35 Å for Si–Si in elemental Si),[19] but whether they are truly strongly bonding of their own accord or a mere consequence of a matrix effect will be discussed later.

In all compounds, the Pd atoms are coordinated in a tetrahedral fashion by four Sb neighbours. These tetrahedra then share opposite edges to form the one-dimensional $^1_\infty[Pd_{0.5}Sb_{4/2}]$ columns that also run along the c direction. The Pd sites have a 50% occupancy to avoid abnormally short Pd–Pd contacts (equal to the Z–Z distances), suggesting a local ordering of alternately empty and filled tetrahedral sites within a column. The $^1_\infty[Pd_{0.5}Sb_{4/2}]$ columns are far apart from each other, so the distribution of locally ordered columns would still be randomized within the ab plane. The observed Pd–Sb distances of ~2.56 Å are shorter than the sum of Pauling single-bond radii, 2.688 Å,[18] or typical distances of 2.6–2.8 Å found in most binary palladium antimonides, although distances as short as 2.54 Å have been observed in Pd_8Sb_3.[26] As discussed in the structure determination section, the elongation of the thermal ellipsoids of the

neighbouring Sb atoms along the *c* axis may reflect slight distortions of the $PdSb_4$ tetrahedra that are averaged out in the partial occupancy model of the structure.

The $^{1}_{\infty}[Nb_{8/2}Z]$ and $^{1}_{\infty}[Pd_{0.5}Sb_{4/2}]$ columns are connected together by Nb–Sb bonds to complete the three-dimensional structure. The Nb–Sb bond distances of ~2.84–2.98 Å are similar to those found in binary niobium antimonides such as $NbSb_2$ [27] and Nb_5Sb_4 [28] (2.73–2.97 Å). There is a short intercolumn Nb–Nb bond (e.g., 3.1448(16) Å in $Nb_4Pd_{0.5}FeSb_2$ or 3.109(4) Å in $Nb_4Pd_{0.5}SiSb_2$), whose magnitude is comparable to the intracolumn Nb–Nb distances, that also connects $^{1}_{\infty}[Nb_{8/2}Z]$ columns together. Both Nb and Sb atoms have rather unusual coordination environments. Each Nb atom has six Nb and two *Z* neighbours within a $^{1}_{\infty}[Nb_{8/2}Z]$ column, one Nb neighbour in the adjacent $^{1}_{\infty}[Nb_{8/2}Z]$ column, and four Sb neighbours located at one side of the coordination polyhedron, resulting in a CN of 13. Each Sb atom is surrounded by eight Nb atoms from two $^{1}_{\infty}[Nb_{8/2}Z]$ columns and by two Pd sites (one of which is empty if the 50% occupancy is taken into account), giving an average CN of 9.

Structural Relationships. One-dimensional columns of interstitially stabilized square-antiprismatic clusters $^{1}_{\infty}[M_{8/2}Z]$ (M = Nb, Ta) are found, albeit infrequently, in other structures related to $Nb_4Pd_{0.5}ZSb_2$, as shown in Figure 6-2. In the Ta_2Si-type structure,[29] the $^{1}_{\infty}[Ta_{8/2}Si]$ columns are connected to each other by sharing all corners (Figure 6-2a). Although this structure appears to be quite dense, the channels in the intercolumn region are able to accommodate additional guest atoms within them, producing the TlSe-type structure.[30]

In contrast, the recently elucidated V_4SiSb_2-type structure contains $^{1}_{\infty}[V_{8/2}Si]$

columns that are capped along their periphery by Sb atoms to yield more open intercolumn regions (Figure 6-2b). Effectively, these Sb atoms are shared between $^{1}_{\infty}[V_{8/2}Si]$ columns and serve to link them together. The Sb atoms also form empty channels along (½, 0, z) and (0, ½, z) consisting of tetrahedral sites spaced evenly along c. Electronic structure calculations confirmed the supposition that the empty channels in the isostructural bismuthides Ti_4ZBi_2 (Z = Cr, Mn, Fe, Co, Ni)[9] contain nonbonding electron density (lone pairs) from the surrounding pnicogen atoms and suggested the possibility of intercalating species such as Li^+ or Na^+ into these channels.[10] Perhaps somewhat astonishingly, the successful filling of these channels came about not from intercalation of Li or Na into the Ti_4ZBi_2 structure, as was proposed, but rather from intercalation (in a *Gedanken* manner) of Pd into a hypothetical "Nb_4ZSb_2" structure, to form the $Nb_4Pd_{0.5}ZSb_2$ compounds (Figure 6-2c). The observed Pd–Sb distances of ~2.56 Å in $Nb_4Pd_{0.5}ZSb_2$ are not that far off from the Li–Bi distance of 2.41 Å in a hypothetical "$LiTi_4FeBi_2$" compound.[10] Of course, the character of a Pd–Sb bond is quite different from that of a Li–Bi bond. We expect that achieving the electronic structure of $Nb_4Pd_{0.5}ZSb_2$ would entail a less severe redistribution of electron density in a hypothetical "Nb_4ZSb_2" compound than in a corresponding intercalation with Li.

The binary version of $Nb_4Pd_{0.5}ZSb_2$ is the well known W_5Si_3-type structure.[14] This is a common intermetallic structure type ($I4/mcm$, $tI32$) adopted by nearly a hundred binary, pseudobinary, and ternary compounds.[31] Of the four different crystallographic sites (4a, 4b, 8h, and 16k) in the W_5Si_3-type structure, metals are usually located in 4b and 16k, and nonmetals or metalloids in 4a and 8h. For example, in the recently discovered ternary antimonides $Zr_5M_xSb_{3-x}$ (M = Fe, Co, Ni; $x \approx 0.5$)[32] and $Hf_{10}M_xSb_{6-x}$

(M = V, Cr, Mn, Fe, Co, Ni, Cu; $0.8 < x < 1.5$),[33] Zr or Hf atoms occupy sites 4*b* and 16*k*, Sb atoms occupy site 8*h*, and *M* and Sb atoms are approximately evenly distributed over site 4*a*. The compounds reported here, $Nb_4Pd_{0.5}ZSb_2$ (Z = Cr, Fe, Co, Ni, Si), are the first quaternary or pseudoquaternary variants of the W_5Si_3-type structure: Nb atoms occupy site 16*k*, Pd atoms site 4*b* (at 50%), *Z* atoms site 4*a*, and Sb atoms site 8*h*. It is remarkable that the structure of $Nb_4Pd_{0.5}ZSb_2$ can contain up to three different transition metals in an *ordered* arrangement.

Like the V_4SiSb_2 structure, the Ta_4SiTe_4 structure[15] contains empty channels formed between $^1_\infty[Ta_{8/2}Si]$ columns, which are further apart and capped by Te atoms (Figure 6-2d). The disparities in these two structures reflect the different chemistry of the pnicogens *vs.* the chalcogens: whereas neighbouring $^1_\infty[V_{8/2}Si]$ columns in V_4SiSb_2 are held strongly together by Sb atoms through V–Sb covalent bonds, the $^1_\infty[Ta_{8/2}Si]$ columns in Ta_4SiTe_4 are merely interacting between Te atoms through van der Waals forces, as frequently found in low-dimensional chalcogenides. Whether additional atoms can be inserted between these columns remains to be seen.

All four structure types shown in Figure 6-2 have representatives in which Si is the interstitial *Z* atom centering the square antiprisms. The *Z* atom can also be replaced by first-row transition metals, but the range of substitution varies; *viz.*, $Ta_2Si \rightarrow Nb_4CoSi$,[29,34] $V_4SiSb_2 \rightarrow Ti_4ZBi_2$ (Z = Cr, Mn, Fe, Co, Ni),[8,9] $Nb_4Pd_{0.5}SiSb_2 \rightarrow Nb_4Pd_{0.5}ZSb_2$ (Z = Cr, Fe, Co, Ni), and $Ta_4SiTe_4 \rightarrow Ta_4ZTe_4$ (Z = Cr, Fe, Co, Ni).[15,35] Attempts to synthesize Ta analogues of $Nb_4Pd_{0.5}ZSb_2$ have thus far been unsuccessful.

Electronic Structure. Band structure calculations for both $Nb_4Pd_{0.5}FeSb_2$ and $Nb_4Pd_{0.5}SiSb_2$ were carried out, but as the conclusions are generally similar, we present

detailed results for only the former. In these intermetallic compounds where electronegativity differences are small, a bonding description involving full transfer of electrons from one component to another is probably quite unrealistic. By analogy with V_4SiSb_2 or Ti_4FeBi_2,[9] one might begin with an improbable formulation such as "$(Nb^{3+})_4(Pd^0)_{0.5}(Fe^{6-})(Sb^{3-})_2$" for which the main insight would be that substantial metal-metal bonding must arise from the presence of such an electron-rich metal centre as Fe^{6-}.

The density of states (DOS) plot for $Nb_4Pd_{0.5}FeSb_2$ is shown in Figure 6-3. As expected for this metal-rich compound, the Fermi level at −10.08 eV falls in a region of high DOS. The DOS around the Fermi level is dominated by Nb 4d states (Figure 6-3a). Most of the Pd 4d states are found below the Fermi level (Figure 6-3b), supporting their crude description above as zero-valent Pd. Although the Fe 3d states are spread over a wide energy range and their contribution at the Fermi level is still substantial (Figure 6-3c), a large proportion is localized between −11 and −14 eV. The Sb 5p states lie mostly below the Fermi level (and the 5s states are even lower) (Figure 6-3d).

As in most polar intermetallic compounds, metal-metalloid bonding interactions are strong and optimized in $Nb_4Pd_{0.5}FeSb_2$: the Mulliken overlap population (MOP) is calculated to be 0.31 for the Nb–Sb bonds and 0.26 for the Pd–Sb bonds. However, as the analysis of the DOS above suggests, it is the strength of homo- and heteroatomic metal-metal bonds involving Nb and Fe atoms that will play the key role in determining the stability of the structure. The crystal orbital overlap population (COOP) curves for Nb–Nb, Nb–Fe, and Fe–Fe interactions in $Nb_4Pd_{0.5}FeSb_2$ are plotted in Figure 6-4. For the Nb–Nb interactions, most bonding levels are occupied, indicating fairly strong Nb–Nb bonding (MOP = 0.19) (Figure 6-4a). The intercolumn Nb–Nb contact of 3.1448(16)

Å is significant (MOP = 0.21), showing that it plays an important role in holding adjacent $^{1}_{\infty}[Nb_{8/2}Z]$ columns together. The Nb–Fe bonding interactions are almost optimized with all bonding states and only a small portion of antibonding states being occupied (MOP = 0.24) (Figure 6-4b). The Fe–Fe COOP curve displays features characteristic of a one-dimensional chain of bonded metal atoms (d_{Fe-Fe} = 2.4772(1) Å) (Figure 6-4c). Interactions involving d_{z^2}–d_{z^2} σ-overlap result in bonding states around –13 eV, which are occupied, and antibonding states around –9.5 eV, which remain unoccupied. Interactions involving d_{xz}–d_{xz} and d_{yz}–d_{yz} π-overlap give rise to bonding levels near –13 eV and antibonding levels near –11.5 eV, both of which are occupied. The overlap population calculated for the 2.4772(1) Å Fe–Fe contact is 0.13, about one-third of the MOP expected for an Fe–Fe single bond.[10]

The electronic structure of $Nb_4Pd_{0.5}SiSb_2$ resembles that of $Nb_4Pd_{0.5}FeSb_2$, except that without any contributing d orbitals from the interstitial Si atom, the DOS near the Fermi level is dominated almost entirely by Nb 4d states and the Si–Si bonds must arise from overlap of sp hybrid orbitals. The 2.4817(2) Å Si–Si contact has an MOP of 0.40, also about one-third of the theoretically maximum MOP expected for a Si–Si bond within a chain, and somewhat stronger than the even shorter Si–Si bonds (2.35–2.45 Å) in Ta_4SiTe_4 (MOP = 0.280).[36]

There are some interesting anomalies in the trends in the composition and structure of $Nb_4Pd_{0.5}ZSb_2$ upon substitution with different interstitial atoms *Z*. The mixing of Si into the interstitial site in $Nb_4Pd_{0.5}Cr_{0.28}Si_{0.72}Sb_2$ is not restricted to Cr; analogous compounds in which Si is mixed with the other transition metals Fe, Co, and Ni can be easily prepared, and indeed improved crystallization is promoted when the

reactions are performed in silica tubes! It is likely that the interstitial *Z*–*Z* distance of ~2.48–2.50 Å remains relatively inflexible, a manifestation of a matrix effect imposed by having to satisfy geometrical requirements to optimize Nb–Nb and Nb–Sb bonding in $Nb_4Pd_{0.5}ZSb_2$ foremost, similar to what has been proposed for the short Si–Si bonds in V_4SiSb_2. Although it is difficult to compare strengths of bonds of different types, we suggest that the host structure would then prefer to accomodate the main-group element rather than a transition metal to form stronger Si–Si bonds (involving overlap of s and p orbitals) than metal-metal bonds (involving overlap of d orbitals). The ideal Cr–Cr distance in a hypothetical all-Cr compound may be on the verge of exceeding that accessible by the host structure. The longest *Z*–*Z* distance found in structures containing square antiprismatic $^{1}_{\infty}[M_{8/2}Z]$ columns without any mixing of *Z* occurring is ~2.49 Å. Compounds that are stabilized by differential fractional site occupancy (DFSO) such as $Hf_{10}M_xSb_{6-x}$ have significantly longer *Z*–*Z* distances (~2.8 Å) where *Z* is a mixture of *M* and Sb.[33]

Unlike the other members, $Nb_4Pd_{0.5}Ni_{0.78}Sb_2$ is substoichiometric in the *Z* site. Assuming a rigid band model, the addition of electrons to $Nb_4Pd_{0.5}ZSb_2$ on progressing to the right along the first-row transition metals raises the Fermi level. Although this strengthens Nb–Nb bonding (Figure 6-4a), it weakens Nb–*Z* and *Z*–*Z* bonding through the occupation of antibonding levels (Figures 6-4b, c). Correspondingly, the Nb-Ni and Ni–Ni distances are longer than expected in $Nb_4Pd_{0.5}Ni_{0.78}Sb_2$ (Table 6-3). The predictions are not perfect (the Nb–Nb distances are actually longer), but the occurrence of the Ni substoichiometry represents an alternative to tolerating further bond distortions.

The absence of a Mn-containing member, "$Nb_4Pd_{0.5}MnSb_2$," is curious, but it

should be noted that the Nb_4ZTe_4 and Ta_4ZTe_4 series also lack this member.[35] (Trace amounts of Mn (< 3%) mixed in with a larger proportion of Si (~11%) were noted in a few small crystals found in some reactions, but as this is near the detection limit of EDX analysis, the verdict remains unclear.)

As expected from the band structure, $Nb_4Pd_{0.5}SiSb_2$ displays metallic behaviour with the resistivity decreasing linearly with temperature ($\rho_{300} = 2.2 \times 10^{-3}$ Ω cm; $\rho_2 = 0.87 \times 10^{-3}$ Ω cm) until it levels off to its residual value below ~25 K (Figure 6-5). The absolute resistivities are somewhat high for a metal, probably an effect of grain boundaries present in the pressed pellet sample.

The $Nb_4Pd_{0.5}ZSb_2$ series expands on the rich structural chemistry of the pnictides, showing that cluster-type extended structures need not be limited to the chalcogenides and halides. The insertion of Pd into the V_4SiSb_2-type structure instead of more electropositive atoms such as Li or Na, as proposed previously,[10] is perhaps surprising, but understandable in view of the need to form covalent bonds of low polarity in an intermetallic structure. As illustrated by the wide range of *Z* atoms that can be substituted in the $Nb_4Pd_{0.5}ZSb_2$ series, interstitial chemistry provides yet another tool in the solid-state chemist's repertoire for imparting stability and flexibility in extended structures.

Table 6-1. Crystallographic Data for $Nb_4Pd_{0.5}ZSb_2$ (Z = Cr, Fe, Co, Ni, Si)

Formula	$Nb_4Pd_{0.5}Cr_{0.28}Si_{0.72}Sb_2$	$Nb_4Pd_{0.5}FeSb_2$	$Nb_4Pd_{0.5}CoSb_2$	$Nb_4Pd_{0.5}Ni_{0.78}Sb_2$	$Nb_4Pd_{0.5}SiSb_2$
Formula mass (amu)	703.11	724.19	727.27	713.88	696.43
Space group	D_{4h}^{18}–*I*4/*mcm* (No. 140)	D_{4h}^{18}–*I*4/*mcm* (No. 140)	D_{4h}^{18}–*I*4/*mcm* (No. 140)	D_{4h}^{18}–*I*4/*mcm* (No. 140)	D_{4h}^{18}–*I*4/*mcm* (No. 140)
a (Å) [a]	10.4407(3)	10.4825(6)	10.4603(5)	10.4332(7)	10.3895(10)
c (Å) [a]	5.0020(2)	4.9543(3)	4.9457(3)	4.9649(3)	4.9634(4)
V (Å^3)	545.26(3)	544.39(6)	541.15(5)	540.44(6)	535.76(8)
Z	4	4	4	4	4
T (°C)	22	22	22	22	22
Diffractometer	Bruker PLATFORM/SMART–1000 CCD				
ρ_{calc} (g cm^{-3})	8.564	8.836	8.927	8.773	8.634
Crystal dimensions (mm)	Needle, 0.108 × 0.042 × 0.042	Needle, 0.120 × 0.028 × 0.026	Needle, 0.110 × 0.026 × 0.026	Needle, 0.046 × 0.005 × 0.005	Needle, 0.146 × 0.014 × 0.014
Radiation	Graphite-monochromated Mo $K\alpha$, λ = 0.71073 Å				
μ(Mo $K\alpha$) (cm^{-1})	200.28	219.18	224.34	221.20	198.97
Transmission factors [b]	0.260–0.477	0.235–0.589	0.252–0.590	0.692–0.899	0.391–0.773

Table 6-1. Crystallographic Data for $Nb_4Pd_{0.5}ZSb_2$ (Z = Cr, Fe, Co, Ni, Si) (continued)

Scan type			ω scans (0.2°)		
2θ limits	5° ≤ 2θ(Mo $K\alpha$) ≤ 66°	5° ≤ 2θ(Mo $K\alpha$) ≤ 66°	5° ≤ 2θ(Mo $K\alpha$) ≤ 66°	5° ≤ 2θ(Mo $K\alpha$) ≤ 66°	5° ≤ 2θ(Mo $K\alpha$) ≤ 53°
Data collected	$-15 \le h \le 15$, $-14 \le k \le 15$, $-7 \le l \le 7$	$-11 \le h \le 15$, $-13 \le k \le 15$, $-7 \le l \le 7$	$-15 \le h \le 14$, $-13 \le k \le 15$, $-7 \le l \le 7$	$-15 \le h \le 15$, $-15 \le k \le 12$, $-7 \le l \le 7$	$-12 \le h \le 12$, $-12 \le k \le 12$, $-6 \le l \le 6$
No. of data collected	3081	1977	2087	2228	1621
No. of unique data, including $F_o^2 < 0$	294 (R_{int} = 0.042)	294 (R_{int} = 0.053)	293 (R_{int} = 0.043)	293 (R_{int} = 0.087)	168 (R_{int} = 0.171)
No. of unique data, with $F_o^2 > 2\sigma(F_o^2)$	291	266	263	216	120
No. of variables [c]	18	16	16	17	16
$R(F)$ for $F_o^2 > 2\sigma(F_o^2)$ [d]	0.031	0.035	0.030	0.034	0.040
$R_w(F_o^2)$ [e]	0.075	0.086	0.077	0.075	0.091
Goodness of fit [f]	1.273	1.157	1.180	0.940	0.971
$\Delta\rho_{max}$, $\Delta\rho_{min}$ (e Å^{-3})	2.25, −1.36	2.78, −1.68	2.20, −2.04	2.60, −1.99	2.18, −2.71

[a] Obtained from a refinement constrained so that $a = b$ and $\alpha = \beta = \gamma = 90°$.

Table 6-1. Crystallographic Data for $Nb_4Pd_{0.5}ZSb_2$ (Z = Cr, Fe, Co, Ni, Si) (continued)

[b] A numerical face-indexed absorption correction was applied, with the use of programs in the SHELXTL package (Sheldrick, G. M. *SHELXTL Version 5.1*; Bruker Analytical X-ray Systems: Madison, WI, 1997).

[c] Including an extinction coefficient.

[d] $R(F) = \sum \left| |F_o| - |F_c| \right| / \sum |F_o|$.

[e] $R_w(F_o^2) = \left[\sum \left[w(F_o^2 - F_c^2)^2\right] / \sum wF_o^4\right]^{1/2}$; $w^{-1} = \left[\sigma^2(F_o^2) + (aP)^2 + bP\right]$ where $P = \left[\max(F_o^2, 0) + 2F_c^2\right]/3$. For $Nb_4Pd_{0.5}Cr_{0.28}Si_{0.72}Sb_2$, a = 0.0302 and b = 23.7359; for $Nb_4Pd_{0.5}FeSb_2$, a = 0.0437 and b = 17.0051; for $Nb_4Pd_{0.5}CoSb_2$, a = 0.0439 and b = 5.3596; for $Nb_4Pd_{0.5}Ni_{0.78}Sb_2$, a = 0.0383 and b = 0.0000; for $Nb_4Pd_{0.5}SiSb_2$, a = 0.0441 and b = 0.0000.

[f] $GooF = \left[\sum \left[w(F_o^2 - F_c^2)^2\right] / (n - p)\right]^{1/2}$ where n is the number of reflections and p is the total number of parameters refined.

Table 6-2. Positional and Equivalent Isotropic Displacement Parameters for $Nb_4Pd_{0.5}ZSb_2$ (Z = Cr, Fe, Co, Ni, Si)

Atom	Wyckoff position	x	y	z	U_{eq} (Å^2) [a]
		$Nb_4Pd_{0.5}Cr_{0.28(3)}Si_{0.72}Sb_2$			
Nb	16*k*	0.08161(6)	0.20758(6)	0	0.0066(2)
Pd [b]	4*b*	0	½	¼	0.0100(4)
Z [c]	4*a*	0	0	¼	0.0083(10)
Sb	8*h*	0.15137(5)	0.65137(5)	0	0.0149(3)
		$Nb_4Pd_{0.5}FeSb_2$			
Nb	16*k*	0.08130(7)	0.20657(7)	0	0.0066(3)
Pd [b]	4*b*	0	½	¼	0.0082(5)
Fe	4*a*	0	0	¼	0.0104(5)
Sb	8*h*	0.15123(6)	0.65123(6)	0	0.0138(3)
		$Nb_4Pd_{0.5}CoSb_2$			
Nb	16*k*	0.08072(6)	0.20643(6)	0	0.0076(2)
Pd [b]	4*b*	0	½	¼	0.0094(4)
Co	4*a*	0	0	¼	0.0078(4)
Sb	8*h*	0.15145(5)	0.65145(5)	0	0.0148(3)
		$Nb_4Pd_{0.5}Ni_{0.78(1)}Sb_2$			
Nb	16*k*	0.08182(10)	0.20813(9)	0	0.0046(3)
Pd [b]	4*b*	0	½	¼	0.0079(7)

Table 6-2. Positional and Equivalent Isotropic Displacement Parameters for $Nb_4Pd_{0.5}ZSb_2$ (Z = Cr, Fe, Co, Ni, Si) (continued)

Ni [d]	4*a*	0	0	¼	0.0042(10)
Sb	8*h*	0.15079(7)	0.65079(7)	0	0.0120(3)
			$Nb_4Pd_{0.5}SiSb_2$		
Nb	16*k*	0.0811(2)	0.2073(2)	0	0.0080(7)
Pd [b]	4*b*	0	½	¼	0.0067(15)
Si	4*a*	0	0	¼	0.006(3)
Sb	8*h*	0.15241(14)	0.65241(14)	0	0.0136(8)

[a] U_{eq} is defined as one-third of the trace of the orthogonalized $\mathbf{U}_{ij}$ tensor.

[b] 50% occupancy.

[c] 28(3)% Cr and 72% Si.

[d] 78(1)% occupancy.

Table 6-3. Selected Interatomic Distances (Å) for $Nb_4Pd_{0.5}ZSb_2$ (Z = Cr, Fe, Co, Ni, Si)

	$Nb_4Pd_{0.5}Cr_{0.28}Si_{0.72}Sb_2$	$Nb_4Pd_{0.5}FeSb_2$	$Nb_4Pd_{0.5}CoSb_2$	$Nb_4Pd_{0.5}Ni_{0.78}Sb_2$	$Nb_4Pd_{0.5}SiSb_2$
Nb–Z	2.6433(6) (×2)	2.6361(7) (×2)	2.6276(6) (×2)	2.6429(9) (×2)	2.624(2) (×2)
Nb–Sb	2.8435(7)	2.8571(8)	2.8474(7)	2.8384(10)	2.830(2)
	2.8490(10)	2.8632(11)	2.8600(9)	2.8531(13)	2.827(3)
	2.9924(4) (×2)	2.9826(5) (×2)	2.9786(4) (×2)	2.9744(6) (×2)	2.972(1) (×2)
Nb–Nb	3.0264(8) (×2)	3.0069(9) (×2)	2.9944(7) (×2)	3.0129(12) (×2)	3.000(3) (×2)
	3.1169(8) (×2)	3.0960(9) (×2)	3.0941(8) (×2)	3.1042(12) (×2)	3.098(3) (×2)
	3.1127(13)	3.1448(16)	3.1487(13)	3.099(2)	3.109(4)
	3.2934(9) (×2)	3.2909(11) (×2)	3.2789(9) (×2)	3.2997(14) (×2)	3.270(3) (×2)
Pd–Sb	2.5611(7) (×4)	2.5612(8) (×4)	2.5589(7) (×4)	2.5477(10) (×4)	2.560(2) (×4)
Z–Z	2.5010(1) (×2)	2.4772(1) (×2)	2.4728(1) (×2)	2.4824(1) (×2)	2.4817(2) (×2)

Table 6-4. Extended Hückel Parameters

atom	orbital	H_{ii} (eV)	ζ_{i1}	c_1	ζ_{i2}	c_2
Nb	5s	−9.04	1.89			
	5p	−5.13	1.85			
	4d	−9.94	4.08	0.6401	1.64	0.5516
Pd	5s	−7.51	2.19			
	5p	−3.86	2.15			
	4d	−12.53	5.98	0.55	2.61	0.67
Fe	4s	−8.40	1.90			
	4p	−5.00	1.90			
	3d	−12.2	5.35	0.5505	2.00	0.6815
Si	3s	−17.3	1.383			
	3p	−9.2	1.383			
Sb	5s	−18.8	2.323			
	5p	−11.7	1.999			

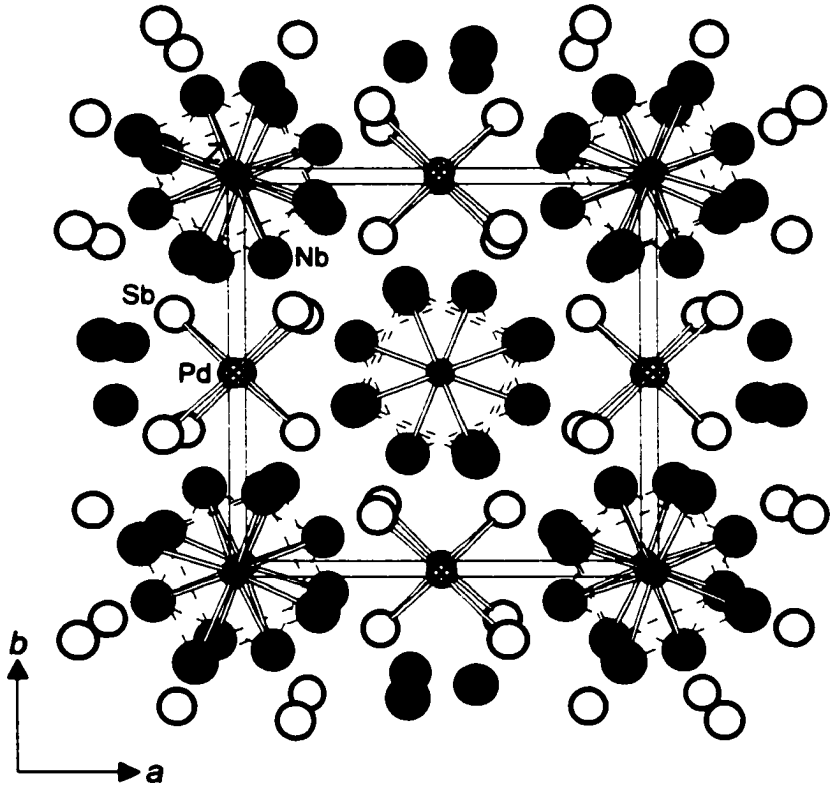

Figure 6-1. Structure of $Nb_4Pd_{0.5}ZSb_2$ (Z = Cr, Fe, Co, Ni, Si) viewed in projection down the c axis. The large lightly shaded circles are Nb atoms, the medium solid circles are Z atoms, the hatched circles are Pd atoms, and the open circles are Sb atoms.

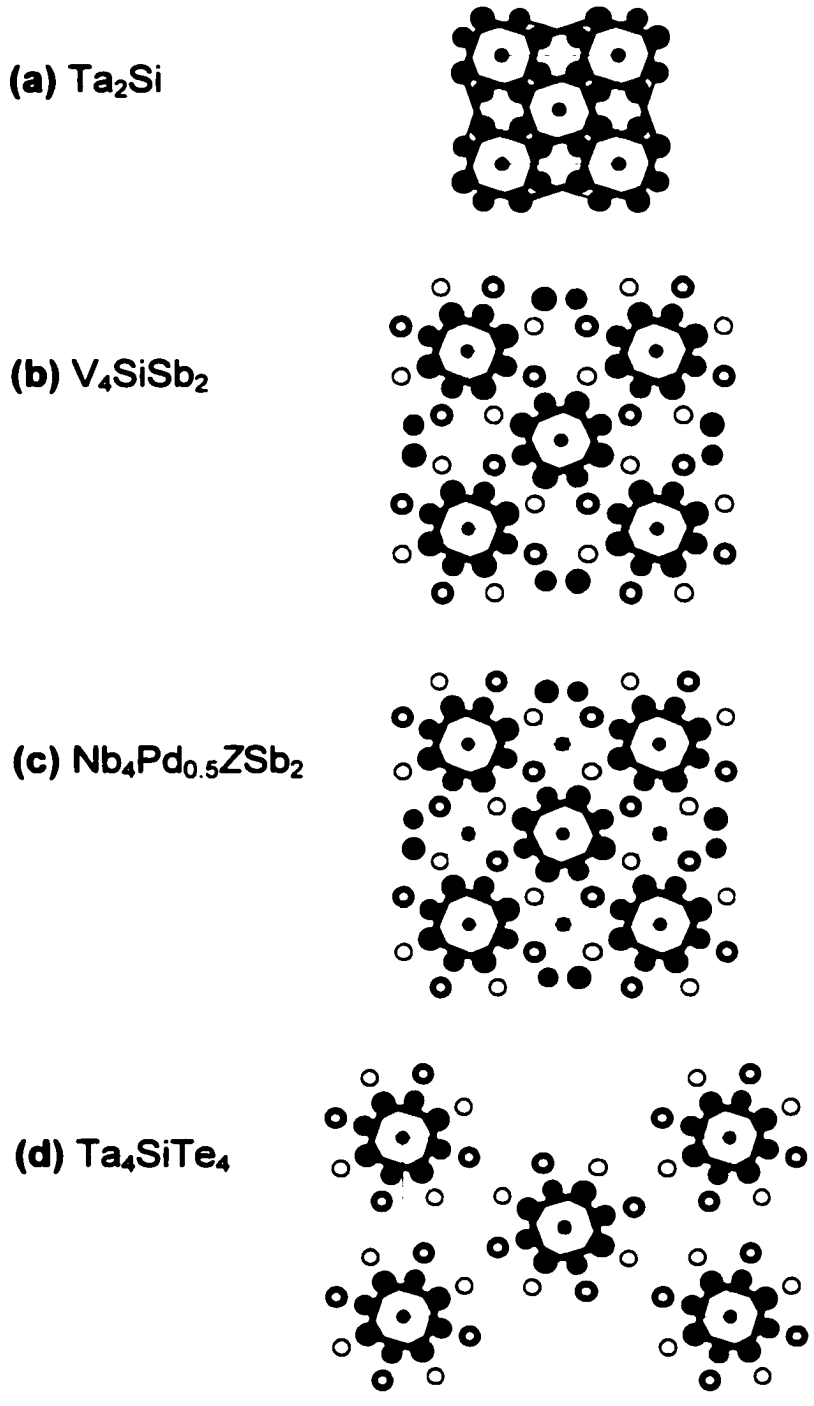

Figure 6-2. Comparison of the structures of (a) Ta_2Si, (b) V_4SiSb_2, (c) $Nb_4Pd_{0.5}ZSb_2$ (Z = Cr, Fe, Co, Ni, Si) and (d) Ta_4SiTe_4, in terms of one-dimensional columns of face-sharing Si- (or other Z-) filled square antiprisms, shown in projection down the c axis. Light and heavy lines indicate a displacement by ½ the repeat along the projection axis.

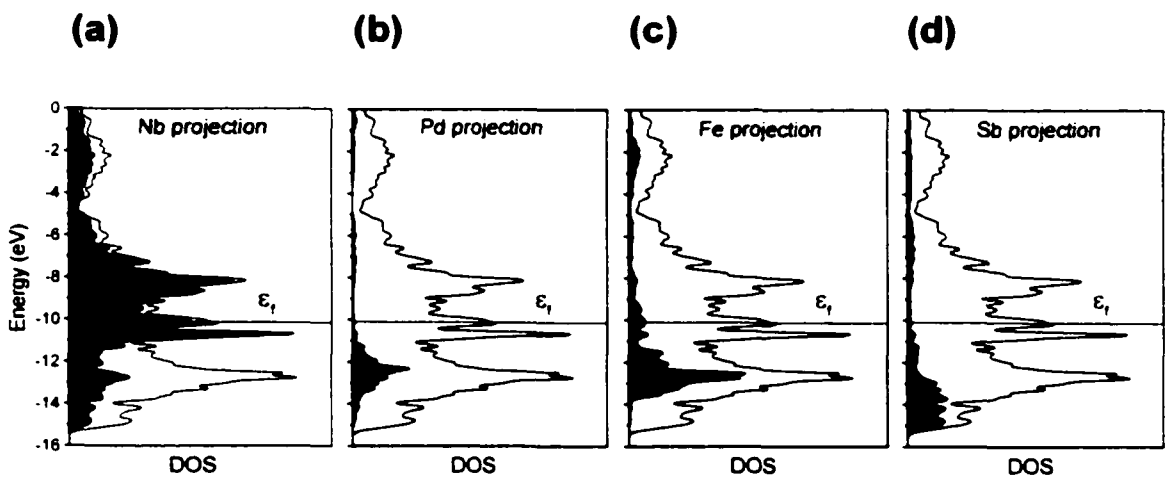

Figure 6-3. Contributions of (a) Nb, (b) Pd, (c) Fe, and (d) Sb (shaded regions) to the total density of states (DOS) (line) for $Nb_4Pd_{0.5}FeSb_2$. The Fermi level, ε_f, is at −10.08 eV.

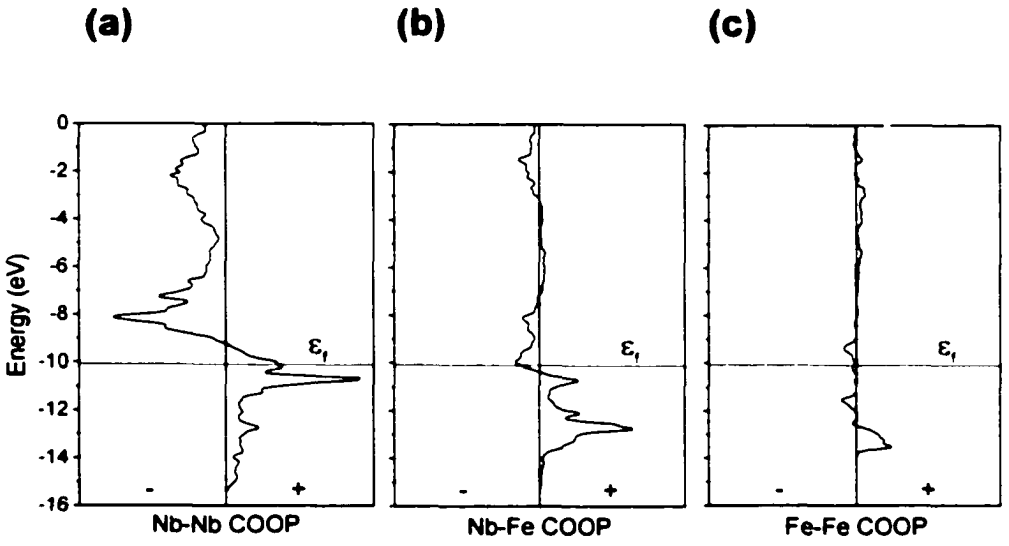

Figure 6-4. Crystal orbital overlap population (COOP) curves for (a) Nb–Nb, (b) Nb–Fe, and (c) Fe–Fe interactions, within the range of distances listed in Table 3, in $Nb_4Pd_{0.5}FeSb_2$.

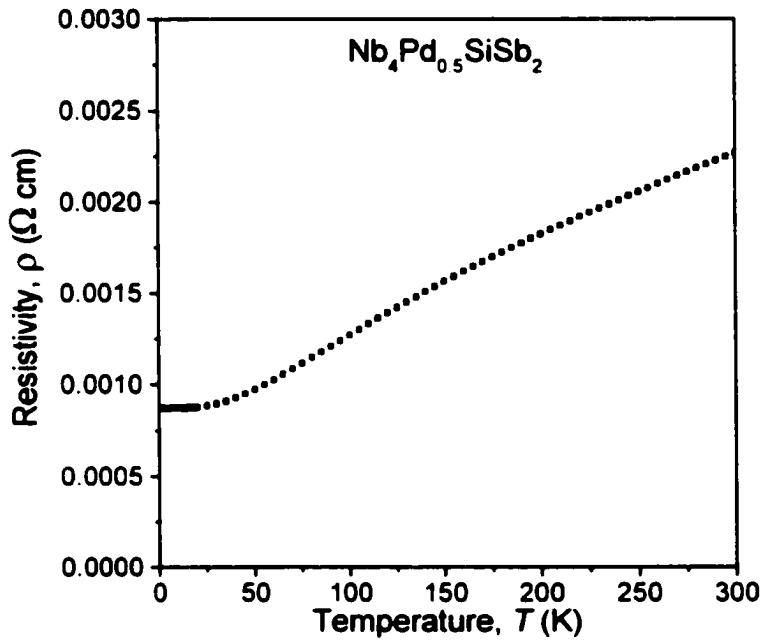

Figure 6-5. Temperature dependence of the resistivity of a pressed pellet of $Nb_4Pd_{0.5}SiSb_2$.

References

(1) (a) *Clusters and Colloids*; Schmid, G., Ed.; Wiley–VCH: Weinheim, 1994. (b) Simon, A. *Angew. Chem., Int. Ed. Engl.* **1988**, *27*, 159.

(2) Corbett, J. D.; Garcia, E.; Kwon, Y.-U.; Guloy, A. *Pure Appl. Chem.* **1990**, *62*, 103.

(3) Corbett, J. D. *J. Alloys Compd.* **1995**, *229*, 10.

(4) Hughbanks, T. *J. Alloys Compd.* **1995**, *229*, 40.

(5) Tremel, W.; Kleinke, H.; Derstroff, V.; Reisner, C. *J. Alloys Compd.* **1995**, *219*, 73.

(6) Garcia, E.; Corbett, J. D. *Inorg. Chem.* **1990**, *29*, 3274.

(7) Melnyk, G.; Bauer, E.; Rogl, P.; Skolozdra, R.; Seidl, E. *J. Alloys Compd.* **2000**, *296*, 235.

(8) Wollesen, P.; Jeitschko, W. *J. Alloys Compd.* **1996**, *243*, 67.

(9) Richter, C. G.; Jeitschko, W.; Künnen, B.; Gerdes, M. H. *J. Solid State Chem.* **1997**, *133*, 400.

(10) Rytz, R.; Hoffmann, R. *Inorg. Chem.* **1999**, *38*, 1609.

(11) Wang, M.; McDonald, R.; Mar, A. *Inorg. Chem.* **2000**, *39*, 4936.

(12) Wang, M.; McDonald, R.; Mar, A. *Inorg. Chem.* **1999**, *38*, 3435.

(13) Wang, M.; Mar, A. *J. Solid State Chem.* In press.

(14) Aronsson, B. *Acta Chem. Scand.* **1955**, *9*, 1107.

(15) Badding, M. E.; DiSalvo, F. J. *Inorg. Chem.* **1990**, *29*, 3952.

(16) Sheldrick, G. M. SHELXTL, version 5.1; Bruker Analytical X-ray Systems, Inc.: Madison, WI, 1997.

(17) *International Tables for X-ray Crystallography*; Wilson, A. J. C., Ed.; Kluwer: Dordrecht, The Netherlands, 1992; Vol. C.

(18) Pauling, L. *The Nature of the Chemical Bond*, 3rd ed.; Cornell University Press: Ithaca, NY, 1960.

(19) Donohue, J. *The Structures of the Elements*; Wiley: New York, 1974.

(20) Gelato, L. M.; Parthé, E. *J. Appl. Crystallogr.* **1987**, *20*, 139.

(21) Whangbo, M.-H.; Hoffmann, R. *J. Am. Chem. Soc.* **1978**, *100*, 6093.

(22) Hoffmann, R. *Solids and Surfaces: A Chemist's View of Bonding in Extended Structures*; VCH Publishers: New York, 1988.

(23) Raman, A. *Z. Metallkd.* **1996**, *57*, 301.

(24) Parthé, E.; Lux, B.; Nowotny, H. *Monatsh. Chem.* **1955**, *86*, 859.

(25) Kubiak, R.; Horyn, R.; Broda, H.; Lukaszewicz, K. *Bull. Acad. Pol. Sci., Ser. Sci. Chim.* **1972**, *20*, 429.

(26) Wopersnow, W.; Schubert, K. *J. Less-Common Met.* **1976**, *48*, 79.

(27) (a) Furuseth, S.; Kjekshus, A. *Acta Crystallogr.* **1965**, *18*, 320. (b) Rehr, A.; Kauzlarich, S. M. *Acta Crystallogr., Sect. C: Cryst. Struct. Commun.* **1994**, *50*, 1177.

(28) Furuseth, S.; Kjekshus, A. *Acta Chem. Scand.* **1964**, *18*, 1180.

(29) Havinga, E. E.; Damsma, H.; Hokkeling, P. *J. Less-Common Met.* **1972**, *27*, 169.

(30) Bradtmöller, S.; Kremer, R. K.; Böttcher, P. *Z. Anorg. Allg. Chem.* **1994**, *620*, 1073.

(31) Villars, P. *Pearson's Handbook, Desk Edition*; ASM International: Materials Park, OH, 1997.

(32) Kwon, Y.-U.; Sevov, S. C.; Corbett, J. D. *Chem. Mater.* **1990**, *2*, 550.

(33) Kleinke, H.; Ruckert, C.; Felser, C. *Eur. J. Inorg. Chem.* **2000**, 315.

(34) Gladyshevskii, E. I.; Kuz'ma, Yu. B. *J. Struct. Chem. (Engl. Transl.)* **1965**, *6*, 60.

(35) (a) Badding, M. E.; Gitzendanner, R. L.; Ziebarth, R. P.; DiSalvo, F. J. *Mater. Res. Bull.* **1994**, *29*, 327. (b) Ahn, K.; Hughbanks, T.; Rathnayaka, K. D. D.; Naugle, D. G. *Chem. Mater.* **1994**, *6*, 418. (c) Neuhausen, J.; Finckh, E. W.; Tremel, W. *Chem. Ber.* **1995**, *128*, 569.

(36) Li, J.; Hoffmann, R.; Badding, M. E.; DiSalvo, F. J. *Inorg. Chem.* **1990**, *29*, 3943.

Chapter 7

Conclusion

Several new ternary transition metal pnictides containing group 10 elements (Ni, Pd, Pt) have been synthesized and characterized: $Zr_3Pd_4P_3$, $Hf_3Pd_4P_3$, $Nb_5Pd_4P_4$;[1] $Nb_5Pd_4As_4$;[2] Nb_9PdAs_7;[3] HfPdSb;[1] $Zr_3Ni_3Sb_4$, $Hf_3Ni_3Sb_4$, $Zr_3Pt_3Sb_4$;[4] and $Nb_{28}Ni_{33.5}Sb_{12.5}$.[5] Some of them are the first examples in their ternary systems, and some of them adopt new structure types. All of them are metal-rich phases whose structures contain no pnicogen–pnicogen bonding contacts. This work also represents the first concerted efforts to extend the relatively well studied early transition metal–Ni–pnicogen systems to the much more poorly investigated Pd and Pt systems. The compounds $Nb_4Pd_{0.5}ZSb_2$ (Z = Cr, Fe, Co, Ni, Si) represent the first examples of quaternary antimonides containing three transition metals in an ordered arrangement.[6] All compounds are metallic based on resistivity measurements or predictions from band structure calculations except for $Zr_3Ni_3Sb_4$ (or $Hf_3Ni_3Sb_4$, $Zr_3Pt_3Sb_4$), which is predicted to be a small band-gap semiconductor from its band structure. Detailed conclusions for individual compounds have been presented in previous chapters. More general conclusions to draw out common themes related to most of these compounds are presented here.

Synthesis and Crystal Growth

Despite the impression that elementary inorganic textbooks may give, many solid state compounds have rather complicated structures, so that single crystal X-ray structure determination is a crucial technique to characterize and identify new phases in products. After the crystal structures are determined and with a knowledge of the correct compositions of compounds, attempts can be made to prepare the desired phases by either direct reactions or arc-melting reactions. How a single crystal can be grown in the first place is a necessary hurdle that every solid state chemist must clear in order to characterize products properly, especially in the course of exploratory chemistry. Although crystal growth is often regarded as an artform, some general trends in the preparation of pnictides were noted throughout our investigations. The crystal growth conditions for some new pnictides are summarized in **1**. For the phosphides, suitably sized single crystals are typically formed on the surface of or inside arc-melted balls. Although these crystals are vulnerable to have more defects and disorder problems owing to the rapid cooldown inherent in the arc-melting method, they are often good enough to

Compounds	Crystal growth conditions
$Zr_3Pd_4P_3$	arc-melting ZrP + 2Pd
$Hf_3Pd_4P_3$	arc-melting 3HfP + 4Pd
$Nb_5Pd_4P_4$	arc-melting NbP + 2Pd
Nb_9PdAs_7	I_2 reaction 9Nb + Pd + 7As
$RECu_{1+x}As_2$	I_2 reactions *RE* + Cu + 2As
$Zr_3Ni_3Sb_4$	anneal arc-melted sample Zr + 2Ni +4.5Sb
$Nb_{28}Ni_{33.5}Sb_{12.5}$	I_2 reaction of arc-melted sample Nb + 6Ni +2$NbSb_2$
$Nb_4Pd_{0.5}ZSb_2$	direct reactions in silica tubes 4Nb + 0.5Pd + *Z* + 2Sb

1

give satisfactory results in structure refinement. The structure determinations of the three phosphides presented in Chapter 2 are examples. If the problems of defects and disorder are serious, annealing arc-melted products at about 800 °C is a way to improve the quality of crystals. For the arsenides, simple chemical transport reactions in the presence of trace amounts of I_2 can give better crystals, although the single crystals of Nb_9PdAs_7 and $RECu_{1+x}As_2$ (RE = La, Ce, Pr; see Appendix B for details)[7] can be obtained by other routes. For the antimonides, matters become more complicated. Single crystals of $Zr_3Ni_3Sb_4$ were obtained by annealing an arc-melted sample in a Ta tube under argon at 1000 °C for 5 days. Single crystals of $Nb_{28}Ni_{33.5}Sb_{12.5}$ were grown by a chemical transport reaction in the presence of I_2 of an arc-melted sample. Direct reactions in silica tubes did give single crystals for the $Nb_4Pd_{0.5}ZSb_2$ (Z = Cr, Fe, Co, Ni, Si) family of compounds, but they are very small and some of them have sizes that challenge the detection limits of modern diffractometers, even those equipped with advanced CCD area detectors. However, on the basis of research in transition metal pnictides in other groups, a general method to grow single crystals of pnictides is to anneal arc-melted samples at about 1500 °C for several hours in an induction furnace (instrumentation currently unavailable in our laboratory).[8] These crystals are usually small, but large enough for X-ray crystal structure determination. Thus, to generalize, the crystal growth of new transition metal pnictides seems to require arc-melting in the phosphides, chemical transport by I_2 in the arsenides, and extended annealing in the antimonides. Although these conclusions are only based on a handful of examples, they may be helpful to newcomers in the area.

Group 10 "Intercalation" Chemistry?

All compounds discussed in Chapters 2 to 6 contain group 10 elements (Ni, Pd, Pt). Although their structures are quite diverse, it is interesting to note that most of them can be related to simpler host structures through a "stuffing" or "intercalation" operation, as summarized here. If all or some of the group 10 atoms are removed from the ternary or quaternary structures, the substructures left are themselves known structure types, or closely related to them (**2, 3, 4, 5**).

After the tetragonal prismatically coordinated Pd atoms are removed from $Zr_3Pd_4P_3$, the underlying "$Zr_3Pd_3P_3$" substructure can be related to the ZrPdSb structure (Co_2Si-type),[9] **2**, which is an extremely common structure type, and is adopted by more than 350 binary and ternary compounds.[10] The difference between ZrPdSb and the hypothetical "$Zr_3Pd_3P_3$" substructure is the manner in which the two-dimensional sheets composed of pnicogen-centred trigonal prisms are corrugated.

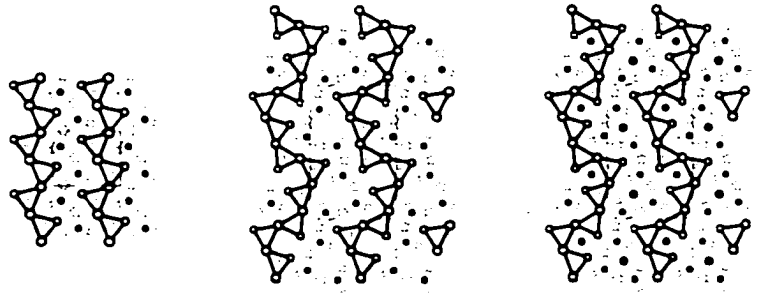

ZrPdSb **"$Zr_3Pd_3P_3$" + Pd** → **$Zr_3Pd_4P_3$**

2

If one-dimensional Pd_4 tetrahedral chains are removed from the $Nb_5Pd_4P_4$ structure, the remaining substructure "Nb_5P_4" will contain empty channels along the *c* direction of the unit cell (**3**). This may look strange, but in fact the rare Ti_5Te_4-type structure has this arrangement.[11] In total, there are about 12 compounds adopting this

structure type.[10] Both Nb_5Sb_4 [12] and Ta_5Sb_4 [13] adopt the Ti_5Te_4-type structure. In contrast to what people thought earlier, a single crystal X-ray structure determination shows that there are no Sb–Sb bonds straddling the Sb channels in Ta_5Sb_4.[13b]

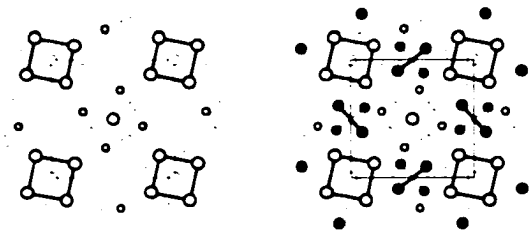

"Nb_5P_4" + Pd_4 → $Nb_5Pd_4P_4$
Nb_5Sb_4

3

Similar empty channels also exist in U_6Mn-type[14] or V_4SiSb_2-type[15] structures, which are adopted by about 17 compounds.[10] Sb–Sb bonds also do not occur in V_4SiSb_2. $Nb_4Pd_{0.5}FeSb_2$ is a stuffed version of the V_4SiSb_2-type structure in which some palladium atoms are inserted into the Sb channels (**4**).

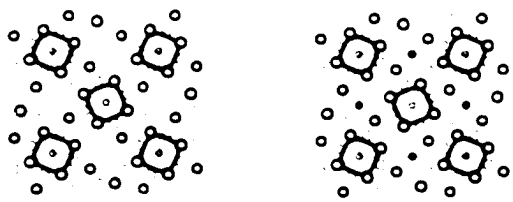

"Nb_4FeSb_2" + 0.5Pd → $Nb_4Pd_{0.5}FeSb_2$
V_4SiSb_2

4

$Zr_3Ni_3Sb_4$ joins the ranks of more than 40 other ternary compounds that have the $Y_3Au_3Sb_4$-type structure.[16,10] If all Ni atoms are removed from $Zr_3Ni_3Sb_4$, the substructure "Zr_3Sb_4" has the Th_3P_4-type arrangement,[17] which is another very common structure type with more than 200 representatives (**5**).[10]

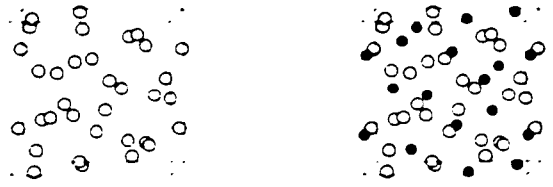

"Zr_3Sb_4" + 3Ni → $Zr_3Ni_3Sb_4$
Th_3P_4

5

To summarize, the recurring pattern seems to be that the group 10 elements can "intercalate" or "stuff" into host structures to give new intermetallic compounds. Our band structure calculations confirm that these elements retain approximately a d^{10} configuration in the ternary or quaternary compounds. This suggests that electronic factors such as crystal field effects will be less significant than steric factors, enabling group 10 atoms to readily enter host structures where the availability of empty sites permits. This generalization holds quite well for Pd, but seems less applicable for Ni. It also provides us a way to design new structures or compounds based on old ones. However, interestingly enough, none of the substructures, "$Zr_3Pd_3P_3$", "Nb_5P_4", "Nb_4FeSb_2", and "Zr_3Sb_4", have been made so far (perhaps they may not even exist), although numerous compounds with identical or similar structures are known. These limitations temper our claim to be able to "design" or "predict" new compounds, a fact well appreciated by solid state chemists.

It is worth mentioning that binary group 10 pnictides are special in showing somewhat different structural chemistry from the other late transition metal pnictides. In particular, binary group 10 pnictides show much more extensive metal-rich chemistry. Many of these group 10 metal-rich phases have unique structures which are not seen in those of other late transition metal or early transition metal pnictides. Binary palladium pnictides (we constrain our discussion to P, As, and Sb) will be considered here as

examples to illustrate some points. Three pnicogen-rich compounds in four phases (PdP_3 ($CoAs_3$-type),[18] $PdAs_2$ (FeS_2-type),[19] $PdSb_2$ (FeS_2-type and NiSSb-type)[19,20] are not unusual. These are common structures for late transition metal pnictides in general. There are 13 palladium-rich compounds in 14 phases. Various amounts of Pd can be incorporated into different phases with palladium-to-pnicogen ratios ranging from 2 to 7.5. Some examples are Pd_2As (2),[21] Pd_7P_3 (2.33),[22] Pd_5Sb_2 (2.5),[23] Pd_8Sb_3 (2.67),[24] $Pd_{20}Sb_7$ (2.86),[25] Pd_3P (3),[26] Pd_9P_2 (4.5),[27] Pd_5As (5),[28] Pd_6P (6),[29] and $Pd_{15}P_2$ (7.5).[30] Most of these structures are eigentypes or exist only in binary group 10 compounds. For example, Pd_5Sb_2 (Ni_5As_2-type) has a complicated structure in a hexagonal cell with irregular coordination for all atoms. This structure is so unique that it is difficult to find any relationship with other structures. Palladium exhibits broad flexibility by fitting in different coordination geometries and structures in these binary pnictides, consistent with our earlier claim that Pd or other group 10 elements may be good candidates to "intercalate" into host structures.

Directions

Most compounds presented in Chapters 2 to 6 are the first examples of the corresponding ternary system, especially for the heavier group 10 elements (Pd, Pt). Our studies have barely touched the surface of a very rich chemistry. When one considers the fascinating compounds found in the binary transition metal-rich pnictides, there should be equally interesting examples expected in the ternary systems. More investigations are needed to discover them. Those compounds would be stabilized by (E-*TM*)–group 10 interactions, and the possible structures may be new and unique owing to the ability of Pd

(or other group 10 elements) to fit into different structural matrices. This exploratory research can be directed towards improvement of crystal growth methods and further development of the idea of group 10 "intercalation." The structural and bonding principles derived from examination of these ternary transition metal-rich pnictides can also help us to develop the chemistry of ternary rare earth (Sc, Y, and lanthanide)-rich pnictides, which remains largely unexplored.[31] The historical evolution has seen extensive research in ternary rare earth-rich halides in the 1980's,[32] progress in new rare earth-rich chalcogenides more recently,[33] and only today have we begun to embark on the long march toward discovering new pnictides.

References

(1) Wang, M.; McDonald, R.; Mar, A. *Inorg. Chem.* **2000**, *39*, 4936.

(2) Wang, M.; Mar, A. Unpublished results.

(3) Wang, M.; Mar, A. *Inorg. Chem.* In press.

(4) Wang, M.; McDonald, R.; Mar, A. *Inorg. Chem.* **1999**, *38*, 3435.

(5) Wang, M.; Mar, A. *J. Solid State Chem.* In press.

(6) Wang, M.; Sheets, W. C.; McDonald, R.; Mar, A. *Inorg. Chem.* In press.

(7) Wang, M.; McDonald, R.; Mar, A. *J. Solid State Chem.* **1999**, *147*, 140.

(8) (a) Marking, G. A.; Franzen, H. F. *Chem. Mater.* **1993**, *5*, 678. (b) Kleinke, H.; Franzen, H. F. *J. Am. Chem. Soc.* **1997**, *119*, 12824.

(9) Geller, S. *Acta Crystallogr.* **1955**, *8*, 83.

(10) Villars, P. *Pearson's Handbook, Desk Edition*; ASM International: Materials Park, OH, 1997.

(11) Grønvold, F.; Kjekshus, A.; Raaum, F. *Acta Crystallogr.* **1961**, *14*, 930.

(12) Furuseth, S.; Kjekshus, A. *Acta Chem. Scand.* **1964**, *18*, 1180.

(13) (a) Furuseth, S.; Selte, K.; Kjekshus, A. *Acta Chem. Scand.* **1965**, *19*, 95. (b) Kang, S. K.; Miller, G. J. *Acta Crystallogr., Sect. C: Cryst. Struct. Commun.* **1999**, *55*, 483.

(14) Baenziger, N. C.; Rundle, R. E.; Snow, A. I.; Wilson, A. S. *Acta Crystallogr.* **1950**, *3*, 34.

(15) Wollesen, P.; Jeitschko, W. *J. Alloys Compd.* **1996**, *243*, 67.

(16) Dwight, A. E. *Acta Crystallogr. Sect. B: Struct. Crystallogr. Cryst. Chem.* **1977**, *33*, 1579.

(17) Meisel, K. *Z. Anorg. Allg. Chem.* **1939**, *240*, 300.

(18) Rundqvist, S. *Nature (London)* **1960**, *185*, 31.

(19) Brese, N. E.; von Schnering, H. G. *Z. Anorg. Allg. Chem.* **1994**, *620*, 393.

(20) Kim, W.-S.; Chao, G. Y. *Can. Mineral.* **1991**, *29*, 401.

(21) (a) Bälz, U.; Schubert, K. *J. Less-Common Met.* **1969**, *19*, 300. (b) Schubert, K.; Frank, K.; Gohle, R.; Maldonado, A.; Meissner, H. G.; Raman, A.; Rossteutscher, W. *Naturwissen.* **1963**, *50*, 41.

(22) Matkovic, T.; Schubert, K. *J. Less-Common Met.* **1977**, *55*, 177.

(23) El-Boragy, M.; Bhan, S.; Schubert, K. *J. Less-Common Met.* **1970**, *22*, 445.

(24) (a) Wopersnow, W.; Schubert, K. *J. Less-Common Met.* **1976**, *48*, 79. (b) Man, L. I.; Imamov, R. M. *Sov. Phys. Crystallogr. (Engl. Transl.)* **1979**, *24*, 365.

(25) Wopersnow, W.; Schubert, K. *J. Less-Common Met.* **1977**, *51*, 35.

(26) Andersson, Y.; Rundqvist, S.; Tellgren, R.; Thomas, J. O.; Flanagan, T. B. *J. Solid State Chem.* **1980**, *32*, 321.

(27) Sellberg, B. *Acta Chem. Scand.* **1966**, *20*, 2179.

(28) Matkovic, T.; Schubert, K. *J. Less-Common Met.* **1978**, *58*, P1.

(29) (a) Andersson, Y.; Kaewchansilp, V.; del Rosario Casteleiro Soto, M.; Rundqvist, S. *Acta Chem. Scand., Ser. A* **1974**, *28*, 797. (b) Andersson, Y.; Rundqvist, S.; Tellgren, R.; Thomas, J. O.; Flanagan, T. B. *Acta Crystallogr., Sect. B: Struct. Crystallogr. Cryst. Chem.* **1981**, *37*, 1965.

(30) Andersson, Y. *Acta Chem. Scand., Ser. A* **1977**, *31*, 354.

(31) Known rare earth-rich transition metal pnictides: (a) RE_5M_2Pn (RE = Gd, Tb, Dy, Ho, Er, Tm, Lu; M = Ni, Pd; Pn = Sb, Bi): Mozharivskyj, Yu.; Franzen, H. F. *J.*

Solid State Chem. **2000**, *152*, 478. (b) RE_5CuBi_3 (*RE* = La, Ce, Pr, Nd, Gd, Tb): Hohnke, D.; Parthé, E. *J. Less-Common Met.* **1969**, *17*, 291.

(32) Simon, A.; Mattausch, Hj.; Miller, G. J.; Bauhofer, W.; Kremer, R. K. In *Handbook on the Physics and Chemistry of Rare Earths*; Gschneidner, K. A., Jr.; Eyring, L., Eds.; Elservier: Amsterdam, 1991; Vol. 15; p 191.

(33) (a) $Sc_5Ni_2Te_2$: Maggard, P. A.; Corbett, J. D. *Inorg. Chem.* **1999**, *38*, 1945. (b) Sc_6MTe_2 (*M* = Mn, Fe, Co, Ni): Maggard, P. A.; Corbett, J. D. *Inorg. Chem.* **2000**, *39*, 4143. (c) Dy_6MTe_2 (*M* = Fe, Co, Ni): Bestaoui, N.; Henle, P. S.; Corbett, J. D. *J. Solid State Chem.* **2000**, *155*, 9. (d) $Y_5M_2Te_2$ (*M* = Fe, Co, Ni), Sc_6PdTe_2: Maggard, P. A.; Corbett, J. D. *J. Am. Chem. Soc.* **2000**, *122*, 10740. (e) $Er_7Ni_2Te_2$: Meng, F.; Hughbanks, T. *Inorg. Chem.* **2001**, *40*, 2482.

Appendix A

The Ternary Silicide $ZrPd_3Si_3$, a Stacking Variant of the α-$FeSi_2$ and Re_3B Structure Types †

Introduction

Metal silicides are valued for their hardness, chemical inertness, and refractory properties, and are involved in applications such as steel production and integrated circuit technology.[1] Many ternary silicides are known, often containing a rare-earth metal or an early transition metal as one component and a late transition metal as another component.[2,3] In systems involving an element from the Group 4 triad (Ti, Zr, Hf) and another from the Group 10 triad (Ni, Pd, Pt), there exist an impressive number of ternary nickel silicides with diverse crystal structures,[4] but surprisingly few palladium or platinum silicides.[5] Of the latter, only the equiatomic phases TiPdSi, ZrPdSi, HfPdSi, ZrPtSi, and HfPtSi are known,[5] all adopting the Co_2Si-type structure.[6] Difficulties in the crystal growth of silicides typically hinder their structural characterization, especially those adopting structure types unrelated to simple ones, and recent efforts in the use of fluxes by others may alleviate this problem.[7] We report here the fortuitous discovery and subsequent rational preparation of $ZrPd_3Si_3$ at high temperature. The novel structure of

† A version of this chapter has been published. Wang, M.; Mar, A. *Chem. Mater.* **1999**, *11*, 3232. Copyright 1999 American Chemical Society.

this compound implies an interesting bonding situation, which is analyzed with the aid of band structure calculations.

Experimental Section

Synthesis. Reagents used were elemental powders of zirconium (99.7%, Cerac), palladium (99.95%, Cerac), silicon (99.96%, Cerac), and antimony (99.995%, Aldrich). $ZrPd_3Si_3$ was originally identified as a side product from a reaction of a 3:3:4 ratio of elemental zirconium, palladium, and antimony in an evacuated silica tube heated at 1000°C for 3 days, in an attempt to prepare an analogue of $Zr_3Ni_3Sb_4$.[8] On the walls of the tube were found a few black plate-shaped crystals, which were confirmed to contain Zr, Pd, and Si according to an EDX (energy-dispersive X-ray) analysis on a Hitachi S-2700 scanning electron microscope. (Anal. 14(1)% Zr, 45(2)% Pd, 41(2)% Si. Calc. 14% Zr, 43% Pd, 43% Si.) Evidently the incorporation of silicon resulted from an attack of the silica tube at the high temperature used. One of these crystals was selected for the structure determination.

With a knowledge of the correct composition, the ternary silicide was subsequently prepared in a rational manner. A 0.25-g mixture of zirconium, palladium, and silicon in a 1:3:3 ratio was pressed into a pellet, which was then melted twice in a Centorr 5TA tri-arc furnace under argon (gettered by melting a titanium pellet). With a few grains of I_2 added, the product of the arc-melting reaction was annealed in a two-zone furnace at 950/900°C for four days. The X-ray powder pattern, obtained on an Enraf-Nonius FR552 Guinier camera (Cu $K\alpha_1$ radiation; Si standard), revealed the presence of $ZrPd_3Si_3$, PdSi,[9] and trace amounts of an unidentified impurity. The cell

parameters of $ZrPd_3Si_3$, refined with the use of the program POLSQ,[10] are: a = 3.805(1), b = 15.515(5), c = 7.022(2) Å, and V = 414.5(2) Å^3. The observed and calculated interplaner distances and intensities are listed in Table C-8. It appears that $ZrPd_3Si_3$ is a metastable phase, since a similar reaction at 950°C of the elements placed in a niobium tube but in the absence of I_2 results only in the formation of the equiatomic phase ZrPdSi [5(b)] as well as Pd_2Si.[11] Attempts to substitute Hf for Zr and Ni or Pt for Pd were unsuccessful under a variety of conditions.

Structure Determination. Weissenberg photography revealed Laue symmetry *mmm* and confirmed the singularity of a crystal selected for data collection. Intensity data were obtained at room temperature with the θ–2θ scan technique in the range 5° ≤ 2θ(Mo $K\alpha$) ≤ 70° on an Enraf-Nonius CAD-4 diffractometer. Crystal data and further details of the data collection are given in Table A-1 and the CIF. Calculations were carried out with the use of the SHELXTL (Version 5.1) package.[12] Conventional atomic scattering factors and anomalous dispersion corrections were used.[13] Intensity data were processed and face-indexed absorption corrections were applied in XPREP. Of the possible space groups consistent with the orthorhombic symmetry and systematic absences observed in the intensity data ($Cmc2_1$, $C2cm$, $Cmcm$), the centrosymmetric space group $Cmcm$ was chosen on the basis of the successful structure solution and refinement. Initial positions of all atoms were found by direct methods, and the structure was refined by least-squares methods. Refinements on occupancy factors confirm that all sites are fully occupied. The atomic parameters were standardized with STRUCTURE TIDY.[14] The final cycle of least-squares refinement on F_o^2 of 26 variables (including anisotropic displacement parameters and an isotropic extinction parameter) and 496

averaged reflections (including those having $F_o^2 < 0$) converged to values of $R_w(F_o^2)$ of 0.047 and $R(F)$ (for $F_o^2 > 2\sigma(F_o^2)$) of 0.023. The final difference electron density map is featureless ($\Delta\rho_{max}$ = 2.15; $\Delta\rho_{min}$ = –2.42 e Å^{-3}). Final values of the positional and equivalent isotropic displacement parameters are given in Table A-2. Selected bond distances are listed in Table A-3. Anisotropic displacement parameters are listed in Table C-9.

Electrical Resistivity. A single crystal of dimensions 0.5 x 0.1 x 0.1 mm, verified to be $ZrPd_3Si_3$ by EDX analysis, was mounted in a four-probe configuration for an ac resistivity measurement between 25 and 290 K. This measurement gives the resistivity along the crystallographic *a* axis.

Band Structure. A three-dimensional tight-binding extended Hückel band structure calculation was performed using the EHMACC suite of programs.[15,16] The weighted Wolfsberg-Helmholz formula for the off-diagonal Hamiltonian matrix elements was employed.[17] The atomic parameters used are listed in Table A-4. Properties were extracted from the band structure using 96 *k*-points in the irreducible portion of the Brillouin zone.

Results and Discussion

Structure and Structural Relationships. Although the structure of $ZrPd_3Si_3$ is three-dimensional in nature, it will be helpful to partition it into component slabs or layers. Figure A-1 shows the structure, viewed along the *a* axis, as being built up from three kinds of metal-centered coordination polyhedra whose vertices are the Si atoms. Pd(1) is coordinated in a square pyramidal geometry to two Si(1) atoms at 2.4744(9) Å

and two Si(2) atoms at 2.5447(8) Å forming the base, and to a Si(2) atom at 2.515(1) Å forming the apex. Pd(2) is coordinated tetrahedrally to two Si(1) and two Si(2) atoms at 2.395(1) and 2.470(1) Å, respectively, at the expected angles (100.78(7)–111.84(6)°). The Pd square pyramids and tetrahedra share their corners and edges to form a slab aligned parallel to the *ac* plane. These slabs, stacked along the long *b* axis, are joined together through pairing of the Si(1) atoms. The Zr atoms are then positioned in an unusual distorted cubic coordination environment with four short (2.778(1) Å) and four long (2.914(1) Å) distances to the Si(1) atoms.

An alternative description, shown in Figure A-2(a), emphasizes the relationship of $ZrPd_3Si_3$ to two simpler structure types adopted by binary silicides. Here, $^{3}_{\infty}[ZrPd_3Si_3]$ can be partitioned into slabs of composition $^{2}_{\infty}[ZrSi_2]$ and $^{2}_{\infty}[Pd_3Si]$ which are stacked in an alternating fashion along *b*. Although $ZrSi_2$ itself does not adopt this structure,[18] the slab $^{2}_{\infty}[ZrSi_2]$ occurs in the rare α-$FeSi_2$ structure type.[19] It is built up by placing metal atoms in half of the interstices of a cubic array of Si atoms (and may thus be regarded as the cubic analogue of the more familiar hexagonal $Cd(OH)_2$ structure).[20] Similarly, the slab $^{2}_{\infty}[Pd_3Si]$ occurs in the Re_3B structure type.[21] In $^{2}_{\infty}[Pd_3Si]$, the Si atoms reside at the centers of Pd_6 trigonal prisms which share their triangular faces to form infinite columns. Adjacent columns are shifted half the height of a trigonal prism with respect to each other so that Si atoms achieve a bicapped trigonal prismatic coordination and the columns are linked together. Pd_3Si [22] itself adopts the Fe_3C structure type,[23] which differs from the Re_3B structure type mainly in the way in which the trigonal prisms are linked.[20] Indeed, trigonal prisms of metal atoms are a common feature in many intermetallic compounds and occur not only in Pd_3Si but also in other binary palladium silicides such as Pd_2Si.[11]

Neither $ZrPd_3Si_3$ nor the parent α-$FeSi_2$ and Re_3B structures are themselves layered compounds in the usual sense because strong bonding is present along the stacking direction.

Partitioning the $ZrPd_3Si_3$ structure into component slabs exposes its connection to the closely related $Li_2Ce_2Ge_3$ structure (Figure A-2(b)).[24] A Re_3B-type slab also occurs in the $Li_2Ce_2Ge_3$ structure, but the vertices in the trigonal prisms are made up of two kinds of atoms, Li and Ce(2). Ge_2 pairs in the intervening slabs are tilted in opposite directions in $Li_2Ce_2Ge_3$ relative to those of the Si_2 pairs in $ZrPd_3Si_3$. Equivalently, the α-$FeSi_2$-like slab is translated half a unit cell edge along *c* in $Li_2Ce_2Ge_3$ compared to $ZrPd_3Si_3$. Lastly, whereas the Zr atoms in $ZrPd_3Si_3$ are located at the centers of cubes formed by eight Si(1) atoms, the corresponding Ce(1) atoms in $Li_2Ce_2Ge_3$ are drastically shifted along *b*. This distortion places the Ge(2) atoms at the centers of trigonal prisms formed by four Ce(1) and two Ce(2) atoms. For this reason, the more natural description for the $Li_2Ce_2Ge_3$ structure that appears in the literature is as a combination of Re_3B- and AlB_2-type slabs.[24]

Bonding. Examination of the interatomic distances (Table A-3) shows that while the Zr–Si and Pd–Si bonds in $ZrPd_3Si_3$ are normal (*cf.*, 2.682–3.057 Å in $ZrSi_2$ [18] and 2.347–2.564 Å in Pd_3Si,[22] respectively), the distinguishing feature is the short distance of 2.340(2) Å within the Si(1)–Si(1) pair. This is essentially identical to the distances found in similar pairs in MNiSi$_3$ (M = Sm, Y) (~2.34 Å)[7(a)] and to that in elemental Si (2.3517 Å).[25] At first glance, the electronic distribution in $ZrPd_3Si_3$ seems to be straightforward. Applying Zintl's concept, we assume that Zr, being the most electropositive component, transfers all its valence electrons to become Zr^{+4}. Since Si(1) forms a homonuclear bond

with itself and Si(2) does not, the appropriate oxidation numbers are $Si(1)^{-3}$ and $Si(2)^{-4}$. This implies an assignment of +2 for the Pd atoms, resulting in the formulation $(Zr^{+4})(Pd^{+2})_3(Si(1)^{-3})_2(Si(2)^{-4})$. Two observations suggest that the electronic distribution is not as simple as this. First, it is Pd, not Si, that is the most electronegative component in this system (Pauling electronegativities Zr 1.4, Pd 2.2, Si 1.8).[26] Thus, unlike typical Zintl compounds, electron transfer should occur from the nonmetal, Si, to the metal, Pd. As has been discussed recently, the conventional electron counting scheme fails to give a realistic picture in cases like these.[27] Second, some of the Zr–Zr, Zr–Pd, and Pd–Pd distances suggest the existence of an extensive metal-metal bonding network within the $ZrPd_3Si_3$ structure. For instance, the Pd(1)–Pd(1) distance forming the base of the isosceles triangles of the Pd_6 trigonal prisms is 2.768(1) Å, only slightly longer than that found in elemental Pd (2.7506 Å).[25]

To interpret the bonding in $ZrPd_3Si_3$ in more detail, a semi-empirical band structure calculation was carried out. Reflecting the reversal in electronegativity of the metal and nonmetal, the atomic Si 3p levels start off higher in energy than the Pd 4d levels (see the Hückel parameters used in Table A-4). The density of states (DOS) curve (Figure A-3) reveals substantial covalent mixing of Zr, Pd, and Si states. Near the Fermi level ($\varepsilon_f = -8.9$ eV), all three elements make equally significant contributions to the DOS. Above the Fermi level, the unfilled states have their major contribution from Zr 4d orbitals, so that electropositive Zr has transferred some of its electrons to the rest of the structure. The narrow peak from −11.0 to −14.0 eV located well below the Fermi level represents filled states composed almost entirely of Pd 4d character. With all its 4d orbitals fully occupied, it would appear that Pd has a configuration of d^{10} (in accordance

with the modified electron counting scheme used in such instances involving weakly electronegative ligands)[27,28] and is either neutral or possibly even negatively charged. Consistent with all these expectations, the calculated charges are +0.144 for Zr, –0.372 for Pd, and +0.324 for Si.

Bonding within $ZrPd_3Si_3$ is highly covalent, and while metal-nonmetal (Zr–Si, Pd–Si) interactions provide the major source of its stability, metal-metal (Zr–Zr, Zr–Pd, Pd–Pd) and nonmetal-nonmetal (Si–Si) interactions play an important role as well. Mulliken overlap populations (MOP) were determined for various contacts in $ZrPd_3Si_3$ to gauge the strength of these interactions and are listed in Table A-3. The Zr–Si and Pd–Si interactions account for most of the bonding energy, the average MOP being 0.276 and 0.223, respectively. (For comparison, 2.738–2.868 Å Zr–Si bonds have an average MOP of 0.276 in ZrSi,[18] and 2.4485–2.5710 Å bonds Pd–Si bonds have an average MOP of 0.230 in PdSi.[9])[29] As shown in the crystal orbital overlap population (COOP) curves, the Zr–Si bonding levels are nearly completely filled up to the Fermi level (Figure A-4(a)), while there remain some Pd–Si bonding levels above the Fermi level (Figure A-4(b)). Although Pd–Si bonding has not been maximized in this structure, this is more than compensated by the formation of metal-metal and nonmetal-nonmetal bonds.

The Pd–Pd, Zr–Pd, Zr–Zr, and Si–Si interactions in $ZrPd_3Si_3$ are not negligible. For the Pd(1)–Pd(1) contact alluded to earlier, the filling of metal-metal bonding levels (–13 eV) is nearly cancelled by the filling of metal-metal antibonding levels (–12 eV) (Figure A-4(c)). If these levels were entirely of d character, the d^{10}–d^{10} interaction would be repulsive. However, there is mixing of Pd 5s and 5p states which stabilizes the bonding levels sufficiently that the Pd(1)–Pd(1) interaction is net bonding (the

configuration of Pd(1) determined from a Mulliken population analysis is $4d^{9.65}$ $5s^{0.36}$ $5p^{0.34}$).[30] The small but positive MOP of 0.030 for this 2.768(1) Å Pd–Pd distance is comparable to that found in elemental (fcc) Pd [25] (2.7506 Å, MOP 0.045).[29] Analysis of the other Pd–Pd contacts (~2.9 Å) gives similar results and suggests weak metal-metal bonding. With electron-rich Pd atoms close to Zr atoms, further metal-metal bonding occurs, as shown by the filling of bonding levels in the COOP curve (Figure A-4(d)) for the Zr–Pd(2) contact of 2.9917(8) Å, with an MOP of 0.110. The longer Zr–Pd(1) distances of 3.217(1) and 3.3149(9) Å also correspond to slightly positive MOPs of 0.047 and 0.041, respectively. Although the Zr-Zr distance of 3.530(1) Å is quite long (*cf.* 3.1793–3.2318 Å in elemental Zr),[25] the MOP of 0.104 and the COOP curve (Figure A-4(e)) imply weak bonding.

The Si(1)–Si(1) pair is confirmed to be a strong homonuclear single bond resulting from overlap of mostly p and some s orbitals. Not all of the bonding levels are occupied (Figure A-4(f)), and the MOP of 0.685 is somewhat smaller than those found in MNiSi$_3$ (M = Sm, Y) (MOP 0.827)[7(a)] and elemental Si (MOP 0.85),[25,29] despite similar bond lengths of ~2.35 Å. Although Figure A-2(a) has been drawn to emphasize the Si(1)–Si(1) pairs, there are two longer Si–Si distances that could be interrogated for bonding, given that weak bonding is implicated even at 2.8 Å in MNiSi$_3$ (M = Sm, Y). The cubic array of Si atoms is distorted so that the Si$_2$ pairs forming the sides are tilted. The shortest distance between these pairs is 3.055(2) Å, corresponding to an MOP of 0.186. The distance from a Si(1) atom in these pairs to an isolated Si(2) atom is 2.969(2) Å, corresponding to an MOP of 0.258. These are substantial bonds that cannot be neglected. Indeed, the 3.055(2) Å bond that straddles adjacent Si$_2$ pairs excludes the

possibility that the apparent cavity above and below the Zr atoms could be occupied by additional atoms.

Consistent with the weakly metallic behaviour observed in $ZrPd_3Si_3$ (Figure A-5), the band structure shows no energy gap and only a low DOS at the Fermi level (Figure A-3). Although the resistivity measurement gives only the component along the *a* direction, $ZrPd_3Si_3$ is predicted to be a three-dimensional metal since bands are crossed in all directions in the band dispersion diagrams. Band dispersion curves along special symmetry directions are shown in Figure A-6.

It is interesting to note that in the Zr–Si and especially the Pd–Si COOP curves, there remain some available bonding levels above the Fermi level (Figures A-4(a) and (b)). The structure may thus be amenable to accepting more electrons, at the expense of weakening the homoatomic metal-metal and nonmetal-nonmetal bonds, suggesting that compounds such as "$NbPd_3Si_3$" may be feasible targets. However, given that both metal-metal and nonmetal-nonmetal bonding provide important contributions to the stability of $ZrPd_3Si_3$, it is perhaps not surprising that even the obvious congeneric substitutions (Zr/Hf, Ni/Pd/Pt) may not be so straightforward and have thus far failed.

Table A-1. Crystallographic Data for $ZrPd_3Si_3$

Formula	$ZrPd_3Si_3$
Formula mass (amu)	494.69
Space group	D_{2h}^{17} – *Cmcm* (No. 63)
a (Å)	3.8127(4) Å [a]
b (Å)	15.551(1) Å [a]
c (Å)	7.0390(5) Å [a]
V (Å^3)	417.35(6)
Z	4
T (°C)	22
Diffractometer	Enraf-Nonius CAD4
ρ_{calc} (g cm^{-3})	7.873
Crystal dimensions (mm)	Plate 0.16 × 0.07 × 0.01
Radiation	Graphite-monochromated Mo *K*α, λ = 0.71073 Å
μ(Mo *K*α) (cm^{-1})	157.95
Transmission factors [b]	0.373–0.802
Scan type	θ–2θ
Scan speed (deg. min^{-1})	1.67
Scan range (deg.)	0.60 + 0.344 tanθ
2θ limits	5° ≤ 2θ(Mo *K*α) ≤ 70°
Data collected	$-6 \le h \le 6$, $-24 \le k \le 24$, $-11 \le l \le 11$
No. of data collected	3576
No. of unique data, including $F_o^2 < 0$	543 (R_{int} = 0.069)

Table A-1. Crystallographic Data for $ZrPd_3Si_3$ (continued)

No. of unique data, with $F_o^2 > 2\sigma(F_o^2)$	496
No. of variables [c]	26
$R(F)$ for $F_o^2 > 2\sigma(F_o^2)$ [d]	0.023
$R_w(F_o^2)$ [e]	0.047
Goodness of fit [f]	1.189
$\Delta\rho_{max}$, $\Delta\rho_{min}$ (e Å^{-3})	2.15, −2.43

[a] Obtained from a refinement constrained so that $\alpha = \beta = \gamma = 90°$.

[b] A numerical face-indexed absorption correction was applied, with the use of programs in the SHELXTL package (Sheldrick, G. M. *SHELXTL Version 5.1*; Bruker Analytical X-ray Systems: Madison, WI, 1997).

[c] Including an extinction coefficient.

[d] $R(F) = \sum \left| |F_o| - |F_c| \right| / \sum |F_o|$.

[e] $R_w(F_o^2) = \left[\sum \left[w(F_o^2 - F_c^2)^2\right] / \sum wF_o^4\right]^{1/2}$; $w^{-1} = \left[\sigma^2(F_o^2) + (0.0185P)^2 + 0.0000P\right]$ where $P = \left[\max(F_o^2, 0) + 2F_c^2\right]/3$.

[f] $GooF = \left[\sum \left[w(F_o^2 - F_c^2)^2\right] / (n-p)\right]^{1/2}$ where n is the number of reflections and p is the total number of parameters refined.

Table A-2. Positional and Equivalent Isotropic Thermal Parameters ($Å^2$) for $ZrPd_3Si_3$

atom	Wyckoff position	*x*	*y*	*z*	U_{eq} [a]
Zr	4c	0	0.01166(3)	1/4	0.0056(1)
Pd(1)	8f	0	0.17553(2)	0.55292(4)	0.0068(1)
Pd(2)	4c	0	0.66047(3)	1/4	0.0066(1)
Si(1)	8f	0	0.42602(7)	0.03248(16)	0.0070(2)
Si(2)	4c	0	0.26196(11)	1/4	0.0073(3)

[a] U_{eq} is defined as one-third of the trace of the orthogonalized $\mathbf{U}_{ij}$ tensor.

Table A-3. Selected Interatomic Distances (Å) and Mulliken Overlap Populations (MOP) for $ZrPd_3Si_3$

	Distance (Å) [a]	MOP
Metal-nonmetal		
Zr–Si(1)	2.778(1) (x4)	0.309
Zr–Si(1)	2.914(1) (x4)	0.243
Pd(1)–Si(1)	2.4744(9) (x2)	0.200
Pd(1)–Si(2)	2.515(1)	0.228
Pd(1)–Si(2)	2.5447(8) (x2)	0.213
Pd(2)–Si(1)	2.395(1) (x2)	0.251
Pd(2)–Si(2)	2.470(1) (x2)	0.257
Metal-metal		
Pd(1)–Pd(1)	2.768(1)	0.030
Pd(1)–Pd(1)	3.0841(8) (x2)	0.009
Pd(1)–Pd(2)	2.8633(6) (x2)	0.023
Pd(1)–Pd(2)	2.8964(9)	0.022
Zr–Pd(1)	3.217(1) (x2)	0.047
Zr–Pd(1)	3.3149(9) (x2)	0.041
Zr–Pd(2)	2.9917(8) (x2)	0.110
Zr–Zr	3.530(1) (x2)	0.104
Nonmetal-nonmetal		
Si(1)–Si(1)	2.340(2)	0.685
Si(1)–Si(1)	3.055(2)	0.186
Si(1)–Si(2)	2.969(2)	0.258

[a] Interatomic distances were calculated based on the cell parameters refined from X-ray powder diffraction data.

Table A-4. Extended Hückel Parameters

atom	orbital	H_{ii} (eV)	ξ_{i1}	c_1	ξ_{i2}	c_2
Zr	5s	−8.52	1.82			
	5p	−4.92	1.78			
	4d	−8.63	3.84	0.6213	1.510	0.5798
Pd	5s	−7.51	2.19			
	5p	−3.86	2.15			
	4d	−12.53	5.98	0.55	2.61	0.67
Si	3s	−17.3	1.383			
	3p	−9.2	1.383			

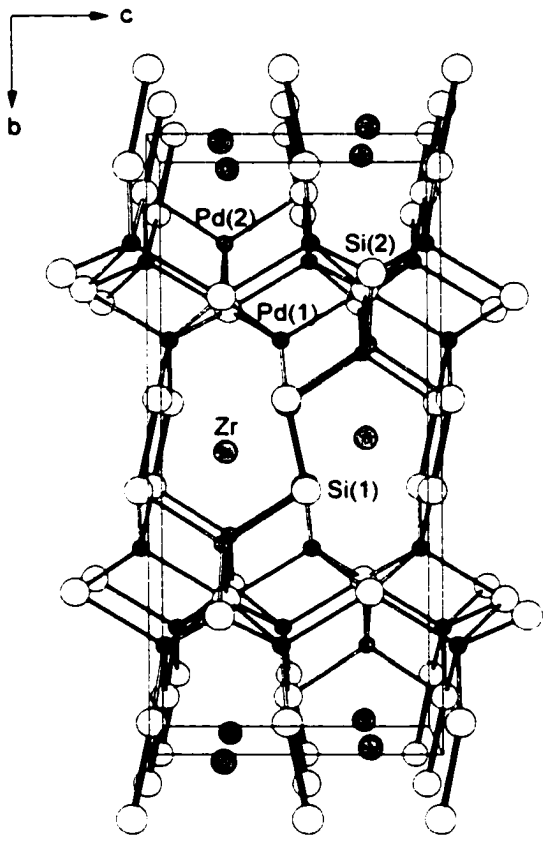

Figure A-1. View of $ZrPd_3Si_3$ along the *a* axis showing the unit cell outline and the labeling scheme. The medium lightly-shaded circles are Zr atoms, the small solid circles are Pd atoms, and the large open circles are Si atoms. The metal-centered coordination polyhedra are emphasized: Pd(1) square pyramid, Pd(2) tetrahedron, and Zr distorted cube.

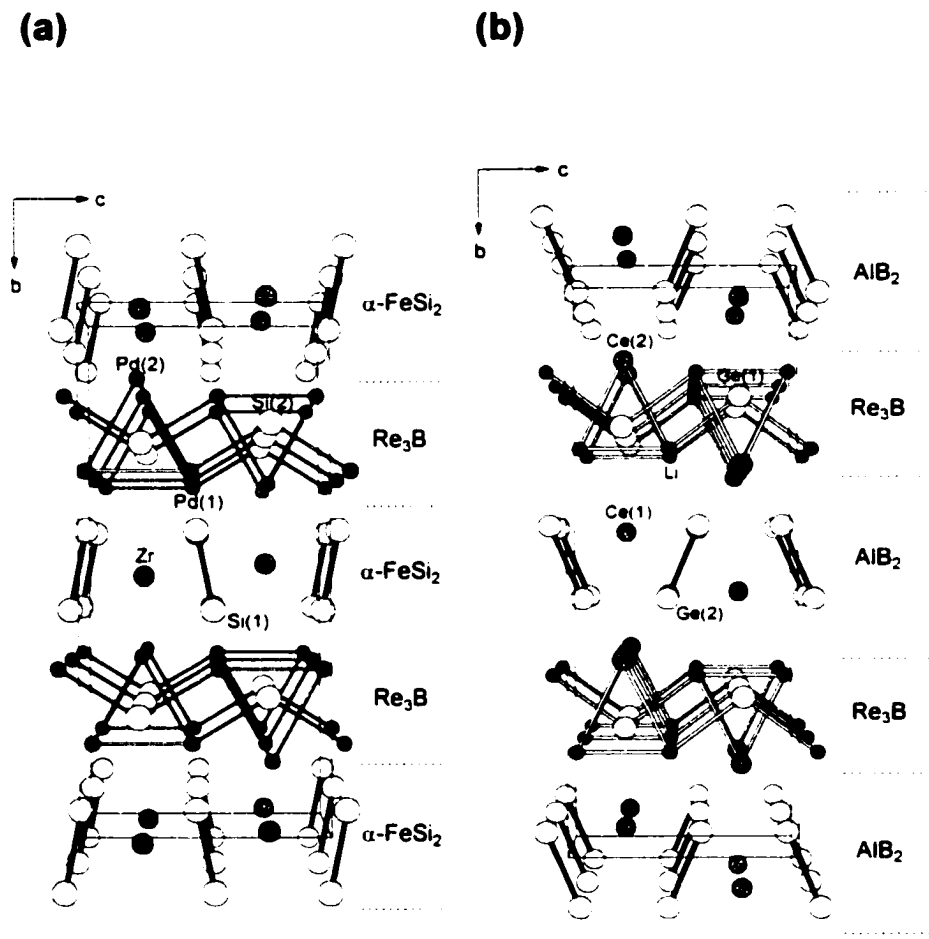

Figure A-2. Comparison of the structures of (a) $ZrPd_3Si_3$ and (b) $Li_2Ce_2Ge_3$ viewed along the *a* axis, showing how they are built up of slabs belonging to the Re_3B, α-$FeSi_2$, and AlB_2 structure types. Standardization of the $Li_2Ce_2Ge_3$ structure gives the atomic labeling scheme shown.[14]

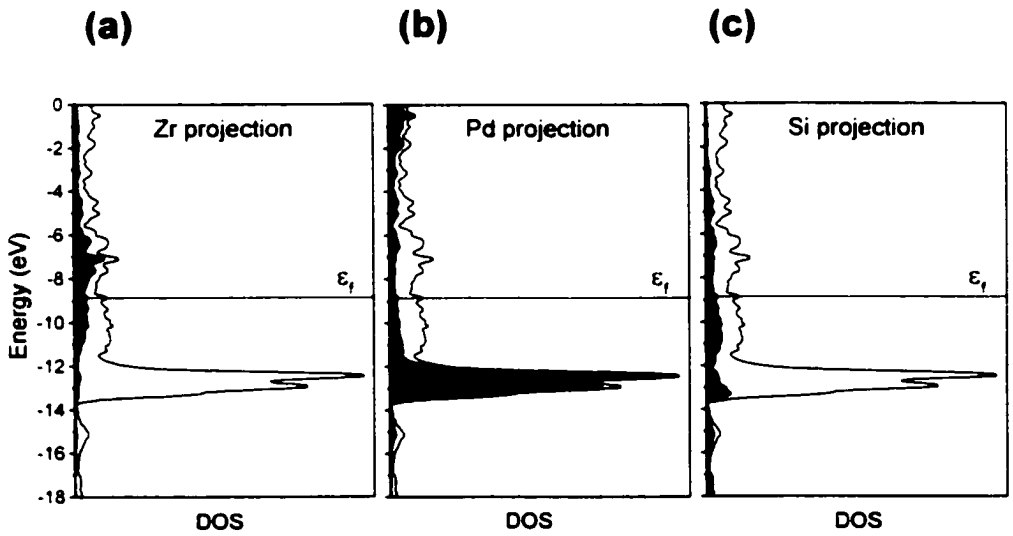

Figure A-3. Contributions of (a) Zr, (b) Pd, and (c) Si (shaded regions) to the total density of states (DOS) (line) for $ZrPd_3Si_3$. The Fermi level, ε_f, is at –8.9 eV.

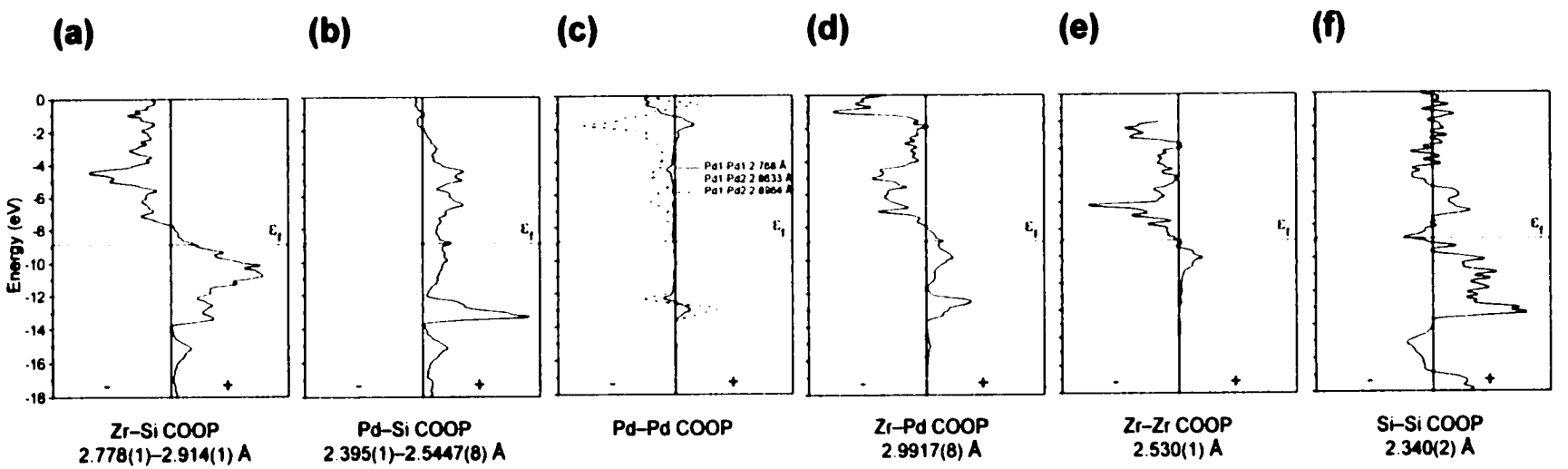

Figure A-4. Crystal orbital overlap population (COOP) curves for the indicated (a) Zr–Si, (b) Pd–Si, (c) Pd–Pd, (d) Zr–Pd, (e) Zr–Zr, and (f) Si–Si contacts in $ZrPd_3Si_3$.

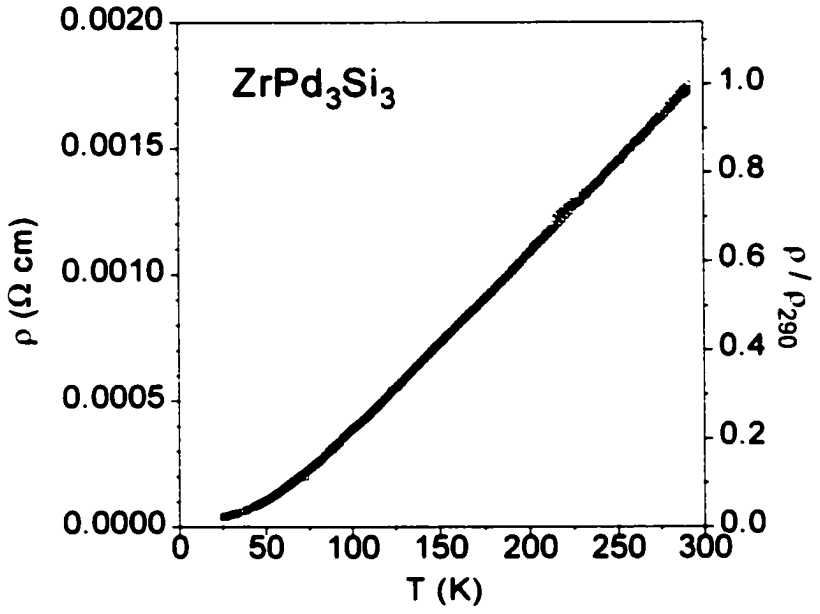

Figure A-5. Resistivity *vs* temperature for $ZrPd_3Si_3$ (ρ_{20} = 4.0 x 10^{-5} and ρ_{290} = 1.7 x 10^{-3} Ω cm; ρ_{20}/ρ_{290} = 0.024).

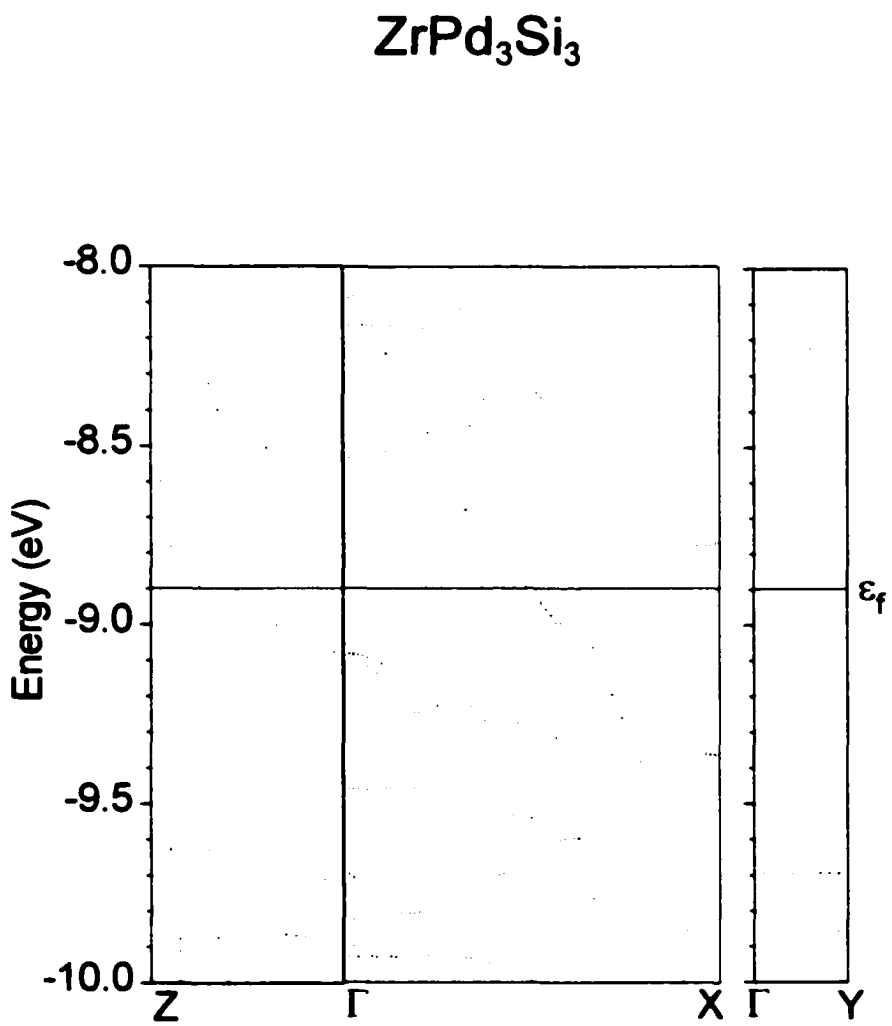

Figure A-6. Band Dispersion Diagram for $ZrPd_3Si_3$.

References

(1) *Kirk-Othmer Encyclopedia of Chemical Technology*, 4th Ed.; Howe-Grant, M., Ed.; Wiley: New York, 1997.

(2) Parthé, E.; Chabot, B. In *Handbook on the Physics and Chemistry of Rare Earths*; Gschneidner, Jr., K. A., Eyring, L., Eds.; Elsevier: Amsterdam, 1984; Vol. 6; p. 113.

(3) Villars, P. *Pearson's Handbook*, Desk Ed.; ASM International: Materials Park, OH, 1997.

(4) (a) TiNiSi: Shoemaker, C. B.; Shoemaker, D. P. *Acta Crystallogr.* **1965**, *18*, 900. (b) ZrNiSi, $ZrNi_2Si_2$, $HfNi_2Si_2$: Voroshilov, Yu. V.; Markiv, V. Ya.; Gladyshevskii, E. I. *Inorg. Mater. (Engl. Transl.)* **1967**, *3*, 1224. (c) HfNiSi: Ganglberger, E.; Nowotny, H.; Benesovsky, F. *Monatsh. Chem.* **1967**, *98*, 95. (d) $TiNiSi_2$, $HfNiSi_2$: Markiv, V. Ya.; Gladyshevskii, E. I.; Skolozdra, R. V.; Kripyakevich, P. I. *Dopov. Akad. Nauk. Ukr. RSR, Ser. A: Fiz.-Tekh. Mat. Nauki* **1967**, *(3)*, 266. (e) Ti_2Ni_3Si: Bardos, D. I.; Gupta, K. P.; Beck, P. A. *Trans. Metall. Soc. AIME* **1961**, *221*, 1087. (f) Zr_2Ni_3Si, Hf_2Ni_3Si: Mittal, R. C.; Si, S. K.; Gupta, K. P. *J. Less-Common Met.* **1978**, *60*, 75. (g) $Hf_3Ni_2Si_3$: Yarmolyuk, Ya. P.; Grin', Yu. N.; Gladyshevskii, E. I. *Sov. Phys. Crystallogr. (Engl. Transl.)* **1977**, *22*, 416. (h) $Zr_2Ni_3Si_4$, $Hf_2Ni_3Si_4$: Yarmolyuk, Ya. P.; Pecharskii, V. K.; Aksel'rud, L. G. *Sov. Phys. Crystallogr. (Engl. Transl.)* **1988**, *33*, 601. (i) $Ti_4Ni_4Si_7$: Horache, E.; Feist, T. P.; Stuart, J. A.; Fischer, J. E. *J. Mater. Res.* **1990**, *5*, 1887. (j) $Zr_5Ni_7Si_{18}$, $Hf_5Ni_9Si_{16}$: Aksel'rud, L. G.; Lysenko, L. A.; Yarmolyuk, Ya. P.; Gladyshevskii, E. I. *Dopov. Akad. Nauk. Ukr. RSR, Ser. A:*

Fiz.-Mat. Tekh. Nauki **1977**, *39*, 657. (k) $Ti_6Ni_{16}Si_7$, $Zr_6Ni_{16}Si_7$: Spiegel, F. X.; Bardos, D.; Beck, P. A. *Trans. Metall. Soc. AIME* **1963**, *227*, 575. (l) $Hf_6Ni_{16}Si_7$: Gladyshevskii, E. I. *Sov. Powder Metall. Met. Ceram. (Engl. Transl.)* **1962**, *1*, 262.

(5) (a) TiPdSi: Johnson, V.; Jeitschko, W. *J. Solid State Chem.* **1972**, *4*, 123. (b) ZrPdSi, ZrPtSi [4(c)] (c) HfPdSi, HfPtSi: Zhao, J. T.; Parthé, E. *J. Less-Common Met.* **1990**, *163*, L7.

(6) Geller, S. *Acta Crystallogr.* **1955**, *8*, 83.

(7) (a) MNiSi$_3$ (M = Sm, Y): Chen, X. Z.; Larson, P.; Sportouch, S.; Brazis, P.; Mahanti, S. D.; Kannewurf, C. R.; Kanatzidis, M. G. *Chem. Mater.* **1999**, *11*, 75. (b) $Ln_2Al_3Si_2$: Chen, X. Z.; Sieve, B.; Henning, R.; Schultz, A. J.; Brazis, P.; Kannewurf, C. R.; Cowen, J. A.; Crosby, R.; Kanatzidis, M. G. *Angew. Chem. Int. Ed. Engl.* **1999**, *38*, 693.

(8) Wang, M.; McDonald, R.; Mar, A. *Inorg. Chem.* **1999**, *38*, 3435.

(9) Engström, I. *Acta. Chem. Scand.* **1970**, *24*, 1466.

(10) POLSQ: Program for least-squares unit cell refinement. Modified by D. Cahen and D. Keszler, Northwestern University, 1983.

(11) Nylund, A. *Acta. Chem. Scand.* **1966**, *20*, 2381.

(12) Sheldrick, G. M. SHELXTL Version 5.1; Bruker Analytical X-ray Systems, Inc.: Madison, WI, 1997.

(13) *International Tables for X-ray Crystallography*; Wilson, A. J. C., Ed.; Kluwer: Dordrecht, The Netherlands, 1992; Vol. C.

(14) Gelato, L. M.; Parthé, E. *J. Appl. Crystallogr.* **1987**, *20*, 139.

(15) Whangbo, M.-H.; Hoffmann, R. *J. Am. Chem. Soc.* **1978**, *100*, 6093.

(16) Hoffmann, R. *Solids and Surfaces: A Chemist's View of Bonding in Extended Structures*; VCH Publishers: New York, 1988.

(17) Ammeter, J. H.; Bürgi, H.-B.; Thibeault, J. C.; Hoffmann, R. *J. Am. Chem. Soc.* **1978**, *100*, 3686.

(18) Schachner, H.; Nowotny, H.; Kudielka, H. *Monatsh. Chem.* **1954**, *85*, 1140.

(19) Aronsson, B. *Acta Chem. Scand.* **1960**, *14*, 1414.

(20) Hyde, B. G.; Andersson, S. *Inorganic Crystal Structures*; Wiley: New York, 1989.

(21) Aronsson, B.; Bäckman, M.; Rundqvist, S. *Acta Chem. Scand.* **1960**, *14*, 1001.

(22) Aronsson, B.; Nylund, A. *Acta Chem. Scand.* **1960**, *14*, 1011.

(23) Herbstein, F. H.; Smuts, J. *Acta Crystallogr.* **1964**, *17*, 1331.

(24) Pavlyuk, V. V.; Pecharskii, V. K.; Bodak, O. I.; Bruskov, V. A. *Sov. Phys. Crystallogr. (Engl. Transl.)* **1988**, *33*, 24.

(25) Donohue, J. *The Structures of the Elements*; Wiley: New York, 1974.

(26) Pauling, L. *The Nature of the Chemical Bond*, 3rd Ed.; Cornell University Press: Ithaca, NY, 1960.

(27) Lee, K.-S.; Koo, H.-J.; Dai, D.; Ren, J.; Whangbo, M.-H. *Inorg. Chem.* **1999**, *38*, 340.

(28) Koo, H.-J.; Whangbo, M.-H. *Inorg. Chem.* **1999**, *38*, 2204.

(29) Wang, M.; Mar, A. Unpublished calculations.

(30) (a) Pyykkö, P. *Chem. Rev.* **1997**, *97*, 597. (b) Dedieu, A.; Hoffmann, R. *J. Am. Chem. Soc.* **1978**, *100*, 2074. (c) Mehrotra, P. K.; Hoffmann, R. *Inorg. Chem.* **1978**, *17*, 2187.

Appendix B

Nonstoichiometric Rare-Earth Copper Arsenides $RECu_{1+x}As_2$ (RE = La, Ce, Pr) †

Introduction

Our continued interest in the preparation of new ternary rare-earth transition-metal pnictides derives from the wide array of physical properties they exhibit. Investigation of these ternary pnictides to date has been largely restricted to the late transition metals, and the arsenides are no exception, with an enormous number of ternary rare-earth nickel arsenides known, for instance.[1] In the RE/Cu/As system (RE = rare-earth), the compounds EuCuAs (Ni_2In-type),[2] $EuCu_{2-x}As_2$ ($ThCr_2Si_2$-type),[3] and $RECuAs_2$ (RE = La–Nd, Sm, Gd–Lu) ($HfCuSi_2$-type)[4] have been reported previously. The isotypy of $RECuAs_2$ to $HfCuSi_2$[5] was assumed based on evidence from powder X-ray diffraction data.[4] We report here the single crystal structures of the nonstoichiometric phases, $RECu_{1+x}As_2$ (RE = La, Ce, Pr), prepared under different synthetic conditions, and demonstrate that the presence of excess Cu can lead to the formation of a stuffed variant of the ideal, stoichiometric $RECuAs_2$ structure. The magnetic susceptibilities of these compounds are also presented.

---

† A version of this chapter has been published. Wang, M.; McDonald, R.; Mar, A. *J. Solid State Chem.* **1999**, *147*, 140. Copyright 1999 Academic Press.

Experimental Section

Synthesis. Reactions of powders of the elements (>99.9% purity, obtained from Alfa-Aesar or Cerac) were generally carried out on a ~0.25-g scale in evacuated fused-silica tubes (8-cm length; 10-mm i.d.). Elemental compositions (EDX analysis) of selected crystals were determined on a Hitachi S-2700 scanning electron microscope. X-ray powder patterns were obtained on an Enraf-Nonius FR552 Guinier camera (Cu $K\alpha_1$ radiation; Si standard).

A ternary phase containing excess copper, $LaCu_{1+x}As_2$, was first identified in a reaction of La, Hf, Cu, and As in a 1:2:4:4 ratio, heated at 1000 °C for 4 days. Among the products, consisting largely of a mixture of known binary phases, were square plate- or block-shaped crystals exhibiting a doubled c axis relative to the reported parameters for $LaCuAs_2$,[4] and an elemental composition consistent with the presence of excess copper (mol %: La, 24(1); Cu, 30(1); As, 46(1)). A series of reactions was then performed, La + (1+x) Cu + 2 As (x = 0, 0.1, 0.2, 0.3, 0.4, 0.5), at 1000 °C for 4 days. The resulting products were microcrystalline powders that consisted essentially of the nonstoichiometric phase identified above, designated as $LaCu_{1+x}As_2$, for $x \leq 0.3$. Beyond x = 0.3, impurities of binary arsenides appear. Single crystals could be obtained via a more rational route by reaction of the elements in a two-zone furnace (900/950 °C) with the addition of I_2 (~10 mg) as a mineralizing agent. Well-formed silver square plates or blocks were found at the hot end of the silica tube. EDX analyses of these crystals invariably revealed a composition with excess copper, $RECu_{1+x}As_2$, independent of the amount of Cu loaded. The crystals used for the structure determinations resulted from the following reactions and possessed the indicated elemental compositions:

$LaCu_{1.23(1)}As_2$, La + 1.1 Cu + 2 As, 23(1)% La, 27(1)% Cu, 50(1)% As; $CeCu_{1.10(1)}As_2$, Ce + 0.7 Cu + 2 As, 23(1)% Ce, 25(1)% Cu, 52(1)% As; $PrCu_{1.09(1)}As_2$, Pr + 1.5 Cu + 2 As, 24(1)% Pr, 25(1)% Cu, 51(1)% As. Powder X-ray diffraction data were obtained on crushed crystals from these reactions, and the cell parameters refined with the use of the program POLSQ[6] are listed in Table B-1. The observed and calculated interplaner distances and intensities are listed in Table C-10.

Structure Determination. Two X-ray structure determinations were performed for $LaCu_{1+x}As_2$, the first on the crystal from the original reaction, which leads to a refined formula of $LaCu_{1.27(1)}As_2$, and the second on a crystal obtained from the rational reaction, which leads to a refined formula of $LaCu_{1.23(1)}As_2$. These formulas are in good agreement with their respective EDX compositions indicated above. It suffices to report only the latter determination, as the results are similar. Weissenberg photography clearly reveals a doubled *c* axis and body centering systematic absences (*hkl*: $h + k + l = 2n + 1$) consistent with several possible tetragonal space groups, the centrosymmetric space group *I*4/*mmm* being chosen on the basis of the successful refinement and the structural relationship to similar compounds. For $CeCu_{1.10(1)}As_2$ and $PrCu_{1.09(1)}As_2$, in contrast, the Weissenberg photographs confirm the presence of an undoubled *c* axis, a primitive unit cell, and systematic absences (0*kl*: $k + l = 2n + 1$) consistent with the tetragonal space group *P*4/*nmm* previously found for *RE*$CuAs_2$,[4] but with slightly larger cell parameters. Final cell parameters were determined from least-squares analyses of 24 reflections centered on an Enraf-Nonius CAD-4 diffractometer in the range $12° \leq 2\theta(\text{Mo } K\alpha) \leq 20°$ for $LaCu_{1.23(1)}As_2$, $20° \leq 2\theta(\text{Mo } K\alpha) \leq 43°$ for $CeCu_{1.10(1)}As_2$, and $25° \leq 2\theta(\text{Mo } K\alpha) \leq 42°$ for $PrCu_{1.09(1)}As_2$. Intensity data were collected at room temperature with the θ–2θ

scan technique in the range $4° \leq 2\theta(\text{Mo } K\alpha) \leq 70°$. Calculations were carried out with the use of the SHELXTL (Version 5.1) package.[7] Conventional atomic scattering factors and anomalous dispersion corrections were used.[8] Intensity data were processed and face-indexed absorption corrections were applied in XPREP.[7] Initial atomic positions were found by direct methods, and refinements were performed by least-squares methods.

Refinements of the $LaCu_{1.23(1)}As_2$ structure to this stage were on a model identical to the atomic arrangement of the $UCuP_2$ ($SrZnBi_2$-type) structure;[9] similarly, the model in $CeCu_{1.10(1)}As_2$ or $PrCu_{1.09(1)}As_2$ was identical to that of the reported *RE*$CuAs_2$ ($HfCuSi_2$-type) structure.[4] In each case, however, the difference Fourier maps reveal pronounced residual electron density in the vicinity of a square pyramidal site that is vacant in the parent structures. Given the consistently higher percentage of Cu observed in the EDX analyses relative to the ideal formula *RE*$CuAs_2$, additional Cu atoms were assigned to this site and allowed to refine isotropically at partial occupancy. These refinements result in significant improvements in the agreement factors (*e.g.*, R/R_w decrease from 0.037/0.110 to 0.021/0.061 for $CeCu_{1.10(1)}As_2$ on the absorption-corrected data). Another possibility is that this site may be fully occupied by oxygen atoms, since the distance to the five surrounding As atoms (~2.4 Å) is also reasonable for an As–O bond. However, this model can be ruled out on the basis of windowless EDX measurements showing no evidence for oxygen, and more convincingly, chemical arguments discussed in more detail below. Refinements were attempted in lower symmetry space groups, specifically those that remove the symmetry plane normal to *c* (*e.g.*, $I\bar{4}$), but these did not lead to any models in which the partially occupied Cu site becomes ordered, nor did consideration of

twinning possibilities prove fruitful.

The atomic positions were standardized in STRUCTURE TIDY,[10] but we have opted to override the atom numbering that the program suggests for $LaCu_{1.23(1)}As_2$ in order to draw structural comparisons with greater ease. The final cycle of least-squares refinement on F_o^2 included anisotropic displacement parameters for all atoms except the partially occupied Cu site, for which simultaneous refinement of occupancy and anisotropic displacement parameters is not recommended because of their strong correlation. Crystal data and further details of the structure determination are given in Table B-2. Final values of the positional and displacement parameters are given in Table B-3. Anisotropic displacement parameters are given in Table C-11.

Magnetic Susceptibility. The magnetic data were collected on a Quantum Design SQUID magnetometer. Powder samples (~20 mg) were placed in gelatin capsules. Zero field cooled data were obtained at applied fields ranging from 0.1 to 3 T at temperatures between 5 K (2 K for $PrCu_{1.09(1)}As_2$) and 300 K.

Results and Discussion

Structures and Structural Relationships. The structures of $RECu_{1+x}As_2$ (RE = La, Ce, Pr) are shown in Figure B-1, and interatomic distances are listed in Table B-4. The structures consist of anionic layers of edge-sharing $CuAs_4$ tetrahedra segregated from square nets of As atoms by the intervening RE cations. $LaCu_{1.23(1)}As_2$ is related to $CeCu_{1.10(1)}As_2$ (or $PrCu_{1.09(1)}As_2$) by a doubling of the c axis, which results from an alternation in the relative orientation of the $CuAs_4$ tetrahedra along this direction. The $CuAs_4$ tetrahedra are fairly regular, with four equivalent Cu(1)–As(2) bonds at angles

close to ideal ($LaCu_{1.23(1)}As_2$: 2.5196(6) Å, 108.52(4)°–109.95(2)°; $CeCu_{1.10(1)}As_2$: 2.5136(5) Å, 106.44(3)°–111.01(1)°: $PrCu_{1.09(1)}As_2$: 2.5118(6) Å, 105.86(4)°–111.30(2)°). These Cu(1) atoms are also arranged in a square net, but the Cu(1)–Cu(1) distances (2.8–2.9 Å) are probably too long to be considered significant. These distances ($= a/\sqrt{2}$) also correspond to the As(1)–As(1) separations in the square net, and while they are long compared to a full As–As single bond length of 2.4–2.5 Å,[11,12] the possibility of weak covalent bonding between the As(1) atoms cannot be ruled out. The *RE* atoms are surrounded by eight As atoms in a square antiprism, at distances that reflect the diminishing size of the rare-earth on progressing from $LaCu_{1.23(1)}As_2$ (3.1054(5)–3.1975(5) Å) to $PrCu_{1.09(1)}As_2$ (3.0333(4)–3.1506(5) Å).

The presence of a square pyramidal site partially occupied by additional Cu(2) atoms is a distinguishing feature of these structures. While the five Cu(2)–As distances are nearly regular in $LaCu_{1.23(1)}As_2$ (2.376(3)–2.378(6) Å), the apical Cu(2)–As(2) distance is longer than the four basal Cu(2)–As(1) distances in $CeCu_{1.10(1)}As_2$ (2.395(10) *vs.* 2.311(5) Å) and $PrCu_{1.09(1)}As_2$ (2.371(14) *vs.* 2.306(7) Å). In $LaCu_{1.23(1)}As_2$, this Cu(2) site faces opposite a symmetry-equivalent site at 2.421(12) Å away. Since Cu(2)–Cu(2) bonding is unlikely to occur across an intervening As(1) layer, a pair of such facing Cu(2) atoms will experience repulsion that may account for the shortened apical Cu(2)–As(2) distance in $LaCu_{1.23(1)}As_2$ relative to those in $CeCu_{1.10(1)}As_2$ and $PrCu_{1.09(1)}As_2$, where the square pyramidal Cu(2) sites are staggered with respect to each other. On the other hand, the low occupancy of this site in $LaCu_{1.23(1)}As_2$ probably reduces the effect of this distortion, and certainly on a local level, two such atoms need not face each other given the ~¼ distribution of atoms among these sites. Whether this distribution is further

ordered on the *ab* plane will be difficult to detect by X-ray diffraction. In any case, long-exposure (24 hrs) oscillation photographs show no evidence for superstructure along *a* or *b*.

These new $RECu_{1+x}As_2$ structures expand on the already extensive series of tetragonal structures built up by the stacking of square nets. $CeCu_{1.10(1)}As_2$ (or $PrCu_{1.09(1)}As_2$) represents a stuffed variant of the prevalent $HfCuSi_2$ structure type,[5] which is adopted by numerous ternary pnictides such as $REM_{1-x}Sb_2$ (M = Mn, Fe, Co, Cu, Zn, Ag)[4,13,14] and $UMPn_2$ (M = Fe, Co, Ni, Cu; Pn = P, As, Sb, Bi).[15] Similarly, $LaCu_{1.23(1)}As_2$ represents a stuffed variant of a parent structure type, $SrZnBi_2$,[16] which possesses a doubled unit cell relative to that of the $HfCuSi_2$ structure type. $LaCu_{1.23(1)}As_2$ is thus nearly isostructural to $CeCu_{1.09}P_{1.87}$,[17] which exhibits a pronounced deficiency in P atoms disordered over closely-spaced sites within the square net. In turn, the $HfCuSi_2$ and $SrZnBi_2$ structure types are derived by inserting atoms into tetrahedral sites of the ZrSiS[18] and UgeTe[19] structure types, respectively. (We have chosen the designations "$HfCuSi_2$" and "$SrZnBi_2$" based on the most prevalent usage in the literature, but include a representative ternary copper pnictide to show more clearly the correspondence with the title compounds.) These structural relationships are illustrated as follows:

P*4/*nmm:

$$\underset{(UAs_2)}{ZrSiS} \xrightarrow{\text{filling of tet. sites}} \underset{(UCuAs_2)}{HfCuSi_2} \xrightarrow{\text{partial filling of sq. pyr. sites}} CeCu_{1.10(1)}As_2$$

I*4/*mmm:

$$UGeTe \xrightarrow{\text{filling of tet. sites}} \underset{(UCuP_2)}{SrZnBi_2} \xrightarrow{\text{partial filling of sq. pyr. sites}} LaCu_{1.23(1)}As_2$$

Just as partial occupation of the tetrahedral sites is common in the $HfCuSi_2$ structure,[5,13,14]

the nonstoichiometry of the new $RECu_{1+x}As_2$ compounds arises from partial occupation of the square pyramidal sites.

Magnetic Measurements. The magnetic susceptibility of $LaCu_{1.23(1)}As_2$ is essentially temperature-independent ($\chi_0 = -2.8 \times 10^{-4}$ emu mol^{-1}), consistent with closed-shell La^{3+} and Cu^{+} (d^{10}) species. $CeCu_{1.10(1)}As_2$ exhibits paramagnetic behaviour down to 5 K, and the susceptibility data were fit to the Curie-Weiss law, $\chi = C / (T - \theta)$ (Figure B-2), giving the parameters C = 0.601(2) emu K mol^{-1} and θ = -2.5(3) K. The small negative value of θ indicates a possibly weak antiferromagnetic interaction, while the effective moment of 2.19 μ_B is somewhat less than the expected value of 2.54 μ_B for Ce^{3+}. $PrCu_{1.09(1)}As_2$ exhibits an antiferromagnetic ordering at 4 K, and the fit of the susceptibility data to the Curie-Weiss law (Figure B-3) yields C = 1.530(5) emu K mol^{-1} and θ = -2.6(4) K. The effective moment of 3.5 μ_B is consistent with the expected value of 3.58 μ_B for Pr^{3+}.

Bonding. Devising a consistent bonding model for $RECu_{1+x}As_2$ is an interesting challenge. The highly electropositive *RE* atoms will form predominantly ionic bonds and adopt an oxidation state of +3, to a first approximation. The Cu–As distances are 2.31–2.52 Å, only slightly shorter than similar distances found in arsenides containing Cu(+1) (*e.g.*, $SrCu_2As_2$, 2.510(1) Å;[3] $UCuAs_2$, 2.514 Å;[20] $U_2Cu_4As_5$, 2.427(2)–2.560(3) Å;[21] $K_3Cu_3As_2$, 2.32 Å [22]). The ambiguity arises from the Cu(2) nonstoichiometry and the intermediate As(1)–As(1) distances (2.83–2.89 Å). If the oxidation state assignment previously proposed for $REAgSb_2$[4] is extrapolated to an assumed isostructural, stoichiometric $RECuAs_2$, $(RE^{+3})(Cu^{+1})(As(2)^{-3})(As(1)^{-1})$, the (–1) oxidation state for the As(1) atoms in the square net is unrealistic because the As(1)–As(1) distances are too

long to be considered even as one-electron bonds. On the other hand, the assignment for $UCuAs_2$, $(U^{+4})(Cu^{+1})(As(2)^{-3})(As(1)^{-2})$, better reflects the weakness of the As(1)–As(1) bonds.[20] Assuming Cu to be in the +1 state, then, the assignment $(RE^{+3})(Cu^{+1})_{1+x}(As^{-3})(As^{-(1+x)})$ is a reasonable approximation. However, the As(1)–As(1) distance is also affected by the geometrical constraints imposed by the rigidity of the tetrahedral Cu/As layer and the size of the *RE* atom, and it may not be very sensitive to changes in the As(1) oxidation state. Consequently, to maintain charge balance, either the oxidation state of some Cu atoms must change from +1 to +2 (mixed valency), or the Cu occupancy can vary, or both. Mixed valency has also been invoked to account for the *sub*stoichiometry observed in $LaCu_{0.85}Sb_2$.[13] Since the degree of mixed valency, if any, will be small, it may be difficult to ascertain this from the magnetic data.

Earlier we alluded to the possibility that the partially occupied Cu site could also be modeled as a fully occupied O site, leading to a formula of "$LaCuAs_2O$". While several layered pnictide oxides with closely related structures have been reported ($AE_2Mn_3Pn_2O_2$ (*AE* = Sr, Ba; *Pn* = P, As, Sb);[23] *REM*PO (*M* = Fe, Ru, Co);[24] $RE_3Cu_4P_4O_2$ (*RE* = La, Ce, Nd);[25] UCuPO;[26] $U_2Cu_2Pn_3O$ (*Pn* = P, As);[27] $ThCu_{1-x}PO$ and ThCuAsO [28]), the oxygen atoms in these structures are coordinated, *without exception*, to the electropositive metals. A hypothetical "$LaCuAs_2O$" structure would have the oxygen atom coordinated to the nonmetal component (four As atoms in the square net), and would result in the chemically unlikely situation of cationic (in the square net) and anionic (in the tetrahedral Cu/As layers) arsenic species co-existing in the same structure.

On progressing from $LaCu_{1.23(1)}As_2$ to $PrCu_{1.09(1)}As_2$, not only does the Cu content decrease, but the Cu(2)–As distances in the square pyramidal site also shorten (to ~2.3

Å), as expected upon concomitant substitution with the smaller rare-earth atoms. Since this appears to be the lower limit for realistic Cu–As bond lengths (to our knowledge, the shortest reported Cu–As distance is 2.32 Å in $K_3Cu_3As_2$ [22]), we do not anticipate the stuffed $HfCuSi_2$-type structure to extend much more beyond Pr as the rare-earth. Extrapolating to a hypothetical "$NdCu_{1+x}As_2$" using the literature cell constants for unfilled $NdCuAs_2$,[4] we calculate distances of 2.28 Å from the square pyramidal site to the neighbouring As atoms, certainly too short to be reasonable.

Why $LaCu_{1.23(1)}As_2$ should adopt a doubled superstructure of $CeCu_{1.10(1)}As_2$ is not clear. Tetragonal layered structures built up from stackings of square nets are highly prone to stacking disorder or intergrowths, and many can be viewed as the superposition of slabs of more basic structures (*e.g.*, $U_2Cu_4As_5$,[21] $U_3Ni_{3.34}P_6$ [29]). Indeed, we have evidence from powder X-ray diffraction for a disordered $LaCuAs_2$ structure built up from $HfCuSi_2$-type slabs, but stacked so that the relative orientation of the tetrahedral Cu/As layers is random between adjoining unit cells along the *c* direction.[30] We propose that this phenomenon may be quite common for this family of structures, the polytype formed depending on the synthetic conditions. The stability of these nonstoichiometric layered structures may depend sensitively on temperature, and this deserves further investigation.

Table B-1. Cell Parameters for $RECu_{1+x}As_2$ (RE = La, Ce, Pr)

Compound	a (Å)	c (Å)	V (Å^3)
$LaCu_{1.23(1)}As_2$	4.0984(9)	20.280(8)	340.6(2)
$CeCu_{1.10(1)}As_2$	4.030(1)	10.089(4)	163.8(1)
$PrCu_{1.09(1)}As_2$	4.011(2)	10.055(4)	161.8(1)

Table B-2. Crystallographic Data for $RECu_{1+x}As_2$ (RE = La, Ce, Pr)

Formula	$LaCu_{1.23(1)}As_2$	$CeCu_{1.10(1)}As_2$	$PrCu_{1.09(1)}As_2$
Formula mass (amu)	367.06	359.85	360.49
Space Group	*I4/mmm* (No. 139)	*P4/nmm* (No. 129)	*P4/nmm* (No. 129)
a (Å) [a]	4.0901(4)	4.0265(4)	4.0086(2)
c (Å) [a]	20.243(3)	10.071(2)	10.0496(9)
V (Å^3)	338.64(7)	163.28(3)	161.49(2)
Z	4	2	2
T (°C)	22	22	22
Diffractometer		Enraf-Nonius CAD4	
ρ_{calc} (g cm^{-3})	7.200	7.319	7.414
Crystal dimensions (mm)	0.30 × 0.29 × 0.08	0.16 × 0.13 × 0.10	0.14 × 0.09 × 0.09
Radiation	Graphite monochromated MoK_α, λ = 0.71073 Å		
μ(MoK_α) (cm^{-1})	392.45	407.13	421.40
Transmission factors [b]	0.010–0.094	0.016–0.101	0.021–0.114
Scan type	θ–2θ	θ–2θ	θ–2θ
Scan speed (deg. min^{-1})	1.67	1.67	1.67
Scan range (deg.)	0.60 + 0.344 tanθ	0.75 + 0.344 tanθ	0.60 + 0.344 tanθ
2θ limits	4° ≤ 2θ(Mo $K\alpha$) ≤ 70°	4° ≤ 2θ(Mo $K\alpha$) ≤ 70°	4° ≤ 2θ(Mo $K\alpha$) ≤ 70°
Data collected	$-6 \le h \le 6$, $-6 \le k \le 6$, $-32 \le l \le 32$	$-6 \le h \le 6$, $-6 \le k \le 6$, $-16 \le l \le 16$	$-6 \le h \le 6$, $-6 \le k \le 6$, $-16 \le l \le 16$
No. of data collected	2990	2844	2801

Table B-2. Crystallographic Data for $RECu_{1+x}As_2$ (RE = La, Ce, Pr) (continued)

No. of unique data, including $F_o^2 < 0$	272 (R_{int} = 0.116)	260 (R_{int} = 0.112)	258 (R_{int} = 0.149)
No. of unique data, with $F_o^2 > 2\sigma(F_o^2)$	264	248	243
No. of variables [c]	16	15	15
$R(F)$ for $F_o^2 > 2\sigma(F_o^2)$ [d]	0.034	0.020	0.039
$R_w(F_o^2)$ [e]	0.073	0.050	0.089
Goodness of fit [f]	1.145	1.114	1.211
$\Delta\rho_{max}$, $\Delta\rho_{min}$ (e Å^{-3})	1.7, −2.4	1.2, −1.5	3.2, −6.3

[a] Obtained from a refinement constrained so that $a = b$ and $\alpha = \beta = \gamma = 90°$.

[b] A numerical face-indexed absorption correction was applied, with the use of programs in the SHELXTL package (Sheldrick, G. M. *SHELXTL Version 5.1*; Bruker Analytical X-ray Systems: Madison, WI, 1997).

[c] Including an extinction coefficient.

[d] $R(F) = \sum \left| |F_o| - |F_c| \right| / \sum |F_o|$.

[e] $R_w(F_o^2) = \left[\sum \left[w(F_o^2 - F_c^2)^2\right] / \sum wF_o^4\right]^{1/2}$; $w^{-1} = \left[\sigma^2(F_o^2) + (aP)^2 + bP\right]$ where $P = \left[\max(F_o^2, 0) + 2F_c^2\right]/3$. a = 0.0310, 0, 0.0457, and b = 4.3152, 0.3448, 0.4457 for $LaCu_{1.23(1)}As_2$, $CeCu_{1.10(1)}As_2$, and $PrCu_{1.09(1)}As_2$, respectively.

[f] $GooF = \left[\sum \left[w(F_o^2 - F_c^2)^2\right] / (n - p)\right]^{1/2}$ where n is the number of reflections and p is the total number of parameters refined.

Table B-3. Positional and Equivalent Isotropic Thermal Parameters $RECu_{1+x}As_2$ (RE = La, Ce, Pr)

Atom	Wyckoff position	Occupancy	x	y	z	U_{eq} (Å^2) [a]
			$LaCu_{1.23(1)}As_2$			
La	4e	1	0	0	0.37858(2)	0.0078(2)
Cu(1)	4d	1	0	½	¼	0.0119(3)
Cu(2)	4e	0.233(8)	0	0	0.0598(3)	0.016(2)
As(1)	4c	1	0	½	0	0.0224(3)
As(2)	4e	1	0	0	0.17729(5)	0.0078(3)
			$CeCu_{1.10(1)}As_2$			
Ce	2c	1	¼	¼	0.24179(4)	0.0081(2)
Cu(1)	2b	1	¾	¼	½	0.0114(2)
Cu(2)	2c	0.101(7)	¾	¾	0.1127(10)	0.013(3)
As(1)	2a	1	¾	¼	0	0.0207(2)
As(2)	2c	1	¼	¼	0.64944(7)	0.0079(2)
			$PrCu_{1.09(1)}As_2$			
Pr	2c	1	¼	¼	0.24189(5)	0.0083(3)
Cu(1)	2b	1	¾	¼	½	0.0118(3)
Cu(2)	2c	0.09(1)	¾	¾	0.1134(14)	0.011(5)
As(1)	2a	1	¾	¼	0	0.0213(4)
As(2)	2c	1	¼	¼	0.6506(1)	0.0079(2)

[a] U_{eq} is defined as one-third of the trace of the orthogonalized $\mathbf{U}_{ij}$ tensor.

Table B-4. Selected Interatomic Distances (Å) in $RECu_{1+x}As_2$ (RE = La, Ce, Pr)

	$LaCu_{1.23(1)}As_2$	$CeCu_{1.10(1)}As_2$	$PrCu_{1.09(1)}As_2$
RE–As(2) (4x)	3.1054(5)	3.0506(4)	3.0333(4)
RE–As(1) (4x)	3.1975(5)	3.1596(4)	3.1506(5)
RE–Cu(2) (4x)	3.150(2)	3.130(4)	3.115(6)
Cu(2)–As(2)	2.378(6)	2.395(10)	2.371(14)
Cu(2)–As(1) (4x)	2.376(3)	2.311(5)	2.306(7)
Cu(1)–As(2) (4x)	2.5196(6)	2.5136(5)	2.5118(6)
Cu(1)–Cu(1) (4x)	2.8921(3)	2.8472(3)	2.8345(1)
As(1)–As(1) (4x)	2.8921(3)	2.8472(3)	2.8345(1)

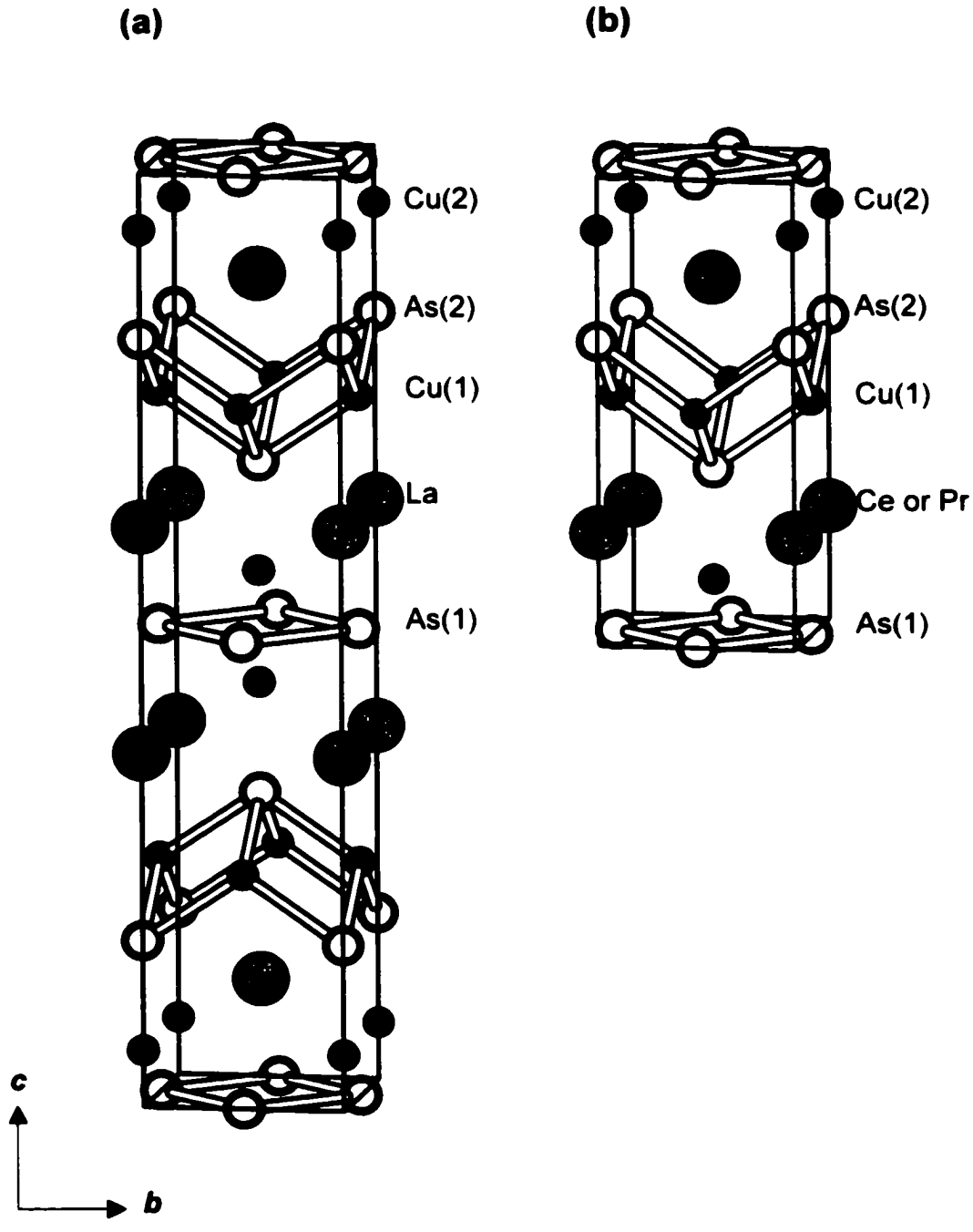

Figure B-1. View down the *a* axis of (a) $LaCu_{1.23(1)}As_2$ and (b) $CeCu_{1.10(1)}As_2$ or $PrCu_{1.09(1)}As_2$, with the unit cell outlined. The large circles are *RE* atoms, the small circles are Cu atoms, and the medium circles are As atoms. The Cu(2) sites are only partially occupied.

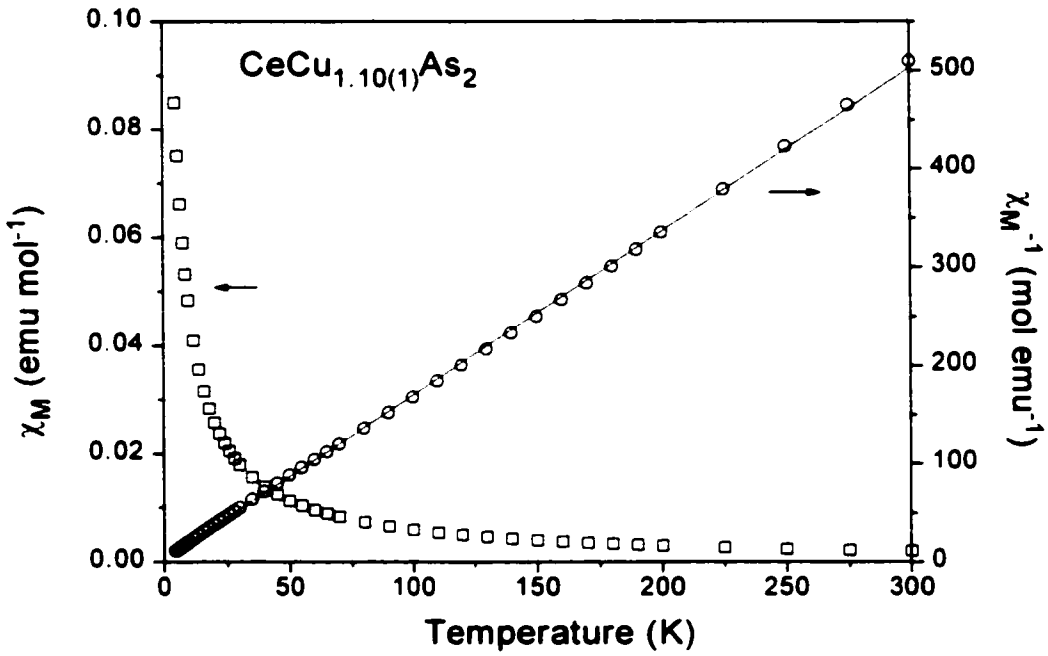

Figure B-2. Susceptibility and inverse susceptibility for $CeCu_{1.10(1)}As_2$ (measured at 2 T), and fit to the Curie-Weiss law.

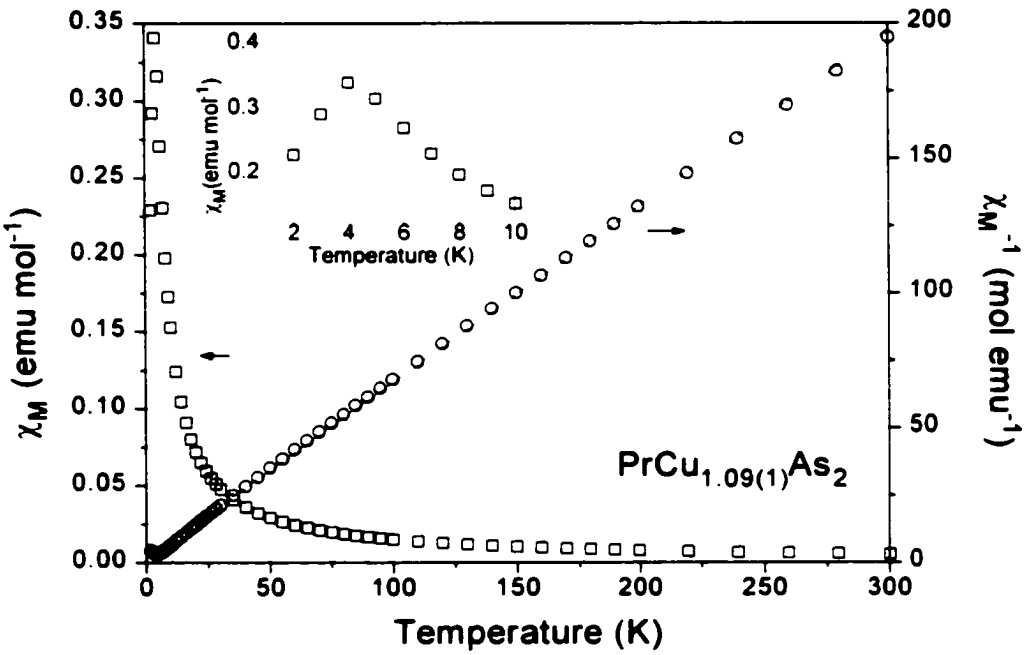

Figure B-3. Susceptibility and inverse susceptibility for $PrCu_{1.09(1)}As_2$ (measured at 0.1 T), and fit to the Curie-Weiss law.

References

(1) Villars, P. *Pearson's Handbook, Desk Edition*; ASM International: Materials Park, OH, 1997.

(2) Mewis, A. *Z. Naturforsch., B: Anorg. Chem., Org. Chem.* **1978**, *33*, 983.

(3) Dünner, J.; Mewis, A.; Roepke, M.; Michels, G. *Z. Anorg. Allg. Chem.* **1995**, *621*, 1523.

(4) Brylak, M.; Möller, M. H.; Jeitschko, W. *J. Solid State Chem.* **1995**, *115*, 305.

(5) Andrukhiv, L. S.; Lysenko, L. O.; Yarmolyuk, Ya. P.; Gladyshevskii, E. I. *Dopov. Akad. Nauk Ukr. RSR, Ser. A: Fiz.-Mat. Tekh. Nauki* **1975**, 645.

(6) POLSQ: Program for least-squares unit cell refinement. Modified by D. Cahen and D. Keszler, Northwestern University, 1983.

(7) Sheldrick, G. M. *SHELXTL*, version 5.1; Bruker Analytical X-ray Systems, Inc.: Madison, WI, 1997.

(8) *International Tables for X-ray Crystallography*; Wilson, A. J. C., Ed.; Kluwer: Dordrecht, 1992; Vol. C.

(9) Noël, H.; Zolnierek, Z.; Kaczorowski, D.; Troc, R. *J. Less-Common Met.* **1987**, *132*, 327.

(10) Gelato, L. M.; Parthé, E. *J. Appl. Crystallogr.* **1987**, *20*, 139.

(11) Somer, M.; Carrillo-Cabrera, W.; Peters, K.; von Schnering, H. G. *Z. Kristallogr.* **1995**, *210*, 876.

(12) Hönle, W.; Lin, J.; Hartweg, M.; von Schnering, H. G. *J. Solid State Chem.* **1992**, *97*, 1.

(13) Cordier, G.; Schäfer, H.; Woll, P. *Z. Naturforsch., B: Anorg. Chem., Org. Chem.*

1985, *40*, 1097.

(14) Leithe-Jasper, A.; Rogl, P. *J. Alloys Compd.* **1994**, *203*, 133.

(15) Kaczorowski, D. *J. Alloys Compd.* **1992**, *186*, 333.

(16) Cordier, G.; Eisenmann, B.; Schäfer, H. *Z. Anorg. Allg. Chem.* **1976**, *426*, 205.

(17) Chykhrij, S. I.; Loukashouk, G. V.; Oryshchyn, S. V.; Kuz'ma, Yu. B. *J. Alloys Compd.* **1997**, *248*, 224.

(18) Haneveld, A. J. Klein; Jellinek, F. *Rec. Trav. Chim. Pays-Bas* **1964**, *83*, 776.

(19) Haneveld, A. J. Klein; Jellinek, F. *J. Less-Common Met.* **1969**, *18*, 123.

(20) Stepien-Damm, J.; Kaczorowski, D.; Troc, R. *J. Less-Common Met.* **1987**, *132*, 15.

(21) Kaczorowski, D.; Noël, H.; Troc, R. *J. Less-Common Met.* **1991**, *170*, 255.

(22) Savelsberg, G.; Schäfer, H. *Z. Naturforsch., B: Anorg. Chem., Org. Chem.* **1979**, *34*, 1033.

(23) Brock, S. L.; Kauzlarich, S. M. *Comments Inorg. Chem.* **1995**, *17*, 213.

(24) Zimmer, B. I.; Jeitschko, W.; Albering, J. H.; Glaum, R.; Reehuis, M. *J. Alloys Compd.* **1995**, *229*, 238.

(25) Cava, R. J.; Zandbergen, H. W.; Krajewski, J. J.; Siegrist, T.; Hwang, H. Y.; Batlogg, B. *J. Solid State Chem.* **1997**, *129*, 250.

(26) Kaczorowski, D.; Albering, J. H.; Noël, H.; Jeitschko, W. *J. Alloys Compd.* **1994**, *216*, 117.

(27) Kaczorowski, D.; Potel, M.; Noël, H. *J. Solid State Chem.* **1994**, *112*, 228.

(28) Albering, J. H.; Jeitschko, W. *Z. Naturforsch., B: Chem. Sci.* **1996**, *51*, 257.

(29) Ebel, T.; Jeitschko, W. *J. Solid State Chem.* **1995**, *116*, 307.

(30) Wang, M.; Mar, A. unpublished work.

Appendix C

Table C-1. Anisotropic displacement parameters [a] ($Å^2$) for $Zr_3Pd_4P_3$, $Hf_3Pd_4P_3$, and $Nb_5Pd_4P_4$

Atom	U_{11}	U_{22}	U_{33}	U_{12}	U_{13}	U_{23}
			$Zr_3Pd_4P_3$			
Zr(1)	0.0050(7)	0.0041(6)	0.0062(7)	0	–0.0004(6)	0
Zr(2)	0.0037(6)	0.0050(6)	0.0065(7)	0	0.0006(6)	0
Zr(3)	0.0031(6)	0.0063(7)	0.0057(7)	0	–0.0003(6)	0
Pd(1)	0.0056(5)	0.0064(6)	0.0077(6)	0	–0.0003(5)	0
Pd(2)	0.0063(5)	0.0054(5)	0.0075(6)	0	–0.0003(5)	0
Pd(3)	0.0062(5)	0.0043(5)	0.0077(6)	0	–0.0002(5)	0
Pd(4)	0.0062(5)	0.0050(5)	0.0077(6)	0	0.0009(5)	0
P(1)	0.0062(17)	0.0025(16)	0.0080(19)	0	–0.0018(16)	0
P(2)	0.0065(19)	0.0039(17)	0.0060(19)	0	0.0014(15)	0
P(3)	0.0071(18)	0.0059(18)	0.007(2)	0	0.0008(17)	0
			$Hf_3Pd_4P_3$ [b]			
Hf(1)	0.0044(9)	0.0044(9)	0.0045(10)	0	–0.0006(8)	0
Hf(2)	0.0061(9)	0.0060(10)	0.0063(11)	0	–0.0008(8)	0
Hf(3)	0.0104(10)	0.0080(10)	0.0094(11)	0	0.0013(9)	0
Pd(1)	0.0072(16)	0.0010(16)	0.004(2)	0	–0.0002(14)	0
Pd(2)	0.0043(16)	0.0013(17)	0.0012(18)	0	0.0011(13)	0
Pd(3)	0.0027(15)	0.0031(16)	0.0065(19)	0	0.0002(14)	0
Pd(4)	0.0045(16)	0.0061(16)	0.0046(19)	0	–0.0002(14)	0

Table C-1. Anisotropic displacement parameters [a] ($Å^2$) for $Zr_3Pd_4P_3$, $Hf_3Pd_4P_3$, and $Nb_5Pd_4P_4$ (continued)

			$Nb_5Pd_4P_4$			
Nb(1)	0.0038(6)	0.0038(6)	0.0094(12)	0	0	0
Nb(2)	0.0046(5)	0.0056(5)	0.0094(6)	0.0009(3)	0	0
Pd	0.0062(5)	0.0057(5)	0.0099(5)	0.0001(3)	0	0
P	0.0059(15)	0.0048(15)	0.0106(17)	0.0017(11)	0	0

[a] The form of the anisotropic displacement parameter is: $exp[-2\pi^2(h^2a^{*2}U_{11} + k^2b^{*2}U_{22} + l^2c^{*2}U_{33} + 2hka^*b^*U_{12} + 2hla^*c^*U_{13} + 2klb^*c^*U_{23})]$.

[b] Sites P(1), P(2), and P(3) were refined isotropically.

Table C-2. Anisotropic displacement parameters [a] ($Å^2$) for Nb_9PdAs_7

Atom	U_{11}	U_{22}	U_{33}	U_{12}	U_{13}	U_{23}
Nb(1)	0.0028(6)	0.0033(6)	0.0034(8)	0.0018(5)	0	0
Nb(2)	0.0045(6)	0.0036(6)	0.0030(8)	0.0019(5)	0	0
Nb(3)	0.0028(6)	0.0042(6)	0.0026(9)	0.0017(5)	0	0
Nb(4)	0.0027(5)	0.0032(5)	0.0040(8)	0.0017(5)	0	0
Nb(5)	0.0034(6)	0.0034(5)	0.0019(7)	0.0018(5)	0	0
Nb(6)	0.0043(6)	0.0039(6)	0.0026(8)	0.0020(5)	0	0
Nb(7)	0.0086(6)	0.0078(6)	0.0051(7)	0.0058(5)	0	0
Nb(8)	0.0033(6)	0.0034(6)	0.0012(8)	0.0019(5)	0	0
Nb(9)	0.0026(6)	0.0033(6)	0.0035(8)	0.0022(5)	0	0
Pd	0.0096(5)	0.0080(5)	0.0109(6)	0.0044(5)	0	0
As(1)	0.0038(7)	0.0049(7)	0.0004(10)	0.0019(6)	0	0
As(2)	0.0043(6)	0.0049(7)	0.0010(9)	0.0023(6)	0	0
As(3)	0.0030(7)	0.0046(7)	0.0013(10)	0.0023(6)	0	0
As(4)	0.0095(7)	0.0052(7)	0.0038(9)	0.0051(6)	0	0
As(5)	0.0051(7)	0.0041(7)	0.0026(10)	0.0030(6)	0	0
As(6)	0.0046(7)	0.0030(7)	0.0036(10)	0.0015(6)	0	0
As(7)	0.0039(8)	0.0039(8)	0.0033(16)	0.0020(4)	0	0
As(8)	0.0031(8)	0.0031(8)	0.0018(15)	0.0015(4)	0	0
As(9)	0.0075(7)	0.0075(7)	0.0045(13)	0.0038(4)	0	0

[a] The form of the anisotropic displacement parameter is: $exp[-2\pi^2(h^2a^{*2}U_{11} + k^2b^{*2}U_{22} + l^2c^{*2}U_{33} + 2hka^*b^*U_{12} + 2hla^*c^*U_{13} + 2klb^*c^*U_{23})]$.

Table C-3. X-ray Powder Diffraction Data for $Zr_3Ni_3Sb_4$, $Hf_3Ni_3Sb_4$, and $Zr_3Pt_3Sb_4$ [a]

hkl	d_{obs} (Å)	d_{calc} (Å)	I/I_o [b]	*hkl*	d_{obs} (Å)	d_{calc} (Å)	I/I_o [b]
			$Zr_3Ni_3Sb_4$				
2 1 1	3.712	3.701	8	5 3 2	} 1.471	1.471	6
3 1 0	2.872	2.867	37	6 1 1		1.471	10
3 2 1	2.426	2.423	100	6 2 0	1.433	1.434	16
4 2 0	2.030	2.027	22	5 4 1	1.399	1.399	12
3 3 2	1.935	1.933	6	6 3 1	1.336	1.337	11
4 2 2	1.852	1.851	21	4 4 4	1.308	1.309	9
5 1 0	} 1.779	1.778	5	5 4 3	1.282	1.282	7
4 3 1		1.778	14	6 4 0	1.256	1.257	6
5 2 1	1.656	1.655	5	5 5 2	1.233	1.234	8
5 3 0	1.554	1.555	5	6 4 2	1.210	1.212	10
			$Hf_3Ni_3Sb_4$				
3 1 0	2.855	2.851	60	6 2 0	1.426	1.426	15
3 2 1	2.412	2.410	100	5 4 1	1.391	1.391	14
4 2 0	2.018	2.016	34	6 3 1	1.329	1.329	10
3 3 2	1.924	1.922	12	4 4 4	1.301	1.301	12
4 2 2	1.841	1.840	17	5 4 3	1.275	1.275	5
4 3 1	1.769	1.768	10	6 4 0	1.250	1.250	10
5 2 1	1.647	1.646	9	5 5 2	} 1.226	1.227	9
5 3 2	} 1.462	1.463	11	7 2 1		1.227	8
6 1 1		1.463	14	6 4 2	1.204	1.205	11

Table C-3. X-ray Powder Diffraction Data for $Zr_3Ni_3Sb_4$, $Hf_3Ni_3Sb_4$, and $Zr_3Pt_3Sb_4$ (continued)

				$Zr_3Pt_3Sb_4$			
2 1 1	3.837	3.821	43	6 2 0	1.479	1.480	15
2 2 0	3.320	3.309	5	6 3 1	1.380	1.380	11
3 2 1	2.504	2.501	100	4 4 4	1.351	1.351	13
4 2 0	2.095	2.093	43	6 4 0	1.298	1.298	13
3 3 2	1.998	1.995	12	5 5 2	} 1.273	1.274	11
4 2 2	1.913	1.910	16	7 2 1		1.274	8
5 1 0	} 1.837	1.836	12	6 4 2	1.250	1.251	12
4 3 1		1.836	17	7 3 0	1.228	1.229	5
5 2 1	1.710	1.709	11	6 5 1	1.188	1.189	6
6 1 1	1.518	1.518	5				

[a] The cell parameters refined from the powder patterns, obtained on a Guinier camera at room temperature and analyzed with the Filmscan and Jade 3.1 software packages (Materials Data Inc.: Livermore, CA, 1996), are a = 9.066(2), 9.016(1), and 9.359(1) Å, and V = 745.1(4), 732.8(4), and 819.8(4) $Å^3$ for $Zr_3Ni_3Sb_4$, $Hf_3Ni_3Sb_4$, $Zr_3Pt_3Sb_4$, respectively.

[b] The intensities were calculated based on positional parameters from the crystal structure of $Zr_3Ni_3Sb_4$ with the use of the program LAZY-PULVERIX (Yvon, K.; Jeitschko, W.; Parthé, E. *J. Appl. Crystallogr.* **1977**, *10*, 73).

Table C-4. Anisotropic displacement parameters [a] ($Å^2$) for $Zr_3Ni_3Sb_4$

Atom	U_{11}	U_{22}	U_{33}	U_{12}	U_{13}	U_{23}
Zr	0.0094(6)	0.0076(4)	0.0076(4)	0	0	0
Ni	0.0064(8)	0.0080(5)	0.0080(5)	0	0	0
Sb	0.0067(2)	0.0067(2)	0.0067(2)	0.00056(15)	0.00056(15)	0.00056(15)

[a] The form of the anisotropic displacement parameter is: $exp[-2\pi^2(h^2a^{*2}U_{11} + k^2b^{*2}U_{22} + l^2c^{*2}U_{33} + 2hka^*b^*U_{12} + 2hla^*c^*U_{13} + 2klb^*c^*U_{23})]$.

Table C-5. Anisotropic displacement parameters [a] ($Å^2$) for $Nb_{28}Pd_{33.5}Sb_{12.5}$

Atom	U_{11}	U_{22}	U_{33}	U_{12}	U_{13}	U_{23}
Nb(1)	0.0163(4)	0.0028(3)	0.0153(4)	0.0000(3)	0	0
Nb(2)	0.0084(3)	0.0052(3)	0.0089(3)	0.0014(2)	0	0
Nb(3)	0.0071(3)	0.0040(3)	0.0087(3)	–0.0002(2)	0	0
Nb(4)	0.0103(4)	0.0049(3)	0.0074(3)	–0.0008(2)	0	0
Nb(5)	0.0071(3)	0.0053(3)	0.0076(3)	–0.0006(2)	0	0
Nb(6)	0.0071(3)	0.0035(3)	0.0073(3)	–0.0001(2)	0	0
Nb(7)	0.0080(3)	0.0056(3)	0.0146(4)	0.0002(3)	0	0
Ni(1)	0.0097(4)	0.0077(3)	0.0078(3)	–0.0003(3)	0.0009(3)	0.0007(3)
Ni(2)	0.0119(4)	0.0072(4)	0.0075(4)	0.0006(3)	0.0009(3)	–0.0015(3)
Ni(3)	0.0101(5)	0.0062(4)	0.0150(5)	–0.0017(4)	0	0
Ni(4)	0.0095(5)	0.0062(5)	0.0095(5)	–0.0018(4)	0	0
Ni(5)	0.0088(5)	0.0070(4)	0.0129(5)	–0.0012(4)	0	0
Sb(1)	0.0074(2)	0.0039(2)	0.0083(2)	0.00075(18)	0	0
Sb(2)	0.0087(4)	0.0053(3)	0.0076(3)	0.0005(3)	0	0
$X(1)$ [b]	0.0099(3)	0.0058(3)	0.0082(3)	–0.00214(18)	0.0027(2)	–0.00220(17)
$X(2)$ [c]	0.0070(3)	0.0039(3)	0.0068(3)	0.00071(19)	0	0

[a] The form of the anisotropic displacement parameter is: $exp[-2\pi^2(h^2a^{*2}U_{11} + k^2b^{*2}U_{22} + l^2c^{*2}U_{33} + 2hka^*b^*U_{12} + 2hla^*c^*U_{13} + 2klb^*c^*U_{23})]$.

[b] Site $X(1)$ contains 59(2)% Ni and 41(2)% Sb.

[c] Site $X(2)$ contains 21(2)% Ni and 79(2)% Sb.

Table C-6. X-ray Powder Diffraction Data for $Nb_{28}Ni_{36}Sb_{10}$ and $Nb_{28}Ni_{32}Sb_{14}$ [a]

Hkl	d_{obs} (Å)	d_{calc} (Å)	I/I_o [b]	*hkl*	d_{obs} (Å)	d_{calc} (Å)	I/I_o [b]
			$Nb_{28}Ni_{36}Sb_{10}$				
3 2 1	3.079	3.070	5	6 4 0	1.942	1.942	5
2 4 1	2.873	2.866	3	6 3 1	1.893	1.892	10
4 2 1	2.618	2.615	3	7 2 0	1.839	1.839	5
0 0 2	2.509	2.506	37	4 7 1	1.790	1.790	8
3 5 1	2.335	2.334	88	3 5 3	1.411	1.411	11
5 2 1	2.249	2.248	100	5 2 3	1.390	1.392	14
2 7 0	2.217	2.216	35	0 7 3	1.361	1.362	11
2 3 2	2.157	2.155	19	8 7 0	1.350	1.352	7
0 4 2	2.141	2.141	22	8 3 2	1.337	1.337	11
0 7 1	2.130	2.130	64	6 10 0	1.319	1.319	2
3 2 2	2.107	2.106	68	3 12 0	1.308	1.310	8
5 5 0	2.062	2.061	40	5 9 2	1.288	1.290	20
1 8 0	2.038	2.034	3	0 0 4	1.252	1.253	9
1 5 2	1.977	1.972	16				
			$Nb_{28}Ni_{32}b_{14}$				
2 4 1	2.885	2.879	3	6 3 1	1.899	1.900	10
0 0 2	2.524	2.520	37	7 2 0	1.845	1.846	5
3 5 1	2.348	2.344	88	3 5 2	1.825	1.825	2
5 2 1	2.258	2.257	100	4 7 1	1.797	1.797	8
2 7 0	2.225	2.225	35	3 5 3	1.418	1.419	11

Table C-6. X-ray Powder Diffraction Data for $Nb_{28}Ni_{36}Sb_{10}$ and $Nb_{28}Ni_{32}Sb_{14}$ (continued)

6 0 0	2.211	2.209	10	5 2 3	1.398	1.399	14
2 3 2	2.168	2.166	19	0 10 2	1.382	1.383	3
0 4 2	2.153	2.152	22	0 7 3	1.369	1.369	11
0 7 1	2.140	2.139	64	8 7 0	1.355	1.357	7
3 2 2	2.118	2.116	68	8 3 2	1.343	1.343	11
5 5 0	2.070	2.069	40	6 10 0	1.322	1.324	2
1 8 0	2.043	2.042	3	3 12 0	1.316	1.316	8
4 0 2	2.007	2.006	8	5 9 2	1.295	1.295	20
1 5 2	1.984	1.982	16	0 0 4	1.258	1.260	9
6 4 0	1.951	1.949	5				

[a] The cell parameters refined from the powder patterns, obtained on a Guinier camera at room temperature and analyzed with the Filmscan and Jade 3.1 software packages (Materials Data Inc.: Livermore, CA, 1996), are a = 13.210(8), b = 16.469(9), c = 5.013(3) Å, and V = 1090.5(8) $Å^3$ for $Nb_{28}Ni_{36}Sb_{10}$, and a = 13.256(6), b = 16.537(7), c = 5.040(2), and V = 1104.9(6) $Å^3$ Å for $Nb_{28}Ni_{32}Sb_{14}$.

[b] The intensities were calculated based on positional parameters from the crystal structure of $Nb_{28}Ni_{33.5}Sb_{12.5}$ with Model B arrangement $Nb_{28}Ni_{36}Sb_{10}$ (Table 5-3) using the program ATOMS (Dowty, E. *ATOMS*; Shape Software: Kingsport, TN, 1999).

Table C-7. Anisotropic displacement parameters [a] (Å^2) for $Nb_4Pd_{0.5}ZSb_2$ (Z = Cr, Fe, Co, Ni, Si)

Atom	U_{11}	U_{22}	U_{33}	U_{12}	U_{13}	U_{23}
			$Nb_4Pd_{0.5}Cr_{0.28(3)}Si_{0.72}Sb_2$			
Nb	0.0056(3)	0.0061(3)	0.0082(3)	0.00022(19)	0	0
Pd [b]	0.0094(6)	0.0094(6)	0.0111(10)	0	0	0
Z [c]	0.0085(11)	0.0085(11)	0.0078(16)	0	0	0
Sb	0.0062(3)	0.0062(3)	0.0323(5)	0.0020(2)	0	0
			$Nb_4Pd_{0.5}FeSb_2$			
Nb	0.0046(4)	0.0064(4)	0.0090(4)	0.0004(2)	0	0
Pd [b]	0.0059(7)	0.0059(7)	0.0129(12)	0	0	0
Fe	0.0118(8)	0.0118(8)	0.0076(11)	0	0	0
Sb	0.0050(3)	0.0050(3)	0.0313(6)	0.0007(3)	0	0
			$Nb_4Pd_{0.5}CoSb_2$			
Nb	0.0063(3)	0.0073(4)	0.0093(4)	0.0002(2)	0	0
Pd [b]	0.0073(6)	0.0073(6)	0.0134(10)	0	0	0
Co	0.0083(6)	0.0083(6)	0.0069(9)	0	0	0
Sb	0.0065(3)	0.0065(3)	0.0315(5)	0.0010(2)	0	0
			$Nb_4Pd_{0.5}Ni_{0.78(1)}Sb_2$			
Nb	0.0022(4)	0.0036(5)	0.0081(5)	0.0003(3)	0	0
Pd [b]	0.0090(10)	0.0090(10)	0.0058(16)	0	0	0
Ni [d]	0.0031(13)	0.0031(13)	0.0064(18)	0	0	0

Table C-7. Anisotropic displacement parameters [a] (Å^2) for $Nb_4Pd_{0.5}ZSb_2$ (Z = Cr, Fe, Co, Ni, Si) (continued)

Sb	0.0036(3)	0.0036(3)	0.0289(7)	0.0009(4)	0	0
			$Nb_4Pd_{0.5}SiSb_2$			
Nb	0.0077(11)	0.0070(11)	0.0093(11)	–0.0007(8)	0	0
Pd [b]	0.005(2)	0.005(2)	0.009(4)	0	0	0
Si	0.009(4)	0.009(4)	0.001(6)	0	0	0
Sb	0.0063(8)	0.0063(8)	0.0282(16)	0.0013(9)	0	0

[a] The form of the anisotropic displacement parameter is: $exp[-2\pi^2(h^2a^{*2}U_{11} + k^2b^{*2}U_{22} + l^2c^{*2}U_{33} + 2hka^*b^*U_{12} + 2hla^*c^*U_{13} + 2klb^*c^*U_{23})]$.

[b] 50% occupancy.

[c] Site Z contains 28(3)% Cr and 72% Si.

[d] 78(1)% occupancy.

Table C-8. X-ray Powder Diffraction Data for $ZrPd_3Si_3$ [a]

hkl	d_{obs} (Å)	d_{calc} (Å)	I/I_o [b]	*hkl*	d_{obs} (Å)	d_{calc} (Å)	I/I_o [b]
0 2 0	7.808	7.758	22	0 0 4	1.755	1.756	8
0 2 1	5.221	5.206	5	0 8 2	1.697	1.698	9
1 1 0	3.701	3.696	7	2 6 0	1.532	1.532	10
1 1 1	3.275	3.270	24	1 3 4	1.523	1.523	4
0 2 2	3.204	3.199	6	0 8 3	1.493	1.493	6
0 4 2	2.603	2.603	6	2 2 3	1.450	1.450	14
0 6 0	2.586	2.586	23	1 9 2	1.433	1.433	13
1 5 0	2.406	2.405	21	2 4 3	1.379	1.380	5
1 3 2	2.310	2.309	100	1 11 0	1.322	1.322	4
1 5 1	2.276	2.275	32	1 1 5	1.312	1.313	7
0 2 3	2.241	2.241	25	1 11 1	———	1.300	4
0 4 3	2.005	2.004	8	0 10 3	} 1.293	1.293	4
1 5 2	1.985	1.984	6	0 12 0		1.293	5
1 1 3	1.978	1.977	4	2 0 4	1.290	1.290	7
2 0 0	1.903	1.902	24	2 8 2	———	1.267	9
0 8 1	1.870	1.869	4	1 5 5	1.212	1.213	14
1 7 1	1.848	1.848	6	2 8 3	1.173	1.175	7

[a] The cell parameters refined from the powder pattern, obtained on a Guinier camera at room temperature and analyzed with the Filmscan and Jade 3.1 software packages (Materials Data Inc.: Livermore, CA, 1996), are: a = 3.805(1), b = 15.515(5), and c = 7.022(2) Å.

[b] The intensities were calculated based on positional parameters from the crystal structure of $ZrPd_3Si_3$ with the use of the program LAZY-PULVERIX (Yvon, K.; Jeitschko, W.; Parthé, E. *J. Appl. Crystallogr.* **1977**, *10*, 73).

Table C-9. Anisotropic displacement parameters [a] ($Å^2$) for $ZrPd_3Si_3$

Atom	U_{11}	U_{22}	U_{33}	U_{12}	U_{13}	U_{23}
Zr	0.0057(2)	0.0054(2)	0.0058(2)	0	0	0
Pd(1)	0.00759(16)	0.00675(14)	0.00616(14)	0	0	–0.00041(8)
Pd(2)	0.0082(2)	0.00523(18)	0.00632(17)	0	0	0
Si(1)	0.0077(5)	0.0053(4)	0.0080(4)	0	0	–0.0007(3)
Si(2)	0.0074(7)	0.0077(6)	0.0068(6)	0	0	0

[a] The form of the anisotropic displacement parameter is: $exp[-2\pi^2(h^2a^{*2}U_{11} + k^2b^{*2}U_{22} + l^2c^{*2}U_{33} + 2hka^*b^*U_{12} + 2hla^*c^*U_{13} + 2klb^*c^*U_{23})]$.

Table C-10. X-ray Powder Diffraction Data for $LaCu_{1.23(1)}As_2$, $CeCu_{1.10(1)}As_2$ and $PrCu_{1.09(1)}As_2$ [a]

Hkl	d_{obs} (Å)	d_{calc} (Å)	I/I_o [b]	*hkl*	d_{obs} (Å)	d_{calc} (Å)	I/I_o [b]
			$LaCu_{1.23(1)}As_2$				
1 1 0	2.901	2.898	6	2 1 5	1.670	1.670	19
1 0 5	2.887	2.883	42	2 0 8	1.593	1.594	12
1 1 2	2.790	2.786	3	2 1 7	1.547	1.549	5
0 0 8	2.535	2.535	11	1 1 12	1.459	1.460	12
1 1 4	2.518	2.516	100	2 2 0	1.448	1.449	17
1 0 7	2.367	2.366	8	2 1 9	1.421	1.422	18
2 0 0	2.051	2.049	44	3 1 0	1.296	1.296	2
1 0 9	1.976	1.975	21	3 0 5	1.294	1.295	5
1 1 8	1.909	1.908	5	3 1 4	1.255	1.256	32
2 1 1	1.826	1.825	3				
			$CeCu_{1.10(1)}As_2$				
1 0 1	3.752	3.742	17	2 1 2	1.697	1.697	5
0 0 3	3.374	3.363	2	2 1 3	1.588	1.588	18
1 0 2	3.154	3.148	14	2 0 4	1.573	1.574	13
1 1 0	2.854	2.849	5	2 1 4	1.466	1.466	3
1 1 1	2.745	2.742	3	1 1 6	1.448	1.448	11
1 0 3	2.584	2.582	34	2 2 0	1.424	1.425	16
0 0 4	2.524	2.522	12	1 0 7	1.357	1.357	5
1 1 2	2.483	2.481	100	2 1 5	1.344	1.344	19
1 1 3	2.177	2.174	1	1 1 7	1.285	1.286	4

Table C-10. X-ray Powder Diffraction Data for $LaCu_{1.23(1)}As_2$, $CeCu_{1.10(1)}As_2$ and $PrCu_{1.09(1)}As_2$ (continued)

1 0 4	2.139	2.138	4	3 1 0	1.274	1.274	2
2 0 0	2.017	2.015	40	0 0 8	1.260	1.261	4
1 1 4	1.889	1.889	3	3 0 3	1.246	1.247	5
1 0 5	1.804	1.804	20	2 2 4	1.238	1.240	8
2 1 1	1.775	1.774	5	3 1 2	1.234	1.235	32
2 0 3	1.729	1.728	2				
			$PrCu_{1.09(1)}As_2$				
1 0 1	3.735	3.726	17	2 1 1	1.766	1.766	5
0 0 3	3.359	3.352	2	2 1 2	1.689	1.690	5
1 0 2	3.142	3.136	13	2 1 3	1.581	1.582	17
1 1 0	2.842	2.836	5	2 0 4	1.567	1.568	13
1 0 3	2.573	2.572	33	2 1 4	1.460	1.460	3
0 0 4	2.515	2.514	13	1 1 6	1.442	1.443	11
1 1 2	2.472	2.470	100	2 2 0	1.417	1.418	15
1 1 3	2.165	2.165	1	1 0 7	1.352	1.352	5
1 0 4	2.132	2.130	4	2 1 5	1.337	1.339	19
2 0 0	2.008	2.006	40	1 1 7	1.280	1.281	4
1 1 4	1.881	1.881	3	3 0 3	1.240	1.242	5
1 0 5	1.798	1.798	20				

[a] The cell parameters refined from the powder patterns, obtained on a Guinier camera at room temperature and analyzed with the Filmscan and Jade 3.1 software packages (Materials Data Inc.: Livermore, CA, 1996), are a = 4.0984(9), c = 20.280(8) Å, and V = 340.6(2) Å^3 for $LaCu_{1.23(1)}As_2$, a = 4.030(1), c = 10.089(4) Å, and V = 163.8(1) Å^3 for

Table C-10. X-ray Powder Diffraction Data for $LaCu_{1.23(1)}As_2$, $CeCu_{1.10(1)}As_2$ and $PrCu_{1.09(1)}As_2$ (continued)

$CeCu_{1.10(1)}As_2$, and a = 4.011(2), c = 10.055(4) Å, and V = 161.8(1) $Å^3$ for $PrCu_{1.09(1)}As_2$.

[b] The intensities were calculated based on positional parameters from the crystal structure of $LaCu_{1.23(1)}As_2$, $CeCu_{1.10(1)}As_2$ and $PrCu_{1.09(1)}As_2$ with the use of the program LAZY-PULVERIX (Yvon, K.; Jeitschko, W.; Parthé, E. *J. Appl. Crystallogr.* **1977**, *10*, 73).

Table C-11. Anisotropic Displacement Parameters [a] ($Å^2$) for $LaCu_{1.23(1)}As_2$, $CeCu_{1.10(1)}As_2$, and $PrCu_{1.09(1)}As_2$

Atom	U_{11}	U_{22}	U_{33}	U_{12}	U_{13}	U_{23}
			$LaCu_{1.23(1)}As_2$ [b]			
La	0.0068(2)	0.0068(2)	0.0097(3)	0	0	0
Cu(1)	0.0129(4)	0.0129(4)	0.0099(4)	0	0	0
As(1)	0.0124(5)	0.0464(8)	0.0084(4)	0	0	0
As(2)	0.0063(3)	0.0063(3)	0.0108(4)	0	0	0
			$CeCu_{1.10(1)}As_2$ [b]			
Ce	0.0068(2)	0.0068(2)	0.0108(2)	0	0	0
Cu(1)	0.0116(3)	0.0116(3)	0.0110(4)	0	0	0
As(1)	0.0265(3)	0.0265(3)	0.0090(4)	0	0	0
As(2)	0.0062(2)	0.0062(2)	0.0114(3)	0	0	0
			$PrCu_{1.09(1)}As_2$ [b]			
Pr	0.0082(3)	0.0082(3)	0.0086(3)	0	0	0
Cu(1)	0.0129(4)	0.0129(4)	0.0098(5)	0	0	0
As(1)	0.0281(5)	0.0281(5)	0.0076(5)	0	0	0
As(2)	0.0076(4)	0.0076(4)	0.0096(5)	0	0	0

[a] The form of the anisotropic displacement parameter is: $exp[-2\pi^2(h^2a^{*2}U_{11} + k^2b^{*2}U_{22}$ $l^2c^{*2}U_{33} + 2hka^*b^*U_{12} + 2hla^*c^*U_{13} + 2klb^*c^*U_{23})]$.

[b] The Cu(2) sites were refined isotropically.